UNIVERITÀ DEGLI STUDI DI PADOVA

Sede Ammistrativa : Università degli Studi di Padova

Dipartimento di Ingegneria Meccanica – Settore Materiali

SCUOLA DI DOTTORATO DI RICERCA IN SCIENZA ED INGEGNERIA DEI MATERIALI

CICLO XXII

Tesi di Dottorato

MULTIFUNCTIONAL NANOSTRUCTURED MATERIALS BASED ON CdSe AND TiO_2 NANOPARTICLES

Direttore della Scuola: Ch.mo Prof. Gaetano Granozzi

Supervisore: Ch.mo Prof. Massimo Guglielmi

Dottorando: Alessandro Antonello

ANNO 2009

Abstract

Nanotechnology has arisen as one of the most important fields in recent research, for the implications in both basic and applied science and technological applications.
The manipulation of matter at the nanoscale is accompanied by the appearance of novel properties and large surface to volume ratio which can be exploited in a number of applications ranging from optics, catalysis and sensing, to name a few.
In this work, we mainly focused on the synthesis and the use of nanomaterials for the preparation of nanocomposites and structures to be employed in the optical field. The main advantage of introducing nanosized inclusions in a host material is that specific functionalities or desired optical change can be imparted while transparency in the visible range can be retained.

The whole activity can be divided in the synthesis and processing of nanoparticles and in their usage for some specific application.
Cadmium selenide (CdSe), Titanium dioxide and layered titanates have been mainly addressed due to PL emission properties and high refractive index. In addition, zinc sulfide (ZnS) nanoparticles have been synthesized.
CdSe nanoparticles (Quantum Dots) have been obtained by colloidal chemistry and part of the work has been spent in the synthesis of core-shell nanoparticles with a CdSe core and a shell of semiconductor materials with wider band gap in order to increase the stability of the emission properties of such materials. These nanoparticles were introduced in sol-gel derived ZrO_2 waveguides to obtain materials showing optical gain which was characterized by ASE (Amplified Spontaneous Emission) experiments.

High refractive index materials are useful in many optical applications. High refractive index depositions were obtained introducing Titania nanoparticles in proper matrices.
A sol-gel synthesis for titanium dioxide nanoparticles has been developed yielding to anatase particles in the 3-5 nm range. These were embedded in an epoxy-based hybrid material obtaining transparent depositions with refractive index in the 1.51-1.89 range.

Layered titanates were further addressed since they allowed extending the processing and engineering of titanium oxide materials. A synthetic colloidal procedure

was developed, in which titanate nano-sheets are produced by reaction of a titanium alkoxide and an organic base.

These materials allowed to obtained composites with multifumctional properties since materials embedding both titanate sheets and quantum dots could be obtained and applied in PL active waveguide and functional coating for LED devices to improve light extraction and produce white light through down-conversion. Coatings for LED were also developed using conventional sol-gel derived hybrid materials.

The obtained layered titanates could also be modified and treated by UV curing, leading to material's densification and enhancement of the refractive index at relatively low temperatures (200 °C). This processing behavior has been exploited in Bragg mirror fabrication and vertical optical microcavity incorporating quantum dots. The procedure employed for microcavity fabrication was found to be effective in keeping the optical properties of quantum dots, allowing for optical characterization of this structure.

The properties of titanium dioxide have been exploited for optical gas sensing applications embedding gold nanoparticles in a crystalline TiO_2 matrix. Anatase TiO_2 particles have been successfully used as matrix material for this application. The employed preparation of such nanocomposites allowed tailoring of porosity and gold-titania interface which could be studied by optical measurements. Optical sensing was evidenced by variation in thin film absorbance at wavelengths near the plasmon resonance of gold nanoparticles caused by the presence of the gas analytes.

Gold nanorods were introduced in the synthesized titanates. Gold nanorods are known to spheroidise upon thermal treatment, losing their peculiar optical properties. We found that the processing treatments developed for titanates resulted in improved thermal stability of such nanostructures as shown by optical measurements. This result is very interesting since it would allow extending gold nanorods's exploitation in optical applications.

Finally, composites with enhanced refractive index were realized by introducing ZnS nanoparticles in hybrid sol-gel material. A synthesis of ZnS nanoparticles has been developed, which allows nanoparticles functionalization and introduction in a hybrid organic-inorganic sol-gel matrix.

Abstract *(Italiano)*

Il campo delle nanotecnologie è diventato tra i più importanti nella recente ricerca scientifica. È' un settore multidisciplinare nelle conoscenze che ne costituiscono le basi e trova applicazione in svariati ambiti della tecnologia.

La manipolazione della materia su nanometrica è accompagnata dalla comparsa di nuove proprietà ed un elevato valore di superficie per unità di volume. Queste proprietà possono essere sfruttate in applicazioni nei campi dell'ottica, della catalisi e della sensoristica, per non citarne che alcuni.

In questo lavoro, l'attività è stata principalmente focalizzata sulla sintesi e l'uso di materiali nanostrutturati per la preparazione di nanocompositi e strutture di interesse nel campo dell'ottica. Il vantaggio principale nell' introdurre particelle nanometriche in un materiale risiede nella possibilità di introdurre specifiche funzionalità o variazioni nelle proprietà ottiche mantenendo nello stesso tempo la trasparenza nel visibile.

L'intera attività può essere divisa nella sintesi e successiva manipolazione di nanoparticelle e nel loro uso in specifiche applicazioni.

Seleniuro di Cadmio (CdSe), Biossido di Titanio (TiO_2) e Titanati a strati sono stati principalmente presi in considerazione per sfruttare specifiche proprietà di fotoluminescenza e di elevato indice di rifrazione. Sono inoltre state sintetizzate nanoparticelle di Solfuro di Zinco (ZnS).

Nanoparticelle di CdSe, anche chiamate Quantum Dots (QDs), sono state ottenute attraverso sintesi di tipo colloidale. Parte del lavoro è stata dedicata al ricoprimento di queste nanoparticelle con semiconduttori a più elevato band gap con lo scopo di aumentare la stabilità delle proprietà di emissione di questi materiali. Queste nanoparticelle sono state introdotte in guide d'onda costituite da Biossido di Zirconio (ZrO_2) ottenuto per via sol-gel per ottenere materiali con proprietà di guadagno ottico testate in esperimenti di emissione spontanea amplificata (ASE).

Materiali ad alto indice di rifrazione trovano utilizzo in molte applicazioni ottiche. Deposizioni a elevato indice di rifrazione sono state ottenute introducendo particelle di biossido di titanio in opportune matrici.

E' stata sviluppata una sintesi di tipo sol-gel in grado di produrre soluzioni colloidali stabili di particelle cristalline con la struttura cristallografica dell'anatase con

diametro intorno a 3-5 nm. Queste nanoparticelle sono state introdotte in una matrice ibrida sol-gel ottenendo deposizioni trasparenti con indice di rifrazione variabile tra 1.51 e 1.89.

Sono stati successivamente presi in considerazione i titanati a strati perché permettono di estendere le possibilità di manipolazione ed ingegnerizzazione di materiali a base di ossido di titanio.

È stata sviluppata una sintesi colloidale in cui "foglietti" nanometrici di titanati sono prodotti per reazione di un alcossido di titanio e una base organica.

Questi materiali hanno permesso di ottenere compositi con proprietà multifunzionali. Infatti, materiali contenenti titanati lamellari e QDs sono stati ottenuti e applicati in guide d'onda con proprietà di fotoluminescenza e ricoprimenti funzionali su dispositivi LED per migliorare la frazione di luce estratta e produrre luce bianca per conversione di parte della luce emessa in luce a lunghezza d'onda maggiore. Ricoprimenti per LED sono inoltre stati sviluppati con materiali ibridi sol-gel più convenzionali.

I titanati stratificati sono stati trattati utilizzando radiazione UV. Questo genere di trattamento porta a una densificazione del materiale con conseguente aumento dell'indice di rifrazione impiegando durante il processo temperature relativamente basse (200 °C). Questo trattamento è stato impiegato nella fabbricazione di specchi multistrato dielettrici e cavità ottiche verticali dove sono stati inseriti QDs come emettitori luminescenti. Il metodo utilizzato è stato verificato essere compatibile con la conservazione delle proprietà di emissione dei Quantum Dots, permettendo la caratterizzazione ottica delle strutture sviluppate.

Sono state inoltre considerate applicazioni sensoristiche per il rilevamento di gas tramite misure ottiche di materiali a base di TiO_2 contenenti nanoparticelle d'oro.

Le nanoparticelle di anatase in precedenza menzionate sono state adoperate come matrice, consentendo sia di agire sulla porosità, sia di caratterizzare l'interfaccia oro/titania tramite misure ottiche. La funzionalità sensoristica è stata determinata studiando la variazione nell'assorbanza ottica a lunghezze d'onda vicine alla risonanza plasmonica delle particelle d'oro, causata dalla presenza di uno specifico gas nell'atmosfera.

Nanorods di oro sono stati inseriti in matrici di titanati lamellari. Queste nanostrutture d'oro tendono ad assumere la forma sferica in seguito a trattamento termico perdendo così le loro specifiche proprietà. Il trattamento di densificazione sviluppato per i titanati è stato applicato per questi compositi, fornendo una migliore stabilità termica dei nanorods, come dimostrato da misure ottiche. Questo risultato è interessante poiché potrebbe permettere di estendere l'utilizzo di queste nanostrutture in applicazioni ottiche.

Infine, sono stati realizzati compositi con aumentato indice di rifrazione utilizzando particelle di solfuro di zinco per le quali è stata sviluppata una sintesi colloidale e una procedura di funzionalizzazione per il loro inserimento in matrici ibride sol-gel.

Acknowledgments

First, I want to thank my supervisor Prof. Massimo Guglielmi for the chance to have a research experience.
Many thanks to Prof. Alessandro Martucci to have been always helpful in the activity carried out in this three years Ph.D period.
They are also gratefully acknowledged for the support in writing the present work.

Many of the data and results presented in this thesis come from very fruitful collaborations. Thus, a lot of acknowledgements are due to many persons who permitted me to develop at best my Ph.D activity.
A great thanks to Prof. Giovanni Mattei and Dr. Valentina Bello for all Transmission Electron Microscopy analyses and relative data processing presented in this work.
Dr. Raffaella Signorini, Dr Ilaria Fortunati and Dr. Francesco Todescato are gratefully acknowledged for Amplified Spontaneous Emission characterization and relative data processing.
Maurizio Ferrari, Dr. Alessandro Chiasera and Dr. Guillame Alombert are acknowledged for the optical characterization regarding waveguides and optical microcavity.
Dr. Brusatin Giovanna and Dr. Della Gustina Gioia are acknowledged for support in the synthesis of sol-gel hybrid materials.
Beyond to the always excellent professional attitude of all the people cited before, I want to thank them also for sharing their knowledge with me and for fruitful discussions.

This three years experience allowed me to work with a lot of people I am honored to have known, not only for their scientific competence but also for the sincere friendship grown during this period. With this respect, I want to acknowledge all my colleagues Enrico, Marco, Gioia, Marta, Giovanni, Anna, Ilenia, Cekdar, Giulio, Dario, Alfredo, Sirio, Roberta and Mauro.

Finally, the most important thanks to my father, my mother, my brother and my sister for the unconditioned support.

Contents

Chapter 1

Introduction

1.1 Introductory remarks

The increasing request of materials possessing novel properties has motivated a considerable part of recent research in this area. In particular, advances in application fields such as optics, catalysis and sensing, to name a few, are strictly dependent on the possibility of optimizing, at the same time, different aspects of the material to be used.
Successful devices fabrication often requires different functional properties to be present in the same material, possibility of shaping and manufacturing to achieve specific structures and compatibility of processing conditions of the different materials used.
Nanoscience and nanotechnology have imposed themselves as important tools in achieving the above described requirements. Relevant features of nano-scaled materials include:

a) arising of new optical and electronic properties with respect to bulk
b) dramatic increase of surface to volume ratio maximizing active interfaces
c) realization of composite materials embedding nano-sized objects in a matrix for imparting desired functionalities while maintaining elevated homogeneity with respect, for example, to light interaction (nanometric phases do not scatter light).

Beyond arising of novel properties, nanoscaled objects can be combined together in the same materials to create nanocomposites. This class of materials consists of a host matrix where one or more nanometric inclusions are embedded. The resulting material can be regarded as a homogeneous medium. This strategy allows for novel functional, physical or chemical properties which can be tailored by acting on the type of inclusion, matrix and their interface.
By proper choice of constituents and their combination, different requirement can be met in the same material.

1.2 Motivation and outline

In the present thesis work, the synthesis and application of nanostructured materials is described with the aim of producing multifunctional innovative materials. Beyond functional properties, the activity has been directed toward materials which could be processed or treated in conditions such that their combination in nanocomposites or devices does not result in loss of their peculiar properties.

These features are extremely relevant in a lot of research fields, even if the main application considered in the present work deals with optical properties.

In this field, not only optical properties of the material are important, but also the possibility of shaping into specific geometry would be desired.

Nanocomposites offer the possibility to introduce and tune more than one properties in a suitable host material. In particular, great interest is found in introducing optically active functionalities such as luminescence properties and in tuning dielectric properties, such as refraction index.

Proper choice of the host matrix can be exploited to give suitable processing behavior with the desired fabrication technique.

These properties can be exploited in a number of devices such as optically-active photonic structures, conformal coatings and waveguides.

The aim of the present work resides in the synthesis of nanoparticles and their introduction in proper matrices in order to obtain nanocomposites and structures to be employed in the optical field. Thus, the main part of the PhD activity has been spent on the synthesis of nanoparticles, their processing and introduction in host materials in order to modify and tune their optical properties.

Basically, the approach we followed consisted in synthesizing NPs separately with respect to composite synthesis (ex-situ approach) using colloidal methods. This allows tailoring optimal conditions for the desired particle crystallinity, structure and subsequent functionalization necessary to make them compatible with the desired host material.

In this work, *Cadmium Selenide* and *Titanium Dioxide* based nanostructured materials have been mainly addressed. Minor work has also been devoted to *Zinc Sulfide* nanoparticles.

CdSe quantum dots (QDs) have been synthesized and used as the optically active component. Semiconductor nanoparticles are very promising as efficient luminescent emitters for preparation of optically active materials. They are more stable than organic

dyes and can be properly functionalized to be homogeneously introduced in different matrices.

In order to have greater stability of emission properties, CdSe core particles are generally covered by shell of semiconductor materials with wider band gap. Thus a part of the thesis work has been spent in the synthesis of such heterostructures.

Optical structures often require high refractive index materials. *Titanium dioxide* has been used as the high refractive index component and the attention has been focused on *Titanium dioxide nanocrystals (NCs)* and *Layered Titanates* which could be processed into nanocomposite.

TiO_2 NCs have already been applied for varying dielectric properties. In this case, we focused on obtaining crystalline particles at mild synthetic conditions while keeping colloidal stability. These are important conditions since crystallinity ensures high refractive index and colloidal stability with absence of large agglomerates is necessary for having transparent materials that does not scatter light.

Layered titanates have attracted our interest since they can be modified and treated by methods other than thermal annealing. In fact UV irradiation has been exploited as an alternative route for densification and refractive index enhancement. Furthermore, specific titanates were found to be compatible with quantum dots.

Transmission Electron Microscopy (TEM) and X Ray diffraction (XRD) analyses were used for structural characterization of nanoparticles. Optical characterization was carried out with UV-Vis spectroscopy and photoluminescence analyses.

The above mentioned materials have been used for fabricating nanocomposites or deposition fabrication. Materials incorporating one type of particles have been obtained to impart a specific modification or functionality. A further development regarding the incorporation of more than one type of particles has also been worked out to obtain multifunctional materials.

These materials were mainly analyzed by means of UV-Vis and FT-IR spectroscopy and spectroscopic ellipsometry for optical characterization, while structural evolution was mainly followed by XRD measurements.

In details, semiconductor QDs have been embedded in sol-gel derived zirconium oxide waveguides that have been used in Amplified Stimulated Emission Experiments (ASE) in order to verify the effectiveness of QDs loaded nanocomposites as optical gain media.

TiO_2 NCs has been introduced in an epoxy-based hybrid organic-inorganic matrix in order to enhance the refractive index.

A multifunctional nanocomposite material embedding both QDs for luminescence properties and layered titanates for for refractive index enhancement was obtained. These properties could be exploited for QDs loaded waveguides.

This strategy was also used for the encapsulation of LED encapsulation, where a thick coating with an high refractive index (due to TiO_2) and down conversion properties (due to QDs) can be used to enhance light extraction from LED and to produce white light through conversion of a part of the LED emission in lower energy radiation. This activity was also developed with a more conventional sol-gel organic-inorganic hybrid material.

The possibility to use QDs for optical gain has motivated their introduction in optically active devices such as coplanar microcavitiy. Bragg mirrors have been obtained using the developed titanates as the high refractive index layer, while sol-gel SiO_2 film has been used as the low refractive index layer.

ZnS is another interesting material due to its high refractive index and transparency in the visible range. For these reasons, nanocomposites with enhanced refractive index were obtained introducing ZnS NCs in sol-gel hybrid materials.

The synthesized TiO_2 nanostructured materials have also been used in combination with gold nanoparticles for optical gas sensing applications.

Finally, gold nanorods were introduced in titanates matrix to improve their thermal stability.

The thesis can be divided in three sections.

The first comprises *Chapter 1* in which the introduction, motivation and outline of the entire work is presented and *Chapter 2* in which there are described the experimental set-up used for the synthesis and the instrumentation used for samples characterization are described.

The second part comprises *Chapter 3* and *Chapter 4*, in which the synthesis of nanocrystals and their characterization is described. In *Chapter 3* a brief literature review on properties and synthesis of core and core@shell CdSe particles is first presented. The colloidal synthesis of such nanostructures is then described along with their TEM and optical characterization. In *Chapter 4* details of the synthesis of anatase-TiO_2 and layered titanates is described after a brief bibliographic summary of the properties and synthesis of these materials.

The last section will deal with applications of the synthesized materials. In *Chapter 5*, the use of TiO_2 and layered titanates for high refractive index depositions and conformal

coatings (i.e. LED encapsulation) is described. Gold loaded titania materials are then presented in the final part of this chapter. In *Chapter 6* the preparation of quantum dots-loaded sol-gel zirconia waveguides for Amplified Spontaneous Emission (ASE) applications and the fabrication of optical coplanar microcavity incorporating quantum dots is described. *In Chapter 7* the results on ZnS NC loaded nanocomposites are presented.

Finally, the conclusions and future perspectives of the PhD activity will be discussed in *Chapter 8*.

Chapter 2

Materials and Methods

In this chapter, a brief description of the instrumentation and methods involved in materials synthesis and characterization is given.

2.1 Materials and Synthesis setup

Synthesis setup

The synthesis setup shown in the picture of figure 2.1 consists in a heating mantle, a temperature controller (J-Kem Gemini-J temperature), a three-necked flask and a glass syringe.
The flask was fitted with a refluxing condenser connected with a Schlenk line for inert gas/vacuum switching operations. Vacuum was obtained with a rotary pump which allows to reach 0,003 bar in the reaction flask.

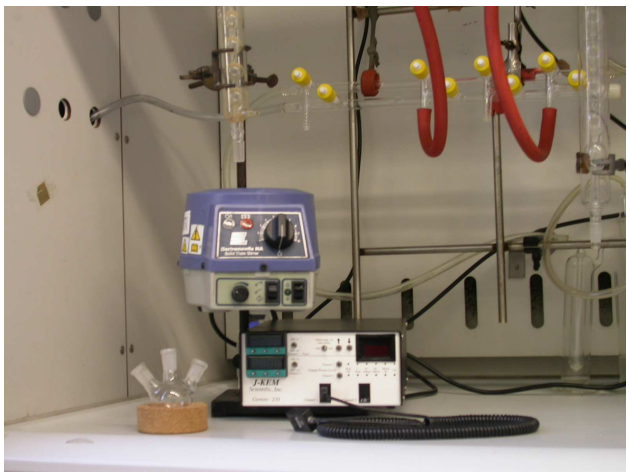

Figure 2.1 Experimental setup used for nanoparticles synthesis

The temperature controller allows achieving the desired temperature through controlling power supply to the heating mantle. The temperature was monitored by means of a J-type thermocouple inserted in the reaction flask through an available neck. The remaining neck

was sealed with a rubber septum through which injection of regents loaded in the syringe was possible.

Chemicals

Glycydoxypropyltrimethoxysilane (GPTMS), Titanium Tetraisopropoxide $Ti(IsPrOH)_4$, Titanium tetraisopropoxide, ethylene glycol, 1-amino-1-hexanol, polyethylene glycol (average molecular weight : 1000), polyvinilpirrolidone (average molecular weight : 10000), cadmium oxide, zinc oxide, oleic acid, diisooctylphosphinic acid, octadecylammine, octadecene, elemental selenium, elemental sulphur and all employed solvents were purchased from Aldrich.
3-isocyanatopropyltrimethoxysilane was purchased from ABCR.
Doubly distilled water was used in the reactions.

2.2 Instrumentation

X-Ray Diffraction

The crystalline phases of produced materials have been characterized by a Philips PW1710 X-Ray diffraction (XRD) using a diffractometer equipped with grazing-incidence X-ray optics. The analysis was performed using CuK_α-Ni filtered radiation at 30 kV and 40 mA. Due to limited amount of produced materials, powder samples were most often analyzed with the grazing angle optics. This was performed by depositing on a quartz or silicon substrate a thick layer (about 1 millimeter) of powder. The X-Ray incident angle was set equal to 3°.
When thin films were analyzed, a grazing angle of 0.5° was used.
The average crystallite size was calculated using the Scherrer correlation after fitting the experimental profiles with a pseudo-Voigt (sum of Gaussian and Lorentzian) function.

Transmission Electron Microscopy

Transmission Electron Microscopy (TEM) measurements were performed on a FEI-Tecnai Field-emission Gun (FEG) (S)TEM F-20 Super Twin, at 200 kV primary tension. Analyses were done on nanoparticles deposited from a colloidal solution on a holey carbon film supported by a copper grid or in cross-sectional samples for NCs embedded in thin films.
In the case of titanates materials described in sections 4.3.2 and 4.3.3, the samples was prepared by just dispersing the titanate powders in methanol without obtaining a clear sol. Thus, particles aggregates were deposited on the copper grid.

UV-Vis and photoluminescence measurements

UV-Vis-NIR absorption spectra were taken using a JASCO V-570 spectrometer.
Absorption measurements of liquid samples was performed with a quartz cuvette (1 cm optical path), while thin films on quartz substrate were analyzed placing the substrate perpendicularly to the light beam.
For measurements of the pure absorption component of a thin film deposition, both transmittance (T) and reflectance (R) spectra were taken using an integrating sphere attachment (Model ISV-469, internally coated with barium sulfate) which could be mounted directly in the spectrophotometer sample chamber. The absorption component could be calculated as *100-T- R.*

Photoluminescence measurements of fluorophores dissolved in a liquid medium were taken on a Jasco FP-6300 standard spectrofluorimeter. A quartz cuvette with 1 cm optical path was used also in this case.
Beyond steady state PL measurements, determination of quantum yield of synthesized fluorophores could be performed through comparison of the integrated PL from an organic dye whose quantum yield is known. We have used Rhodamine 6G for this purpose with a quantum yield value of 0.98 for an excitation wavelength of 480 nm.
The absorbance of both sample and organic dye was kept low (in the 0.01-0.1 range) to avoid re-absorption phenomena and assure the same exited volume and light generation geometry.
The following relationship has been used for quantum yield determination [1]:

$$QY = QY_R \frac{I}{I_R} \frac{(1-10^{-abs_R})}{(1-10^{-abs})} \frac{n^2}{{n_R}^2}$$

Where *QY, I, (1-10^{-abs})* and *n* are the quantum yield, the integrated PL emission, the fraction of absorbed light at PL excitation wavelength (480 nm) and refractive index of the solvent used respectively. Analogues quantities are indicated with subscript *"R"* for the organic dye reference sample.

FT-IR and Raman spectroscopy

Fourier Transform Infrared Spectroscopy (FTIR) measurements were performed in the 400-4000 cm^{-1} range using a JASCO FT-IR 6300 system using a resolution of 2 cm^{-1} on films deposited on silicon wafer substrate. If powders were to be analyzed, they were embedded in a KBr pellet which was then analyzed.

Raman spectroscopy (FT-Raman) measurements were performed with a JASCO RFT-600 Raman attachment operating at a 1064 nm wavelength excitation laser. In this case, samples were analyzed as powders.

Spectroscopic ellipsometry

Spectroscopic ellipsometry analyses were done with a VASE32 J. A. Wollam Co. Measurements.
This is a rotating analyzer ellipsometer, whose main components are:

Light source / Polarizer / Sample /Continuously Rotating Analyzer / Detector

A light with known polarization (generally linearly polarized) is obtained through a polarizer placed after the light source. This beam interacts with the sample (i.e. a substrate coated with a thin film) and the resulting reflected wave is analyzed to get its polarization state. In the employed configuration, this operation is done by modulating the signal with a rotating polarizer placed before the detector. The modulated signal can be processed in order to get the ellipsometer parameter of ψ e Δ.
These parameters are related to the "s" (TE) or "p" (TM) polarization state of the electromagnetic wave which respectively have the electric field vector (TE) or magnetic field vector (TM) perpendicular to the plane of incidence.

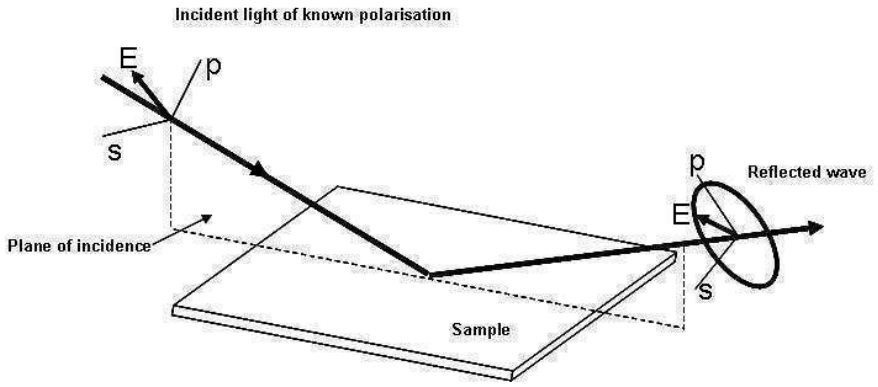

Figure 2 Schematic of light interaction with an interface

The Fresnel coefficients define the reflection of a light beam from a single interface and are different for "s" and "p" states.

In their polar form, the reflected waves can be expressed as:

$$\tilde{E}_r^{p,s} \equiv \tilde{r}^{p,s}\,\tilde{E}_i^{p,s} \equiv r^{p,s} e^{i\Delta^{p,s}}$$

where Δ is the phase change upon reflection, r is ratio between the amplitude of incident ($\tilde{E}_i^{p,s}$) and reflected ($\tilde{E}_r^{p,s}$) electric field vectors and $\tilde{r}^{p,s}$ is the Fresnel coefficients [2,3].

Fresnel coefficients are expressed from the relationships reported in figure 2.3:

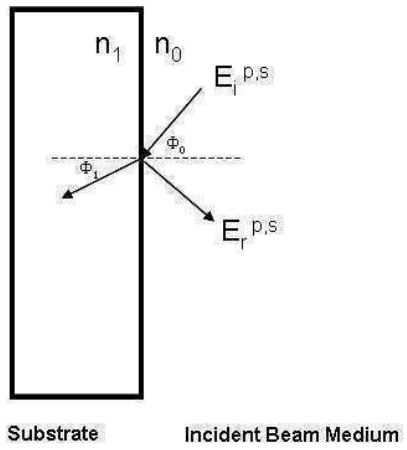

$$\tilde{r}^{s} \equiv \frac{\tilde{E}_r^{s}}{\tilde{E}_i^{s}} \equiv r^{s} e^{i\Delta^{s}} = \frac{\tilde{n}_0 \cos(\phi_0) - \tilde{n}_1 \cos(\phi_1)}{\tilde{n}_0 \cos(\phi_0) + \tilde{n}_1 \cos(\phi_1)}$$

$$\tilde{r}^{p} \equiv \frac{\tilde{E}_r^{p}}{\tilde{E}_i^{p}} \equiv r^{p} e^{i\Delta^{p}} = \frac{\tilde{n}_1 \cos(\phi_0) - \tilde{n}_0 \cos(\phi_1)}{\tilde{n}_1 \cos(\phi_0) + \tilde{n}_0 \cos(\phi_1)}$$

Figure 2.3 Fresnel coefficients for a single interface

where subscripts "0","1", refers to thin film and substrate (Figure 2.3) respectively.

$\tilde{n}$ is the complex refractive index, $\tilde{n} = n - ik$, being n the real component and k the extinction coefficient related to the absorption coefficient α as $\alpha = \frac{4\pi k}{\lambda}$.

Analogue pseudo-Fresnel coefficients can be defined for a *substrate/thin film/incident medium* system. They are reported in figure 2.4.

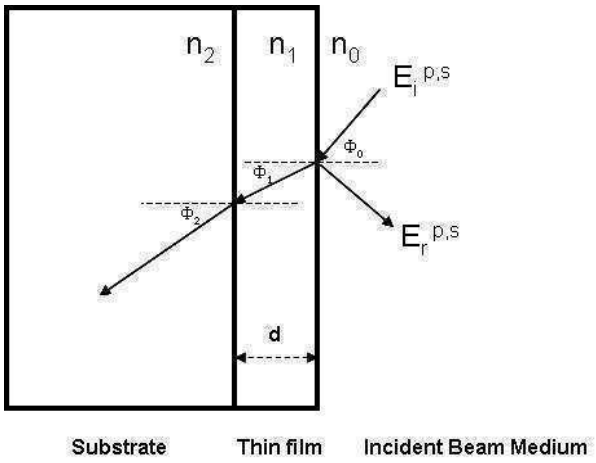

$$\tilde{r}^p \equiv \frac{\tilde{E}_r^p}{\tilde{E}_i^p} \equiv r^p e^{i\Delta^p} = \frac{\tilde{r}_{01}^p + \tilde{r}_{12}^p e^{-i2\beta}}{1 + \tilde{r}_{01}^p \tilde{r}_{12}^p e^{-i2\beta}}$$

$$\tilde{r}^s \equiv \frac{\tilde{E}_r^s}{\tilde{E}_i^s} \equiv r^s e^{i\Delta^s} = \frac{\tilde{r}_{01}^s + \tilde{r}_{12}^s e^{-i2\beta}}{1 + \tilde{r}_{01}^s \tilde{r}_{12}^s e^{-i2\beta}}$$

$$\beta = 2\pi \tilde{n}_1 \frac{d}{\lambda} \cos(\phi_1)$$

Figure 2.4 Pseudo-Fresnel coefficients for substrate/film system

$r_{01}^{p,s}$, $r_{11}^{p,s}$ are the Fresnel coefficients at *incident-beam-medium/thin film* and *thin film/substrate* interfaces respectively.

The ratio $\rho = \frac{\tilde{r}^p}{\tilde{r}^s} = \frac{r^p}{r^s} e^{i(\Delta^p - \Delta^s)} = \tan\Psi e^{i\Delta}$, establishes the relationship between the experimentally

accessible parameters $\Psi = \arctan(\frac{r^p}{r^s})$ and $\Delta = \Delta^p - \Delta^s$ with pseudo-Fresnel coefficients related to the optical constants of material constituting the system and film thickness.

The determination of optical constants and film thickness from measured Ψ and Δ is done by fitting procedures using the provided software. It is possible to build a model for the measured system, whose parameters are varied to minimize the model-generated Ψ and Δ values with the experimental ones.

Measurements were typically performed at three different incident angles (65°, 70° and 75°) in the 300-1200 nm range.

Generally, a Cauchy dispersion model was assumed for non-absorbing depositions. If information about the extinction coefficient *k* were desired, the "General Oscillator" model was adopted, which allowed to model *k* curves with different curves. The Tauc-Lorentz curve was most often assumed for modelling *k* behaviour.

The ellpsometry instrument allows to measure specular reflectance and transmission spectra at different incident angles between the incident light beam and the sample. Due to physical limitation of the instrument it was not possible to measure the reflectance at normal incidence, being the minimum incident angle equal to 15°.

M-line spectroscopy

M-line technique is used to determined the allowed mode of light propagation in a waveguide structure of a film on a substrate.
It is based on the optical coupling between an high refractive index prism and the deposition [4], as schematized in figure 2.5.

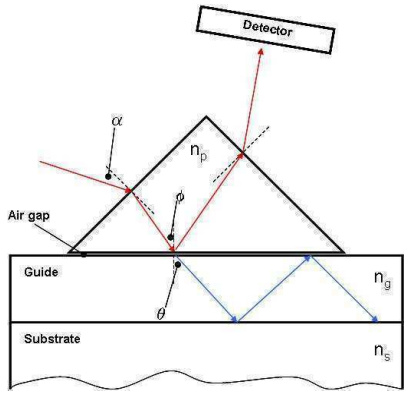

Figure 2.5 Schematic representation of prism-guiding film coupling

An air gap is always present between the two components. The incident beam is first refracted at the prism interface and it is totally reflected at the prism/air gap interface. Under this condition, an evanescent wave is established in the air gap region. The intensity of the reflected beam is then determined at the detector.
By moving the incident beam angle α, the evanescent field can be coupled into an allowed mode of the guiding layer. This can be detected by the intensity loss of the totally reflected wave, since part of its full intensity is coupled in the waveguide.
The coupling occurs when phase matching condition occurs, that is when the parallel component of propagation constant in the prism and in the guiding layer are equal :

$$\beta_p = \beta_g \Rightarrow \frac{2\pi}{\lambda} n_p \sin(\phi) = \frac{2\pi}{\lambda} n_g \sin(\theta)$$

where n_p and n_g are te refractive index of the prism and guiding layer respectively. $n_g \sin(\theta)$ is referred to as the effective refractive index n_{eff}

A typical data presentation is a plot of the effective refractive index versus the reflected intensity. A dip in this spectrum appear when the allowed mode is excited.

From this measurement, the refractive index and the thickness of the guiding film can be determined if more than one allowed mode is seen. If only one mode is detected, either the refractive index or the film thickness need to be known.

Amplified Spontaneous Emission (ASE) measurements

A titanium sapphire laser system at 800 nm delivering 150 fs pulses, with a maximum of 0.7 mJ per pulse energy at 1 kHz repetition rate was used for ASE experiments.

A 400 nm wavelength beam was obtained with a BBO doubling crystal and a cut-off filter. The intensity was varied with a half wave plate, a polarizer and a set of filters. The incident beam was focused with a 200 mm focal length cylindrical lens onto slide samples.

The sample edge emitted beam, in a lateral configuration, was detected by an optical fiber connected to a micro-spectrometer (Ocean Optics). A vertical aperture was utilized to control the stripe length on the surface.

References

[1] Demas J. N. and Crosby G. A., J. Phys Chem., 1971, **75**, 991

[2] Handbook WVASE32® , J.A. Woollam Co., Inc.

[3] F. L. Pedrotti and L. S. Pedrotti, Introduction to Optics, 2nd ed. (Prentice Hall, 1993).

[4] R. Syms and J. Cozens. Optical Guided Waves and Devics (McGraw-Hill International Limited,London, 1992).

Chapter 3

CdSe core and CdSe@ZnS core@shell nanoparticles: Properties, Synthesis and Processing

3.1 Introduction

It is well known that semiconductor materials change their electronic and optical properties when size become sufficiently small, typically in the few nanometers range. This effect has been verified for various systems including oxides [1-3] (TiO_2, ZnO), II-VI semiconductors [4-6] (CdSe, CdS, ZnS, ZnSe), III-V compounds [7-12] (InP, GaP GaAs, InAs,) and IV-VI compounds [13] (PbS, PbTe PBSe,).

The size dependence of electronic structure and carrier dynamics is among the most important topic of nanoscience and nanotechnology and attracts much interest not only in fundamental research but also in a great variety of applications including optics, electrochemistry, photochemistry, for which advantages deriving from nanometric dimension, i.e. large surface area and absence of light scattering, are coupled with new electronic structure

Optical applications will be mainly addressed in this thesis. Semiconductor nanoparticles (NPs), or quantum dots (QDs), are very attractive in this field because of their absorption and emission properties dependence on particles size, enhanced stability compared to organic dye or molecules, large non-linear optical properties and availability of different processing procedures allowing functional materials fabrication.

Such flexibility in properties and synthetic manipulation has already been exploited in various applications of semiconductor quantum dots such as light emitters in functional depositions and LEDs, optical gain material for lasing purposes and biological fluorescent labels.[14-25].

In order to successfully employ QD in optical applications, high quality samples are required. This imply mainly good size monodispersion and stability in the host environment.

The former can be satisfied if high temperature colloidal synthetic approaches are adopted. Actually, techniques such as (Chemical Vapour Deposition) CVD, solid state precipitation or low temperature colloidal syntheses do not allow monodispersion, size tuning to very small dimension and good crystallinity.

Stability of emission properties can be achieved by inorganic wide bang gap semiconductor shell to be grown on QD surface. Once again, synthesis of this type of heterostructures is possible within the high temperature colloidal synthesis framework.

Among semiconductor materials, cadmium selenide can be considered archetypal for quantum-sized particles study and preparation and a lot of novel approaches have been proposed with this compound in the scientific literature. Furthermore, its absorption and emission spectra can be varied throughout almost all the visible frequency range by varying particle size.

For these reasons, this material has been chosen during the present research activity.

In this chapter, fundamental properties including crystal structure and optical features coming from quantum size effects are first described both for CdSe core and CdSe@ZnS core@shell particles. A brief description of the theoretical basis and state of art of the available high temperature colloidal syntheses in non-polar solvents developed during last years is presented along with synthetic requirements for core and core@shell particles.

In the second part, the detailed experimental procedures of core and core@shell synthesis are given and the characterization of synthesized particles is presented and discussed.

3.2 Structure and optical properties of CdSe and CdSe@Shell nanocrystals

3.2.1 CdSe core particles

Both bulk and nano-sized CdSe assume the cubic zinc blend structure or the hexagonal wurtzite structure (see figure 3.1). The latter is the most stable and occurs more frequently in colloidally synthesized nanocrystals.

Nanocrystals typically exhibit crystal facets due to differential surface energy of crystallographic planes [61] and often possesses stacking fault defects which occur as grain boundaries mainly occurring on specific planes separating hexagonal and cubic local structures [58,62].

The lattice parameters of nano-sized QD are close to bulk material, even if the incomplete coordination of surface atoms, which are a non-negligible fraction of the total number of atoms, causes surface reconstruction of some planes [26].

Crystallographic phase can be controlled, to some extent, by changing synthesis environment [27-31]. In particular, it has been shown that the cubic structure is assumed in the early stages of nucleation and growth and is replaced by wurtzite in the later stages. Particles obtained with methods involving specific ligands, rapid nucleation and slow growth can kinetically retain the cubic structure.

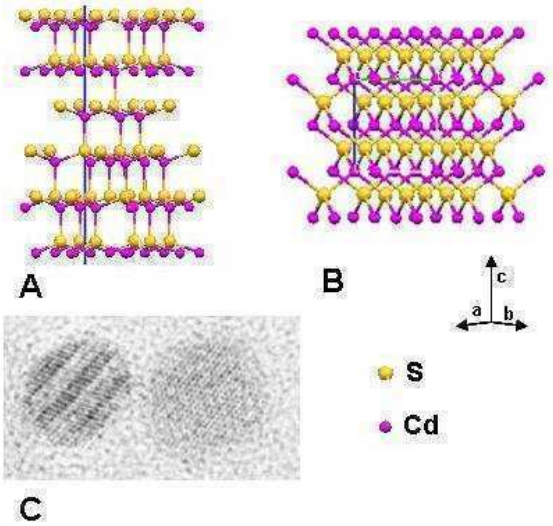

Figure 3.1 Cadmium selenide wurtzite (A) and zinc blend (B) structure and TEM micrograph showing four stacking faults defects (C) (Source : Schrier [61])

Absorption of light in a semiconductor causes the formation of an exciton consisting in an electron (*e*) and hole (*h*) pair, each considered as charge carriers with a defined effective mass and mobility.

Once this pair has been formed, in most cases this system can be described with the electron turning around the hole bound with a screened coulombic potential. The most probable charge carriers separation is defined by the exciton Bohr radius a_B in Equation 3.1, corresponding to the lowest Bohr state if an hydrogen-like motion for the *e-h* pair is assumed [32],

$$a_B = \frac{4\pi\varepsilon\hbar^2}{m^* m_0 e_2} \tag{3.1}$$

where ε is the dielectric permittivity of the semiconductor, $\hbar$ is the Plank constant , m_0 is the free electron mass, *e* is the electron charge, m^* is the reduced mass of the exciton defined as $\frac{m_e^* m_h^*}{m_e^* + m_h^*}$ with m_e^* and m_h^* the effective masses of electron and hole respectively.

When particle size is significantly smaller than the exciton Bohr radius, discretization and change of energy levels structure is mainly due to size quantization effect [32, 33, 34]. This situation is referred to as *strong confinement regime* and regards CdSe quantum dots whose typical dimension falls below 6 nm, which is the a_B value for CdSe also reported in Table 3.1 along with other II-V semiconductor's data. In these conditions, only the quantization effect can be considered for a qualitative description of the electronic structure, while other contributions such as e-h coulomb interaction can be accounted as corrections.

	Bulk band gap (eV)	**Exciton Bohr Radius (nm)**
CdSe [39]	**1.74**	**6**
CdS [68]	**2.58**	**3.0**
ZnS [68]	**3.83**	**2.2**
CdTe [69]	**1.43**	**7.3**

Table 3.1 Bulk band gap and exciton Bohr radius for some wurtzite II-V semiconductors

If nanocrystals size is similar or grater than a_B *intermediate and weak confinement regimes* are present, respectively, and other interactions such as coulomb attraction between *e* and *h* have much more influence if compared to quantization effects.

The size quantization effect can, at a good approximation, be approached by the effective mass model with infinite energy barrier at nanoparticles surface.

This leads to the following equation for electron and hole energy dependence on particle size [32,33], where the zero energy level is the bulk conduction and valence band for electron and hole respectively:

$$E_{n,L}^{e,h} = \frac{\hbar^2 \varphi_{n,L}^2}{2m_{e,h}^* a^2} \tag{3.2}$$

where a is the particle radius and $\varphi_{n,L}$ is a numerical value depending on quantum numbers whose first three values are $\varphi_{1,0} = \pi$, $\varphi_{1,1} \approx 4.49$, $\varphi_{1,2} \approx 5.76$.

This relationship defines energy level position for *e* and *h* independently, leading to the situation depicted in figure 3.2. Due to larger effective mass of the hole, valence states are denser in the energy scale, while electron state are more separated.

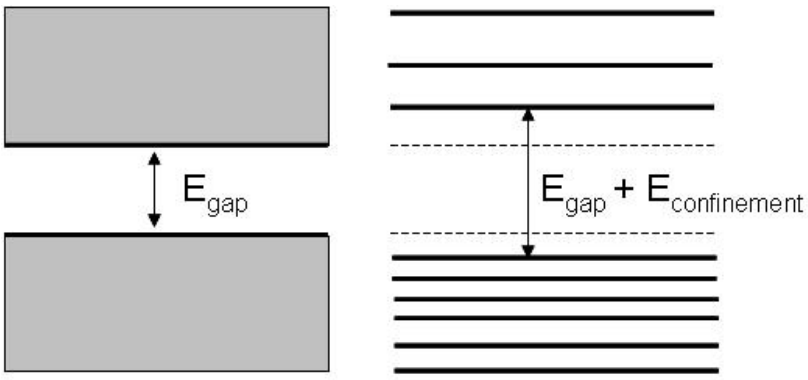

Figure 3.2 Confinement effect in nanometer sized semiconductor

The lowest energy optical transition ΔE, which actually corresponds to the band gap of the semiconductor nanocrystals, is the sum of electron and hole energy shift due to quantum confinement. It is described by Eq. 3.3 where particle band gap is shown to be inversely proportional to the square of particle radius.

$$\Delta E = E_{g,bulk} + \frac{\hbar^2 \pi}{2m^* a^2} \tag{3.3}$$

If the coulomb interaction is also considered as contribution to the energy of electronic states, the energy gap is determined as follows [33-36]:

$$\Delta E = E_{g,bulk} + \frac{\hbar^2 \pi}{2m^* a^2} - \frac{1.8e^2}{\varepsilon a} \tag{3.4}$$

A more precise relationship is derived in ref. [37] by Brus which takes into account also for polarization effects.

The reported equations can be used for qualitative understanding of size dependence of electronic properties, but the observed allowed transition under optical excitation can be explained only if the real semiconductor band structure, spin-orbit coupling and valence band mixing are considered [32,35,38]. These effects results in the valence band electronic levels shown in figure 3.3. In this figure the strongest allowed optical transitions are also assigned in a typical absorption spectrum of CdSe quantum dots following a work of Norris et Bawendi [38].

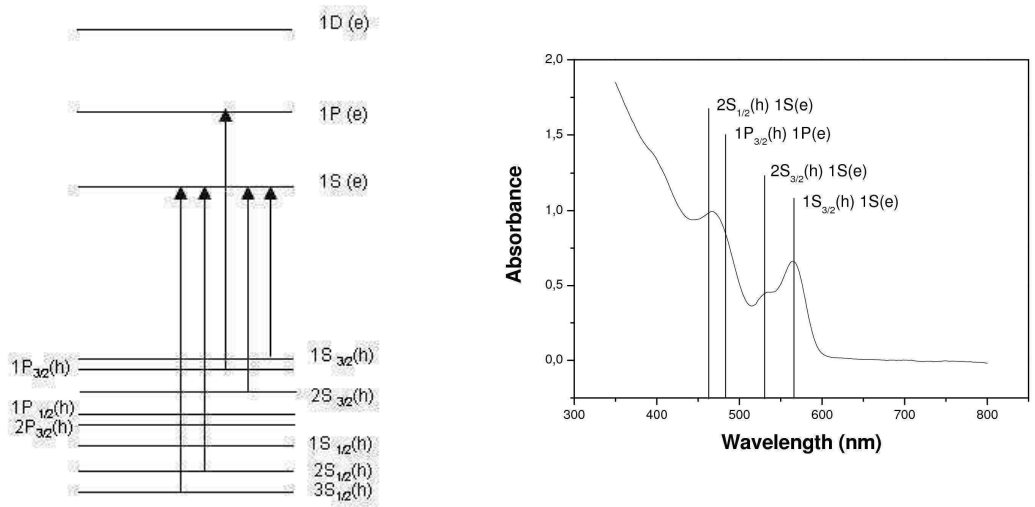

Figure 3.3 Quantum dot electronic structure and strongest optical transition [38] (right) . 3.2 nm diameter CdSe quantum dot with assigned optical transitions (left)

The absorption spectrum is then determined by the oscillator strength of every transition. The oscillator strength per unit volume has been predicted to be proportional to $\frac{1}{a^3}$ [71] for the lowest band edge transition, due to increasing overlap of electron and hole wavefunctions with decreasing sizes which causes an enhanced transition probability. Thus the absorption cross section at the band edge per particle should be independent on particle size, since particle volume scales as a^3. Experimental measurements of absorption cross section actually found a size dependence of this parameter which resulted to be linear with particle diameter for the lowest energy allowed transition [70,72]. At higher transition energies where NC optical transitions merge to a structureless bulklike absorption, the absorption cross section per particle scales with particle volume as for bulk semiconductor.
The knowledge of extinction coefficient is of paramount importance since it allows for de determination of the concentration by simple optical measurement. A widely used relationship for the molar extinction coefficient dependence on QD size has been reported by Yu et al.[102], along with the first exitonic peak dependence on particle diameter. These relationship are reported in table 3.2.

ε (Liter/mol/cm)	$5857 \text{ X } (D)^{2.65}$
D (nm)	$(1.6122 \text{ X} 10^{-9})\lambda^4 - (2.6575 \text{ X } 10^{-6})\lambda^3 + (1.6242 \text{ X } 10^{-3})\lambda^2 - (0.4277)^{\lambda} + (41.57)$

Table 3.2 Molar extinction coefficient (ε) and first optical transition wavelength position (λ) as a function of particle diameter (D)

Other factors such as polydispersion of NCs ensembles modify absorption spectra causing line broadening with respect to otherwise extremely narrow single NC emission. PL emission profile has also been used to estimate particles size distribution [40]. Also the increase in dielectric constant of the environment can shift particle's transition energy at the band edge toward longer wavelengths (solvatochromic shift) [41].
Furthermore, due to second order effects (exchange interaction between electron and hole, non-spherical shape of the particle and crystal field effect) the exciton energy structure is composed of five energy sub-levels [42, 32] resulting in further band splitting of the $1S_{3/2}$ highest energy valence state. These sub-bands can be grouped in two main level of the $1S_{3/2}$ state, which have been referred to as *absorbing state* and *emitting state*, since the

absorption is much more probable for the former. In fact, the excitation of the lowest energy sub-level of the emitting state is forbidden and, for this reason, it is called *dark exciton*. Optical excitation is indeed possible for other higher exciton energy sub-levels whose relative oscillator strength changes with NP radius and shape and determine the exact position of the first absorption band [42].

Once an electron-hole pair is produced after optical absorption, the electron relaxes to the lowest energy 1S state and hole relaxes to the *emitting state* in the picoseconds time scale. Thereafter e-h recombination can occur with emission of a photon [43,44], giving rise to spontaneous photoluminescence. At very low temperatures the hole relaxes to the lowest energy *dark exciton* sub-band from which the emission is predicted to be very slow leading to luminescence lifetimes of the order of 1μs. At higher temperatures also the other sub-band levels of the *emission state* can be populated from which the emission is much faster in the commonly observed nanosecond lifetimes [43,44]. The overall situation is schematically shown in figure 3.4.

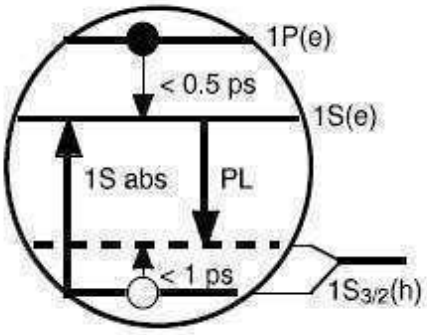

Figure 3.4 Schematic representation of near-band-edge-levels involved in absorption and emission processes [Source: Klimov et al. [16]]

The luminescence peak is observed to be red-shifted with respect to the first absorption peak. Such shift is referred to as *Stoke shift* and it is due to the fact that the energy of exciton *emitting state* from which recombination occurs is lower than the energy of the *absorbing state*, as explained above [32].

The quantum yield of luminescence emission is strongly dependent on surface states. Nanocrystals possess a great fraction of surface atoms, which are not completely coordinated. The presence of a large number of unsaturated dangling bonds originates trapping states whose energy position [45] can be located inside the band gap. Electron and hole radiative recombination can be prevented by relaxation of charge carriers to such

surface trapping states, thus lowering band edge luminescence quantum yield (PL QY) [32]. Charge carriers in the surface states can further recombine with non-radiative process or by radiative process with emission of light typically at the red-side of the PL band edge transition.

Indeed, it is known that surface passivation with organic molecules, such as aliphatic amines or with inorganic shell results in dramatic increase of photoluminescence quantum yield.

CdSe quantum dots exhibit non-linear optical features such as two-photon absorption and multi exciton processes such as Auger recombination .

Two photon absorption occurs at high incident energy at frequencies at which linear absorption is not possible. The two photon absorption cross section increases with particles diameter and results to be much bigger than organic dyes [46-48], which makes quantum dots particularly interesting in non-linear optics application. A linear relationship between quantum dot diameter (D) and two photon absorption (σ_{TPA}) has been found with a slope of 3.45 at 800 nm excitation wavelength [46].

At high excitation power, more than one exciton can be produced in a single quantum dot. As a consequence of the multi-exciton process, the oscillator strength and the energy of transitions are modified due to state filling and Stark effect. The former regards the decreasing of absorption band due to depletion of charge carriers in the already exited ground state, while the latter is related to the changes of electronic structure following the strong electric fields created after e-h pair formation [32,72].

These effects are relevant in optical gain experiments where processes involving typically two exciton states per quantum dots are involved. In particular, the emission from which optical gain is obtained regards the transition of one of the two e-h pairs with energy $h\omega_{bx}$ from a biexciton state to the single exciton state, as shown in the figure 3.5.

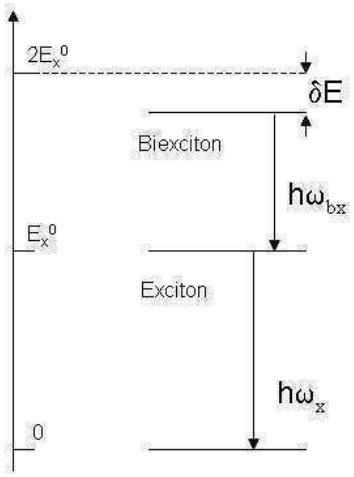

Figure 3.5 Peak energy shift δE of luminescence emission from bi-exciton state compared to single exciton state

This transition energy is observed to be lower if compared to single exciton transition energy $h\omega_x$ [32,101]. This shift is mainly due to the attractive coulomb interaction between the two excitons which causes a transition energy difference δE (see figure 3.5). This emission shift is normally observed in lasing applications and it is an evidence of the multi-exciton nature of this process, as it will be discussed in Chapter 6.

Another multi-exciton process relevant in lasing is Auger recombination. This is a process which happens when more than one exciton is created inside the nanocrystal and consists in relaxation of an e-h pair and energy transfer to a third charge carrier (figure 3.6). This process has much faster rates in quantum-confined particles than in bulk semiconductors and the decay time of exited states due to Auger processes is strongly dependent on particle size and scales with a^3.

This is an important process if QD are used as gain media since it soon depletes the multi exciton states necessary for amplified emission to occur. Auger process happens in a very short time scale as low as 45 picoseconds, if the auger relaxation of the biexciton state is considered [32].

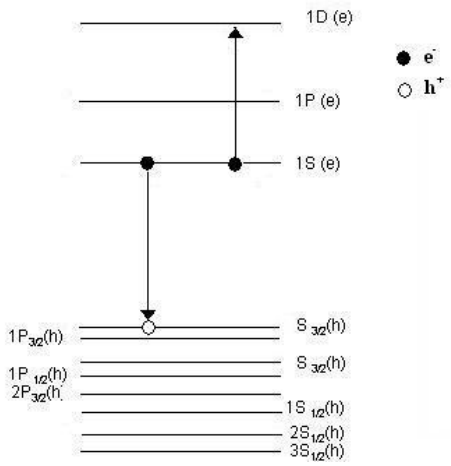

Figure 3.6 Schematic representation of Auger process

3.2.2 Core@Shell particle

As previously mentioned, fluorescence quantum yield is typically strongly reduced to low values for as-synthesized CdSe core particles. This is mainly due to presence of surface electronic disorder caused by unsaturated dangling bonds of surface atoms [45].

Passivation by organic molecules, particularly amines [49,50], is effective in raising PL QY, but it relies on surface adsorption equilibrium instead of stable bonds. Attaching organic ligands to nanocrystal surface can provide a useful tool for solubility in desired solvents and raise of quantum yield, but they are labile and in dynamic equilibrium with surrounding environment. This strategy does not guarantee stability of particle emission properties and usually PL QY reduction is observed due to photooxidation [51].

Application of QD mainly requires high luminescence quantum efficiency, stability of emission properties for long time in the desired environment and particle compatibility in the desired solvents or solid matrix in order to achieve optimal processing behavior.

These aspects can be fulfilled by inorganic coverage of quantum dots, where shell of semiconductor materials are deposited on pristine dot surface.

Several types of such heterostructures depending on the relative position of conduction and valence band gap have been developed in order to manipulate and alter the electronic properties of the particle [52].

Structures ensuring high QY and enhanced stability are the so-called type 1 heterostructures, where shell material has an higher band gap than core's one (figure 3.7).

This solution relies on charge carriers confinement inside the core with the goal of preventing electrons and holes interactions with the surrounding media. Physical separation of the optically active surface of the core from, for example, oxygen or water molecules has been verified to strongly increase photostability and the resistance towards photooxidation, which mainly involve Se surface sites to form SeO_2 oxide species in CdSe particles [53].

At the same time, shell growth eliminates surface defect states and prevent carriers to combine with the outer surface of the structure, thus leading to substantial increase in PL QY.

To maximize effectiveness of this solution, the shell should ideally be thick and have wide band gap in order to result in wide band gap offsets with regard to both conduction and valence band of core material.

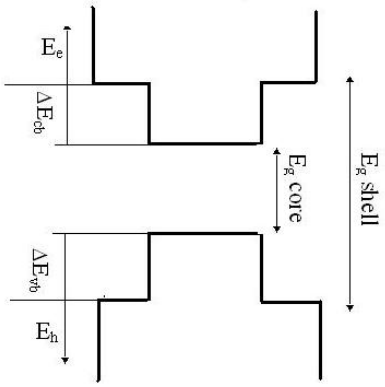

Figure 3.7 Type 1 heterostructure (ΔE_{cb} and ΔE_{vb} are conduction and valence band gap offsets respectively)

Different materials have been deposited on CdSe particles to form core@shell (CS) structures. Several candidates as material for shell deposition can be found in other II-VI semiconductors. In Figure 3.8 band gap position of some semiconductor materials are reported. It is evident that CdS, ZnS and ZnSe have favorable band offsets both for conduction and holes with respect to CdSe.

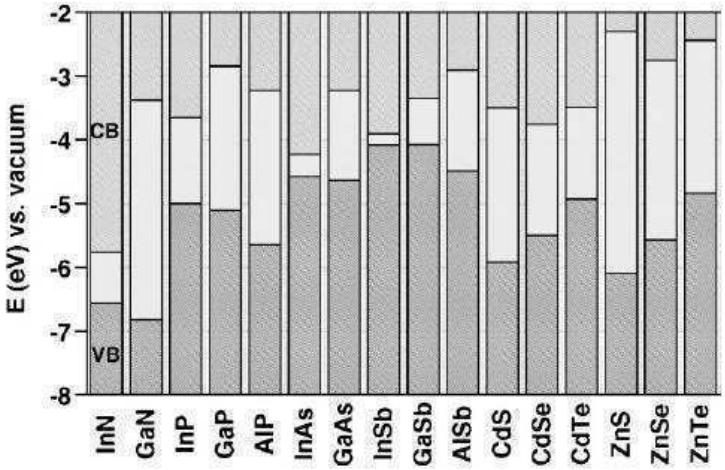

Figure 3.8 Conduction and valence band gap position of some II-VI semiconductors with respect to vacuum (Source : Reiss et al. [52])

CdSe@CdS structures have been widely studied [49,50,51,54,55]. Peng et al.[55] demonstrates through TEM, XPS and XRD analyses that epitaxial growth of several monolayers of CdS on CdSe is possible. This is favored by the small lattice mismatch (around 4%) between these materials which is fundamental for minimization of structural defects in the final structure.

Nonetheless, arising of defects to relief stress buildup in the structure such as misfits dislocations is very probable and a critical thickness of two monolayer has been be estimated for this system [56]. Beyond this limit dislocations should arise which are most likely not able to completely relief stresses. Thus, incoherent strain is supposed to be created which is responsible for electronic traps that reduces band edge luminescence.

In any case CS with quantum yield approaching 50% has been synthesized with improved stability with respect to bare cores.

Despite the good structural compatibility, the band gap of CdS is not sufficiently large to block holes and electrons inside the core. This is particularly true for electrons since conduction band offset is rather small, while the holes results to be more confined. Since photoxidation requires the presence of an hole and oxygen at particle surface [57], this lead to the observed improvement of photostability.

A comparison of photostability between different structures is depicted in figure 3.9

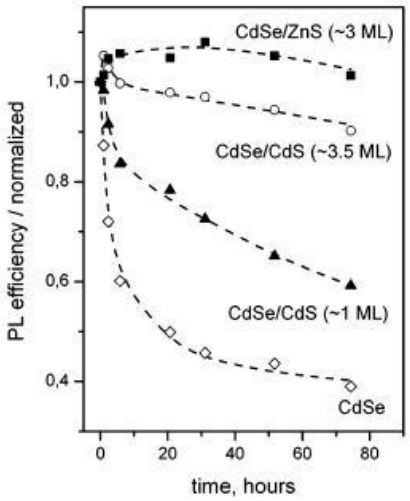

Figure 3.9 PL quantum yield evolution under UV illumination for different CS systems to test effect of shell structure on photostability (Source: Mekis et al.[51])

Thus, even if stability is improved, sensitivity toward external environment is not always satisfactory.

Lack of strong confinement also bring to a red shift increasing of the absorption peak with increasing shell coverage, since charge carriers wavefunctions can partially leak into the shell [49,58]. This effect has been recently extensively studied by Van Embden et coworkers [105], who also reported correlations between absorption peak shift and CdS shell thickness for different sizes of starting CdSe cores.

In addition, absorption at shorter wavelength is increased due to the presence of CdS shell absorbing at that spectral regions.

The CS CdSe@ZnSe structure is analogue to the previous system for which the band gap of shell material is not much wider than CdSe core. However, in this case conduction band offset is much greater providing efficient confining for electrons while a smaller barrier exist for the holes. Even if the 6.3% lattice mismatch value with respect to CdSe is greater with respect to CdS, epitaxial growth is possible and favoured by the common anion structure.

Narrow distributions with PL QY in the 60-85% range has been obtained within this system [59], with improved stability with respect to cores[60].

Lattice distortion effect on optical properties basis has also been studied on these particles[74], as well as ripening behavior of bare and ZnSe covered CdSe nanocrystals [73].

The most studied CS system is CdSe@ZnS. The reason is in the wide band gap which ensures a very limited leakage of carriers wavefunction into the shell. This also results in a lot of beneficial aspects including the best stability of emission properties and high PL QY.

In order to have the maximum efficiency, the shell should be as thicker as possible. Unfortunately, the wide band gap comes along with the larger lattice mismatch with respect to CdSe core (12%) if compared with shell materials considered so far, as shown in figure 3.10.

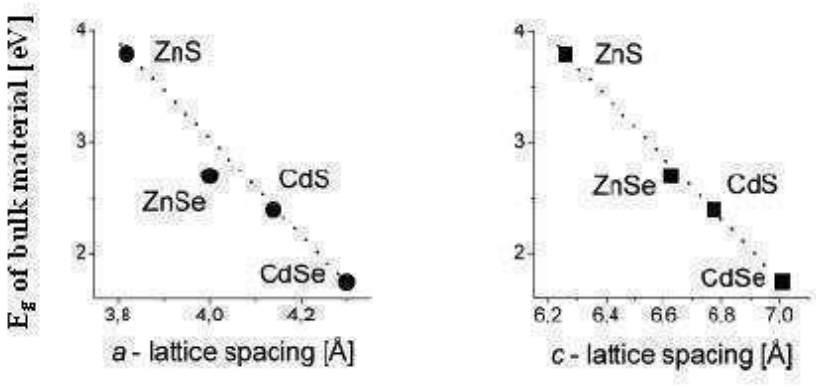

Figure 3.10 Band gap energy versus lattice parameters **a** and **c** of wurzite CdSe,CdS, ZnSe and ZnS (Source: ref [60])

In ref. [58], a comprehensive characterization of a wide size-series ZnS shell deposition on CdSe has been carried out by means of optical, TEM, Small and Wide angle diffraction techniques.

The main features observed were a maximum PL QY of 50% after 1.3 ML ZnS (a monolayer "ML" thickness can be approximately taken as half the *c* lattice constant of the wurtzite shell material) coverage and a progressive decreasing of emission yield with further increase of shell thickness.

The former was explained with the progressive elimination of surface vacancies and non-radiative recombination sites. This coverage was also found to be the minimum to completely passivate surface Se sites, since no SeO_2 was detected after prolonged exposure to air with XPS measurements.

Thicker shell resulting in the decrease of luminescence is likely due to arising of structural defect.

Three possible way for shell growth are possible : epitaxial coherent growth, incoherent epitaxial (with misfits dislocations) and highly disordered.

Highly disordered growth was excluded because diffraction analyses showed distinct diffraction peaks of ZnS shell.

Small coverage could not be detected with diffraction techniques due to dominant diffraction of core, but TEM analyses reveals no presence of interfaces and continuity of lattice fringes throughout the particle. Thus coherent epitaxial growth could be assumed for thin shell. Thicker shell were detectable with diffraction analyses and resulted to have the ZnS bulk lattice parameter. This means that incoherency exists between core and shell materials. TEM measurements reveals also in this case absence of interfaces and extension of lattice planes, but presence of defects or dislocations could not be detected with this type of analyses. Thus, the most likely scenario consists in an incoherent epitaxial growth for thick shells where defects such as misfit dislocations or low-angle grain boundary can account for incoherent growth and structural accommodation of the arising strain, as previously discussed for the CdSe@CdS system. These defects can, nonetheless, provide electronic traps for non-radiative recombination that caused the observed decrease in PL QY.

Also ZnS shell lead to a small red-shift of the absorption peak due to a not complete confinement of ZnS shell, even if the extent of this effect is much lower with respect to the case of CdS shell, as shown in figure 3.11.

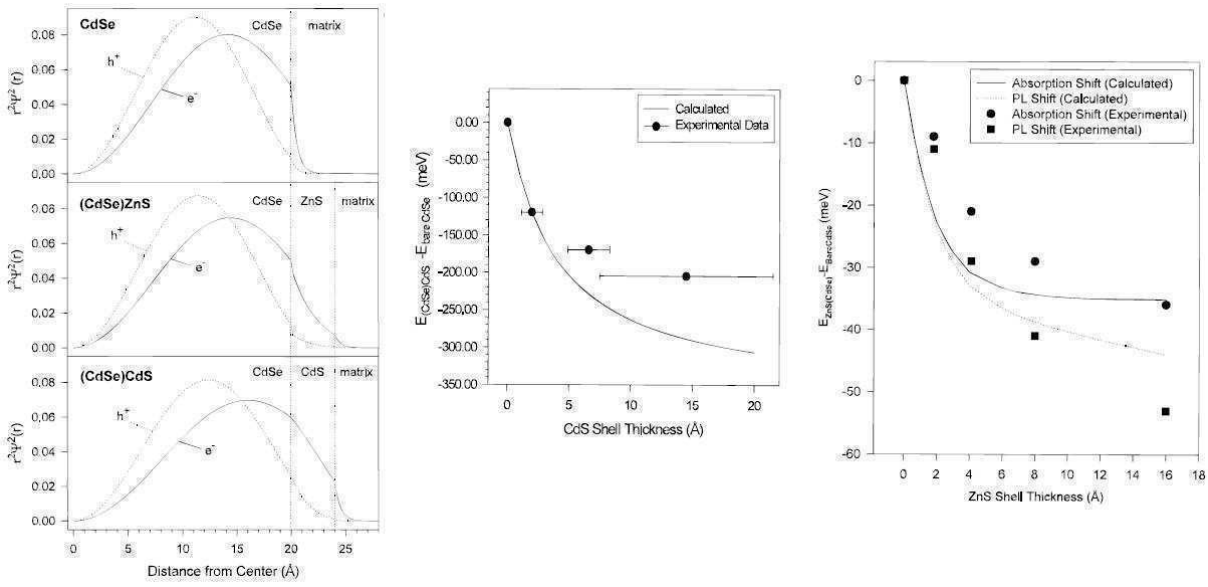

Figure 3.11 Representation of the radial probability for both electrons and holes is shown for CdSe, CdSe@CdS and CdSe@ZnS (left) and absorption shift for increasing CdS and ZnS shell (right) (Source: Dabbousi et al. [58]).

This shift tends to become less evident with increasing shell thickness [63], due to longer tunnelling distances which cause a minor extent of carrier delocalization.

Deposition of ZnS shell often results in non-spherical particles with typical aspect ratio around 1.2. This results from preferential shell growth on crystallographic planes showing lower superficial energy or higher reactivity. These differences are amplified by the large lattice mismatch of shell material resulting in elongated particles [58]

In order to encounter both electronic and structural requirement for high performance core@shell particles, multiple shell structures (CSS) have been adopted in the last few years. These particles consists of an intermediate layer (generally around 2 ML) of CdS or ZnSe deposited between the CdSe core particle and the outer wide band gap ZnS shell. This solution provides efficient confinement and minimization of structural defects because of a smooth change of lattice parameter due to introduction of materials with minor lattice mismatch (see figure 3.9).

This approach was first exploited for the CdSe@ZnSe@ZnS CSS system [64,65] and further extended also to CdSe@CdS@ZnS by Talapin et al.[60]. In this paper it was shown that a contraction and an expansion of the CdSe core and ZnS outer shell respectively was obtained in the CSS structure by means of XRD measurements. This suggested that this graded shell assumes a coherent epitaxial growth without dislocations or other defects which should otherwise be necessary to accommodate interfacial strain if bulk parameters were assumed from particle's constituent materials.

For these reasons, the CSS structure had much higher PL QY (up to about 80%) and was much less sensitive to the PL QY decrease with increasing ZnS thickness if compared to the CdSe@ZnS structure.

As far as emission stability is concerned, the multishell approach resulted to be comparable with CdSe@ZnS particles and better than CdSe@ZnSe CS one.

The CdSe@CdS@ZnS structure was also studied by Z-contrast STEM analyses in order to understand the structural basis for PL QY maximization [66]. It was shown that uniform shell coverage was assumed only for multiple shell structures and that this was crucial for high PL QY.

Finally, this idea was further extended to structures comprising alloy layers, as described in [67]. A CdSe@CdS@$Cd_{0.5}Zn_{0.5}S$@ZnS was synthesized through the SILAR (Successive Ion Layer Adsorption Reaction) technique with the aim of making lattice parameter variation as smooth as possible, resulting highly luminescent and stable particles also in aqueous environments.

3.3 Colloidal synthesis of CdSe and CdSe@Shell nanoparticles

3.3.1 Nucleation and growth: a theoretical overview

A phase transformation is driven from a difference in chemical potential μ between phases constituting a system. In transformation like crystallization of a single element from its liquid state (or precipitation from a solution), the process is caused by higher chemical potential of the element in the liquid state compared to solid state (or higher μ with of solute with respect to the precipitated solid state).

In single element transformations, the key parameter is the temperature of the system, while in precipitation-from-a-solution processes, the concentration of solutes is also important.

If we consider a system comprising an element X in solution at a fixed temperature, it would precipitate to form a solid phase if an equilibrium concentration C_{eq} is exceeded.

In equilibrium condition, the chemical potential of the element X in the solution phase μ^l is equal to the chemical potential of the same element X in the solid state μ^s.

If μ_e is taken as the equilibrium chemical potential, μ^l and μ^s can be expressed as follows :

$$\mu_C^l = \mu_{eq} + RT\ln(\frac{C}{C_{eq}}) \quad , \quad \mu_C^s = \mu_{eq} \tag{3.5}$$

The term C/C_{eq} is the supersaturation S of the system. The difference in chemical potential that causes phase transition is $RT\ln(S)$, which is related to the Gibbs free energy change per unit volume ΔG_V of transformed solid phase by the molar volume V_m through the relation $\Delta G_V = -\frac{RT\ln(S)}{V_m}$ (3.6). This treatment is valid for flat surfaces but it needs to be corrected since formation of a particle precipitate occurs with creation of a surface which is associated with a surface energy γ. This energy actually modifies the chemical potential μ^s and equilibrium concentration C_{eq} in the solid state through Equations 3.7a and 3.7b , known as the Gibbs-Thomson equation [75].

$$\mu_{C,r}^s = \mu_{eq} + \frac{2\gamma V_M}{r} \qquad C_{eq,r} = C_{eq}\exp(\frac{2\gamma V_M}{RTr}) \tag{3.7a,b}$$

Thus, the actual ΔG_V becomes :

$$\Delta G_{V,r} = -\frac{RT\ln(S)}{V_m} + \frac{2\gamma}{r} \tag{3.8}$$

At equilibrium ΔG_V is zero, thus from Eq. 3.8 it can be concluded that the concentration of species in solution in equilibrium with a particle with radius r is greater than the equilibrium concentration in the case of flat surfaces.

On this basis the classical nucleation theory can be described. Within this framework, the stability of formed particles is predicted and the radius of metastable nuclei can be determined. Once this radius is reached, further growth is energetically favored.

The free energy change ΔG involved in the formation of a nucleus can be separated in a term related to ΔG_V and one related to surface energy as follows :

$$\Delta G = \frac{4}{3}\pi r^3 \Delta G_V + 4\pi r^2 \gamma \tag{3.9}$$

where ΔG_V is related to supersaturation S (Eq. 3.6), in the case of precipitation from solution.

A plot of the two contribution and of the overall energy change is shown in figure 3.12.

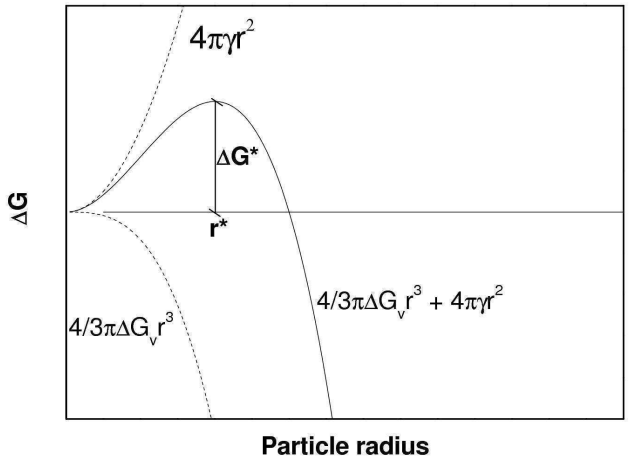

Figure 3.12 Free energy evolution of a particle versus its radius

The radius corresponding to maximum value of energy change is the critical radius r* of the metastable nucleus and the energy associated with it is the critical energy barrier ΔG* that need to be overcome to form a metastable particle are reported below.

$$\Delta G^* = \frac{16\pi\lambda^3}{(3\Delta G_V)^2} = \frac{16\pi\lambda^3 V_M{}^2}{(3RT\ln S)^2} \tag{3.10}$$

$$r^* = -\frac{2\gamma}{\Delta G_V} = \frac{2\gamma V_M}{RT\ln S} \tag{3.11}$$

It is possible to see that the supersauration value, along with surface tension has a dramatic effect on the thermodynamics of the process. In particular, an increase in supersaturation leads to a decrease of both the energy barrier and the smaller stable nucleus radius, while the opposite effect holds true for surface tension.

Once a population of stable nuclei has been formed, growth of particles becomes the relevant process. The classical approach to the overall process of particles nucleation and growth has been first proposed by La Mer [76]. Within this framework, the nucleation event (stage II in figure 3.13) occurs when a critical supersaturation value C^*_{min}, higher than equilibrium concentration is reached. As a consequence of nuclei formation, the concentration of monomer in solution decreases below the threshold value for nucleation but it is still greater than equilibrium concentration C_{eq}. At these conditions the process enters the growth stage (stage III in figure 3.13) . At even later periods, when almost all monomers are depleted, Ostwald ripening starts and dissolution of smaller particles in favor of bigger particles growth is observed due to chemical potential dependence on particle radius.

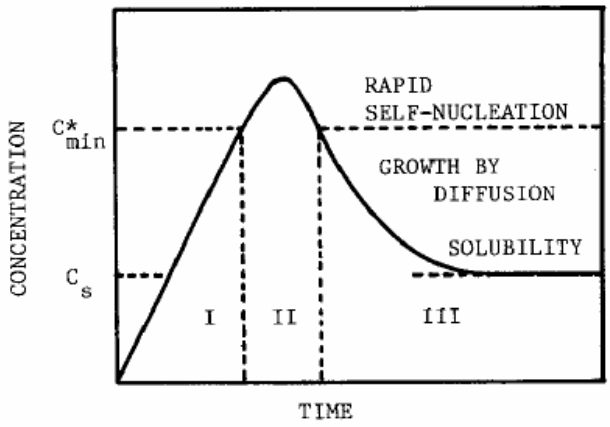

Figure 3.13 Schematic representation of stages involved in nucleation and growth process. C_s is the equilibrium concentration and C^*_{min} is the minimum concentration necessary for nucleation. (Source : Sugimoto [77])

Stage I, which occurs before the nucleation event, accounts for the increase of monomer concentration in solution typically due to decomposition of the precursors adopted in the synthesis.

The existence of a critical supersaturation threshold is related with the kinetic aspect of nucleation. The rate of nucleation can be expressed as follows [75]:

$$J = B\exp(-\frac{\Delta G^*}{RT}) \tag{3.12}$$

Where ΔG* is the energy barrier as expressed in Eq. 3.10. From this equation it could be shown that the rate of nucleation become significant at a concentration greater than C_{eq}, that is the above mentioned $C^*_{min.}$ The threshold C value for nucleation is strongly dependent on surface tension values increasing for higher values of this parameter.

For the synthesis of colloidal particles with good monodispersion, nucleation should be a rapid event and separated from the growth stage. These conditions should guarantee the production of a population of nuclei with small size dispersion because of the similar condition experienced in the short nucleation period, without secondary nucleation. Furthermore, if nucleation is too long, growth occurs at the same time amplifying size differences of produced nuclei. Thus a rapid burst of nucleation is desired for good monodispersion. This principle is assumed in " hot injection protocols ", where an explosive-like nucleation is sought as described in the following sections.

Size distribution evolution is then determined also by the growth stage. Different types of growth regimes have been identified and described in detail [75,77].

The main processes involved in the growth of a nucleus are the diffusion flux of monomer from bulk solution to particle surface and subsequent reaction leading to monomer deposition and particle accretion.

In order to explain the main features regarding particle's growth, the same approach developed by Sugimoto is here described [77].

Monomer concentration profile near particle surface is schematically shown in figure 3.14.

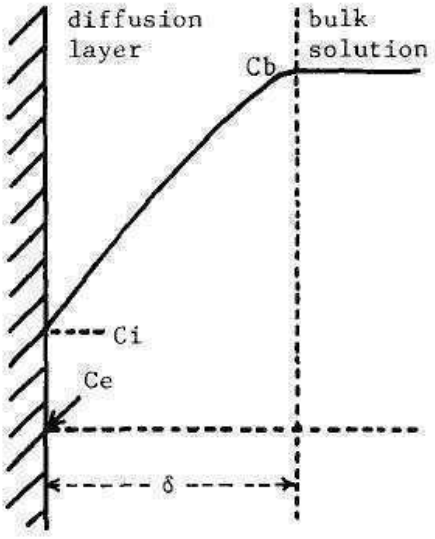

Figure 3.14 Monomer concentration profile near particle surface during growth stage (Source : Sugimoto [77])

The diffusion flux J_{Diff} is activated by the concentration difference between the bulk monomer concentration C_b and the concentration at the particle-solution interface C_i across the diffusion layer δ. If D is the diffusion coefficient and r the particle radius, J_{Diff} can be expressed as follows:

$$J_{Diff} = 4\pi Dr\frac{(r+\delta)}{\delta}(C_b - C_i) \tag{3.13}$$

Assuming a simple first-order kinetic for monomer reaction on particle surface, the flux of reacting monomer J_{React} is :

$$J_{\mathrm{Re}act} = 4\pi r^2 k(C_i - C_{eq}) \tag{3.14}$$

with k being the rate constant and C_{eq} the equilibrium concentration. Under steady-state conditions, $J_{Diff}=J_{React}=J$ leading to the following equation:

$$\frac{(C_i - C_{eq})}{(C_b - C_i)} = \frac{D}{kr}(1+\frac{r}{\delta}) \tag{3.15}$$

If D<<kr, the diffusion controlled regime is established. In such conditions, from Eq. 3.15 C_i becomes equal to C_{eq}. Substituting C_i for C_{eq} in Eq. 3.13 we obtain the following relationship for the diffusion controlled growth :

$$J = 4\pi Dr\frac{(r+\delta)}{\delta}(C_b - C_{eq}) \qquad \text{Eq. 3.16}$$

If D>>kr, the growth is reaction.controlled and C_b results equal to C_i and J

$$J = 4\pi r^2 k(C_b - C_{eq}) \qquad \text{Eq. 3.17}$$

Till now the dependence of equilibrium concentration Ceq on particle radius r as expressed in Eq 3.7b has not be considered. If this is taken into account Ceq can be expressed as follows if the exponential factor in 3.7b is assumed to be small:

$$C_{eq,r} \cong C_{eq}(1 + \frac{2\gamma V_M}{RTr}) \qquad \text{Eq. 3.18}$$

Analogously the bulk concentration is expressed as :

$$C_b \cong C_{eq}(1 + \frac{2\gamma V_M}{RTr*}) \qquad \text{Eq. 3.19}$$

where r* is the particle radius in equilibrium with bulk concentration C_b.
Using these equation, we obtain the following corrected relationship for diffusion limited (Eq, 3.20) and reaction limited (Eq. 3.21) regimes:

$$J = 8\pi Dr \frac{(r+\delta)}{\delta} \frac{C_{eq}\gamma V_M}{RT}(\frac{1}{r*} - \frac{1}{r}) \qquad \text{Eq. 3.19}$$

$$J = 8\pi kr^2 \frac{C_{eq}\gamma V_M}{RT}(\frac{1}{r*} - \frac{1}{r}) \qquad \text{Eq. 3.21}$$

By using the relation $J = \frac{4\pi r^2}{V_M}\frac{dr}{dt}$ it is possible to get the particle radius evolution from Eq. 3.210 and 3.21.
For diffusion limited growth, Eq. 3.22 is derived if an infinite diffusion layer δ is assumed.

$$\frac{dr}{dt} = \frac{2\gamma D V_M^2 C_{eq}}{RTr}(\frac{1}{r*} - \frac{1}{r}) \qquad \text{Eq. 3.22}$$

While for reaction-limited growth Eq.3.23 is found.

$$\frac{dr}{dt} = \frac{2\gamma k V_M^2 C_{eq}}{RT}(\frac{1}{r*} - \frac{1}{r}) \qquad \text{Eq. 3.23}$$

In both cases particles with a radius smaller than r* dissolve (negative growth rate), as expected also from thermodynamics considerations. In reaction limited regime, the growth rate increases with particle radius and this acts to further broaden the size distribution.
In diffusion limited regime, the growth rate diminishes with particle radius, thus smaller particles will grow more rapidly with respect to bigger one. This process results in progressive size distribution narrowing and it is often referred to as "focusing" [78].
Focusing condition requires supersaturation to be high enough. This can be understood if growth rates expressed in Eq. 3.22 and 3.23 are plotted as a function of particle radius. This has been done in ref. [75] using more detailed formulations, and reproduced here in figure 3.15, where the parameter *K* is proportional to *D/k*, while *S* is proportional to the supersaturation. It can be seen that for high K values (reaction controlled growth) growth rate increase with particle radius, while the opposite holds true for low *K* values (diffusion limited regime) if particle radius is larger than that corresponding to growth rate maximum. In this range smaller particles grow faster then bigger ones leading to narrowing of the size distribution with time. This process has been observed and studied also in semiconductor particles synthesis [79]. The conditions under which this process occurs are favored at high supersaturation values, as shown in figure 3.15 b. In fact, for low supersaturation values, which can occur at the end of particle growth when most monomer are depleted, growth rate is almost independent from particle radius and it also increases with particle radius for a non-negligible range and this can eventually results in size broadening ("defocusing").

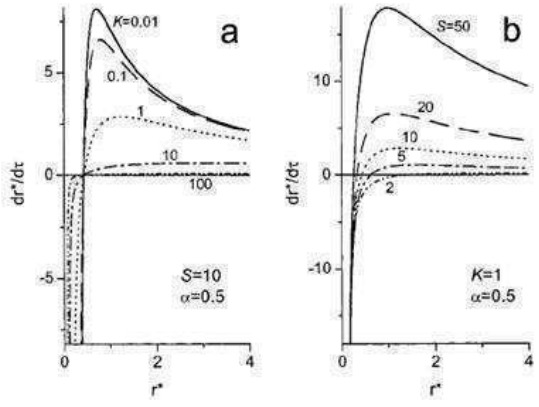

Figure 3.15 Growth rate as function of particle radius expressed in r* units. Parameter K is proportional to D/k, while S is proportional to the supersaturation (Source : Talapin et al. [75])

Furthermore, at the end of particle growth, supersaturation is small and further growth can occur only through Ostwald ripening, which results in smaller particle dissolution and

deposition on bigger ones, with final increasing of mean particle radius (coarsening), while maintaining a stable size distribution, after an initial transient in which defocusing can occur [75].

Thus, in order to obtain monodisperse colloidal particle, diffusion limited regime must be sought providing high enough supersaturation to make focusing process effective. Of course, supersaturation need to be kept below the critical value C^*_{min} to avoid secondary nucleation.

3.3.2 CdSe NPs synthesis

Most synthetic approaches have been based on colloidal chemistry and two main general strategies in semiconductor particles can be identified [78]. The first is based on kinetic control of particle formation in bulk solution by varying ligand and precursor's concentration or temperature. The second relies on particle formation within nanocavities, such as micelles, dendrimers or other types of template [80-84].

The latter approach is not generally flexible, since the condition required for template formation in solution are quite strict and factors such as temperature and ligand type and concentration cannot be exploited. Monodispersion and crystallinity are indeed difficult to obtain with such methods.

Bulk solution approaches are much more promising since a great variety of parameters can be attempted in a wide range. Actually, the first syntheses of this type were performed in aqueous solution and limited at low temperatures[85,86]. Thus, the quality of nanoparticles were quite poor.

Nonetheless, a lot of effort has been devoted to development of this route especially after the inaugural synthetic protocol by Murray et al. [87] which employed organometallic precursors in coordinating solvent.

This protocol, further optimized by Peng et al. [88], can be summarised as follows :

- Usage of coordinating solvents such as trioctylphosphine (*TOP*) and trioctylphosphine oxide (*TOPO*, Tech grade)
- Dimethyl Cadmium $Cd(CH_3)_3$ and elemental selenium dissolved in *TOP* as precursors
- High reaction temperatures in the 150°C-360°C and air-free environment

Fast injection of cold precursors in hot *TOPO*, "hot injection protocol", promotes an efficient nucleation event and subsequent growth necessary for good monodispersion, as

described in the previous section. In figure 3.16, the typical experimental set up is presented. The solvent is degassed and heated at elevated temperatures in a three necked flask and the cold precursors are then rapidly injected. Nucleation is rather explosive in nature and soon stopped by the decrease in temperature caused by injection of cold reagents. Growth is then performed at lower temperatures.

Figure 3.16 Typical experimental set up for "hot injection protocols" for QD synthesis

TOPO is considered a coordinating solvent since it is able to complex cadmium and give control over the extremely reactivity of organometallic precursors. Finally, this method ensures samples with good crystallinity due to high synthesis temperature, good monodispersion and some control over size by simply quenching the reaction at different growth times.

Size focusing and defocusing were verified in such systems applying the theoretical concept described before [88].

These protocols also enabled synthesis of anisotropic CdSe nanorods [89] and was applied to other types of semiconductors with poor results.

The high toxicity of organometallic compounds, its difficult handling and the difficulty in synthesize good quality particles other than CdSe motivated researchers toward so called "alternative routes"[90]. These are based on air-stable inorganic salts, oxides or organic salts as precursors complexed by organic ligands which can be chosen among a lot of chemicals including fatty acids, phosphines, amines, phosphinic and phosphonic acids. The first syntheses [90,91] were performed in coordinating solvents and leads to good quality samples for CdSe particles. The greater stability of precursors used in this methods compared to organometallic compound is a desirable property since it make it easier to control the reaction. Widely tunable CdSe quantum dot sizes were obtained by

simply changing type of ligand and precursors [91], enabling obtainment of particles emitting in all the visible range. Also shape control of nanocrystal resulted to give much more possibilities [92]. Furthermore, the dependence of synthetic environment on usually unpredictable and irreproducible PL emission properties of CdSe core has been studied as a function of synthetic parameter [93]. It was shown that a maximum in PL QY exists during growth time which was attributed to the maximum quality of surface reconstruction achievable only in certain stage of the synthesis when particle surface is in equilibrium with bulk solution.

Other semiconductor particles such as PbS, PbSe[94], CdS and CdTe[90] could be synthesized withy improved quality.

Even thought coordinating solvents led to high quality CdSe NPs, particles of different semiconductor type could not be synthesized with the same quality. Most likely, the same solvents has not always the same efficacy in coordinating all semiconductor compounds.

For these reason, alternative approaches in non-coordinating solvents have been attempted in which complexation of precursors is assigned only to organic ligands, while the solvent is intended to have no influence on synthetic evolution.

The most common solvent used so far has been 1-octadecene which is liquid at room temperature and boils at 320°C. CdS was the first system to be synthesized within these methods, using oleic acid as complexing agent for CdO and elemental sulfur dissolved in octadecene[95]. The obtained particles were of extremely high quality, despite the simplicity of the reaction scheme and also III-IV semiconductor particles could be successfully synthesized [96].

The most important feature in non-coordinating solvent approach is the possibility to tune the reactivity of precursor by changing type and relative quantity of complexing agent, providing one to optimize for nucleation and growth events.

This fact can be rationalize if the activity coefficient γ is introduce in the definition of monomer chemical potential as follows :

$$\mu_C^l = \mu_{eq} + RT\ln(\gamma S) \tag{3.23}$$

This coefficient accounts for change in chemical potential and reactivity due to factors other than concentration, such as ligand concentration and type.

If the above mentioned synthesis is taken as an example, the cadmium precursor might not be the simple cadmium oleate salt at those elevated temperatures, since ligands can be

expected to be quite labile. Thus, if ligand concentration is increased, their number nearby cadmium ion should also increase resulting in major stability of cadmium monomer in solution and decreased reactivity toward particle formation.

In fact, it has been observed that both particle radius after short periods from injection (which can be taken as the initial nucleation radius) and the final unreacted monomer concentration in solution increase upon increasing of ligand concentration. This can be explained by the reduced reactivity which acts to increase the critical radius during nucleation through Eq. 3.11 and to diminish nucleation rate through Eq. 3.12 leaving greater amounts of unreacted monomers available for particle growth.

The possibility to tune monomer reactivity allows for good balance between nucleation and growth. This means that monomer reactivity should be high enough for a good nucleation event but not too high to consume all monomers in the nucleation step. If all monomer are soon consumed, Ostwald ripening and defocusing occur since supersaturation need to be sufficiently high for maintenance of narrow dispersion during growth.

The flexibility of these approaches has been further exploited by using binary ligand system, where two different complexing agents, oleic acid (*OA*) and diisooctylphosphinic acid (*TMPPA*), are used for the metal [97].

In this work, the role of these molecules are discuss and a detailed insight in particles evolution from nucleation to growth stages by means of UV-Vis spectroscopy is provided from size and number of particles variation during time (see figure 3.17).

The general trend consisted in an increase in particle number over the first 30 seconds from the injection, and this can be considered the nucleation period. Then, particles number decreases and particles size increases over the following 400 seconds after which period growth is almost concluded. Interestingly, the total volume of the precipitated phase does not change in this second stage, thus the observed decrease in particle number is not simply dissolution of smaller particle but dissolution and re-precipitation on bigger particle as typical of Ostwald ripening even if this process generally occurs in the later stages of the synthesis.

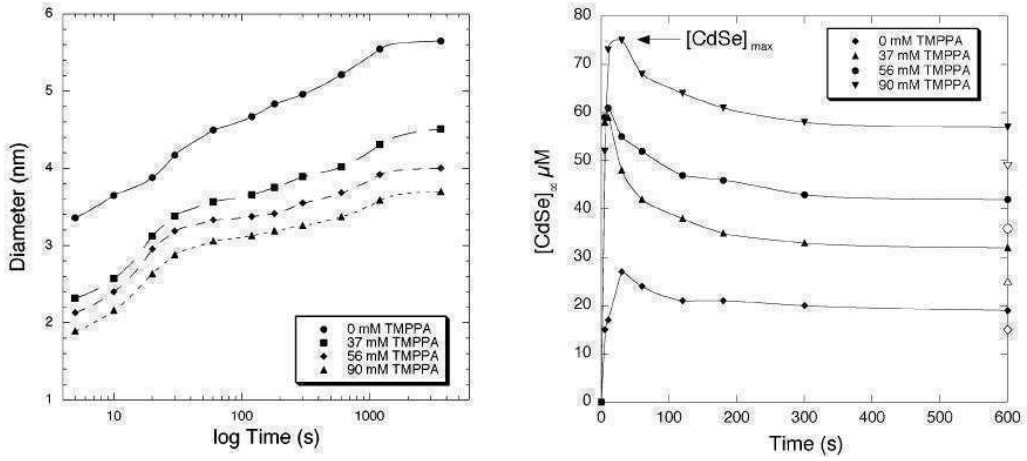

Figure 3.17 Particle number and size evolution at different Cd:TMPPA ratio with constant Cd:OA ratio (Source : Van Embden et al. [97])

This scenario is quite different from the classical one proposed by La Mer and summarized in Fig. 3.13. First of all nucleation period is prolonged in time and not a discrete event. This is likely to be caused by the continuous decrease in temperature due to injection of cool reagents which in turn acts to decrease solubility of monomer keeping supersaturation quite high for nucleation over 30 seconds.

This prolonged nucleation do not cause however a polydispersed ensemble of initial nuclei, since the decrease in supersaturation due to monomer consumption causes an increase of the critical radius r* over time. Thus, at a given time, previously formed nuclei with smaller radius will dissolve while new nuclei tends to a have a dimension similar to the critical radius of that moment. As a result, it can be argued that the nanocrystal population will tend to have the same radius r*.

Also the stage following nucleation period is not coherent with the classical view since simple growth is not the only process but also ripening seems to be present. The authors refers to such anticipated ripening as Early Time Ripening (ETR).

The picture coming out from this study shows that nucleation, growth and ripening are most likely to occur at same time.

While keeping the same nanocrystal evolution trend, number of particles and their sizes were demonstrated to be highly dependent on the type of ligands used and their relative amount. By keeping the same Cd:OA ratio and varying *TMPPA* content, an increase of initial nuclei and final particle number and a decrease of their size was observed. In the following stage, the number of particle decreases to a minor extent if more *TMPPA* is used.

Furthermore, if *TMPPA* is added to a composition initially comprising only *OA*, particle number decreasing is stopped soon after *TMPPA* injection.

If OA content is increased while keeping *TMPPA* constant, smaller particle size and number of particles are obtained.

The above results can be explained by the different complexing behavior of the two ligands.

TMPPA is supposed to bind more strongly to particle surface than to monomer in solution. This leads to a greater driving force toward precipitation and particle formation and a decrease of surface energy due to stable chemisorption bond on particle surface. These factors diminish the energy barrier of nucleation and the critical nuclei radius, resulting in a greater number of particles and decrease of final particle size. Thus *TMPPA* can be considered as a "nucleating agent".

On the contrary stability of cadmium oleate complex in the solution phase is believed to be higher with respect to the TMPPA counterpart. Thus OA acts as a solubilizing agent, lowering the effective supersaturation and inducing particle number decreasing to be more pronounced and particle sizes to be larger. For this reason it is referred to as " ripening agent".

A combination of the two ligands has been verified to provide the best conditions for highly reproducible size tuning in the 2.4-5.6 nm diameter range while keeping monodispersion.

The discussion has so far dealt with synthetic environment effect on nucleation and growth, without considering the chemistry behind the process.

The simplest view which can be suggested implies complex thermal decomposition and further reaction of cadmium with selenium.

Recent studies by Alivisatos et al. [98] shed light on the mechanistic aspect of reaction between phosphonate and oleate cadmium complexes with selenium complexed with phosphines.

Cadmium complexes were prepared by heating cadmium oxide (*CdO*) in presence of the complexing agents. The reaction with oleic acid upon heating occurs with release of water, as described from the following reaction :

$$CdO + 2OA \rightarrow Cd(OA)_2 + H_2O$$

An analogue reaction occurs with phosphonic acid.

The reaction leading to semiconductor monomer CdSe has been suggested to be initiated by an elettrophilic attack of the chalcogenide in the P=Se bond by the cadmium atom and a concomitant nucleophile attack of the phosphorous center by an oxygen from the carboxyilic or phosphonate groups. This leads to cleavage of the P=Se bond to form CdSe and formation of trialkylphosphine oxide.

Among reaction product it was found also anhydrides of oleic acid or phosphonic acid. The suggested reaction scheme is depicted in figure 3.18.

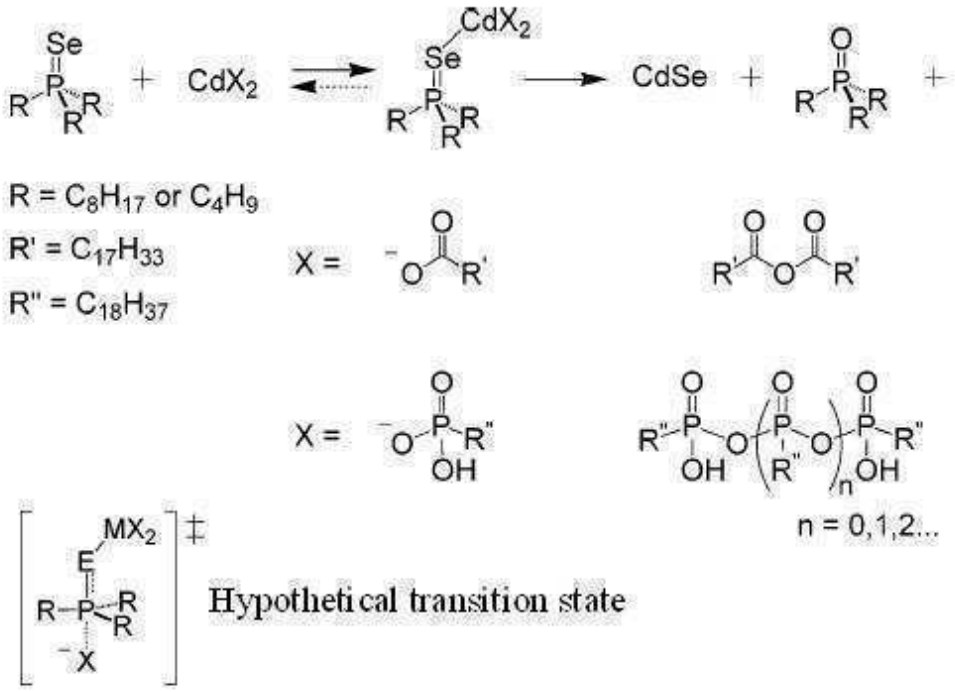

Figure 3.18 Proposed reaction scheme leading to CdSe formation and supposed transition state (Source : Haitao et al. [98])

The kinetic of this reaction has been studied also considering sulfur and tellurium as chalcogenide and zinc as metal. It was found that reaction kinetic increases in the order S<Se<Te and Zn<Cd, which can be related to the stability of initial complexes.

Thus, the rate of P=Se bond cleavage is likely an important step in determining the following nucleation and growth stage, since avaible CdSe monomers are determined by the above-described reactions.

3.3.3 Core@Shell NPs synthesis

As far as shell synthesis is concerned, several issues can be in principle considered to get the desired properties [63].
The main goal in shell growth is to obtain uniform, defects-free coverage of core particle.
In order to achieve this, three main obstacles need to be overcome :

- too high monomer solubility and low reactivity
- too strong binding of ligand to particle surface
- homogeneous nucleation of shell precursors

The role of complexing agents is fundamental to impart the right solubility and reactivity to ensure slow and uniform growth. This is particularly true if highly reactive organometallic precursors are used. However, if too many ligands or metal-complex bonds are too stable, shell growth can be prevented since deposition become unfavorable. Moreover, synthetic environment where equilibrium are driven mostly toward solubilisation can facilitate Ostwald ripening and defocusing or dissolution of deposited shell material.
Increase in temperature can enhance reactivity of precursors but at the same time it increase solubility and cause ripening and loss of particle stability. Precursors reactivity should be such that the temperature for slow and uniform growth is not too high to cause ripening and particle dissolution, but the higher is possible to achieve good crystallinity and annihilation of possible structural defects.
On the other hand, ligands should not bind too strongly to particle surface since this can block reactive site for monomer in solution. In other words, particles should be not too stable, but have labile ligands on the surface , as demonstrated by Peng et al. [49], where pyridine was used since it was known to bind weakly to cadmium sites.
Finally, if monomer reactivity is too high or ligand type and concentration is not optimized, homogeneous precipitation of shell precursor can occur.
It is difficult to satisfy all these requirements and the possibility to do that is obviously linked with the progress in synthetic methods.

The first core@shell syntheses were based on aqueous colloidal chemistry at low temperature [99]. Henglein et al. showed that PL-QY could be enhanced to 50% by growing a $Cd(OH)_2$ on CdS NPs. Also Brus et al. successfully deposited ZnS on CdSe

particles [106]. Even if fluorescence enhancement and stability were obtained, broad distribution of cores and thin shells with poor crystallinity due to low synthesis temperature were typical.

The possibility to produce particles in non-polar, high boiling point solvents not only allowed for semiconductor NCs with higher quality but also brought to new approaches for shell growth as demonstrated by Hines and Guyot-Sionest. Core@shell structures with improved PL-QY and narrow distribution were obtained using organometallic precursors such as diethyl zinc and bis(trimethylsilyl)sulphide for ZnS shell growth [100]. This synthesis was then optimized by Dabbousi et al. [50] growing thicker shell and presenting detailed structural data also reported in section 3.2.2.

Further development of organometallic approach for shell growth has been achieved by using solvent mixtures comprising amines, which were found to provide a good media or particle stability during growth retaining good monodispersion [50].

The use of "greener" salt based precursor for shell growth was first introduced by Mekis et al.[51] using H_2S and cadmium acetate and Reuss et al. who synthesized CdSe@ZnSe with high PL-QY and stable emission properties also in aqueous media [59].

The use of less reactive monomer led to higher control of shell growth, even if good precursors for ZnS shell other than organometallic precursor are difficult to find since zinc complex tend to be less reactive with respect to cadmium ones [107].

Salt based precursors in non-coordinating solvent were adopted by Li et al. employing the SILAR method for CdSe@CdS particles [55]. In this protocol, the chalcogen and metal precursors are alternatively injected and allowed to adsorb on particle surface in order to minimize the risk of homogeneous nucleation since their coexistence in solution is reduced. The method also allows for monolayer by monolayer deposition with the possibility of finely tune the composition of the shell and surface stoichiometry.

Multiple shell CdSe@CdS@ZnS systems were then synthesized employing greener precursors for CdS and diethyl zinc for the final layer. SILAR approach was further developed for "super" graded shell of the CdSe@CdS@$Cd_{0.5}Zn_{0.5}$ S@ZnS employing only oleic acid as comlexing agent for both zinc and cadmium [67].

Such methods have been recently used for synthesis of CdSe@CdS@ZnS for lasing application by Jaseniak et al.[17]. Van Embden et al. also employed the SILAR method for CdSe@CdS NPs [63] by using the binary ligand approach already described in the previous section. In this thesis *TMPPA* was used to complex cadmium since it is more

reactive than cadmium oleate, but it tends to bind strongly to particle surface and to cause significant homogeneous nucleation. Addition of *OA* help to enhance particle reactivity aiding for the displacement of *TMPPA* molecules out from surface sites. This results in uniform coverage of CdSe core achieving optimized condition for right shell monomer reactivity eliminating homogeneous nucleation.

3.4 Experimental

3.4.1 CdSe Core synthesis and results

CdSe NPs were prepared according to the procedure described in ref [97], using the binary ligand approach described in section 3.3.2. This protocol enables for size particle tuning , good monodispersion and reproducibility. The procedure consists in preparing a cadmium containing solution, *CdO solution*, and a selenium containing solution, *Se solution*. The quantity of chemicals used are reported in Table 3.3, while the synthesis set-up is described in Chapter 2. The detailed procedure is described in the following steps:

- A *CdO solution* is prepared by adding cadmium oxide powder to a solution of 1-octadecene (*ODE*) and oleic acid (*OA*) or diisooctylphosphinic acid (*TMPPA*) depending on the desired size (see Table 3.3). The solution is degassed under vacuum at 100°C for 1 hour and then switched to nitrogen atmosphere using conventional Schlenk line. The solution is then heated to 300°C and held a this temperature for two hours. A clear solution where the cadmium oxide powder is completely complexed is so obtained
- A *Se solution* is obtained by weighting selenium powder in a glass vial. Then trioctylphosphine (*TOP*) is added and complete dissolution of selenium in *TOP* is observed. The solution is completed with the addition of *TMPPA* and *ODE*.
- The cold *Se solution* is loaded in a syringe and rapidly injected in the hot *Cd solution* and the resulting solution is held at the growth temperature for 45 minutes.
-

Recipe	Cd solution				Se solution				
	CdO (mg)	OA (g)	TMPPA (g)	ODE (g)	Se (m)	TOP (g)	TMPPA (g)	ODE (g)	Growth Temperature (°C)
C1	30	-	0,3	12	158	1.16	0.3	4.0	200
C2	60	1.5	-	12	37.2	1.16	0.767	3.55	230
C3	60	1.5	-	12	37.2	1.16	0.250	4.0	230

Table 3.3 Employed compositions for synthesis of CdSe synthesis with the protocol described in ref.[97]

The evolution of particle diameter using recipes in table 3.3 has been followed by optical absorption measurements on aliquot extracted at different time. The particle diameter is calculated from the equation reported in table 3.2 and evolution during synthesis is shown in figure 3.19 A, while the absorption spectrum for the final particle around the band-edge onset is reported in figure 3.19 B.

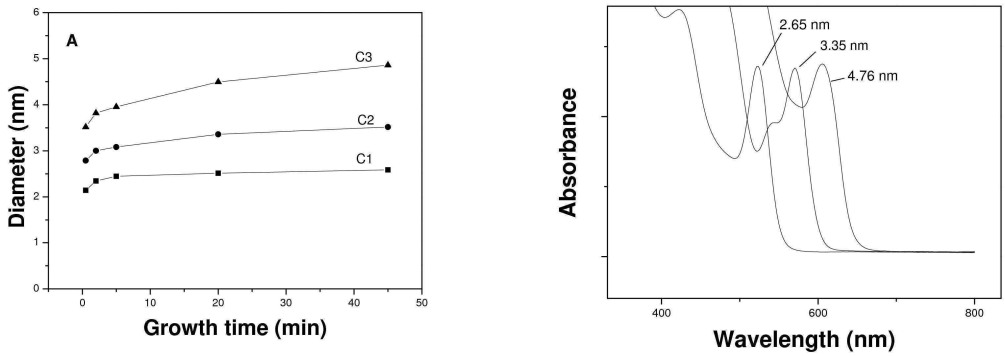

Figure 3.19 Particle diameter evolution during synthesis(A) and absorption spectra near the band edge for final particle foe recipes **C1**,**C2**,**C3** (B)

Thus particle's size tuning is possible and quite reproducible dimension are obtained by simply varying the synthetic parameters and allowing for equilibrium dimensions to be reached. Recipes **C1**, **C2** and **C3** allows for CdSe diameter of 2.65 nm, 3.35 nm and 4.76 nm. respectively These sizes are not the same predicted in ref [97] for the same composition, but differences in experimental set up, temperature profile after injection and minor growth times (45 minutes instead of 60 minutes adopted to minimize the risk of Ostwald Ripening) can account for these differences. Anyway reproducibility of dimensions are indeed quite good. A TEM mage of a particle obtained from recipe **C2** is shown in figure 3.20. A mean diameter of 3.2 ± 0.5 nm has been estimated from TEM data

and interplanar distances determined through FFT (Fast Fourier Transformation) analysis are in good agreement with the wurtzite hexagonal structure.

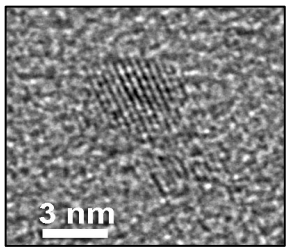

Figure 3.20 TEM micrograph of cores obtained from recipe **C2**

The band edge luminescence of as-synthesized core nanoparticles is very low (lower than 1%) and a broad band at the red-side of then main peak due to defect-state emission can be observed, as shown in figure 3.21, for particles obtained from recipe **C1**.

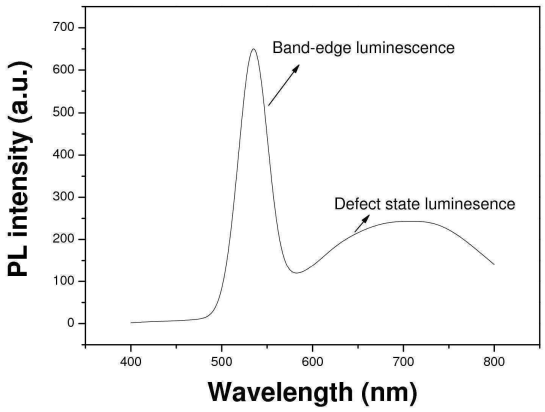

Figure 3.21 PL spectrum of as-synthesized particles obtained from recipe **C1**

These core particles have been mainly used for core@shell synthesis. Before shelling protocol, cores must be purified to remove excess ligands and unreacted precursors. The washing and extraction protocol is analogue to that reported in ref [102] and it applies to lipophobic coated particles.

The synthesis batch (about 20 ml in volume) is first loaded in a separating funnel . A methanol/chloroform equivolume mixture is then added. Subsequently, methanol is slowly added until the solution became turbid. At this stage the mixture undergoes phase-separation due to immiscibility between methanol and *ODE*. A particle-free bottom liquid layer and un upper particle containing layer is then obtained. The bottom layer is mainly a methanol/chloroform mixture that tend to dissolve ligands or precursors impurities, while

the upper layer is mainly a chloroform/*ODE* mixture in which particle are stable. If some acetone is added, particles tend to be more concentrated in the upper layer probably because of the increased solubility of *ODE* in the bottom layer. Once a clearly defined phase boundary is achieved, the bottom layer is discarded.
This procedure is repeated at least two-times to improve purification. The so-obtained particles are stored under dark.

3.4.2 Core@Shell synthesis

3.4.2.1 The SILAR method

The method we decided to employ for core@shell synthesis has been first proposed by Peng et al. [55] for CdSe@CdS, further developed by Mews et al.[67] for production of graded structures and used by Jaseniak et al. [17] for QD synthesis for optical amplification purposes.
This procedure relies on the knowledge of the number and mean diameter of initial CdSe cores in the starting solution. This is possible through the relationships proposed by Yu et al. [102] that correlate the first absorption peak to particle diameter and the particle diameter to extinction coefficient.
Once these data are known, the method consists in providing the amount of shell material precursor necessary for one monolayer growth. The addition is such to alternatively provide only one of the two shell constituents allowing for their deposition on the growing particle. Thus, two consecutive addition are required to grow a monolayer.
The moles to be added in one addition N_{shell} can be calculated from the following relationship, which is based on a spherical concentric model for the shell.

Eq. 3.24
$$N_{shell} = n_{CdSecore} \frac{4\pi}{3}((R + r_{ML})^3 - R^3)) \frac{\rho_{shell}}{MW_{shell}}$$

Where $n_{CdSecore}$, is the number of CdSe cores to be covered, R is the particle radius before monolayer growth, r_{ML} is the monolayer thickness of the bulk semiconductor material to be deposited, ρ_{shell} and MW_{shell} are shell material's density and molecular weight. These data

for semiconductor materials of interest are given in table 3.4. The monolayer thickness is here assumed as half the lattice constant c of the wurtzite structure [63].

	CdSe	**CdS**	**ZnS**	**$Cd_{0.5}Zn_{0.5}S$**
r_{ML} (nm)	0,35	0.335	0.31	0,322*
ρ_{shell} (Kg/m^3)	5.81	4.82	3.98	4.61*
MW_{shell} (gr/mol)	191.37	144.47	97.44	120.9

***** Lattice parameter estimated from linear interpolation (Vegard law) between CdS and Zns lattice constant. Density is then estimated from this unit cell parameters

Table 3.4 Material's data for semiconductors of interest [103]

This method allows for monolayer by monolayer growth whose composition can, in principle, be finely tuned. In the work of Mews [67], it was shown the possibility to tune the composition of the shell from CdS to ZnS with an intermediate layer of $ZnS_{0.5}Cd_{0.5}S$.
In the present experimental activity, two types of structures have been targeted.
The first comprises a shell structure composed of 2 ML of CdS and 2 ML of ZnS (referred to as the **CSS** system), while the second is composed of ML of CdS, 3 ML of $ZnS_{0.5}Cd_{0.5}S$ and 2 ML of ZnS (referred to as **CSSS** system). A schematic representation is given in figure 3.22.

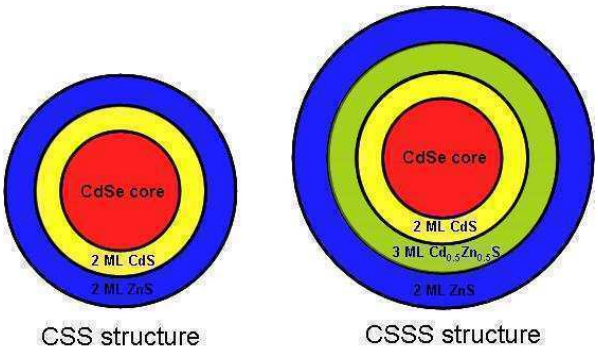

Figure 3.22 Schematic representation of target **CSS** and **CSSS** structure

3.4.2.2 Core@Shell synthesis procedure

The first stage is the preparation of Cadmium, Zinc and Sulphur precursors for shell growth. The procedures for precursor's preparation is given below :

- *Sulfur precursor* (*S-ODE*) : 96 mg of elemental sulfur are loaded in 50 ml three-necked flask with 30 ml of *ODE* for a concentration of 0.1M sulfur. The solution is heated under vacuum at 100°C for one hour. The atmosphere is then switched to nitrogen and the temperature is brought to 180°C for 30 minutes. The solution is then allowed to cool and switched to vacuum when the temperature reaches 100°C. At room temperature the flask is again filled with nitrogen.
-
- *Cadmium Precursors* : two cadmium solution, *TMPPA-Cd* and *OA-Cd* were prepared using either *TMPPA* or *OA* as complexing agents respectively.
  0,38 g of cadmium oxide are loaded in a 50 ml three-necked flask with 3.48 g of *TMPPA* or 3.38 g of *OA* and 26.19 ml of *ODE* giving a metal concentration of 0.1M and *OA/Cd* or *TMPPA/Cd* of 4. The solution is heated at 100°C under vacuum for one hour, then the temperature is raised to 300°C for 2 hours, obtaining a clear solution. The solution is then allowed to cool down to 100°C and put under vacuum for degassing and eliminating residual moisture released from complexation reaction. The solution is then allowed to cool at room temperature and stored under nitrogen.

- *Zinc precursor* (*TMPPA-Zn*) : 0.24 g of zinc oxide powder are loaded in a 50 ml three-necked flask with 3,48 g of *TMPPA* and 26.19 ml of *ODE* giving a metal concentration of 0.1M and a *TMPPA/Zn* ratio of 4 . The solution is heated at 100°C for 1 hour under vacuum and then heated to 310°C under nitrogen. Since complexation reaction is quite slow, the solution is kept at this temperature for 4 hours. It is then cooled to 100°C and put under vacuum for 30 minutes and further heated to 310°C for 4 hours. The resulting solution is quite clear and is allowed to cool, degassed under vacuum and finally stored under nitrogen at room temperature.

In a typical core@shell synthesis, 1.2 g of octadecylamine (*ODA*) and 2.36 g (3 ml) of *ODE* are loaded in a three-necked flask and heated under vacuum at 100°C for 30 minutes. The mixture is allowed to cool at 40°C under vacuum. The atmosphere is switched to nitrogen and 1.83 μmol of purified CdSe cores (in a mixture of *ODE* and chloroform) are added.

The solution is again put under vacuum to remove residual traces of chloroform and then heated at 100°C for one hour. Then core nanocrystals are slowly heated to the initial growth temperature at which the first cadmium precursor injection is performed. This temperature depends on the diameter of the initial core used.

In the present thesis **C1** and **C2** core particles (respectively obtained from synthesis recipe **C1** and **C2** described in section 3.4.1) have been used. For **C1** the initial growth temperature is 195°C, for **C2** particles it is 210°C. This is due to the fact that smaller cores tend to dissolve at temperature lower than bigger ones and stable initial cores are desirable for further growth.

All precursors additions are performed using a syringe pump, setting addition rates and volumes in order to provide the necessary amount of precursor's solution in 5 minutes for the first three addition and in 10 minutes for the remaining ones. The amount of precursor for each addition is calculated as describe in the preceding section and a 10% excess metal is used in order to account for non complete reaction of all the monomer added as suggest in ref. [63]. The final addition consists in zinc precursor since a metal rich surface ensure better photostability [104] and easier capping ligand exchange procedure, as discussed in Chapter 6.

Precursor's addition temperatures are progressively increased during the synthesis and are reported in table 3.5. Reaction times occurring between the beginning of two consecutive additions were equal to 10 minutes for the first three addition, while in the remaining synthesis 20 minutes are allowed for metal reaction and 30 minutes for sulfur reaction.

The CS particles are then cooled at 200°C and annealed at this temperature for 1 hour.

A

CSS structure		2 ML CdS				2 ML ZnS				
	Starting core	cd	s	cd	s	zn	s	zn	s	zn
Temperature (°C)	**C2 core**	210	210	220	220	230	235	240	240	240
	C1 core	195	210	220	220	230	235	240	240	240

B

CSSS structure		2 ML CdS				3 ML $Cd_{0.5}Zn_{0.5}S$					2 ML ZnS					
	Starting core	Cd	s	cd	s	cdzn	s	cdzn	s	cdzn	s	zn	s	zn	s	zn
Temperature (°C)	**C2 core**	210	210	220	220	230	230	230	230	230	230	240	240	240	240	240
	C1 core	195	210	220	220	230	230	230	230	230	230	240	240	240	240	240

Table 3.5 Reaction temperatures during cadmium (cd), sulfur (s) and zinc (zn) addition stages for CSS (A) and CSSS (B) shell growth

The batch is then cooled to 60°C and 20 ml of isopropanol are added to cause flocculation. The particles are centrifuged at 6000 rpm for 5 minutes and redispersed in chloroform. Another purification round is performed by adding methanol and centrifuging the particles at the same conditions. Finally the particles are dispersed again in chloroform and used for further capping ligand exchange as describe in Chapter 6.

3.4.2.3 Results and discussion

In the first attempts to produce CS structures, we tried to reproduce the Mews recipe which employs only oleic acid as complexing agent. We couldn't reproduce that procedure since it resulted in broad distribution as deduced from optical spectra due to excess ripening of the particles. This can be attributed to the use of oleic acid which is likely to induce excess monomer solubility and thus ripening.

For these reasons we moved toward the use of *TMMPA* which was demonstrated to enhance particle stability. Furthermore *TMPPA* complex are more reactive being this a desirable condition. The complexing agents to metal ratio was also changed from 8:1 to 4:1 to raise monomer reactivity. Greater reactivity also enhance the probability of homogeneous nucleation of shell material. For this reason we decided to employ a drop-wise addition of the precursor, in order to avoid supersaturation build-up.

To grow the intermediate alloy layer we used *Cd-OA* as metal precursors, in order to balance the reactivity of zinc and cadmium. In fact, cadmium precursors are more reactive, thus in this step we used *OA* since it lowers reactivity of cadmium with the aim of depositing zinc and cadmium with the same rates. In the CdS layer growth the *Cd-TMPPA* precursor was used.

Solvent mixture (*ODE* + *ODA*) was kept since it has been shown to offer good stability [55] and good growth of monodispersed particles [50]. In fact, only small dissolution was observed from optical measurements comparing starting core particles with particles heated at the initial shell growth temperature in this solvent mixture.

Finally also the CSSS "super graded" structure was retained in these first attempts and the 3.2 nm **C2** CdSe core was employed in this shelling procedure.

Using these conditions the first batch of core shell particles was obtained.

Aliquots were extracted from the solution after the additions necessary for CdS, $Cd_{0.5}Zn_{0.5}S$ and ZnS (after the annealing step) and used for TEM and optical measurements

The TEM micrographs for each of this stage are shown in figure 3.23.

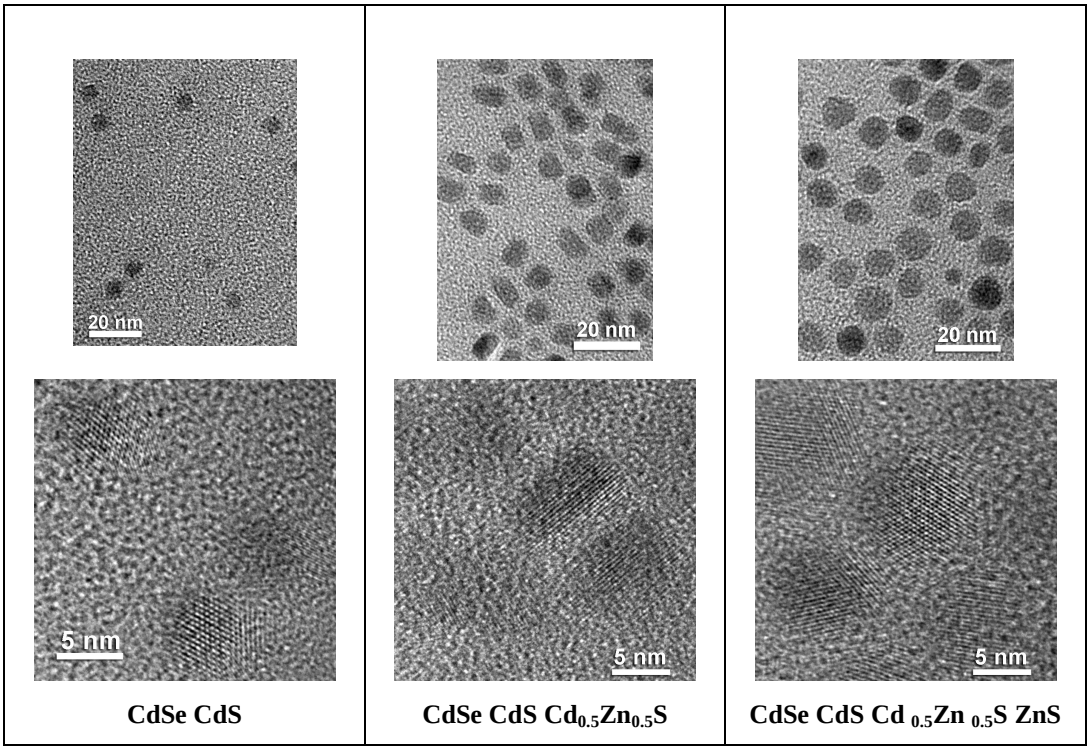

Figure 3.23 Bright field (top) and HR-TEM (bottom) images of particles extracted from batch solution at different stages. Cd-OA was used in the intermediate alloyed layer

Sample	$D_{obs} \pm \sigma$ (nm)	$D_{Expected}$ (nm)	Phases (from FFT-HR TEM analysis)
CdSe CdS	5.1 ± 0.9	4.52	CdSe + CdS + $CdSe_{0.5}$ $S_{0.5}$
CdSe $Cd_{0.5}Zn_{0.5}S$	7.1 ± 1.3	6.46	CdSe + CdS + $CdSe_{0.5}$ $S_{0.5}$ + ZnS + $Cd_{0.7}$ $Zn_{0.3}$ S
CdSe $Cd_{0.5}Zn_{0.5}S$ ZnS	8.5 ± 1.0	7.70	CdSe + CdS + $CdSe_{0.5}S_{0.5}$ + ZnS+ $Cd_{0.7}$ $Zn_{0.3}$ S + ZnS

Table 3.6 Observed and expected diameters along with possible assignation of phases detected from FFT analysis

Diameters of the particles are seen to progressively increase. FFT analyses was also performed to get interplanar distances. From these data it was possible assign the different phases present in a single particle, which are summarized in table 3.6.

In the CdSe CdS $Cd_{0.5}Zn_{0.5}S$ stage the particles resulted to be anisotropic. In this case the mean value between long and short axis was assumed. In the other cases almost spherical particles were obtained.

In table 3.6, there are also reported the expected diameters ($D_{Expected}$) estimated from a concentric shell model using monolayer parameters in table 3.4 and an initial CdSe core diameter of 3.2 nm.

The observed diameters are consistently greater than the theoretical ones. This can be related to ripening of the particles or to presence of unreacted precursors from core synthesis due to non complete purification. Such unreacted precursors (cadmium and selenium) can deposit on growing particle increasing the diameter. Furthermore, the growth most probably is not epitaxial since a lot of reflection attributable to different phases are detected, while pure epitaxial growth would result in reflection attributable to only one structure. The absorption and emission spectra (normalized for the absorption at the 480 nm excitation wavelength) for starting CdSe cores and final core@shell particles are presented in the figure 3.24.

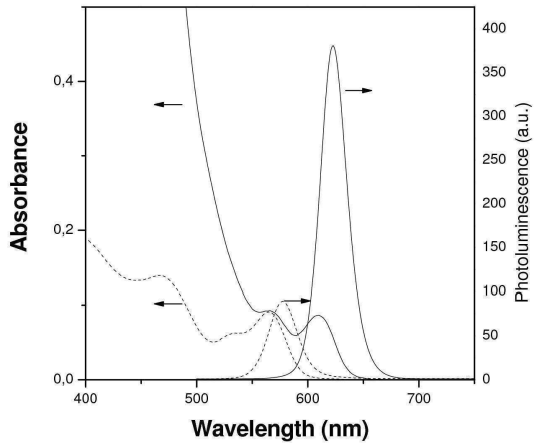

Figure 3.24 Absorption and emission spectra for CdSe cores (dashed line) and core@shell (solid line) in chloroform obtained using Cd-OA in the intermediate alloy layer

Fluorescence quantum yield is consistently enhanced up to almost 40%, showing an effective influence of the shelling procedure. Also the resulting absorption and emission features are quite narrow.

Anyway, this procedure is not satisfactory since it doesn't provide homogeneous coverage through all the stages (anisotropy is observed during synthesis) probably due to presence of different ligands, epitaxial growth is not followed and ripening is very probable which can be favored by presence of oleic acid. Thus, employment of two type of ligands does not seem to be beneficial.

For these reasons we moved to a synthesis employing only *TMPPA* as capping ligand.

Further, we decided to test both CSS and CSSS structure on CdSe core with two different diameters, in order to understand the effectiveness of an alloy layer and the possibility to obtain different color with core@shell structure.

The procedure for the synthesis is the same unless for the use of *Cd-TMPPA* also in the alloy layer in the CSSS structure synthesis. The CdSe core employed were the 2.65 nm **C1** particles and the 3.2 nm **C2** particles as described in section 3.4.1. These samples will be referred to as **C1-CSS**, **C1-CSSS**, **C2-CSS** and **C2-CSSS**.

TEM analyses were performed only on the final **CSSS** and **CSS** core@shell particles employing **C2** CdSe core (see figure 3.25).

In this case, from FFT analyses on **CSS** particles it is possible to conclude that about 70% of particles shows one single reflection, while the remaining particles shows different reflections which could be attributable to the same phase reported in table 3.6.

The same holds true for the CSSS particles unless that only 30% of the analyses particles shows only one reflection.

These data suggest a better epitaxial growth of these samples if compared with the previous one.

From comparison of observed and expected diameters, it can be observed that in this case lower experimental values are obtained than those expected (see table 3.7).

This suggests that the reactivity of some precursors is not high enough to deposit shell material completely.

To have a deeper insight on this problem, the single particle composition measured with Energy-Dispersive X-ray Spectroscopy (EDS) technique during TEM measurement has been taken and presented in figure 3.26 as the atomic ratios Se/Cd, S/Cd and S/Cd. These data are also compared with the theoretical ones calculated from a concentric model and presented in the bar graph in the same figure.

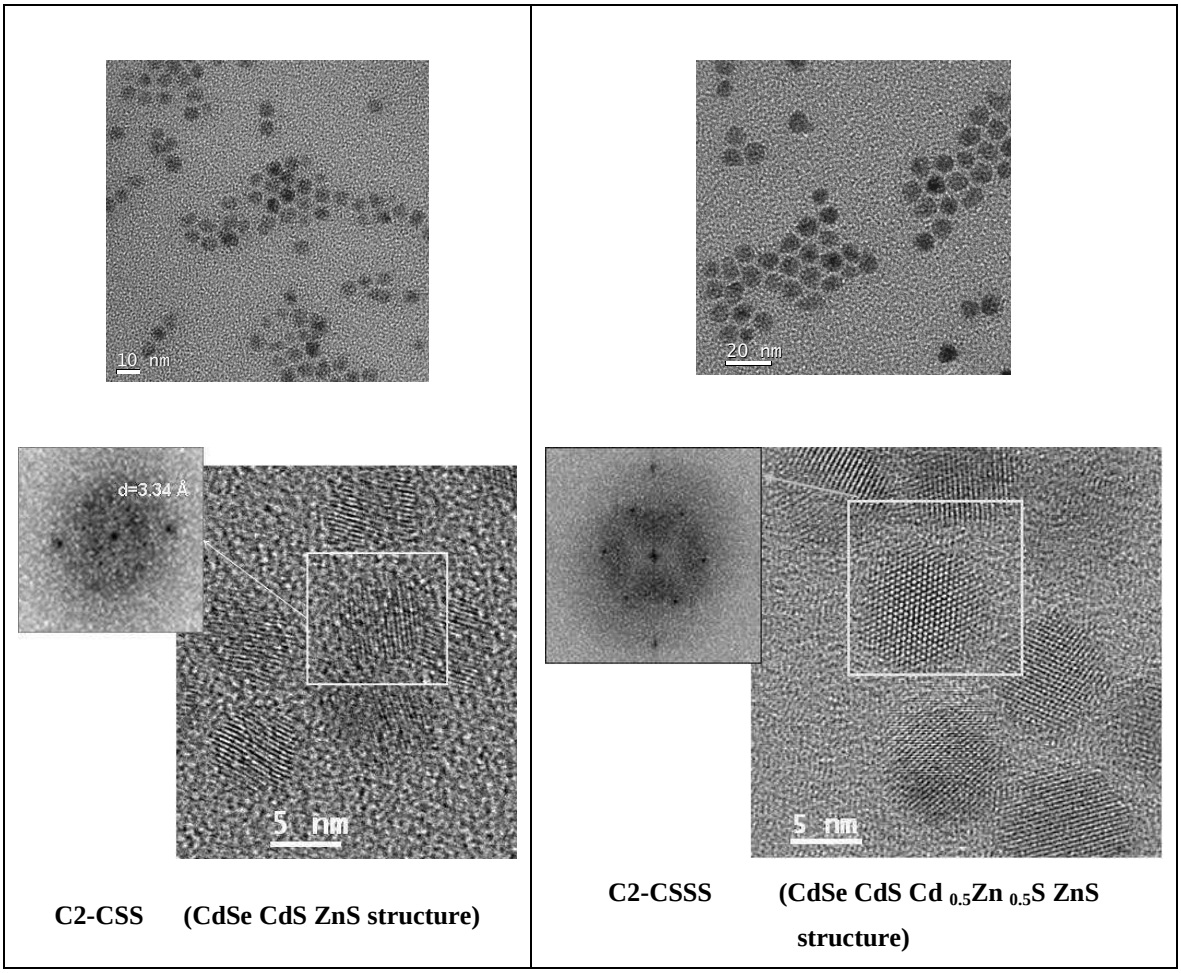

Figure 3.25 Bright field (top) and HR-TEM with FFT analysis (bottom) data of samples C2-CSS and C2-CSSSS employing only TMPPA as complexing agent

Sample	$D_{obs} \pm \sigma$ (nm)	$D_{Expected}$ (nm)
CdSe CdS ZnS (CSS)	5.2 ± 0.8	5.77
CdSe CdS $Cd_{0.5}Zn_{0.5}S$ ZnS (CSSS)	7.3 ± 0.9	7.70

Table 3.7 Observed and expected diameters are reported in the table below

	C2-CSS		C2-CSSS	
	Observed Values	Expected for C2-CSS	Observed Values	Expected for C2-CSSS
Se/Cd	0.4	0.33	0.1	0.16
S/Cd	1.1	2.03	1.4	2.59
Zn/Cd	0.7	1.36	0.6	1.75

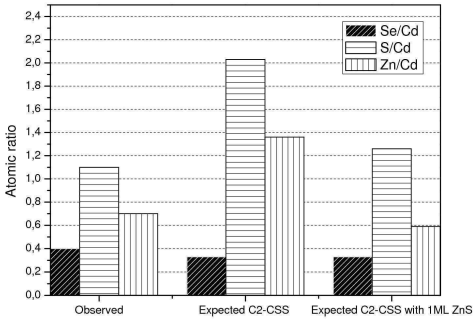

Figure 3.26 Observed and expected atomic ratios for a single particle. In the bar-graph observed values are represented with those expected for C2-CSS structure and C2-CSS structure with only one ML of outer ZnS

As it is evident, the atomic ratios does not fit with the theoretical values for the targeted desired structures. In particular, mainly sulfur and zinc seems to be in a lower amount than that predicted. In the case of the **CSS** structure, experimental data seem to be in accordance with a particle where the outer ZnS layer is not complete and consists in only one monolayer. Thus, it can be argued that after the deposition of one monolayer of zinc, the particle do not grow further, probably due to less reactivity of the zinc site on particle surface toward sulfur.

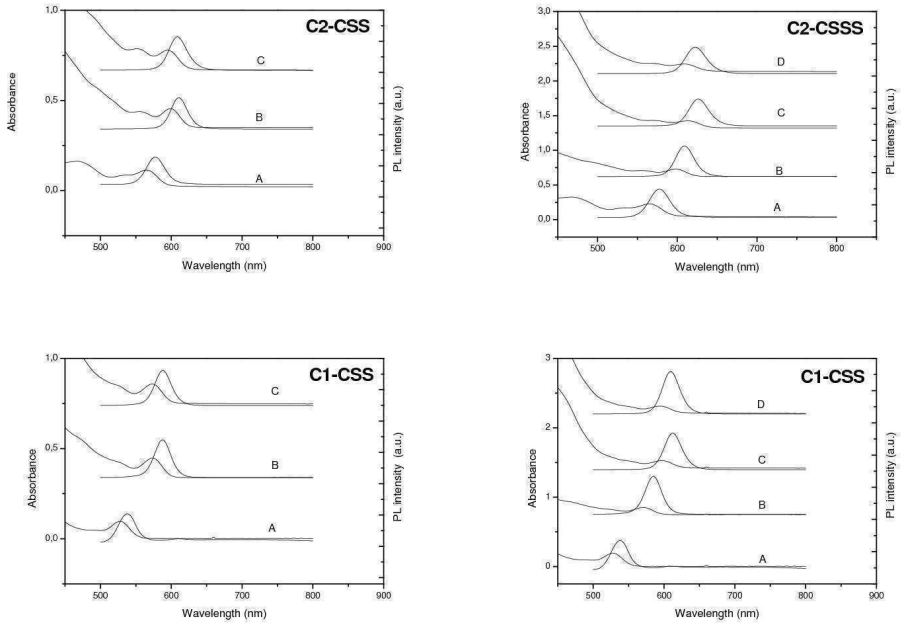

Figure 3.27 Absorption and emission spectra of particles extracted during the synthesis of core@shell nanocrystal with different targeted shell structure (**CSS** and **CSSS**) on different core (**C1** and **C2**). For CSS structure A, B and C refer to CdSe core particles, CdSe CdS and CdSe CdS ZnS synthesis stages respectively, while for CSSS structure A, B, C and D refer to CdSe core, CdSe CdS, CdSe CdS $Cd_{0.5}Zn_{0.5}$ ZnS and CdSe CdS CdS $Cd_{0.5}Zn_{0.5}$ ZnS respectively.

		CSS			**CSSS**			
		A	**B**	**C**	**A**	**B**	**C**	**D**
C2 starting core	**PL-QY (%)**	**1.5**	**48**	**44**	**1.5**	**43**	**40**	**38**
	λ_{em} (nm)	**577**	**611**	**609**	**577**	**609**	**626**	**623**
	PL FWHM (nm)	**30.2**	**27.4**	**29.9**	**30.2**	**27.0**	**28.9**	**30.6**
C1 starting core	**PL-QY (%)**	**1.8**	**48**	**48**	**1.8**	**51**	**53**	**57**
	λ_{em} (nm)	**538**	**588**	**588**	**538**	**585**	**612**	**609**
	PL FWHM (nm)	**27.8**	**27.3**	**27.4**	**27.8**	**27.4**	**29.2**	**28.8**

Table 3.8 Fluorescence quantum yield (PL-QY), emission peak position and emission peak width are reported

This point will be discuss later on in more details. As for the **C2-CSSS**, the real structure is more difficult to estimate from compositional data, since zinc is introduced in the synthesis also in the earlier alloy layer stage. In any case, it is possible to conclude that a thick ZnS layer is not present in the real structure, which would be desirable in order to have stable nanocrystals.

Optical characterization has been carried out on these samples and presented in figure 3.27 and table 3.8.

The absorption and emission peaks are observed to shift toward longer wavelengths after deposition of the CdS and $Cd_{0.5}Zn_{0.5}S$ layer. This is due to the incomplete electronic confinement offered by this materials toward CdSe, as described in section 3.2.2 and extensively studied in a recent work by Van Embden et al.[105].

Not only the first absorption peak is shifted with the shelling procedure, but also the absorption profile result to be changed, as clearly shown in figure 3.28.

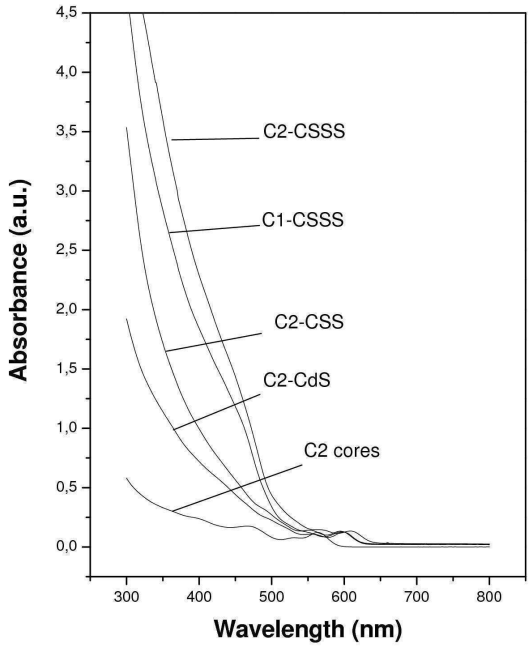

Figure 3.28 Absorption spectra for the CdSe@Sample obtained in this work. Spectra are normalized at the band edge. (C2 CdS sample refer to C2 core covered by two ML of CdS)

It can be seen that after normalization of the absorption at the band-edge, the cadmium sulfide layer causes an higher absorption at smaller wavelengths with respect to core particles. This effect is slightly enhanced with the ZnS layer and it is much more pronounced for structures comprising the alloy layer.

This effect is explained by the increasing thickness of the shell material which absorbs at shorter wavelengths ranges [105].

Fluorescence quantum yield is observed to consistently increases from the very low value of CdSe cores after the CdS shell and remain constant after the ZnS growth stage.

The difference in the size of starting cores also allows for emission color tuning, as shown in figure 3.29.

Figure 3.29 Emission from colloidal solution of orange-emitting C2-CSS (left) and yellow emitting C1-CSS (right) under standard UV-lamp illumination (Glass vials are 1 cm in diameter and 6 cm height)

These particles have been successfully used in amplified stimulated emission applications as described in Chapter 6.

The main problem encountered in those experiments was related with the poor stability of ASE emission of the particles with time. A possible cause of this behavior can be found on the small thickness of the ZnS layer.

Thus we tried to increase the ZnS layer thickness by simply increasing the amount of ZnS precursors, with the aim of balancing the lower yield of the reaction leading to ZnS formation by extending the SILAR procedure with further additions of ZnS precursors equivalent to 2 ML of ZnS on the **C2-CSS** particles.

TEM analyses were performed on these particles and revealed a slight increase in diameter to 5.6 ± 0.7 nm (still much lower than the expected 7.02 nm value), but the composition of the particle was almost unchanged with respect to **C2-CSS** sample, indicating that further growth was limited.

An explanation of this effect can be related to a scenario in which the zinc-rich surface obtained after the first zinc precursor addition is not so reactive toward the sulfur precursor used. This can be attributable to the presence of *TMPPA* as stabilizer on the surface which has been argued to bound strongly to metal surface sites [97], limiting particle reactivity

and stopping particle growth after initial stages. This is not the case when growing the CdS layer, since cadmium precursors are much more reactive.

For these reasons we tried to employ a more reactive sulfur precursor in order to balance this effect.

Thus, maintaining the same SILAR procedure we substituted *S-ODE* with *$(TMS)_2S$* dissolved in *ODE*. In these attempts, slightly larger CdSe core particles than **C2** samples were used with a 3.57 nm diameter (as estimated from first absorption peak position).

The first attempts resulted in coarsening of the particles with broader size distribution, as deduced from increased absorption linewidth. Thus we lowered the growing temperature in the final ZnS to 230°C.

In this case we obtained particles with a good PL-QY of 33%, even if the some ripening was still observed. TEM data are shown in figure 3.30 and table 3.9.

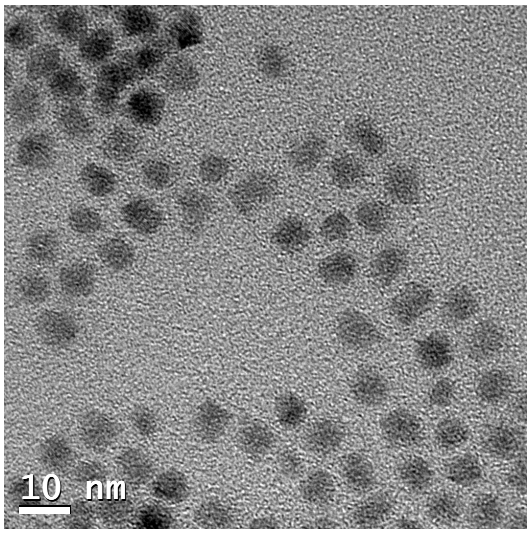

Figure 3.30 TEM images for core@shell particles with a CSS target structure on a 3.57 nm CdSe core

Sample	$D_{obs} \pm \sigma$ (nm)	$D_{Expected}$ (nm)
CdSe CdS ZnS (CSS) on 3.57 nm core	6.1 ± 0.8	6.15

Table 3.9 Obserrved and expected final diameters are reported in the table

In table 3.9 observed and expected diameters are reported analogously to previous samples. In this case good agreement between these values is obtained suggesting for obtainment of the desired structure, even if zinc content seems to be still slightly lower than the expected one. This is further suggested from compositional data reported in figure 3.31, which are in good agreement with the expected values calculated from a concentric model.

	3.57nm CdSe-CSS	
	Observed Values	Expected for 3.57 nm CdSe-CSS
Se/Cd	0.4	0.36
S/Cd	1.4	1.87
Zn/Cd	1.2	1.23

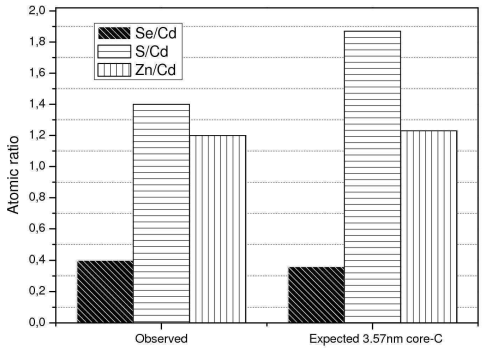

Figure 3.31 Measured and expected composition for single core@shell particles with a CSS target structure on a 3.57 nm CdSe core using $(TMS)_2S$ as sulphur precursor for ZnS shell growth

The presence of ripening may suggests that sulfur is depositing on the particles, since no stabilizer for sulfur is present in the reaction system causing an increase of surface energy and Ostwald ripening kinetics. Even if ripening is an adverse effect to be avoided because it indicates instability of particles in some stages, in our case it can be related to the desired enhanced sulfur precursor reactivity. In any case, further optimizations are necessary also taking into consideration zinc precursor reactivity.

Optical data for these particles are summarized in figure 3.32.

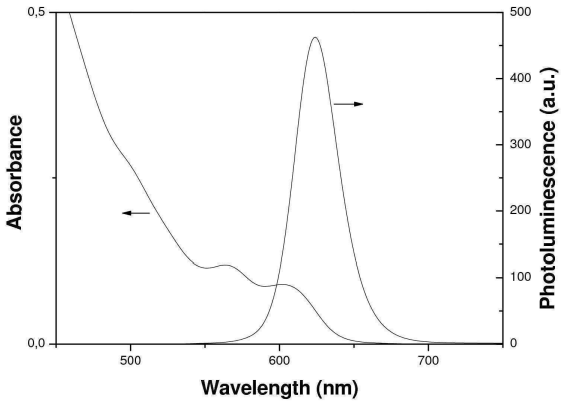

Figure 3.32 Absorbance and PL spectra core@shell particles synthesized employing $(TMS)_2S$ for ZnS shell growth

The luminescence emission is at 623 nm and the estimated quantum yield is 30%. The FWHM PL peak width is 34.3 nm, slightly larger than values reported in table 3.8. for previously synthesized particles, due to the already discussed ripening phenomena.

Interestingly, the capping ligand exchange described n Chapter 6 worked only if Zn $(Acetate)_2$ was introduced with the amino-functionalized molecule used in the ligand exchange. This is because these particles likely resulted in a sulfur rich surface which is not good for binding with amines, since amines bind to metal sites.

These particles have been used for ASE experiments to improve particle stability.

References

[1] Kava L., Stoto T., Gratzl M., Fitzmaurice D., Shklover V., J. Phys. Chem., 1993, **97**, 9493

[2] Joselevich E., Willner I., J. Phys. Chem., 1994 **,98**, 7628

[3] Wong E.M., Bonevich J.E., Searson P.C, .J. Phys. Chem. B, 1998, **102**, 7770

[4] Malik M.A., Revaprasadu N., O'Brien P., Chem. Mater., 2001, **13**, 913

[5] Peng X., Chem. Eur. J., 2002, **8**, 335

[6] Steigerwald M., Brus L., Acc. Chem. Res. 1990, **23**, 183

[7] Olshavsky M. A., Goldstein A. N., and Alivisatos A. P. , J. Am. Chem. Soc**.,** 1990, **112,** 9438

[8] Wells R.L., Gladfelter W.L. *P* J. Cluster Science, 1997, **8**, 217.

[9] Uchida H., Curtis C.J., Kamat P.V., Jones K.M., Nozik A.J., J. Phys. Chem., 1992**, 96**, 1156

[10] Uchida H., Curtis C.J., Nozik A.J., J. Phys. Chem.,, 1991, **95**, 5382

[11] Butler L., Redmond G., Fitzmaurice D., J. Phys. Chem., 1993, **97**, 10750

[12] Micic O.I., Curtis C.J., Jones K.M, Sprague J.R, Nozik A.J., J. Phys. Chem., 1994, **98**, 4966

[13] Pietryga J.M., Werder D.J., Williams D.J., Casson J.L., Schaller R.D., Klimov V.I., Hollingsworth J.A., J Am. Chem Soc., 2008, **130**, 4879

[14] Colvin V. L., Schlamp M. C., Alivisatos A. P., Nature 1994, **370**, 354

[15] Nie S., Chan W., Amory S. R., Science, 1998, **281**, 2016

[16] Klimov V. I., Mikhailovsky A. A., Xu S., Malko A., Hollingsworth J. A, Leatherdale C. A., Eisler H. J. , Bawendi M. G., Science, 2000, **290**, 314

[17] Jasieniak J., Pacifico J., Signorini R., Chiasera A., Ferrari M., Martucci A., Mulvaney P., Adv. Funct. Mater, 2007, **17**, 1654

[18] Jasieniak J. J., Fortunati I., Gardin S., Signorini R., Bozio R., Martucci A. and Mulvaney P., Adv. Mater., 2008, **20**, 69

[19] Kazes M., Lewis D. Y., Ebenstein Y., Mokari T. and Banin U., Advanced Materials, 2002, **14**, 317

[20] Coe S., Woo W.-K., Bawendi M., Bulovic V., Nature 2002, **420**, 800

[21] Bruchez M., Moronne M., Gin P., Weiss S., Alivisatos A. P., Science, 1998, **281**, 2013

[22] Gao X., Cui Y., Levenson R. M., Chung L. W. K., Nie S., Nature biotechnology, 2004, **22**, 969

[23] Eisler H.-J., Sundar V. C., Bawendi M. G., Walsh M., Smith H. I. and Klimov V, Appl. Phys. Lett., 2002, **80**, 4614

[24] Konstantatos G., Howard I., Fischer A., Hoogland S., Clifford J., Klem E., Levina L., Sargent E. H., Nature, 2006, **442**, 180

[25] Larson D., Zipfel W. R., Williams R. M., Clark S. W., Bruchez M. P., Wise F. W., Webb W. W., Science, 2003, **300**, 1434

[26] Blanton S. A., Leheny R. L., Hines M. A., Guyot-Sionnest P., Phys. Rev. Lett. 1997, **79**, 865

[27] Cao Y. C. and Wang J., . J. Am. Chem. Soc., 2004, **126**, 14336

[28] Yang Y. A., Wu H., Williams K. R., Cao Y. C., Angew. Chem. Int. Ed., 2005, **44**, 6712

[29] Jasieniak J., Bullen C., van Embden J. and Mulvaney P., J. Phys. Chem. B 2005, **109**, 20665

[30] Mohamed M. B., Tonti D., Al-Salman A., Chemseddine A. and Chergui M., J. Phys. Chem.B., 2005,**109**, 10533

[31] Peng Z.A., Peng X., J. Am. Chem. Soc, 2002, **124**, 3343

[32] Victor I. Klimov "*Semiconductor and metal nanocrystals*", 2004 (Marcell Dekker, Inc)

[33] Woggon, U., *Optical properties of semiconductor quantum dots*. Vol. 136. 1996: Springer

[34] Efros A.L., Rosen M.,. Annual Review of Materials Science, 2000, **30**, 475

[35] Ekimov A. I., Hache F., Schanne-Klein M. C., Ricard D., and . Flytzanis C., Kudryavtsev I.A., , Yazeva T. V., Rodina A. V., Journal of the Optical Society of America B-Optical Physics, 1993, **10**, 100

[36] Ekimov A.I., Efros A.L., Ivanov M.G., Onushchenko A.A., Shumilov S.K**,** Solid State Communications, 1989. **69**, 565

[37] L. E. Brus., J. Chem. Phys., 80, 4403 (1984)

[38] Norris D. J., Bawendi M. G., Phys. Rev. B, 1996, **53**, 16338
[39] Trindade T., O'Brien P., Pickett N.L., Chem. Mater., 2001, **13**, 3843

[40] Krishnadasan S., Tovilla J., Vilar R., deMello A. J., deMello J. C. , J. Mater. Chem., 2004 ,**14** , 2655

[41] Leatherdale C.A., Bawendi M.G., Physical Review B, 2001, **63,** art. no.-165315.

[42] Efros A. L., Rosen M., Kuno M., Nirmal M., Norris D. J., Bawendi M., Phys. Rev. B, 1996, **54**, 4843

[43] Crooker S. A., Barrick T.,. Hollingsworth J. A and Klimov V. I., App. Phys. Lett., 2003, **82**, 2793

[44] Califano M., Franceschetti A., Zunger A., Nano Lett., 2005, **5**, 2360

[45] Bawendi M. G., Carroll P. J., Wilson W. L., Brus L. E., J. Chem. Phys. ,1992, **96**, 946

[46] Pu S. C., Yang M. J., Hsu C. C., Lai C. W., Hsieh, C. C., Lin S. H., Cheng Y. M., Chou P. T., Small, 2006, **2**, 1308

[47] Schmidt M. E., Blanton S. A., Hines M. A., Guyot-Sionnest P., Phys. Rev. B, 1996, 53, 12629

[48] Padilha L. A., Fu J., Hagan D. J., Van Stryland E. W., Cesar C. L., Barbosa L. C., C. Cruz H. B., Buso D., Martucci A., Phys. Rev. B, 2007, **75**, 075325

[49] Peng X., Schlamp M. C., Kadavanich A. V., Alivisatos A. P., J. Am. Chem. Soc., 1997, **119**, 7019

[50] Talapin D. V., Rogach A. L., Kornowski A., Haase M., Weller H., Nano Lett. 2001, **1**, 207

[51] Mekis I., Talapin D.V., Kornowski A., Haase M., Weller H.**,** J. Phys. Chem. B, 2003**,** **107**, 7454

[52] Reiss P., Protiere M., Li L., Small, 2009, **5**, 154

[53] Bowen Katari J. E.,. Colvin V. L, Alivisatos A. P., J. Phys. Chem., 1994**, 98,** 4109

[54] Talapin D.V., Koeppe R, Go1tzinger S., Kornowski A., Lupton J.M.,. Rogach A.L., Benson O., Feldmann J., Weller H., Nano Lett., 2003, **3**, 1677

[55] Li J., Wang Y.A., Guo W., Keay J.C., Mishima T.D., Johnson M.B., Peng X., J. Am. Chem. Soc., 2003, **125**, 12567

[56] Xiaobo Chen, Yongbing Lou, Anna C. Samia, and Clemens Burda* Nano Lett 2003,3,799

[57] Spanhel L., Haase M.; Weller H., Henglein A. , J. Am. Chem. Soc., 1987, **109**, 5649

[58] Dabbousi B.O., Rodriguez-Viejo J., Mikulec F. V., Heine J. R., Mattoussi H., Ober R., Jensen K. F., Bawendi M. G., J. Phys. Chem. B, 1997, **101**, 9463

[59] Reiss P., Bleuse J., Pron A., Nano Lett., 2002, **2**, 781

[60] Talapin D.V., Mekis I., Gotzinger S, Kornowski A., Benson O., Weller H., J. Phys. Chem. B, 2004, **108**, 18826

[61] Schrier J., Wang L.W., J. phys chem B, 2006, **110**, 11982

[62] Murray C.B., Norris D.J., Bawendi M.G., J Am. Chem. Soc., 1993, **115**, 8706

[63] Van Embden J., Jaseniak J., Gomez D.E., Mulvaney P., Giersig M., Aust. J. Chem. 2007, **60**, 457

[64] Bleuse J., Carayona S., Reiss P., Physica E, 2004, **21**, 331

[65] Reiss P., Carayon S., Bleuse J., Pron A., Synthetic Metals, 2003, **139**, 649

[66] McBrideJ., Treadway J., Feldman L. C.,. Pennycook S.J., Rosenthal S.J., Nano Lett., 2006, **6,** 1496

[67] Xie R., Kolb U., Li J., Basche T., Mews A., J. Am. Chem. Soc., 2005, **127**, 7480

[68] Chen D., Gao L., Solid State Communications, 2005, **133**, 145

[69] Ma S.M., , Seo J.T., , Yu W., Yang O., Tabibi B., Temple D., Min N., Jung S., Kim W., Journal of Physics: Conference Series, 2008, **109,** 012025

[70] Leatherdale C. A.,. Woo W.-K, Mikulec F. V., Bawendi M. G., J. Phys. Chem. B, 2002, **106**, 7619

[71] Kayanuma J., Phys rev B, 1988, **38**, 9797

[72] Klimov V.I., J. Phys. Chem. B, 2000, **104**, 6112

[73] Sung Y.O, Park K.S., Lee Y.L., Kim T.G., J. Phys. Chem. *C,* 2007**, 111**, 1239

[74] Lee Y.J., Kim T.G., Sung Y.M., Nanotechnology 2006 17, 3539-3542

[75] Talapin D.V., Rogach A.L., Haase M.,Weller H., J. Phys. Chem. B, 2001**, 105**, 12278

[76] La Mer V.K., Dinegar R.K., J am chem. Soc, 1950, **72**, 4847

[77] Sugimoto T., *Advances in Colloid and Interface Science,* 1987, **28**, 65

[78] Peng X., Thessing J., Struc Bond, 2005, **118**, 79

[79] Peng X., Wickham J., Alivisatos A. P., J. Am. Chem. Soc, . 1998, **120**, 5343-5344

[80] Tricot Y.M., Fendler J.H., J Am. Chem. Soc. , 1984, **106**, 2475

[81] Steigerwald M.L,, Alivisatos A.P., Gibson J.M., Harris T.D., Kortan R., Muller A.J., Thayer A.M., Duncan T.M., Douglass D.C, Brus L.E., J. Am. Chem. Soc., 1988, **110**, 3046

[82] Petit C., Pileni M.P., J. Phys. Chem. 1988, **92**, 2282

[83] Lemon B.I., Crooks R.M., J. Am. Chem. Soc., 2000, **122**, 12886

[84] Hanus L.H., Sooklal K., Murphy C.J., Ploehn H.J., Langmuir, 2000, **16**, 2621

[85] Rossetti R., Brus L. , J. Phys. Chem. 1982, **86**, 4470

[86] Vossmeyer T., Katsikas L., Giersig M, Popovic I.G., Diesner K., Chemseddine A., Eychmuller A., Weller H., J. Phys. Chem. , 1994, **98**, 7665

[87] Murray C.B., Norris D.J., Bawendi M.G., J. Am. Chem. Soc., 1993, **115**, 8706

[88] Peng X., Wickham J, Alivisatos A.P., J. Am. Chem. Soc., 1998, **120**, 5343

[89] Peng X., Manna L., Yang W.D., Wickham J., Scher E., Kadavanich A., Alivisatos A.P., Nature, 2000, **404**, 59

[90] Peng Z.A., Peng X., J. Am. Chem. Soc., 2001, **123**, 183

[91] Qu L., Peng Z.A., Peng X., Nano Lett., 2001, **1**, 333

[92] Peng Z.A, Peng X., J. Am. Chem. Soc., 2002, **124**, 3343

[93] Qu L., Peng X., J. Am. Chem. Soc., 2002, **124**, 2049

[94] Du H., Chen C., Krishnan R., Krauss T.D., Harbold J.M., Wise F.W., Thomas M.G., Silcox J., Nano Lett. , 2002, **2**, 1321

[95]Yu W.W., Peng X., Angew Chemie Int. Ed., 2002, **41**, 2368

[96]Battaglia D., Peng X., Nano Lett, 2002, **2**, 1027

[97] van Embden J., Mulvaney P., Langmuir, 2005, **21**, 10226

[98] Liu H., Owen J.S., Alivisatos A.P., J. Am. Chem. Soc., 2007, **129**, 305

[99] Spanhel L., Haase M., Weller H., Henglein A., J. Am. Chem. Soc., 1987,**109**, 5649

[100] Hines M.A., Guyot-Sionnest P., J. Phys. Chem, 1996, **100**, 468

[101] Achermann M., Hollingsworth J. A., Klimov V. I., Phys. Rev. B, 2003, **68**, 245302

[102] Yu W.W., Qu L., Guo W., Peng X, Chem. Mater., 2003, **15**, 2854

[103] Handbook of chemistry and physics Lide 72 ed.; JCPD 80-0007 for ZnS ; JCPD 77-2306 for CdS ; JCPD 77-2307 for CdSe

[104] Jasieniak J., MulvaneyP., J. Am. Chem. Soc., 2007, **129**, 2841

[105] van Embden J., Jasieniak J., Mulvaney P., J. Am. Chem. Soc., 2009, **131**, 14299

[106] Kortan A. R., Hull R., Opila R. L., Bawendi M. G., Steigerwald M. L., Carroll P. J., Brus L. E., J. Am. Chem. Soc., 1990, **112**, 1327

[107] Protiere M., Reiss P., Small, 2007, **3**, 399

Chapter 4

TiO_2 nanomaterials: Synthesis and Properties

4.1 Introduction

Titanium dioxide (TiO_2) has advantageous physical and chemical properties that makes it among most used and studied oxides for scientific and industrial purposes.
It is cheap, chemically stable and non-toxic in the bulk state (toxicological effects of nanoscale TiO_2 is not yet known).
Titanium dioxide has been largely employed as white pigment and used as material for dental and orthopaedic implants due to its biocompatibility.
From the application point of view, the most important property is represent by the semiconducting behavior of this material. This makes it an ideal material for photovoltaic application in dye-sensitized solar cell fabrication [1,2], gas sensing [3,4], low temperature oxidation of carbon monoxide if used in combination with gold [5,6,7] and electrocromic devices [8].
The possibility of optically exciting titanium dioxide with UV radiation along with its catalytic properties justifies its wide use in photocatalysis. Water treatment by oxidation of organic impurities in presence of TiO_2 is a common example. These properties are related to the ability of generating hydroxyl radicals possessing strong oxidising power [9,10,11].

Titanium dioxide is an interesting material also for optical applications.
This is due to transparency in the visible spectral region, UV absorption properties and high refractive index.
The wide range of processing methods developed so far makes it very attractive for photonic applications.
In particular, colloidal syntheses allows toobtain nanometric particles which can be used for functional nanocomposites [12-14], optical devices in which high refractive index

materials are required such as optical waveguides, Bragg reflectors and optical micro-cavities [15-20], and materials with controlled morphology exhibiting porosity in the nanometer scale with large surface area suited in photochemical or electrochemical applications.

In this chapter, the synthesis and processing of colloidal TiO_2 based nanomaterials is presented, while their application will be described in Chapter 5.

Two basic types of materials have been addressed : *TiO_2 colloidal nanoparticles* in the anatase crystal structure and *layered titanates* consisting, in their dried powder form, of nanometric layers with general composition $[Ti_mO_{2m+1}]^{2-}$ stacked in an ordered layered fashion with a cation intercalated between the layers.

Layered titanates have been studied [21-25] and used as precursors for titania with controlled morphology and crystalline structure. These compounds are also very attractive due to optical, photochemical and electronic properties. Furthermore, ion-exchange, intercalation of functional organic molecules and possibility of hybrid assemblies can be applied to titanates materials [29-39].

Very interestingly, UV irradiation has been shown to be a useful tool for material modification allowing for densification strategies different from heat treatment [40,41].

In the first part of this chapter, a brief survey of the general properties of these materials is presented. In the experimental part, the synthesis and the results regarding TiO_2 anatase particles are first described. Layered titanates synthesis and results are then described.

For clarity, layered titanates are further divided in Tetramethylammonium hydroxide (*TMA-Ti*) and 6-amino-1-1hexanol derived (*AH-Ti*) titanates, which differs in the reagents used for their synthesis, in the structure and processing behavior.

4.2 Properties and Synthesis of TiO_2 and Layered Titanates

4.2.1 Titanium dioxide NPs: Properties and Synthesis

Titanium dioxide exists in three major polymorphs: rutile, anatase and brookite. The most thermodynamically stable phase at ambient condition is rutile which is the common phase of titanium dioxide found in nature.

Rutile and anatase have tetragonal unit cells, while brookite has an othorombic structure.

The structures are shown in figure 4.1, while more detailed data are reported in a table 4.1

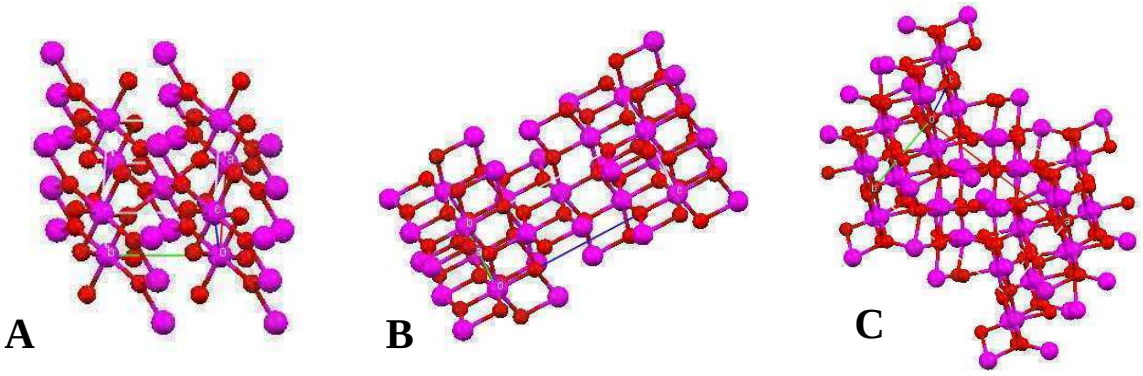

Figure 4.1 Structures of anatase (A), rutile (B) and brookite (C) TiO_2 polymorphs

	RUTILE	**ANATASE**	**BROOKITE**
Structure	*Tet*	*Tet*	*Orth*
Unit cell parameters (Å) [42]	a 4.584 b 4.584 c 2.953	a 3.783 b 3.783 c 9.497	a 5.472 b 5.172 c 9.211
Density (Kg/m^3) [43]	4.26	3.84	4.17
Band gap (eV) and optical absorption onset (nm) [44,45]	3.0 eV 410 nm	3.2 eV 385 nm	3.4 eV 365 nm
Refractive index (in the visible range)[43]	⊥ c axis 2.609 // c axis 2.90	⊥ c axis 2.561 // c axis 2.488	⊥ c axis 2.583 // c axis 2.70

Table 4.1 Main data for TiO_2 major polymorphs

The most opened structure is that of anatase, resulting in the lower density if compared to other polymorphs. The thermodynamic stability of each phase has been showed to be size dependent [47]. Rutile is the most stable for particle size above 35 nm, brookite in the 11-35 nm range and anatase below 11 nm. This behaviour is due to the different surface enthalpy being larger for rutile and lower for anatase.

The titanium atoms in TiO_2 exists the 4^+ oxidation state with neighbouring oxygen atoms in the octahedral coordination. Thus, the basic unit in titanium dioxide is an octahedron and the way these units arrange themselves gives rise to different polymorphs.

In particular, in the rutile structure octahedral units share all corners and only two edges, while in the anatase structure they share all corners and fours edges in a "zig-zag" fashion.

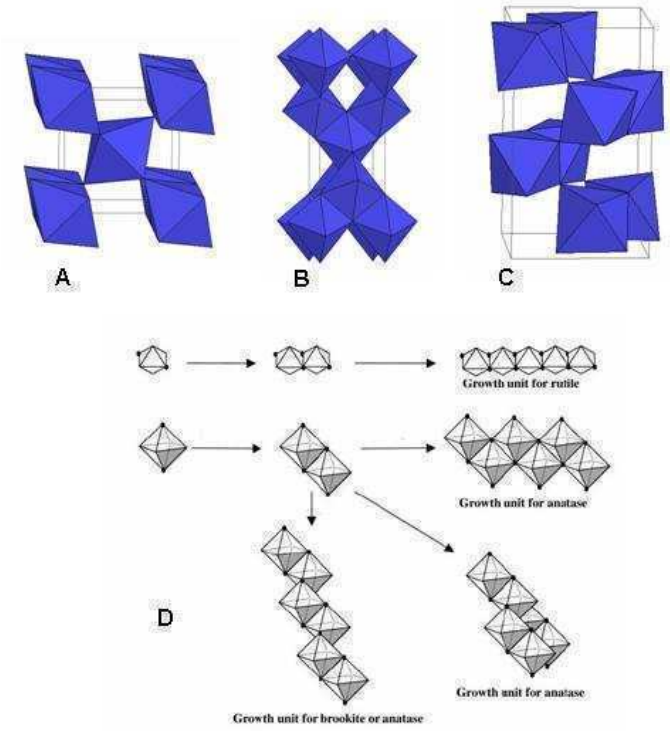

Figure 4.2 TiO_6 octahedral units arrangement in rutile (A), anatase (B) and brookite (C) (Source [92]). Growth schemes resulting into growth units of different TiO_2 polymorphs (D) (Source : [48])

In figure 4.2 D, the growth units for different structures arising from different arrangements of octahedral units is shown [48]. Since the way titania octahedra bonds to each other is dependent on synthetic parameters, the reason why different phases can be obtained with different synthesis is apparent.

Different structures can be easily distinguished not only through XRD diffraction analysis but also through Raman spectroscopy. Raman patterns are in fact completely different for each phase. Furthermore XRD can be used to estimate particles size through the Scherrer formula. In figure 4.3, XRD diffraction patterns of very small TiO_2 crystals whose dimensions were measured by TEM analysis [52] are shown.

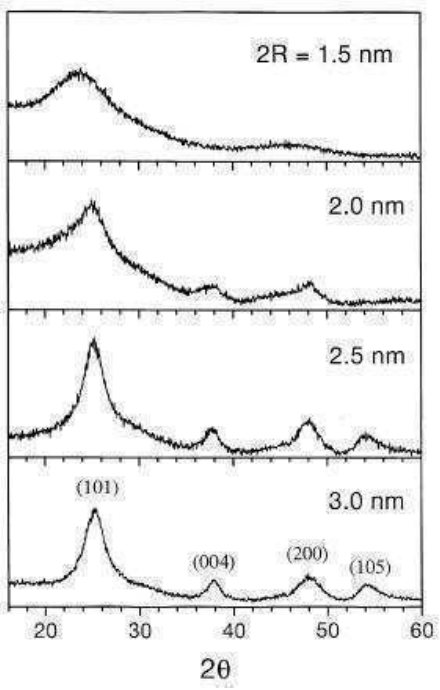

Figure 4.3 XRD diffraction patterns for very small TiO2 NCs (Source : Monticone et al. [52])

Also Raman peak broadening and position are dependent on particle size [49], allowing for convenient use of this technique for particle's sizing.

The main optical properties of titania are transparency in the visible range, UV absorption and high refractive index (values reported in Table 4.1).

The band gap is in the UV (see Table 4.1) range and can be enlarged by size quantization phenomena occurring for sufficiently small particle sizes.

The exciton Bohr radius, as defined in Chapter 3, has been estimated to be very small for titanium dioxide, in the range of 0.75-1.90 nm [50] or as small as 0.3 nm [51].

Furthermore, small band gap shifts with respect to the bulk value has been measured even for 2 nm particles and in general band gap shifts smaller than 0.5 eV have been found.

Thus, size quantization for titanium dioxide is not expect to have a striking effect on optical properties, unless particle's size is very small, at least below 1 or 2 nm [52].

Various synthetic approaches are available for TiO_2 NPs synthesis [53 and ref.s therein] including direct oxidation, aerosol pyrolisis, physical vapor deposition, and solution chemistry. The latter is the most interesting from our point of view since it allows to obtain of stable colloidal sols consisting of extremely dispersed particles which can be processed and used in optical applications or where a large surface to volume ratio is needed.

Sol-gel chemistry plays a crucial role in these approaches, where titanium halides (as $TiCl_4$) or titanium alkoxides are used as precursors.

In hydrolytic syntheses, these precursors are first hydrolyzed and then condensed to give the oxide network.

When these molecules interact with water without proper tailoring of the synthetic parameters such as pH and temperature, titanium hydroxides with a certain degree of condensation are obtained in the amorphous state [54]. The easiest way to crystallize this material is to heat it up (i.e. 400°C-500°C) and anatase is generally obtained which undergo coarsening of the grain size. Obviously further processing is limited by the high degree of aggregation preventing obtainment of a transparent colloidal sol.

Large crystals or particles without structural defects and with good crystallinity can be achieved by hydrothermal synthesis where temperature can be consistently raised up, even if large aggregates are usually obtained whose size and morphology can be tailored by controlling a great number of synthetic parameters [11,48,55,56,57,58,59,60,61]. Nonetheless, optical applications are not possible with such products, since light scattering from large crystals or aggregates do not allow for transparency.

Also non-hydrolytic routes are available for synthesis of small and non-aggregated particles [62], but they are not here described here since they are not relevant for the present work.

Hydrolytic synthesis will be briefly described in order to put in evidence the synthetic conditions necessary for (a) having a crystalline material just in the solution synthesis stage and (b) a non-aggregated colloidal state of such crystalline domains.

It is generally accepted that acidic conditions are necessary to have the formation of crystalline titania particles [54,63-67].

In highly acidic media, the pH is well below the isoelectric point resulting in highly protonated titania particle surfaces. Highly acidic condition leads to solubilization of the initial amorphous hydrolyzed product. It is argued that in these conditions titanium octahedra are present as single units which reprecipitate by reciprocal condensation.

Sufficient solubility and structural rearrangement is given to the system to evolve from the amorphous state.

Since crystalline phases are more stable (and much less soluble [68]) than the amorphous phase, crystalline nuclei formed by reprecipitation processes would remain stable and further undergo growth processes.

The crystalline phase which is obtained under these conditions strongly depends on the pH, anion type present in the solution and synthesis temperature [55,61,69].

The general (simplified) formula describing the structural titania unit can be written as $Ti(O)_a(OH)_b(OH_2)_{6-a-b}$ [66,64]. In acidic condition this is reduced to $Ti(OH)_a(OH_2)_{6-a}$ with the number of OH decreasing with increasing pH [11,61,58]. Furthermore alkoxy groups can still be present if the hydrolysis has not proceed to completeness.

Condensation happens between two Ti-OH groups of different octahedral. Thus, the suggested scenario is that species comprising more OH will preferentially give rise to anatase structure since bond through edges of the TiO_6 units is favored, while more acidic conditions limit OH presence in the coordination shell of titanium leading to preferential corner condensation and minor edge condensation. Rutile is then formed in these conditions.

In presence of anions, such as chlorine, titanium unit undergoing condensation may comprise also these species in its coordination sphere, affecting the way octahedral units are condensed and the resulting phases [49].

Beyond the above described considerations, other arguments can be assumed to explain phase dependence on process parameters which are instead related to reaction-rate concepts [54,64]. If condensation rate is quite low, the formation of the more thermodynamically stable phase is preferred since this is expected to have the lower activation energy of nucleation. Higher precipitation rates can results in the metastable anatase phase since the way TiO_6 bond to give anatase is statistically favored with respect to that resulting in rutile (edge bonding is more probable during octahedral collision than corner bonding [70])

Thus, higher temperature may favor anatase formation, while lower temperature (and longer times for crystalline phase formation) may results in rutile, as schematized in figure 4.4.

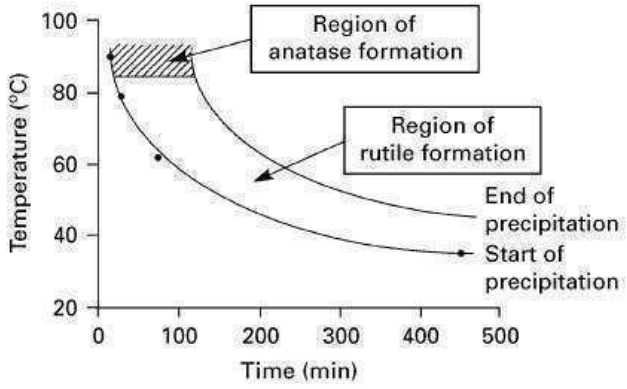

Figure 4.4 Effect of temperature on precipitation time and crystalline phase (Source : Gopal et al. [64])

The above-described arguments are related to crystallinity, without taking into account the colloidal stability of the obtained particles. Acidic conditions obviously help in preventing particles agglomeration through electrostatic repulsion, even if many of reported synthesis end up with large particles precipitate.

Particle's colloidal stability can be limited by formation of large particles (bigger particles has higher attractive Van Der Waal forces), high ionic strength (i.e. high electrolytes concentration) and can be enhanced by the use of stabilizing or complexing agents. The latter approach has been used, for example, by Sanchez et al.[71] and Cozzoli et al. [72]. These methods can results in perfectly dispersed nanometric crystalline domain, with a protected surface.

Major disadvantages are related to organic molecules adsorbed on particle surface which can be detrimental if the particle surface is meant to be the active interface for application purposes. Furthermore, a non-negligible fraction of organic material is bound to the material, limiting the full exploitation of titania in optical applications such as enhancement of refractive index (organic materials have low refractive index) and transparency loss (certain stabilizing agents can absorbs in the visible when complexed with titanium).

In optical applications, transparent colloidal solution of small particles with high degree of stability is required. Thus synthetic conditions need to be adjusted in order to limit extreme particle coarsening, assuring crystallinity and avoiding aggregation.

To the best of our knowledge, these aspects have been considered simultaneously only by Nussbaumer et al. [73], who reported the synthesis of 3 nm (diameter) pure rutile phase nanoparticles from $TiCl_4$ in water. The process basically consisted in an initial hydrolysis step at low temperature (0-10°C) and further heating at 60°C. The solution is transparent for about 80 minutes and then it gets cloudy.

A mechanism of titania formation for every stage of the process was suggested. The hydrolysis of the precursors was argued to lead to positively charged mononuclear oxo-hydroxo-chloride ,$TiO_a(OH)_b(Cl)_c^{a+}$, which initially form oligomers through condensation. Subsequently, these oligomers would bind together to form particles consisting of an highly crosslinked network. Particles evolution was analyzed through TEM and found to be amorphous during almost all the entire heating step. Just before the solution become cloud, particles become crystalline. There is a small window-time in which particles are crystalline and colloidaly stable at the same time.

During the heating stage, particles do not change their diameter and only an "internal" aging process is argued that leads to further condensation, higher crosslinking density and rearrangement of the network toward greater order and crystallization.

The condensation during the aging process occurs with production of water and expulsion of positive charges. The reduced charge due to condensation has been suggested as the reason why particles aggregate soon after densification and crystallisation, introducing another element to be kept into consideration if crystallisation and colloidal stability is desired.

Influence of synthetic parameters was in agreement with the concept introduced so far. For example, increased acidity lead to larger time for observation of precipitation due to increasing electric charge of the particle, while increased temperature in the heating stage leads to anatase product since this it is considered kinetically favoured.

4.2.2 Layered Titanates

Several types of layered titanates with different compositions have been studied.

Common titanates incorporate alkaline metal cations to achieve charge neutrality. Their general formula can be written as $A_2Ti_nO_{2n+1}$ where A represents the alkaline metal cation intercalated in the layered structure.The layers are composed of $[Ti_nO_{2n+1}]^{2-}$ polyanions which arrange themselves in a stepped fashion as shown below for a sodium trititanate and potassium tetratitanate .These types of structures generally have monoclinic unit cells [74,76].

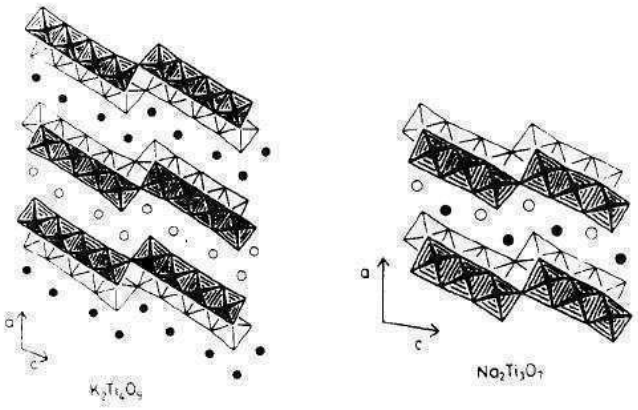

Figure 4.5 Structure of potassium tetratitanate and sodium trititanate (Source : Izawa et al. [74])

Other titanates structures can occurs. For example, titanates with intercalated cesium cations with general formula $Cs_xTi_{2-x/4}\square_{x/4}\ O_4$ (□: vacancy) have an orthorhombic structure isomorphic to lepidocrocite (a layered iron hydroxide) [75].

Also in these structures the basic unit is the TiO_6 octahedron.

In a titanate layer, a definite number of TiO_6 octahedra (depending on the type of octahedral units) share edges to form a linear sequence in the same plane. Each sequence is joined above and below to similar groups by further edge sharing, resulting in a zig-zag ribbon structure. Finally, these ribbons forms the layer by connecting through terminal corners [77].

Thus, the TiO_6 octahedron share four edges with other units. The zigzag ribbon assembly and the octahedron sharing four edges are also observed in the anatase lattice.

These similarities can be observed just looking to XRD diffraction data.

In fact, anatase XRD diffraction peaks corresponding to (200) and (213) planes (which appears at 48 deg and 61 deg 2θ diffraction angles if CuKa is used as X-ray source) are

also observed in titanates diffraction pattern and are related to unit periodicities of the in plane crystallinity of the titanate layer having an anatase-like arrangement of constituting titanium octahedra [25,28]. These peaks are not present in the rutile structure since octahedral arrangement is different.

A consequence of such structural similarity is the easiness with which it is possible to switch from titanate to anatase. In fact, an in-situ rearrangement is sufficient for phase changing resulting in lower temperatures of anatase formation as compared with other titania precursors. It has been found that acid environment and low temperatures are sufficient to induce phase change, which could be exploited to obtain very interesting morphologies [77].

A scheme showing this phase switching is shown in figure 4.6.

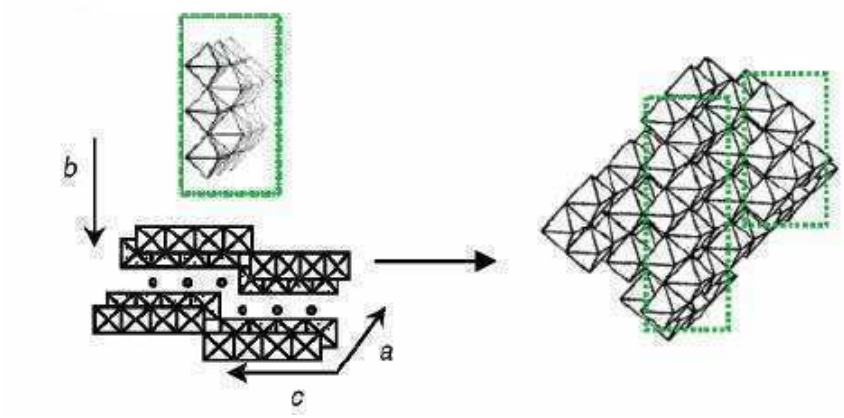

Figure 4.6 Schematic representation of phase switching from a layered titanate to anatase (Source : Zhu et al. [74])

Layered titanates can undergo ion-exchange processes where the pristine metal cation can be substituted with H^+ (proton exchanged), with other metal cation or with organic cations such as protonated amines or ammonium cations.

XRD is a powerful tool to characterize these materials since the layer structure give rise to diffraction peaks in the low-angle region which corresponds to interlayer distance.

Evolution of interlayer distance can be followed by looking to diffraction peak position. For example, ion exchange of potassium tetratitanate with amines molecules with increasing alkyl chain length results in increasing interlayer distance in order to accommodate larger molecule between titanate hosts [78,79]. This process can be readily followed with XRD diffraction analysis, as shown in Figure 4.7.

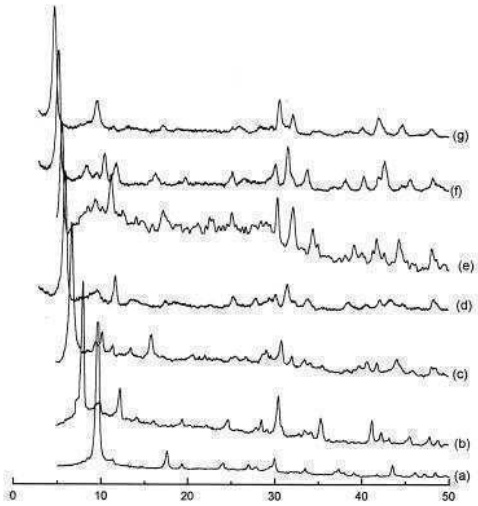

Figure 4.7 XRD data for potassium tetratitanate intercalated with alkyldiamines with increasing chain length from a to g. Progressive shift of the lower angle peak is observed. (Source : Airoldi et al. [78])

In proton exchanged [23] or alkyl ammonium titanate[80], water molecules can also be present between the layers, contributing to the final interlayer distance.

The use of alkyl ammonium molecules with titanates can results in the formation of colloidal solutions [25,36]. In such solution state, titanates were demonstrated to be completely exfoliated, that is in a single-sheet condition. This was proved by in-situ XRD analysis of layer restacking upon drying. Beyond interlayer distance, the number of coherently stacked layer could be deduced from XRD peak width.

It was observed that with the ongoing of the drying process, broad XRD peaks at low angle initially appeared which could be associated with formation of a pair of titanate sheet separated by a large interlayer of water molecules. This peak moves toward shorter distances due to increasing water removal through evaporation. In addition, the number of stacked layer increased from the initial pair resulting in narrow peaks indicative of good crystallinity of the layered structure.

Since the initial XRD signal was attributable to a titanate layers pair, it is apparent that the starting solution consisted of exfoliated layers.

Dynamic light scattering on similar titanate colloidal solutions, but prepared in different conditions, was used for measuring the diameter of the objects in the solution and it was found to be 15 nm [22], probably indicating only partial exfoliation.

Titanate nanosheets have been shown to have photocatalityc properties [81,40]. This property can be used to remove under UV irradiation organic cations intercalated in the layered structure resulting in interlayer contraction, giving another possibility for material's modification.

These properties have been used for material's modification, as will be described in Chapter 5.

Optical properties of titanate nanosheets have been studied [41,46,82] for colloidal layered titanates obtained through exfoliation of protonic titanates by ammonium molecules. Both absorption features in the exfoliated colloidal solution state and in thin film have been measured and found to present a large blue-shift with respect to anatase bulk absorption onset .

Both optical and spectroelectrochemical experiments found a band gap value of about 3.8 eV, much greater than the 3.2 eV value for anatase. The suggested electronic structure for the titanate nanosheet layer is shown in figure 4.8 and compared with anatase.

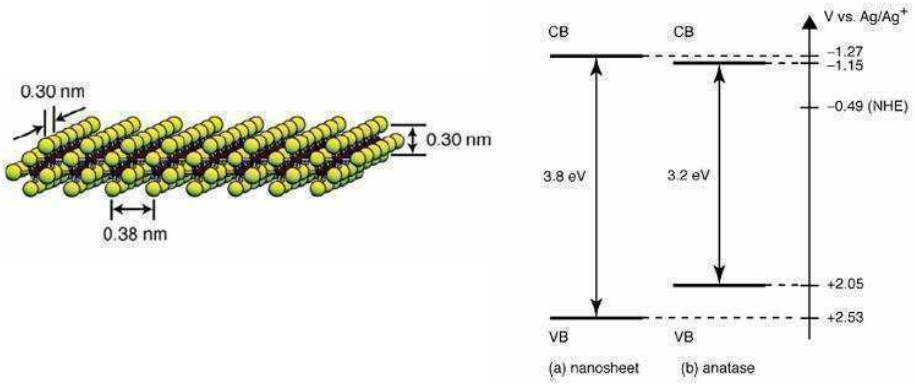

Figure 4.8 Representation of a titanate layer (left) and suggested electronic structure compared with that of anatase (right) (Source : Sakai et al. [82])

This observation has been explained with quantum confinement effects due to the extremely small thickness of the layer (0.7 nm). In the case of a two dimensional structure the following reference relationship can be assumed to determine the band gap shift

$$\Delta E_g = \frac{h^2}{4\mu_{xy} L_{xy}^{\ 2}} + \frac{h^2}{8\mu_z Lz^2} \qquad \text{Eq. 4.1}$$

where μ_{xy} and μ_z are the reduced effective masses of electron-hole pair in parallel and perpendicular directions to the plane defining the layer respectively while L_{xy} and L_z are the lateral dimension and thickness of the layer.

For the previously described titanates, the term related to lateral dimensions could be neglected in Eq. 4.1.since lateral extension was in the 0.1-1μm.

In Figure 4.4, the absorption spectra of these titanate layers in solutions are reported. Beyond the strong blue-shift of the absorption onset at around 330 nm (corresponding to about 3.8 eV), a definite peak is observed at 266 nm which was explained as the exciton transition peak similar to CdSe nanoparticles and its analogues.

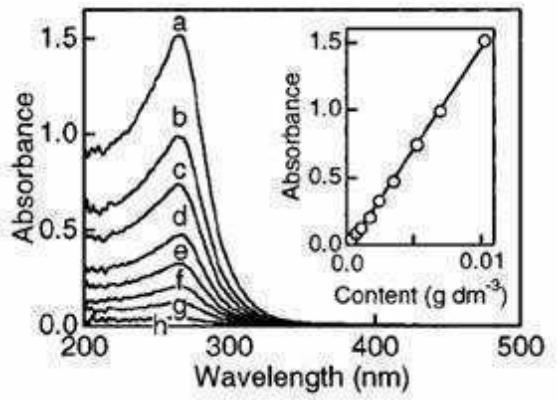

Figure 4.9 UV-Vis absorption spectra of colloidal layered titanates solution at different concentrations (Source : Sasaki et al. [41])

The absorption features of this material were unchanged if measured after deposition on a substrate, intercalation of a polycation and its photodecomposition using UV radiation [].

Synthesis of titanate nanosheets is not a strongly developed field as for titanium dioxide NPs. A common approach [25] consists in the solid state reaction at high temperature from titanium oxide and the desired intercalated cation precursor.

If a colloidal solution of layers is desired, this solid can be put in solutions containing ammonium salt which finally leads to exfoliation as previously described [25,36].

In this case, the lateral extension of lamellae is large, in the 0.1-1 μm range.

Other approaches are based on acid-base reactions between hydrolysis products of titanium alkoxides and ammonium hydroxide or alkylamines [22].

The general pathway is summarized in the following reaction scheme.

Hydrolysis :

$$mTi(OPr)_4 + (2m+1)H_2O \longrightarrow H_2Ti_mO_{2m+1} + 4mPrOH$$

Acid-base reactions :

$$H_2Ti_mO_{2m+1} + RnH_{4-n}N^+OH^- \longrightarrow [\,RnH_{4-n}N^+][\,HTi_mO_{2m+1}^-\,] + H_2O \quad \text{for weak bases}$$

$$H_2Ti_mO_{2m+1} + 2R_4N^+OH^- \longrightarrow [\,R_4N^+]_2[\,Ti_mO_{2m+1}^{2-}\,] + H_2O \quad \text{for strong bases}$$

The first stage is the hydrolysis and condensation of the alkoxide leading to polymeric titanic acid or hydrous titanium oxide. Then, depending on the alkaline strength of the base used, only the first or both of the subsequent acid-base reactions occurs where the hydrous titanium oxide can be deprotonated by the base assuming a negative charge.
At this stage a layered structure can be formed that can be partially exfoliated in the solution state or orderly layered in the dried powder state.
It was found that the exact type of titanate (*m* value in the above reactions) changes with the type of used base. It was suggested that a mixture of trititanate, tetratitanate, hexatitanates and so on, is likely to be the product of this type of synthesis.

4.3 Experimental

In the following sections, the experimental procedures, results and discussion for anatase TiO_2 particles and layered titanate are described. Titanates are divided in Tetramethyl-ammonium hydroxide derived (*TMA-Ti*) and 6-amino-1-hexanol derived (*AH-Ti*) for clarity of exposition.

4.3.1 TiO_2 anatase nanocrystals

4.3.1.1 Synthesis

TiO_2 NCs were synthesized by adding dropwise 10.5 mmol of Titanium Tetraisopropoxide (*$Ti(OPr^i)_4$*) into a previously prepared solution containing water, hydrochloric acid and methanol in a 50 ml glass flask. The quantity of methanol was adjusted to give a concentration of titanium equal to 0,7 M and thus a final solution volume of 15 ml, while the water to titanium and acid to titanium ratios were varied as described in Table 4.2 in order to study the influence of synthesis parameters on particles formation and sol stability.

	A	**B**	**C**	**D**	**E**
H_2O/Ti	12.5	25	55	25	25
HCl/Ti	1.72	1.72	1.72	0.86	3.44

Table 4.2 Compositions tested for TiO_2 nanoparticles synthesis

From composition A to C the water content is increased reaching a water to titanium molar ratio of 55 which corresponds to a methanol free solution with water as the only solvent. Compositions D and E present an acid to titanium ratio lower and higher than the one adopted in the recipes previously mentioned, respectively.

The solution is stirred for 60 minutes at room temperature after *$Ti(OPr^i)_4$*addition and then heated in an oil bath at 70 °C and kept at this temperature for one, two or four hours under refluxing.

A clear sol is generally obtained in these conditions and TiO_2 powders are retrieved by adding the minimum quantity of acetone necessary to have flocculation of the oxide and subsequently centrifuging at 4000 rpm for 2 minutes. The obtained precipitate can be dispersed again in methanol obtaining a clear solution.
The evolution of the powders with varying annealing temperatures from 150°C to 500°C is also analyzed by XRD and Raman spectroscopy.

4.3.1.2 Results and discussion

Figure 1A shows the evolution of XRD patterns of the nanopowders obtained for composition A (see table 4.2) after one (diffraction pattern a), two (diffraction pattern b) or four (diffraction spectrum c) hours of refluxing time at 70 °C, respectively. It is evident a clear sharpening of the diffraction peaks with the reaction time, leading to a pattern which can be assigned to anatase crystal structure (JCDS 86-1157).

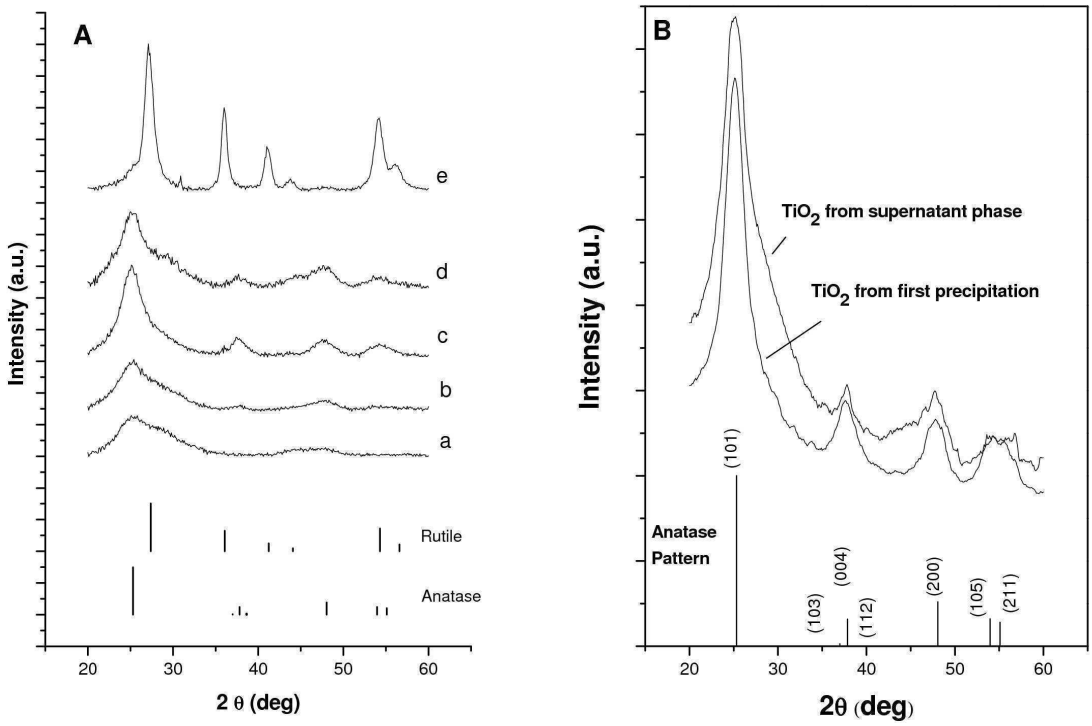

Figure 4.10 XRD patterns of TiO_2 NCs obtained from recipe A after 1h (a), 2h(b) and 4h (c) of refluxing at 70°C. Pattern "d" belong to the material obtained from recipe A after 4 hours of heating using excess acetone for precipitation. Pattern "e" refers to TiO_2 NCs obtained from recipe C after 1 hour of heating time. Main diffraction peaks position and relative intensities of rutile and anatase TiO_2 crystal structures are reported at the bottom of the figure (A); XRD patterns of comparison of TiO_2 NCs obtained from first acetone flocculation and from a second flocculation of the supernatant solution obtained after the first precipitation round (B).

The product isolated after flocculation is dependent on the amount of acetone used. This is shown in spectrum “d” of figure 1 for the material obtained from composition “A” after four hours of reaction time. In this case, a 5:1 volume ratio of acetone to as synthesized solution instead of 3:1, which is the minimum amount necessary to have a precipitate. It is evident that broader features in diffraction pattern are present if excess acetone is used.

To further analyze this aspect, the clear supernatant solution obtained after acetone precipitation (with a 3:1 volume ratio) has been collected and flocculated with further addition of acetone, in order to analyze the material not retrieved after the first precipitation round. In figure 4.10B, XRD data of such powders are compared with those obtained from the first precipitation (analogue to spectrum “c” in Figure 4.10A). The material in the supernatant has broader diffraction peaks.

Recipe C produced a spontaneous white precipitate during heating. This precipitate has been collected by centrifugation and found to be crystalline titania in the rutile structure (spectrum “e” in figure 4.10A, JCPDS 87-0710).

The results obtained employing recipe A can be ascribed to the evolution of titanium oxide from amorphous to crystalline state. In highly acidic media, titania is peptized leading to soluble six-fold coordinated titanium octahedral complexes, which can condense forming a crystalline structure at the reaction temperature as explained previously. In the conditions corresponding to recipe A, octahedral units condense with the kinetically favored edge sharing mechanism, leading to anatase instead of rutile structure.

A possible mechanism explaining our XRD results is consistent with the formation of crystalline nuclei from amorphous titanium hydroxide initially present in the solution. This nuclei grow with time due to deposition of titanium oxide monomers from solution leading to powders with more defined diffraction features.

Thus, broad peaks observed in the early stages are likely to result from the presence of amorphous phase or smaller crystals. They become sharper with the ongoing of crystallization process in the final stage.

The effect of precipitation conditions can be explained considering the different solubility of the amorphous and the smaller particles fraction with respect to the bigger crystallites one, resulting in a size-selective precipitation [83]. Since the latter has minor colloidal stability with respect to the former, the use of the minimum amount of acetone allows for precipitation of the bigger crystalline particles, while the remaining smaller (or still amorphous) fraction is left in the supernatant. This is supported by data reported in figure 4.10B.

Thus, if properly done, the described processing method allows for crystalline titania extraction and separation from smaller particles and amorphous matter.

The composition was found to affect the described behavior significantly. Water content increases from compositions A to C ,while keeping other parameters constant. The most evident effect is the increasing instability of the solution with increasing amount of water. Solution B is opalescent after two hours of reaction time and a small amount of spontaneous precipitate is formed after four hours. Precipitate induced with flocculation with acetone also resulted to be TiO_2 anatase (XRD spectra not shown).

Solution C, where water is the only solvent, gave a large amount of spontaneous precipitate in the rutile structure after only one hour of heating.

Solutions D and E have, respectively, a lower and higher content of acid with respect to solution B. Solution D gelled within one hour, while solution E remained transparent for two hours, after which time a small amount of precipitate was formed.

The increasing amount of water is likely to enhance the rate of hydrolysis and further condensation of the alkoxide precursor, thus reducing the stability of the solution. As expected, if the quantity of acid is too small, there is not sufficient repulsion between the growing particles, leading to extensive interactions and finally to a gel.

The compositional-dependent crystalline structure has been a topic widely discussed in the literature, and briefly discussed in section 4.2.1. In particular, the nature of the titanium species present in solution has been correlated to the way titanium species condense to originate a specific crystal structure. Chlorine, hydroxyl and alkoxy ligands can coordinate titanium in our solution, thus a large variety of titanium species can be present. The number and type of the species coordinated to titanium can force and direct the condensation into a crystalline form or another.

The obtainment of rutile from synthesis employing only water is not surprisingly, since very acidic media and the use of HCl has been shown to favour rutile formation.

Since in these conditions only aggregated titania was obtained, we tried to control reactions by lowering the amount of water for hydrolysis in methanol as the main solvent.

It is likely that the presence of methanol as the main solvent affects crystallisation and favours the anatase structure.

In addition, replacement of water with methanol was found to lead to sols with good colloidal stability, which can be processed and used to make nanocomposite materials.

For this reason, further structural and optical characterizations will refer to TiO_2 particles obtained from composition A with four hours of refluxing time, since it gave the best colloidal stability and transparency.

TEM data of titania particles are shown in figure 4.11. These were obtained depositing a diluted colloidal TiO_2 sol on a copper grid.

In figure 4.11a well dispersed particles can be appreciated, showing absence of aggregates. Crystalline NPs, as evident from HR-TEM of figure 4.11b, with a mean diameter of 4.0 ± 1.5 nm have been identified and the crystalline phase deduced from Fourier Transform of HR-TEM images (see the inset of figure 4.11b) was anatase, in accordance with XRD measurements, even if the presence of brookite can't be excluded.

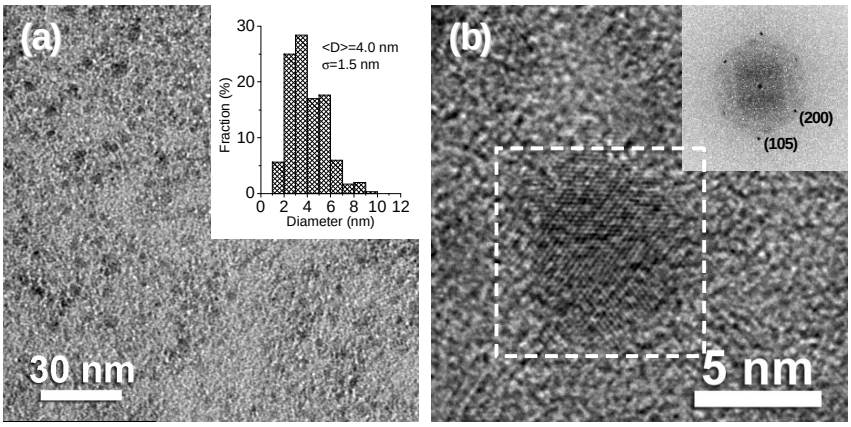

Figure 4.11 TEM images of TiO_2 NCs obtained with recipe A: bright-field (BF-TEM) image with the histogram of size distribution (a); HR-TEM of a NC with the FFT in the inset showing some reflections of the anatase phase(b)

UV-Vis absorption spectrum of 20-times diluted TiO_2-solution used for sol-gel film doping is presented in figure 4.12. An absorption edge in the UV region at around 370 nm can be seen, in accordance with UV absorption properties of TiO_2. In order to quantitatively estimate the band gap energy from absorption spectra, the following relationship has been used to fit the absorption behavior of TiO_2 [92,93] :

$$\alpha = \frac{(h\upsilon - E_g)^2}{h\nu} \qquad \text{Eq.4.1}$$

where α is the absorption coefficient, $h\nu$ the photon energy of radiation and E_g the band gap of the material. The absorption coefficient α is linearly correlated to the measured absorbance A. Thus, by plotting $(Ah\nu)^{0.5}$ versus $h\nu$, a linear behavior is obtained in the absorption range which can be used for the determination of E_g, as shown in figure 4.12B.

An absorption onset of 3.21 eV (386 nm) is retrieved using this method. This value is almost equal to that of bulk anatase (3.2 eV). Quantum size effect have been clearly seen for particles diameters smaller than 2 nm [52] or 2,4 [50]. Thus, this effect is not present in our samples, whose mean size resulted to be 4 nm from TEM measurements, or around 3.5 from Raman or XRD measurements (see below).

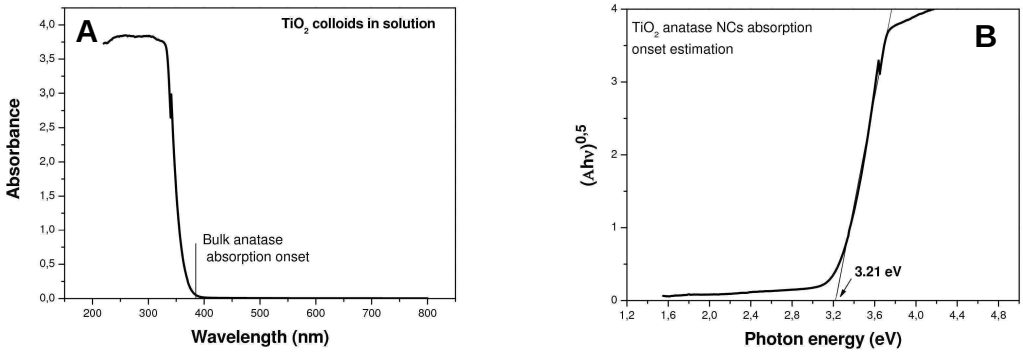

Figure 4.12 UV-Vis spectrum of TiO_2 nanocrystals in methanol (A) and estimation of absorption onset of particles in solution (B).

Formation of non- aggregated crystalline particles from alkoxide precursors using chelating agents have already been reported [71,72]. In the synthetic approach here reported, no specific organic molecules are used for colloidal stability. In our case, after precipitation it was possible to redisperse the particles in methanol because of the strong electrostatic repulsion due to the highly acidic environment and eventually also to alkoxide organic groups bound to particle surface. Indeed, TG analysis on TiO_2 powders previously vacuum-dried and heat treated at 150°C for one hour, shows (figure 4.13) a weight loss up to 300°C which can be attributed to organic decomposition, even if most of the weight loss occurs below 200°C and is likely due to water or solvent adsorbed on particles. Thus, the presence of organic matter is low and can be roughly estimated to be less than 5 % by weight.

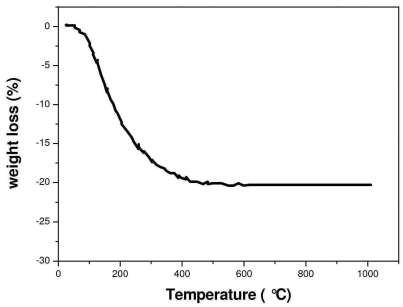

Figure 4.13 Thermogravimetric analysis of vacuum-dried TiO_2 NCs obtained after acetone-flocculation

FT-Raman spectroscopy was performed on titania powders heat treated at different temperatures, in order to understand the stability of NCs toward growth or coarsening with temperature. In fact, a peak shift and width variation of Raman bands are expected to be evident upon changes in size of TiO_2 anatase NCs, particularly in the size range obtained within the described procedures [49]. The same process has been followed also by XRD measurements, and the two results are compared.

FT-Raman spectra shown in figure 4.14A are typical of anatase (bands at 144 cm^{-1}, 197 cm^{-1}, 399 cm^{-1}, 513 cm^{-1}, 519 cm^{-1} and 639 cm^{-1}) [84]. With the increase of annealing temperature a continuous shift and sharpening of the characteristic Raman bands of anatase is clearly observed and evidenced in the inset of figure 4.14A for the main peak. This can be attributed to growth and coarsening of crystalline domains [49]. This is confirmed also by XRD measurements shown in figure 4.14B, where sharpening of diffraction peaks with annealing temperature is evident.

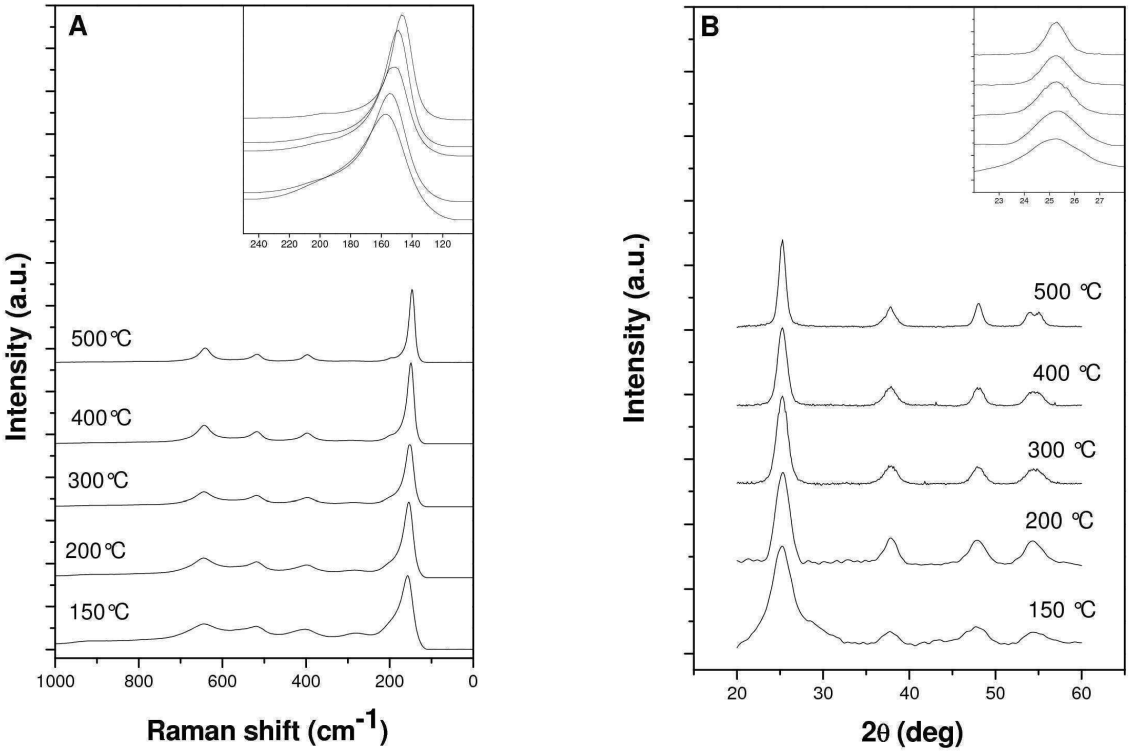

Figure 4.14 Raman spectra (A) and XRD patterns (B) of TiO_2 powders heat treated at different temperatures. Magnification in the main peak region is shown in the inset.

In table 4.3 it is reported the mean diameter of TiO_2 NCs estimated from the main Raman band position using the following relationship derived in ref [49] :

$$\omega = 100(\frac{1}{D^{1.5}}) + 142 \qquad \text{Eq. 4.2}$$

where ω [cm^{-1}] is the peak position wavenumber and D [nm] is the particle diameter.
Particle diameter has been also estimated by XRD line broadening of the main diffraction peak through Scherrer formula.

.

	D FT-Raman (nm)	**D XRD (nm)**
150°C	3.6	3.1
200°C	4.0	3.9
300°C	5.0	4.8
400°C	5.9	5.6
500°C	7.5	7.4

Table 4.3 TiO_2 NCs mean diameter (D) estimated from main Raman peak position and from XRD line broadening.

Both measurements gave similar results: in particular the size of the crystalline domains increases of about 1 nm at each temperature step above 200 °C, with a slightly more pronounced increase for annealing at 500 °C. Thus, it is likely that coarsening occurs till 400 °C with more pronounced sintering and densification at 500 °C.
This information about particle tendency toward sintering and coarsening will be used to explain the morphological structure evolution of TiO_2 NCs depositions upon different annealing temperature, as it will be discussed in Chapter 5.

4.3.2 Layered titanates from 6-amino-1-hexanol (AH-Ti)

As anticipated in the Introduction, two type of titanates were produced depending on whether 6-amino-1-hexanol (*AH*) or Tetramethylammonium hydroxide (*TMA*) were used as bases.

Titanates obtained with *TMA*, referred to as *TMA-Ti*, are very useful compounds since depositions of this material can be modified by methods other than thermal treatment, as shown in the section 5.2.2.

On the other hand, this material can be dispersed to obtain a stable colloidal solution only if water is used as solvent. Solvent mixture comprising methanol or ethanol can also be used along with water, which has to be present in considerable amount in any case.

This is not favourable if the introduction of semiconductor quantum dot particles in titanate matrix is desired. Even if it is possible to transfer quantum dots in water (and thus probably in the titanate matrix), this normally results in decreasing of the emission properties of QDs. Furthermore, *TMA* is a strong and oxidising base which can degrade the host particles.

For these reasons, we have tried to synthesise in an analogue manner titanate nanosheets using weaker bases. We choose 6-amino-1-hexanol since it is the same capping ligand used for QD particle transfer in alcoholic media. This strategy allowed for titanate to be stable in alcohol and to be compatible with quantum dots. This material will be referred to as *AH-Ti*.

4.3.3.1 Synthesis

In a typical synthesis, 15 g (241 mmol) of anhydrous ethylene glycol (*EG*) were loaded in a three necked flask fitted with a refluxing condenser. The flask was placed in an heating mantle and heated at 60°C under vacuum for 20 minutes. Subsequently the temperature was raised to 100°C after switching to nitrogen flow using conventional Schlenk line setup. 1.19 g (4.2 mmol) of titanium isopropoxide ($Ti(OPr^i)_4$) were injected with a syringe and the solution turned immediately opaque, forming a precipitate.

A second injection consisting in 1.5 g (12.7 mmol) of 6-ammino-1-hexanol (*AH*) dissolved in 7.6 g (422 mmol) of water was quickly performed and an optically clear solution was obtained within few seconds. The synthesis was carried on for 8 hours at 100°C. Finally the particles were collected by centrifugation at 4000 rpm for 4 minutes after inducing flocculation by adding the minimum amount of acetone which corresponded to a 3 to1

acetone to TiO_2 synthesis-solution ratio. This precipitate, referred to as *AH-Ti*, was dispersed in methanol resulting in an opaque dispersion, which was made transparent by applying a 20 mbar vacuum for 10 minutes, as will be explained in the following. This solution was then used for UV-Vis optical measurements.

If used for XRD measurements, the powders were vacuum-dried soon after acetone precipitation at 3 mbar for 10 minutes. TEM analyses were done on the dried powders data, previously suspended in methanol (without achieving colloidal stability) and deposited on a copper grid.

4.3.2.2 Results and discussion

In the synthesis of titanate nanosheets, ethylene glycol was used as solvent due to its high boiling point which allows for stable heating. Furthermore, flocculation of titanates using acetone was easy from the resulting solvent phase. The use of ethylene glycol also affects the reaction. In particular, the starting precursor undergoing hydrolysis and condensation is a titanium glycolate complex, which is formed when TIP is injected into ethylene glycolresulting in a spontaneous precipitates. This compound has been collected by centrifugation, washed with acetone, vacuum-dried and characterized by XRD (see figure 4.15A). This pattern is in good agreement with those reported in [29] for titanium glycolate complex.

The XRD patterns of the vacuum-dried *AH-Ti* are shown in figure 4.15B for different heat-treatment temperatures.

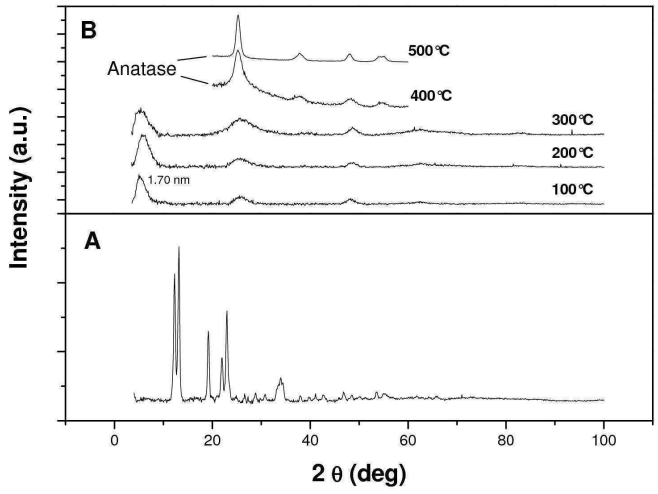

Figure 4.15 XRD patterns of the product obtained from TIP and ethylene glycol reaction (A) and of the final synthesized titanates aannealed at different temperatures (B)

The pattern cannot be assigned to anatase, brookite or rutile TiO_2 crystalline structure. In particular, a wide peak at low diffraction angles at 5.2 deg is present. This can be attributed to a layered structure composed of titanates with the intense peak at low angle corresponding to diffraction from the layers. Diffraction peaks in the higher diffraction angles region at about 48° and 62° are most likely related to the in plane crystallinity of the single titanate sheet, as observed for similar compounds by Sasaky et al.[25,41], while the peak at about 26° can arise from a periodicity of the layer stack superstructure.

The formation of this type of structures in synthesis involving titanium alkoxides and amines has already been reported [22], even if in our case an amino-alcohol is used. The synthetic route employed in this work results in broad XRD peaks analogous to those reported in [86-88] for similar compound. XRD data suggests the formation of domains with a limited number of packed layers. It is likely that *AH* does not promote large stacking of ordered sheets. From the position of the XRD peak in the low diffraction angle region, an interlayer distance of 1.70 nm can be calculated from Bragg relationship.

From figure 4.15B, it can also be seen that this structure remains stable up to 300 °C, indicating a good thermal stability of the obtained crystalline structures, switching to anatase at 400°C and 500°C. Moreover, by comparing the glycolate with titanate pattern it is worth noting that no diffraction peak of the titanium glycolate is discernible in the final titania powders, suggesting complete reaction of this complex.

TEM micrographs of such crystallites are presented in figure 4.16.

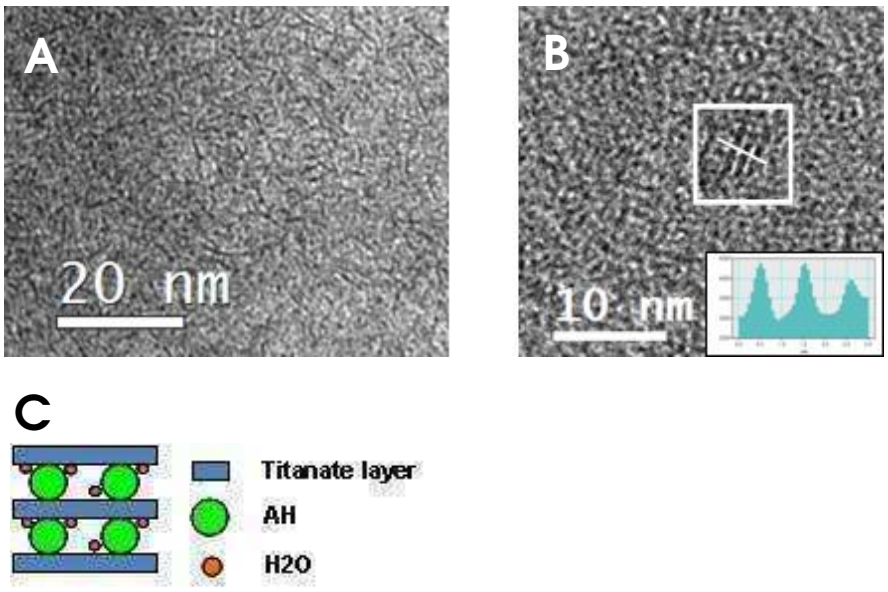

Figure 4.16 Bright field TEM (A) and HR-TEM (B) analyses for *AH-Ti* layered titanate; Schematic representation of a possible structure for stacked titanate nanosheets (In Figure 4.16B, the intensity profile along the white line is reported (C)

The sheet-like nature of this material is apparent in figure 4.16a, even if layered stacks are not easily detected. Few stacked layers (2 or 3) were detected and figure 4.16b shows in an example of a three layers stack. The observed dimension of the layered structure is in agreement with XRD data, from which a dimension of 3.1 nm along the stacking direction was calculated from Scherrer relationship. Since the interlayer distance is estimated to be 1.70, it is apparent that few sheets are stacked. The lateral dimension of the layers is around 5 nm.

FT-IR spectra of the titanate powder (embedded in a KBr pellet) and titanium glycolate is shown on figure 4.17.

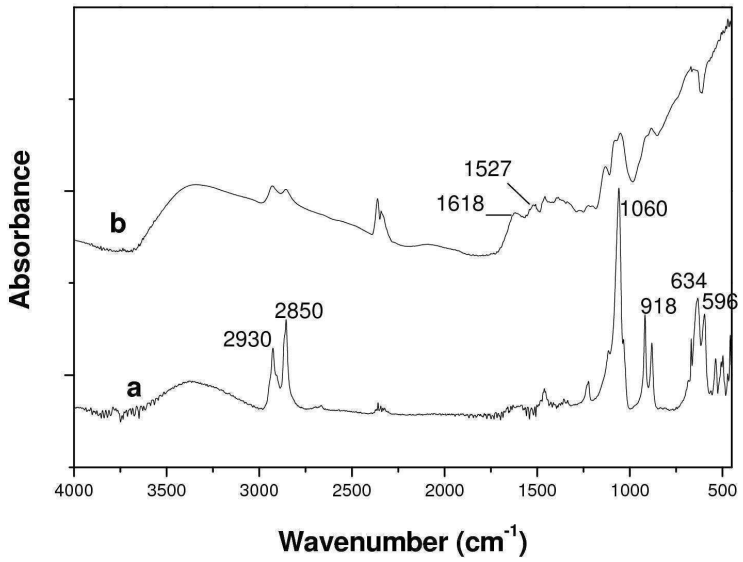

Figure 4.17 FT-IR spectrum for titanium glycolate (a) and titanate powder (b)

FT-IR of the titanium glycolate is similar to that reported in ref.s [89-90], where bands at around 595 cm^{-1} and 635 cm^{-1} were assigned to Ti-O-C of the titanium glycolate complex. This complex can contribute also to the band detected at around 1060 cm^{-1}, even if also C-C-O bond of ethylene glycol has vibrations in the 1050-1150 cm^{-1} region [95]. Bands at 2950 cm^{-1} and 2850 cm^{-1} can be assigned to stretching vibrations of C-H bond, while bands in the 918-880 cm^{-1} region can be assigned to C-C stretching vibration and to C-H out of plane bending.

In the titanate spectrum, absorption in the low wavenumber region in the 450-550 cm^{-1} range can be assigned to Ti-O vibration [89,94] of the titanate, while those in the 1550-1650 cm^{-1} range can be assigned to NH_3^+ vibration [74] of intercalated and protonated *AH*.

Bands in the 1050-1150 cm^{-1} are still present in the titanate spectrum, suggesting the presence of ethylene glycol molecules, even if we cannot say if this is free or bound to titanium sites of titanates sheets. Bands associated to titanium glycolate complex are in fact not clearly seen in the spectrum, probably because of the much lower number with respect to non-hydrolysed titanium glycolate. Anyway, the presence of EG bound to titanium cannot be excluded, since titanium glycolate is known to be more stable than other alkoxides with respect to hydrolysis [90].

The TG-DTA on this powder is presented in figure 4.18.

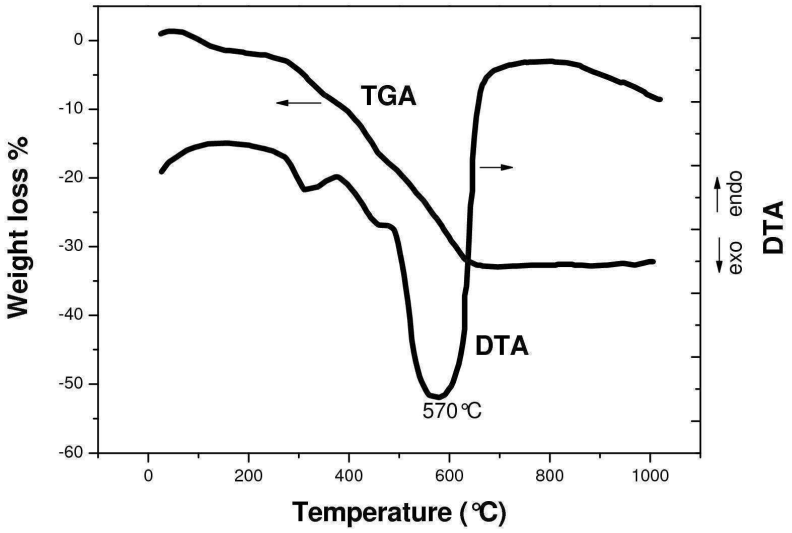

Figure 4.18 TGA and DTA analysis of titanate powders

Thermal degradation of titanate powders can be mainly associated with loss of the layered structure due to decomposition of intercalated AH molecules.

The broad band at 3400 cm^{-1} can be assigned to OH vibration of adsorbed water molecules. Weight loss continues up to about 600°C and a strong exothermic peak is observed at 570°C. The final weight loss is about 30%. Degradations temperatures are higher than those for *TMA* derived titanates (see next section), as observed by Ohya et al. [22] for titanates from triethylamine. This behavior suggests an enhanced stability of this titanate with respect to titanates from *TMA* where thermal decomposition ended at temperature lower than 500°C. This can be explained by the fact that *AH* is not a sufficiently strong base to undergo a second acid-base reaction in the synthesis pathway presented in section 4.2.2. This material is most likely composed of hydrogen alkylammine titanate of the type $[R_nH_{4-n}N]^+ [HTi_mO_{2m+1}]^-$. The interaction between the titanate layers can be argued to be

enhanced by the presence of hydrogen through, for example, hydrogen bonding [22]. This can in turn lead to higher thermal stability of the titanate where higher temperatures are required to remove *AH* from the structure. Furthermore, the hydroxyl group in the *AH* molecule may take part in such interactions mechanisms.

As described in the experimental section, the titanates were flocculated by adding acetone, centrifuged and redispersed in methanol. A clear colloidal solution was then obtained after applying vacuum. This can be explained considering that under vacuum the quantity of acetone still remaining after the precipitation procedure is removed. Since acetone acts as a non-solvent, its removal allows for colloidal stability to be achieved again.

The clear solution obtained in this way can be further diluted with methanol maintaining good colloidal stability. In this state titanate layers are most probably to be exfoliated, since most titanate layers appear as single sheets in TEM images or as two or three layers stacks.

The UV-Vis spectrum presented in figure 4.19 for titanate in methanol shows a significant blue-shift of the absorption edge with respect to bulk titania, in agreement with quantum confinement due to extremely small thickness of the layers. An absorption onset of 3.68 eV (336 nm) could be estimated using the same procedure described above.

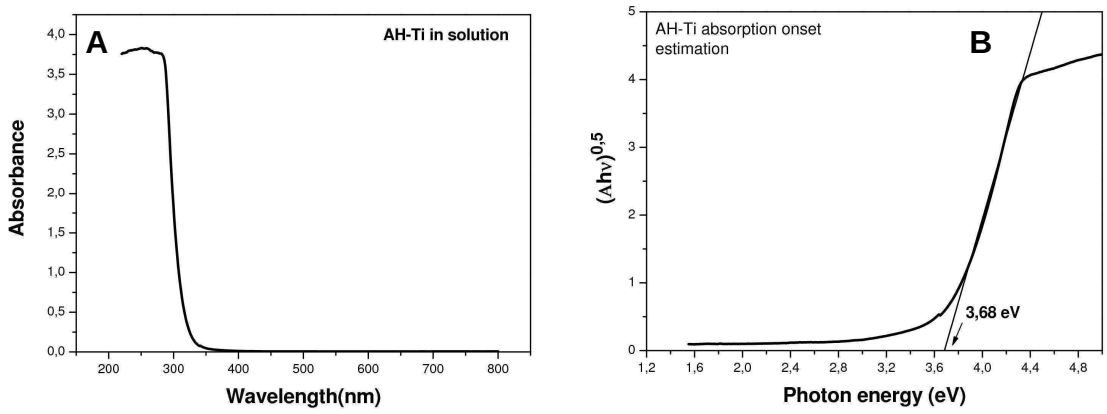

Figure 4.19 UV-Vis spectrum of *AH-Ti* titanate in methanol (A) and estimation of absorption onset of titanate layers in solution (B)

4.3.3 Layered titanates from Tetramethylammonium hydroxide (TMA-Ti)

4.3.3.1 Synthesis

Layered titanates were synthesized from ethylene glycol (*EG*), Titanium tetraisopropoxide (*$Ti(OPr^i)_4$*), water and Tetramethyammonium hydroxide (*TMA*). The relative amount of the reagents was varied as summarized in table 4.4, in order to study the influence of solution composition on the final product. The final volume of the resulting solution was kept equal to 15 ml.

	[TI] (M)	**[TMA]/[Ti] (mol/mol)**	**[H_2O]/[Ti] (mol/mol)**
c1	0,2	0,75	100
c2	0,2	1,5	100
c3	0,2	3	100
c4	0,4	0,75	50
c5	0,8	0,75	25

Table 4.4 Compositions tested in *TMA-Ti* synthesis

The procedure is analogue to that described for *AH-Ti*.

EG was heated with an heating mantle in a 50 ml three necked flask fitted with a refluxing condenser at 60°C under vacuum (3mbar) for 20 minutes. Subsequently the temperature was raised to 110°C after switching to nitrogen flow using conventional Schlenk line setup. *$Ti(OPr^i)_4$* was then injected with a syringe and the solution turned immediately opaque. A second injection consisting in Tetramethylammonium hydroxide dissolved in water was quickly performed and an optically clear solution was obtained within few seconds. The synthesis was carried on at 110°C . The reaction time was held constant to 8 hours when compositional parameters were varied, while we tested the effect of heating time from 30 minutes to 8 hours only on composition **c5**.

Finally, the product were collected by centrifugation at 4000 rpm for 4 minutes after inducing flocculation with acetone.

The so obtained precipitate was washed two times with acetone and two times with methanol and dried under vacuum.

The powders was subsequently used for XRD,TEM, FT-IR, FT-Raman analyses and heat treated at 200°C, 300°C, 400°C and 500°C.

4.3.3.2 Results and discussion

XRD data shown in figure 4.20 refers to the product obtained from composition **c5** after four hours of reaction time and it is representative of the material synthesized in this work.
The XRD patterns do not belong to typical titanium dioxide phases (anatase, rutile or brookite). In particular, strong diffraction peaks in the low angle region are seen, suggesting for a layered structure analogue to those reported in [22] and described in section 4.2.2.

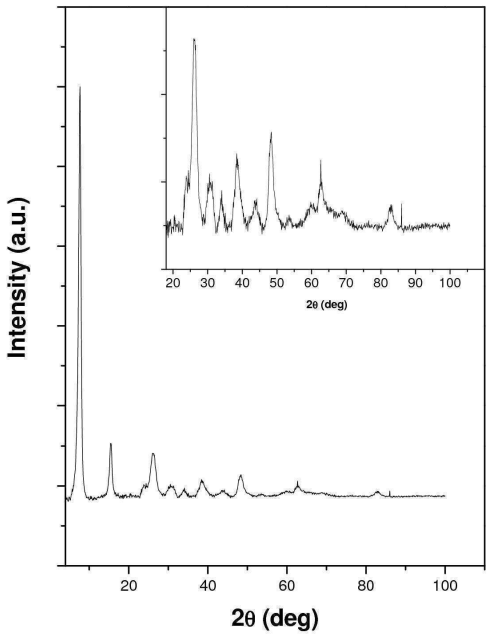

2θ (deg)	D (nm)
7.7	1.14
15.5	0.57
23.9	0.37
26.3	0.34
30.6	0.29
34.1	0.26
38.4	0.23
44.2	0.20
48.4	0.18

Figure 4.20 XRD pattern of powders obtained from recipe c5, 4 hours heating time. A magnification in the wider diffraction angle range is shown in the inset. Diffraction angles and deduced interplanar distance from Bragg relationship are reported in the table

The obtained layered titanates have an interlayer distance of 1.14 nm, as deduced from diffraction peak position and confirmed by TEM analyses shown in figure 4.21.
TEM analyses were done on the dried powder prepared as for XRD data, previously suspended in methanol (without achieving colloidal stability) and deposited on a copper grid.

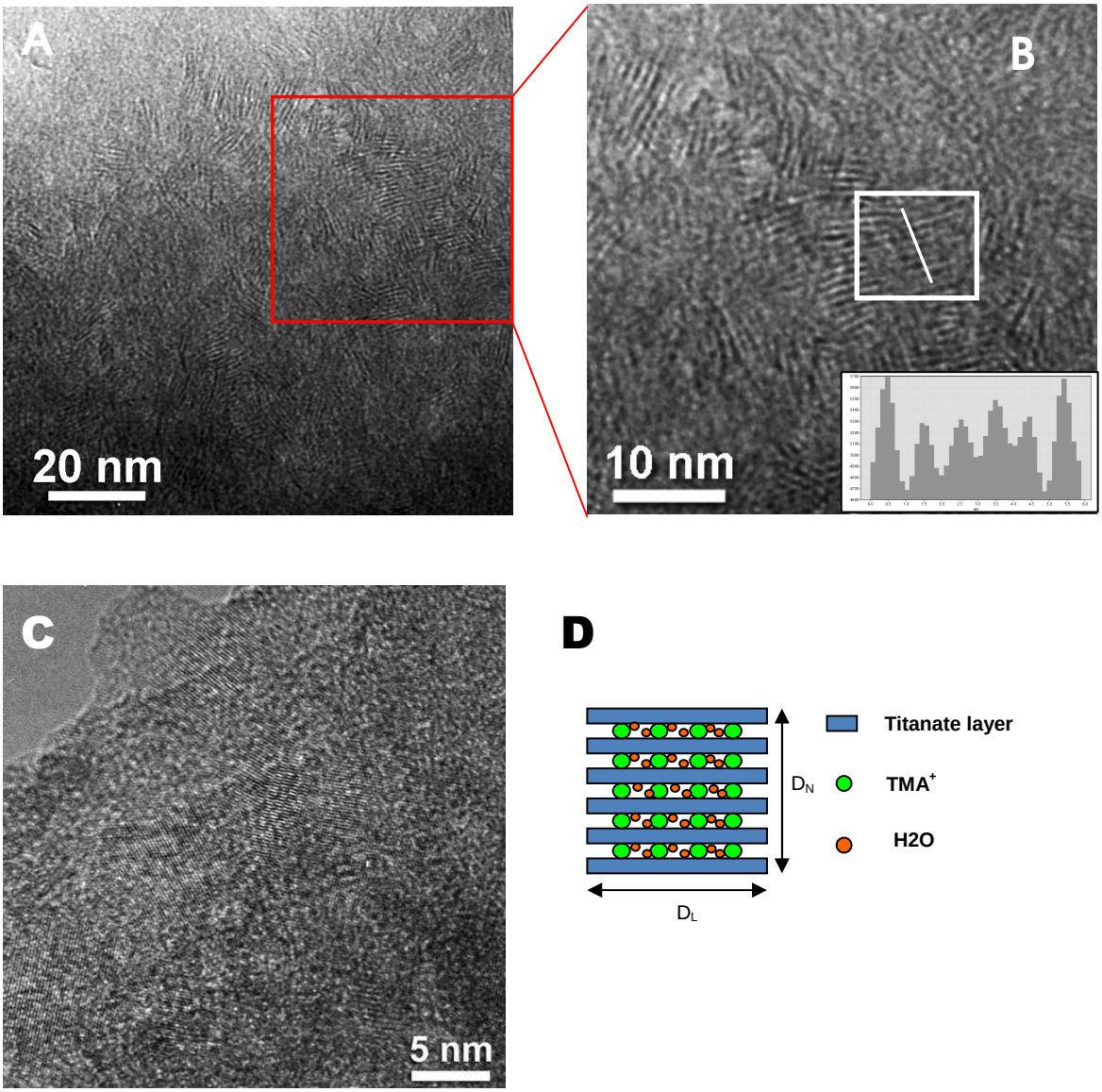

Figure 4.21 Bright field TEM (A) and HR-TEM (B) analyses for layered titanate synthesized from recipe c5, 4h heating time; HR-TEM showing periodicities belonging to single titanate layer (C); Schematic representation of a possible stacked titanate nanosheets (D). (In Figure 4.21B, the intensity profile along the white line is reported)

A layered structure is clearly seen. The interlayer distance is estimated to be around 1 nm. Domains with a number of 6-8 stacked layers are seen, each having a mean lateral dimension of about 5 nm.

HR-TEM in figure 4.21C shows periodicities attributable to single layer 2-D crystal arrangement.

The particular structure assumed gives rise to the diffraction features at wider angles, even if the exact structure has not yet been determined. Thus we cannot assign specific index to XRD peaks. The peak observed at 7.7° corresponds to the interplanar distance which is

exactly two times that corresponding to the diffraction peak at 15.5°. They correspond to different orders of diffraction from the same interlayer periodicity.

XRD peaks corresponding to interlayer distance are broad, implying that few layers are stacked in the powder state, coherently with TEM data.

Powders derived from different synthesis conditions show the same diffraction pattern in terms of peak position (figure 4.22A), thus we focused our attention on the more concentrated solution to see the effect of heating time (figure 4.22B).

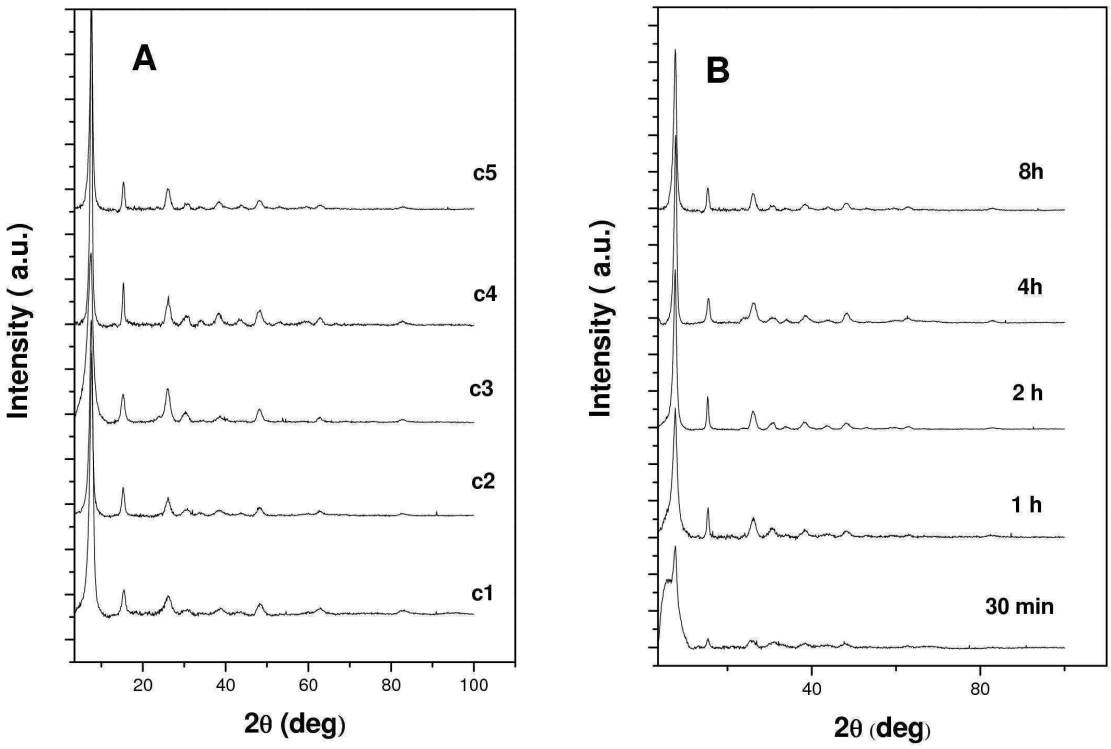

Figure 4.22 XRD diffraction spectra for powders obtained from different composition (A) and different heating time for recipe c5 (B)

In table 4.5, the size of the nano-layered domain estimated with Scherrer formula using the peaks at 7.7 deg and at 48.4 deg are reported for all tested synthetic parameters, including composition and time. The former gives indications about the dimension perpendicularly to the layer (D_N in figure 4.21D) and the number of stacked layers, while the latter gives information about the lateral extension (D_L) of the titanate sheet. The peak at 48.4 deg is always present in the XRD pattern of layered titanates reported in the literature, independently on the particular structure assumed. It can be assigned [25,41] to the periodicity arising from the anatase-like arrangement of TiO_6 octahedra that constitute the two-dimensional layer, as described in section 4.2.2. In fact, this diffraction peak is present

in the XRD pattern of anatase. Thus, even if we couldn't solve yet the structure from XRD data, we can assign this peak to an in plane single layer periodicity.

Recipe	Synthetis parameters			D_N (7.7 deg)	D_L (48.4 deg)
c1	[Ti]0.2 M	[TMA]/ [Ti]0.75	8h	5.9	4.9
c2	[Ti]0.2 M	[TMA]/ [Ti]1.5	8h	7.1	6.0
c3	[Ti]0.2 M	[TMA]/ [Ti]3	8h	3.7	6.3
c4	[Ti]0.4 M	[TMA]/ [Ti]0.75	8h	11.6	6.0
c5	[Ti]0.8 M	[TMA]/ [Ti]0.75	8h	7.1	6.3
c5	[Ti]0.8 M	[TMA]/ [Ti]0.75	30 min	6.8	3.3
c5	[Ti]0.8 M	[TMA]/ [Ti]0.75	1h	4.8	5.4
c5	[Ti]0.8 M	[TMA]/ [Ti]0.75	2h	6.8	5.7
c5	[Ti]0.8 M	[TMA]/ [Ti]0.75	4h	8.6	5.5

Table 4.5 Layered titanate domain characteristic dimensions D_N and D_L as defined in Figure 4.x7d for all employed synthetic conditions (synthetis parameters are reported for clarity)

Compositional parameters seem to have no effect on the number of stacked layers, while a trend is seen for the lateral extension. In particular, this becomes larger for compositions employing higher [*TMA*] and [*Ti*] concentration which results in increasing titanates formation and growing kinetics. Also increasing reaction time leads to wider sheets.

The erratic behavior of the dimension relative to the interlayer distance is explained considering how the powders are obtained. In the initial colloidal state, before the precipitation procedure, nanosheets are, very likely, partially or completely exfoliated [25,36]. Once precipitated and dried, titanate nanosheets tend to stack in an ordered fashion. Thus, the number of stacked layers depends on the precipitation and drying procedures rather than on synthesis parameters.

In the applications described in Chapter 5, titanates from recipe **c5** with four hours heating time has been used since it is the most concentrated in titanium precursors and longer heating time does not produce significant changes in the diffraction pattern. For this reason we carried out TEM analysis and the measurements described in the following only on this sample.

FT-IR spectrum (figure 4.23A) of the powder reveals the presence of water (adsorbed or in the interlayer space, band at 1655 cm^{-1} and 3400 cm^{-1}) and *TMA* (1489 and 949 cm^{-1}) which is most probably intercalated between the titanate layers [22].

FT-Raman (figure 4.23B) does not match with rutile or anatase structure, as expected, while pattern from peaks at 278 cm^{-1}, 384 cm-1, 443 cm-1 and 663 cm^{-1} is analogue to that reported for other titanates [22,91]. Also in this spectrum *TMA* bands are detectable.

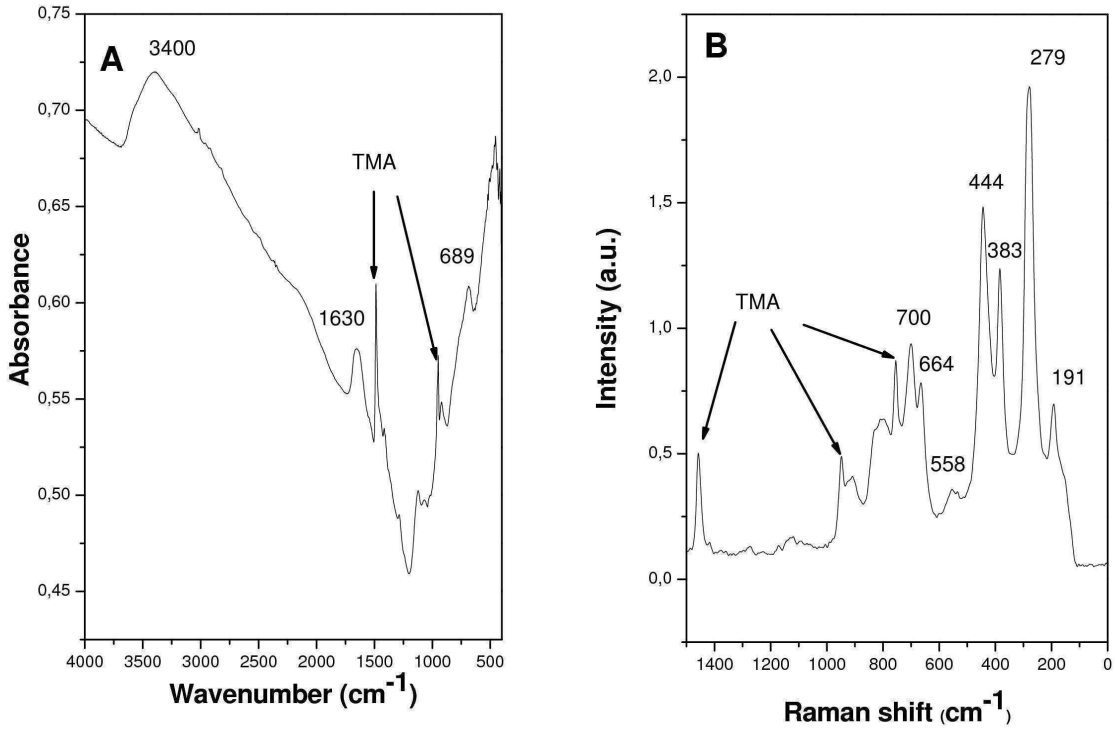

Figure 4.23 FT-IR (A) and FT-Raman (B) spectra of layered *TMA-Ti* titanates synthesized using recipe c5 with four hours of heating time

TG-DTA analysis in figure 4.24 shows two weight loss steps at about 330°C and 438°C, analogously to those reported for similar *TMA* intercalated titanates. These feature are likely due to *TMA* cations decomposition, associated with exothermic DTA peaks, with a final weight loss of about 20%.

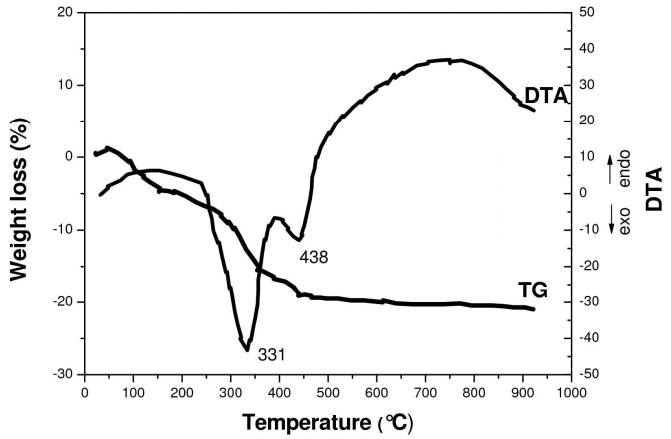

Figure 4.24 TG and DTA curve of layered TMA-Ti titanates synthesized using recipe c5 with four hours annealing time.

Ethylene glycol is here used as solvent and allows for stable and high temperature synthesis condition. Furthermore, after $Ti(OPr^i)_4$ injection, a titanium glycolate complex

forms as described in the previous section. This complex subsequently undergoes hydrolysis and reaction with *TMA*. This complex is likely to play a role during the synthesis. It can play an important role in the formation of the final structure since the interlayer distances obtained in this work are different from the 1.7 nm value reported in other works where *TMA* is used [22,80].

Using ethylene glycol along with water also allows for easy flocculation using small amount of acetone, leading to convenient processing and washing of the product, eliminating excess *TMA*.

UV-Vis absorption properties of colloidal titanate nanolayers in water are shown in figure 4.25. The colloidal solution was obtained dispersing the powder prepared as previously described in a aqueous solution containing *TMA*. This likely causes a complete or at least a partial exfoliation of layers resulting in an optically clear solution.

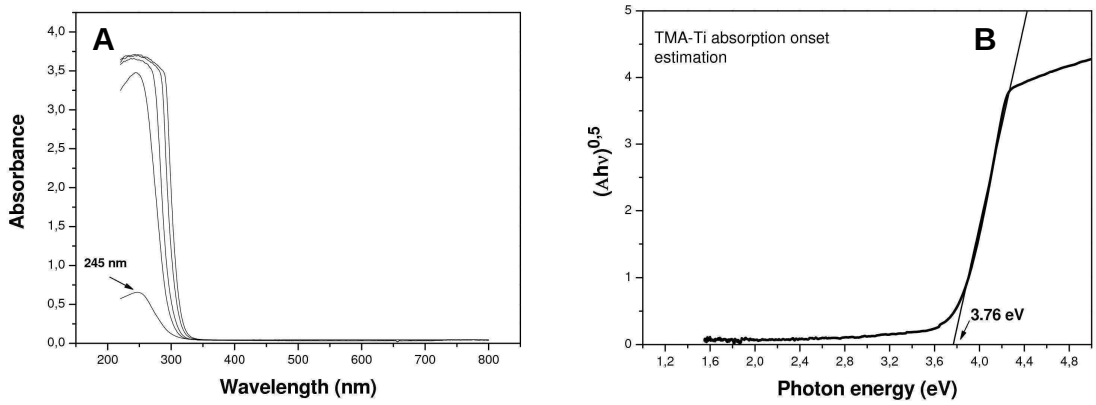

Figure 4.25 UV-Vis absorption spectra for *TMA-Ti* colloidal solutions in water at different concentration in the 0.01-0.3 g/L (A) and estimation of absorption onset of titanate layers in solution (B)

The absorption edge is in the UV region at about 330 nm, largely blue shifted with respect to anatase. A band gap value of 3.76 eV could be retrieve from UV-Vis absorption spectrum data using Eq. 4.1.

Furthermore, at increasing dilution a peak at 245 nm appears, analogously to spectra obtained for other titanates by Sasaki et al. [42]. In that work, this peak was attribute to optical transition of quantum confined electronic states of the titanate single sheet.

Thermal stability of this titanate has been assessed at different temperatures. XRD data are shown in figure 4.26 and reveal that the layered structure is maintained until 200°C, while it is lost at 300°C due to decomposition of TMA^+ ions. At 400°C anatase structure is obtained whose crystalline domains became greater at 500°C.

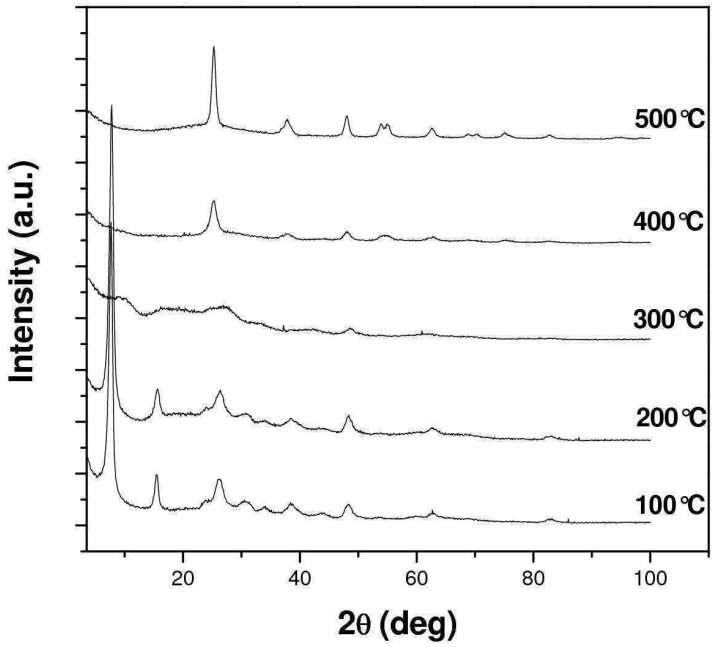

Figure 4.26 XRD data for titanate powder heat treated at different temperatures for 1 hour in air

References

[1] O'Regan B., Grätzel M., Nature, 1991, **353**, 737

[2] Barbe´C.J., Arendse F., Comte P., Jirousek M., Lenzmann F., Shklover V., Grätzel M., J. Am. Ceram. Soc.,1997, **80,** 3157

[3] Ferroni M., Guidi V., Martinelli G., Faglia G., Nelli P., Sberveglieri G., Nanostructured Materials, 1996, 709

[4] Buso D., Post M., Cantalini C., Mulvaney P., Martucci A., Adv. Funct. Mater. 2008, **18**, 3843

[5] Kim Y.D., Fischer M., Ganteför G., Chemical Physics Letters 2003, **377,** 170

[6] Schumacher B., Plzak V., Kinne M., Behm R.J., Catalysis Letters 2003, **89, 109**

[7] Haruta M., Daté M., Appl. Catal A: Gen., 2001, **222,** 427

[8] Bonhote, P., Gogniat, E., Grätzel M.,.Ashrit P. V., Thin Solid Films 1999, **350,** 269

[9] Linsebigler A. L., Guangquan Lu, Yates J.T, Chem. Rev., 1995, *95*, 735-758

[10] Herrmann J.M.,.Catalysis Today 1999, **53**, 115

[11] Testino A., Bellobono I.R., Buscaglia V., Canevali C., D'Arienzo M., Polizzi S., Scotti R.,Morazzoni F., J. Am. Chem. Soc., 2007, **129**, 3564

[12] Liu Y.F., Lu C.L., Li M.J., Zhang L., Yang B., Coll. And Surf. A, 2008, **328**, 67

[13] Nussbaumer R. J., Caseri W., Tervoort T., Smith P., J. of Nanoparticle Research, 2002, **4**, 319

[14] Nussbaumer R. J., Caseri W.R., Smith P., Tervoort T. Macromol. Mater. Eng., 2003, **288**,

[15] Rabaste S., Bellessa J., Brioude A., Bovier C., Plenet J.C., Brenier R., Marty O., Mugnier J., Dumas J., Thin Solid Films, 2002, **416** , 242

[16] Almeida Rui M., Goncalves M. C. , Portal S., J. Non. Cryst. Solids, 2004, **345&346**, 562

[17] Yoon J., Leea W., Caruge J.M., Bawendi M, Thomas E.L., Kooi S., Prasad P. N., Appl. Phys. Lett., 2006, **88**, 091102

[18] Chiasera A, Belli R., Bhaktha S. N. B., Chiappino A. , Ferrari M., Jestin Y. , E. Moser, Righini G. C. , Tosello C., Appl. Phys. Lett., 2006, **89**, 171910

[19] Rabaste, S., Bellessa, J., Bonnand, C.' Plenet, J., Spanhel, L., Eur. Phys. J. B, 2004, **42**, 47

[20] Poitras C.B., Lipson M., Du H., Hahn M.A., Krauss T..D., Appl. Phys. Lett., 2003, **82**, 4032

[21] Feist T.P., Davies P.K., J. Solid State Chemistry, 1992, **101**, 275

[22] Ohya T., Nakayama A., Ban T., Ohya Y., Takahashi Y., Chem. Mater., 2002, **14**, 3082

[23] Sasaki T., Watanabe M., Michiue Y., Komatsu Y., Izumi F., Takenouchi S., Chem. Mater., 1995, **7**, 1001

[24] Gao T., Fjellv T., Norby P., Chem. Mat., 2009, 21, 3503

[25] Sasaki T., Watanabe M., Hashizume H., Yamada H., Nakazaw H., J Am. Chem Soc., 1996, **118**, 1329

[28] Sasaki T., Watanabe M**.**, J. Am. Chem. Soc, 1998**, 120**, 4682

[29] Chen Q., Zhou W., Du G., PengM.L., Adv. Mat, 2002, **14,** 1208

[30] Yong Yuan Z., Su B.L., Coll. Surf. A, 2004, **241**, 173

[31] Sasaki T., Nakano S., Yamauchi S., Watanabe M., Chem. Mat., 1997, **9**, 602

[32] Sasaki T, Komatsu Y., Fujiki Y., Chem. Mat., 1992, **4**, 894

[33] Kotov N.A., Meldrum F.C., Fendler J.H., J. Phys. Chem., 1994, **98**, 8827

[34] Xu X. G., Ding X., Chen Q., Peng L.-M., J Phys Rev B., 2006, 73, 165403

[35] Riss A., Elser M. J., Bernardi J., Diwald O., J. Am. Chem. Soc., 2009, **131**, 6198

[36] Miyamoto N., Kuroda,K., Ogawa M., J. Mat. Chem, 1994, **14**, 165

[37] Choy J-.H., Lee H.-C., Jung H, Kim H, Boo H., Chem. Mat., 2002, **14**, 2486

[38] Umemura Y., Shinohara E., Koura A., Nishioka T., Sasaki T, Langmuir, 2006, **22**, 3870

[39] Jang J.-H., Jeon K.S., Oh S.,Kim H.-J., Asahi T.,Masuhara H., Yoon M., Chem..Mat., 2007, **19**, 1984

[40] Sasaki T., Ebina Y., Fukuda K., Tanaka T., Harada M., Watanabe M., Chem.. Mat. 2002, **14**, 3524

[41] Sasaki T., Watanabe M., J. Phys. Chem. B, 1997**, 101**, 10159

[42] JCPDS # 86-1157 for anatase ; JCPDS # 87-0710 for rutile ; JCPDS # 76-1937 for brookite

[43] Lide DR *Handbook of Chemistry and Physics*, CRC Press, 72nd edition.

[44] Koelsch M., Cassaignon S., Guillemoles J.F., Jolivet J.P, Thin Solid Film, 2002**, 403 – 404**, 312

[45] Tang H., Prasad K., Sanjines R., Schmid P. E, Levy F., J. Appl. Phys., 1994, **75**, 2042

[46] Sato H., Ono K., Sasaki T., Yamagishi A. J. Phys. Chem B, 2003, **107**, 9824

[47] Hengzhong Zhang* and Jillian F. Banfield *J. Phys. Chem. B* **2000,** *104*, 3481-3487

[48] Yanqing Z., ErweiS., Zhizhan C., Wenjun L., Xingfang H., J. Mater. Chem., 2001, **11**, 1547

[49] Pottier A., Chaneac C., Tronc E., Mazerolles L., Jolivet JJ.P., J. Mater. Chem., 2001, **11**, 1116

[50] Kormann, C., Bahnemann, D. W., Hoffmann M. R,. J. Phys. Chem., 1988, **92**, 5196.

[51] Enright B., Fitzmaurice, D. J. Phys. Chem., 1996, **100**, 1027

[52] Monticone S., Tufeu R., Kanaev A.V., Scolan E., Sanchez C., Applied Surface Science 2000, **162**, 565

[53] Chen X., Mao S.S., Chem. Rev., 2007**, 107**, 2891

[54] Brian L. Bischoff, and Marc A. Anderson *Chem. Mater.* **1995,** *7*, 1772-1778

[55] Wu M., Lin G., Chen D., Wang G., He D., Feng S., Xu R., Chem. Mater**.** 2002**, 14**, 1974

[56] Bacsa R.R., Grätzel M., J. Am. Chem. Soc , 1996, **79**, 2185

[57] Yang J., Mei S., Ferreira J. M. F., J. Am. Ceram. Soc., 2001, **84,** 1696

[58] Yanagisaw K., Ovenstone J.**,**J. Phys. Chem. B, 1999**, 103**, 7781

[59] Yin H., Wada Y., Kitamura T., Sumida T., Hasegawa Y., Yanagida S., J. Mater. Chem., 2002, **12**, 378

[60] Yang J., Mei S., Ferreira Jose M. F., J. Am. Ceram. Soc., 2000, **83,** 1361

[61] Cheng H., Ma J., Zhao Z., Qi L., Chem. Mater., 1995**, 7**, 663

[62] Niederberger M., Bartl M..H., Stucky G.D., Chem. Mater., 2002**, 14**, 4364

[63] Huang O., Gao L., Chemistry Letters., 2003, **32,** 860

[64] Gopal M., Moberly Chan W.J., De Jonghe L.C., L., Mat, Sci, 1997, **32**, 6001

[65] Aruna S. T., Tirosh S., Zaban A., J. Mater. Chem., 2000, **10**, 2388

[66] Yanqing Z., Erwei S., Zhizhan C., Wenjun L., Xingfang H., J. Mater. Chem., 2001, **11**, 1547

[67] Yin H., Wada Y., Kitamura T., Kambe S., Murasawa S., Mori H., Sakatac T., Yanagida S., J. Mater. Chem., 2001, **11**, 1694

[68] PottierA., Cassaignon S., Chaneac C, Villain F., Tronc E., Jolivet J.P.,J. Mater. Chem., 2003, 1**3**, 877

[69] Sun J., Gao L., J. Am. Ceram. Soc., 2002, **85,** 2382

[70] Watson S.S, Beydoun D., Scott J,A., Amal R.,Chemical Engineering Journal, 2003, **95,** 213

[71] Scolan E., Sanchez C., Chem. Mat. 1998, **10**, 3217

[72] Cozzoli P.D., Kornowski A., Weller H., J. Am. Chem. Soc. 2003, **125**, 14539

[73] Nussbaumer R., Smith P., Caseri W. , Journal of Nanoscience and Nanotechnology , 2007, **7**, 2422

[74] Izawa H., Kikkawa S., Koizumi M., J. Phys. Chem**,.** 1982, **86**, 5023

[75] Sumida T., Takahara, Y**.,** Abe R., Hara M., Kondo J.N., Domen K., Kakihana M, Yoshimura M., Phys. Chem. Chem. Phys., 2001, **3**, 640

[76] Sasaki T., Komatsu Y., Fujiki Y., Chem. Mater., 1992**,4,** 894

[77] Zhu H., Gao X., Lan Y., Song D., Xi Y., Zhao J., J. Am. Chem. Soc. 2004, **126**, 8380

[78] Airoldi C., Nunes L.M., de Farias R.F., Materials Research Bulletin, 2000 **35** 2081

[79] Sasaki T., Watanabe M., Komatsu Y., Fujiki Y., Inorg. Chem**,.** 1985**, 24,** 2265

[80] Liu C.H., Rouet A., Sutrisno H., Puzenat E., Terrisse H., Brohan L., Richard-Plouet M, Chem. Mater., 2008**, 20**, 4739

[81] Ohya T., Nakayama A., Ban T., Ohya Y., Takahashi Y., Bull. Chem. Soc. Jpn, 2003,**76**, 429

[82] Sakai N., Ebina Y., Takada K., Sasaki T., J. Am. Chem. Soc**.,** 2004, **126**, 5851

[83] Murray C. B., Norris D. J., Bawendi M. G., J. Am. Chem. Soc**.,** 1993, **11**, 8706

[84] Liu K., Zhang M., Shi K., Zhou W., Fu H., J. Non-Cryst Solids, 2006, **352**, 2284

[85] Jiang X., Wang Y., Herricks T., Xia Y., J. Mat. Chem., 2004, **14**, 695

[86] Chen Q., Zhou W., Du G., Peng L.M., Adv. Mat., 2002, **14**, 1208

[87] Suzuki Y., Yoshikawa S., J. Mat. Res., 2004, **19**, 982
[88] Chen Q., Du G.H., Zhang S., Peng L.M., Acta Cryst., 2002, **B58**, 587

[89] Jiang X, Wang Y., Herricks T, Xia Y., J . Mater . Chem. , 2004 , **14** , 695

[90] Wang D., Yu R., Kumada N., Kinomura N., Chem. Mater.**,** 1999**, 11**, 2008

[91] Gao T., Fjellvag H., Norby P., J. Phys. Chem. B, 2008, **112**, 9400

[92] Kava L., Stoto T., Gratzel M., Fitzmaurice D., Shklover V., J. Phys. Chem., 1993, **97**, 9493

[93] Souri D., Shomalian K., Journal of Non-Crystalline Solids, 2009, **355**, 1597

[94] Yang L.L., Lay Y.S., Chen J.S., Tsai P.H., Chen C.L., Chang C.J., J Mat. Res., 2005, **20**, 3141

[95] Mansur H.S., Oréfice R.L., Mansur A.A.P., Polymer, 2004, **45,** 7193

Chapter 5

TiO_2 nanomaterials: Optical applications

5.1 Introduction

Nanocomposite are a powerful tool for properly tune dielectric, optical and functional properties of the resulting material.

TiO_2 nanocomposites are interesting materials due to UV absorption properties and optical transparency. The high refractive index of titania can be used to prepare high refractive index films or variable refractive index materials by changing the titania to matrix ratio [1]. These materials have also been studied for non-linear optical applications [2]. In particular, third order effects have been evaluated and measurements of two-photon absorption coefficient and non-linear refractive index have been performed and their dependence upon particles crystallinity and concentration has been studied [3,4].

Titania-polymer nanocomposites have been applied in optical data storage since they enhance refractive index contrast upon application of modulated light intensity with respect to pure polymer [5].

Thus, such materials allows for convenient engineering of linear and non-linear optical properties.

A lot of synthetic approaches are available in the literature for TiO_2 embedding materials fabrication.

They can be mainly divided in :

a) in situ synthesis where TiO_2 particles are synthesized in the preformed matrix or where the matrix is polymerized through organic or sol-gel reactions around the nanoparticles [6-10]

b) ex situ synthesis where the particles are synthesized in an independent reaction system and then introduced in the desired matrix material [11-16].

In situ methods generally allows for good homogeneity of the materials if optimization of matrix/particle interface is tailored [9]. If a titanium alkoxide is used as precursor, it can be mixed with alcohol or water soluble polymers. Compatibility between the two phases can

be promoted by introduction of silane groups in the polymer backbone [10]. This approache generally leads to amorphous inorganic domains which ca be made crystalline by subsequent material treatment such as thermal annealing in wet atmosphere or dipping in hot water [4, 17-19].

Homogeneity in ex-situ synthesis is harder to achieve, because of the inherent tendency toward agglomeration, thus surface chemistry and functionalization play a crucial role.

On the other hand, this strategy is much more flexible since it allows more degrees of freedom on the choice of matrix and particles and synthesis of particles can be tailored to get the desired size, crystallinity and surface chemistry without any limitations imposed by polymerization reaction or solubility behavior of the matrix constituents.

Post synthesis functionalization has been applied to water-born titania nanocrystals synthesized via hydrolytic methods in order to make them compatible with apolar matrix such as polystyrene [11] using sulfonic acid terminated ligands. Silane based ligands can also be used relying on Ti-O-Si bond formation. Glycidoxypropyltrimethosysilane has been used to impart a photopolymerisable moiety on TiO_2 particle surface, allowing for photocurable materials with high refractive index [13]. A lot of more recent excellent example of silane functionalization have been applied to non-hydrolytic synthesis, where stable and transparent colloidal oxide sols in the desired solvent can be obtained [20] which can be further used for nanocomposites preparation [21].

In order to have transparent composites, scattering from embedded particles has to be avoided. The loss of transparency due to scattering can be expressed by the following formula derived from the Mie theory [22]:

$$\frac{I}{I_0} = \exp[\frac{-3\phi_p x r^3}{4\lambda^4}(\frac{n_p}{n_m} - 1)] \qquad \text{Eq. 5.1}$$

which refers to spherical particles with radius r and refractive index n_p,, n_m is the matrix refractive index, I and I_0 are the intensity of the transmitted and incident light respectively, ϕ_p the volume fraction of the particles, λ the wavelength of light and x the optical path length.

In the figure below, a plot of Eq.5.1 is shown for a matrix refractive index of 1.5, a particles volume fraction of 0.2 and increasing refractive index of the particles.

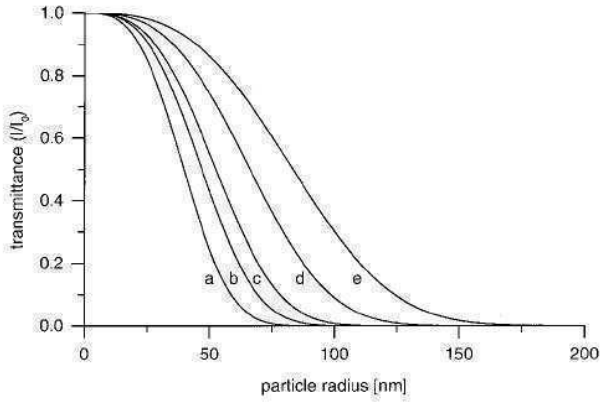

Figure 5.1 Plot of Eq. 5.1 for a matrix refractive index of 1.5, a particles volume fraction of 0.2 and increasing refractive index of the particles of 1.75 (a), 2 (b), 2 .5 (c), 3 (d), 4 (e) (Source : Caseri [22])

Unless the refractive index of the particles is the same of the matrix, transparency losses due to scattering always exist, even if they are negligible for particles with diameter of about 20 nm in the case of a n_p value of 2.5 (curve c in Figure 5.1), which is the case of titania in the anatase structure.

Thus, it appears very important to have highly homogeneously dispersed particles in the host material in order to avoid large aggregates that scatter light.

As previously stated, refractive index can be tuned with particles volume fraction in the host matrix. The dielectric behavior of a composite material made of spherical particles embedded in a solid matrix can be analyzed through various models [23] such as Maxwell Garnett and Bruggeman. These are effective medium models valid if particles are sufficiently small to consider the resulting material homogeneous with respect to light interaction.

Experimentally, refractive index is found to be linearly dependent on the volume fraction of the particles, at least for not extremely high volume fraction [24].

In the following, the synthesis of high refractive index nanocomposites obtained from anatase TiO_2 particles and *TMA-Ti* titanates is described. Further, the obtainment of a multifunctional material both possessing high refractive index and luminescent properties is reported and applied for waveguide fabrication and LED encapsulation.

Finally, the synthesized titania nanomaterials were used as matrix for gold particles to investigate optical gas sensing behavior and improve gold nanorods stability upon thermal treatment.

5.2 High refractive index films

5.2.1 Fabrication of high refractive index and porous thin films fromTiO_2 anatase particles

4.2.1.1 Synthesis of nanocomposite films

Nanocomposite films where TiO_2 NCs are embedded in an hybrid sol-gel matrix are produced by mixing a colloidal TiO_2 NCs solution with the matrix precursors sol.
The hybrid material was synthesized from 3-Glycidoxypropyltrimethoxysilane (*GPTMS*) and Titanium Tetraisopropoxyde ($Ti(OPr^i)_4$) following synthetic strategies similar to those reported in [25]. 27 mmol of *GPTMS* was first hydrolyzed with a stoichiometric amount of water under vigorous stirring at ambient temperature for five hours. Then, 3 mmol of $Ti(OPr^i)_4$ dissolved in methoxyethanol was added drop wise.
The quantity of methoxyethanol was adjusted to give a final volume of 10 ml and thus a 3M final alkoxides concentration. The solution was stirred at ambient temperature for 30 minutes, refluxed for 1 hour at 80 °C, cooled to ambient temperature and finally three-fold diluted with methoxyethanol.

Nanocomposite and TiO_2 films were made using particles obtained with recipe A with four hours reaction time (see chapter 4.3.1). TiO_2 NCs were collected with the procedure described in section 4.3.1.1 using the minimum amount of acetone to have a precipitate.
TiO_2 particles obtained from 5 ml of as-synthesized solution were collected and dispersed again with 150 µl of methanol, obtaining a clear colloidal sol. This solution was then mixed with the hybrid sol-gel solution in different proportion in order to obtain five TiO_2 NCs loading ranging from 20 wt% to 80 wt% with 15 wt% increasing step. These percentages were based on the weights of TiO_2 particles and sol-gel solution measured after drying at 150°C in an oven. The obtained solutions were diluted with methoxyethanol and spun at 5000 rpm for 20 seconds under nitrogen atmosphere.
Films consisting of pure TiO_2 NCs were prepared by diluting the titania colloidal sol with ethanol and spun at 3000 rpm for 20 seconds under nitrogen atmosphere. The films were heat treated at 150 °C, 200 °C, 300 °C, 400 °C and 500 °C for one hour in air.
Films have been deposited on silica glass or silicon substrate.

5.2.1.2 Results and discussion

The matrix used to obtain nanocomposite films (**GlyTi**) is an epoxy-based hybrid sol-gel system where $Ti(OPr^i)_4$ is used to promote the organic polymerization of the epoxy group of *GPTMS* which should result in a polyethyleneoxide network interconnected to the inorganic network formed by hydrolysis and condensation of the metal alkoxide.

FT-IR analysis (figure 5.2A) of the undoped hybrid sol-gel film showed no absorption band corresponding to C-H stretching of closed epoxy ring at 3060 –2995 cm^{-1}, which can be correlated to epoxy polymerization [25]. Bands at about 3400-3300 cm^{-1}, 2900-2800 cm^{-1} and 1100 cm^{-1} can be assigned to O-H, C-H and Si-O-Si vibrations, respectively.

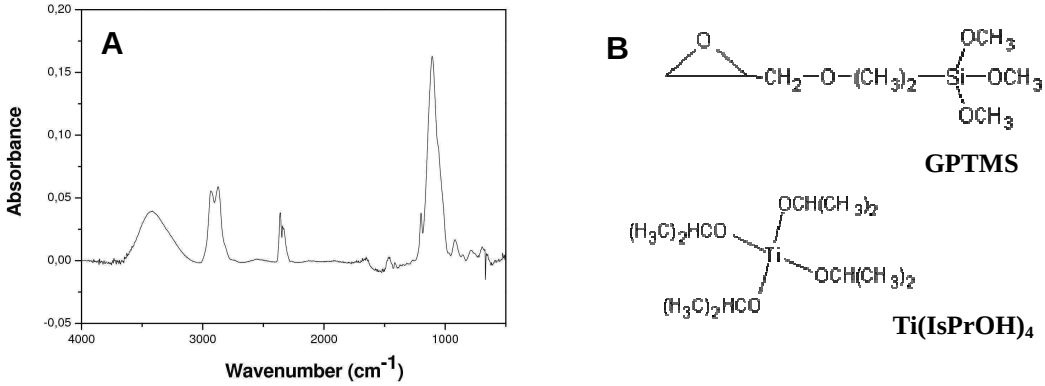

Figure 5.2 FT-IR spectrum of **GlyTi** hybrid matrix deposited on silicon substrate (A). A scheme of the alkoxide precursors of the hybrid material is also presented (B)

The hybrid deposition containing 80%wt of TiO_2 nanocrystals has been analyzed with cross section TEM. Dispersed TiO_2 crystalline domains are seen in the HR-TEM image presented in figure 5.3a, while the STEM analysis reported in figure 5.3b shows a uniform composition of the film without TiO_2 aggregation, which is necessary for optical transparency.

In Figure 5.4 refractive index and extinction coefficient curves in the 300-1000 nm wavelength range are presented. Refractive index values (measured at 630 nm) can be easily tuned between 1.51 (pure matrix) up to almost 1.89, corresponding to the 80 %wt TiO_2 loaded nanocomposite coating, while pure TiO_2 film (100%wt TiO_2 in figure 5.4) treated at 150 °C has a refractive index value of 1.93.

Extinction coefficient values are almost zero in the 450-800 nm range, implying a good transparency in the visible while the absorption is increasing in the UV range with the increasing TiO_2 content.

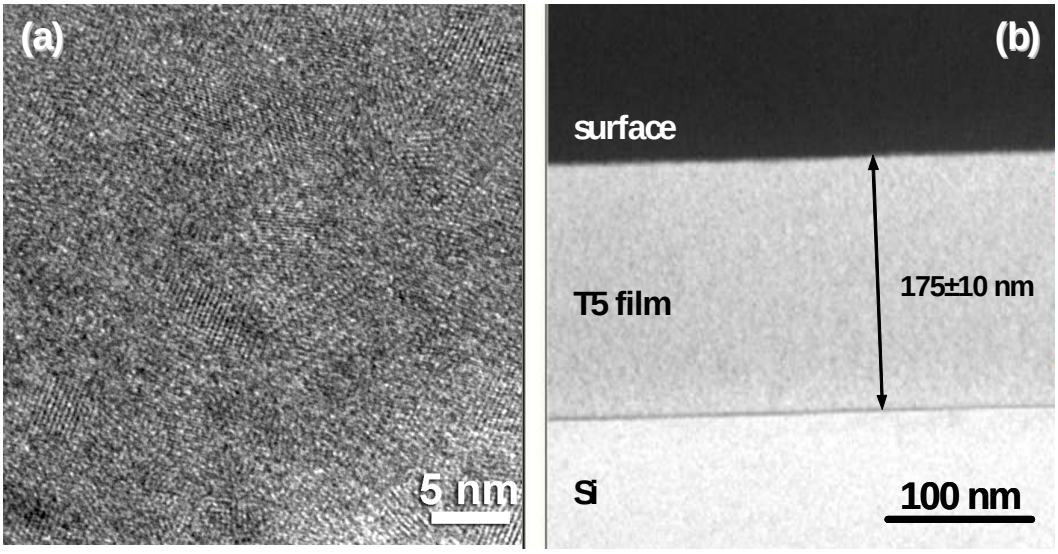

Figure 5.3 Cross-section HR-TEM image (a) and STEM image (b) of 80 wt% TiO_2 loaded composite film.

Using a TiO_2 density of 3.84 Kg/m^3 [26] and a density of 1.24 Kg/m^3 for the hybrid matrix, estimated with Archimedean method, it is possible to convert weight fractions to volume fractions. The experimental refractive index values show a linear relation with TiO_2 volume fraction incorporated in the material. This behavior has been observed also in previous publications [6, 21, 22]. However, extrapolation from the obtained linear fit for a 100% titania gives a refractive index value of about 2.19, which is much lower than reported values for anatase, i.e. 2.493-2.554 [19]. Possible explanations may include the presence of amorphous TiO_2 (which has lower refractive index) or lower refractive index values for nanometric TiO_2 with respect to bulk material, as observed for PbS nanoparticles [24].

More likely, porosity has to be considered as a third phase in our depositions, where matrix material is not able to fill the voids completely. This causes the refractive index values to be lower than those for porosity-free samples, thus lowering the extrapolated values for pure TiO_2. In the pure TiO_2 film heat treated at 150 °C, where voids among particles are not filled with any matrix, the refractive index is much lower than the literature value for anatase, suggesting for high porosity of this film.

Since porous deposition of crystalline TiO_2 can be interesting in different application area, the effect of thermal treatment on the structure of this film has been investigated.

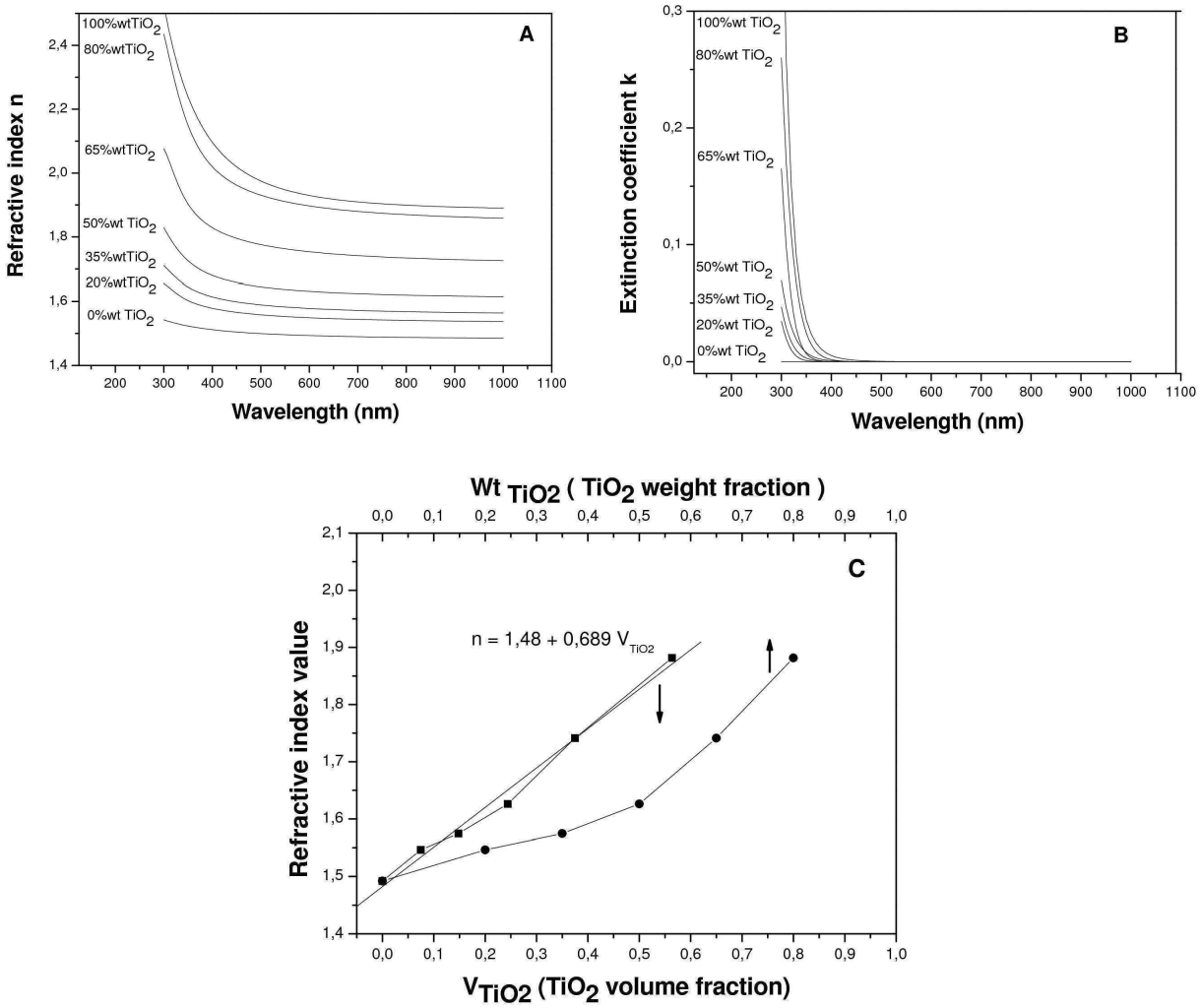

Figure 5.4 Refractive index n (A) and extinction coefficient k (B) dispersion curves of TiO_2-doped and undoped films. (C) Experimental refractive index values at 630 nm plotted versus TiO_2 volume fraction and TiO_2 weight fraction.

Refractive index values and film thickness of pure TiO_2 NCs films annealed at different temperatures are reported in Table 5.1. The most pronounced enhancement in refractive index is obtained by annealing the film at 500 °C and film thickness consistently decreases for heat treatments at temperatures above 200 °C.

From measured refractive index it is possible to estimate the volume fraction of porosity by the following relationship derived from the Bruggeman model for the effective medium [27]:

$$Porosity = \left(\frac{n_{TiO_2}{}^2 - n^2}{n_{TiO_2}{}^2 + 2n^2}\right) \Big/ \left(\left(\frac{n_{TiO_2}{}^2 - n^2}{n_{TiO_2}{}^2 + 2n^2}\right) - \left(\frac{1-n^2}{1+2n^2}\right)\right) 100\%$$

where n_{TiO2} is the refractive index of fully densified TiO_2, here assumed to be 2.52, and n the experimental refractive index of the film. Porosity remains quite high up to 400 °C, while at 500 °C it is drastically reduced (see table 5.1).

	Refractive index (@630 nm)	**Film thickness (nm)**	**Porosity (% vol)**
150°C	1.92	82	38
200°C	1.94	85	36
300°C	1.98	75	34
400°C	2.03	61	31
500°C	2.21	55	20

Table 5.1 Refractive index values, thicknesses and estimated porosity of TiO_2 NCs thin films under different thermal treatment temperatures

This behavior can be correlated to that observed for the evolution of TiO_2 NCs powders previously described in section 4.3.1, where a more pronounced increase in mean crystallite size was observed between 400 °C and 500 °C. Thus, it is likely that porosity decreases with temperature due to coarsening and sintering of the particles leading to progressive densification. These processes seems to be enhanced above 400 °C.

SEM micrographs of pure TiO_2 NCs films (see figure 5.5) shows that film annealed at 150 °C are highly porous (figure 5.5A), while films annealed at 500 °C are much more densified (figure 5.5B).

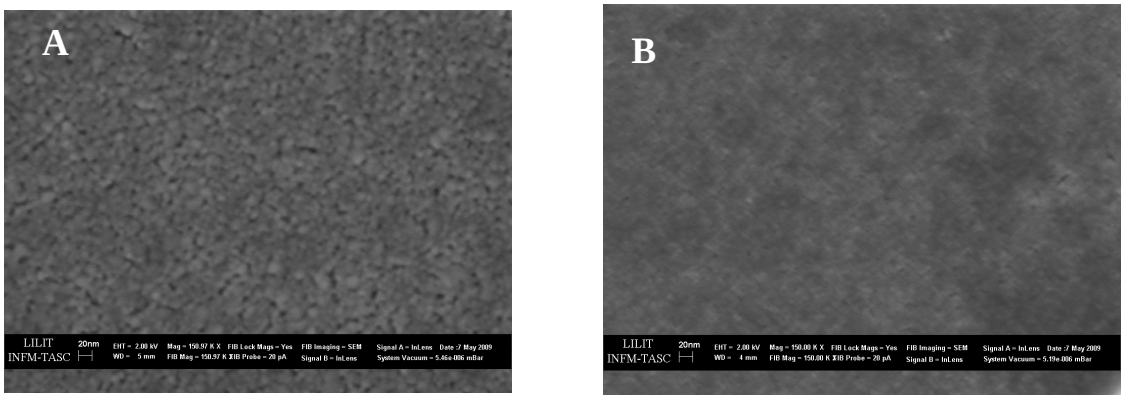

Figure 5.5 SEM micrograph of TiO_2 NCs film annealed at 150 °C (A) and 500 °C (B)

In figure 5.6A and B refractive index and extinction coefficient are reported, while in Figure 5.6C XRD diffraction pattern with grazing angle technique are shown for TiO_2 NCs depositions on silicon substrate treated above 300 °C. At lower annealing temperatures of 150 °C and 200 °C, XRD signal could not be detected from TiO_2NC's films. Since starting material is crystalline, as proved from XRD on powders, it is likely that the signal from the thin film is too weak due to small crystal size and small film thickness. XRD of TiO_2 NCs powders could instead be detected due to higher TiO_2 volume fraction present in the X ray radiation penetration volume. The XRD patterns of films annealed at higher temperatures belong to the anatase structure and narrowing of XRD peaks is seen due to increasing TiO_2 NCs size, as observed for titania powders.

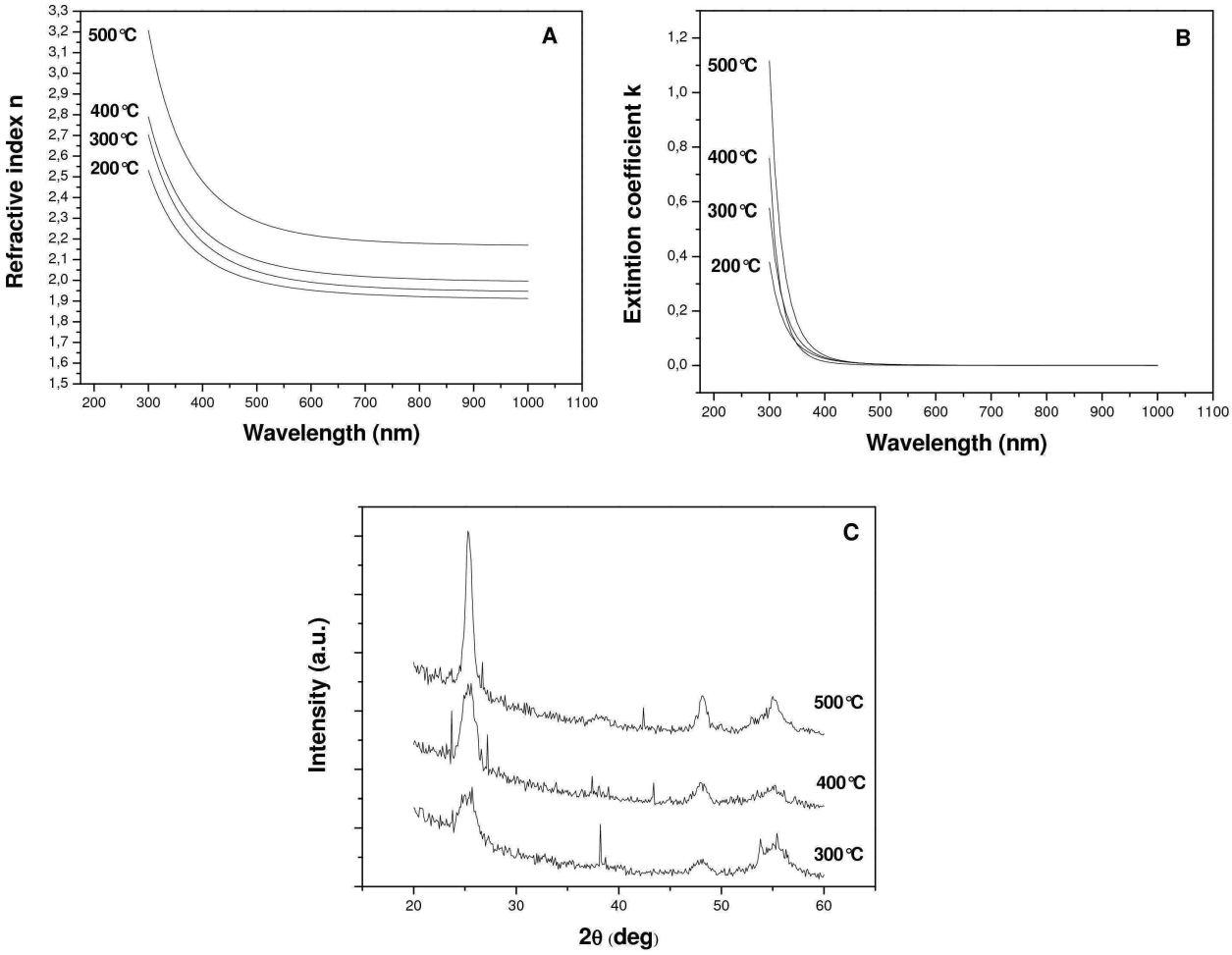

Figure 5.6 Refractive index (A), extinction coefficient (B) curves and XRD diffraction spectra (C) for TiO2 NCs depositions treated at different temperatures

Extinction coefficients in the UV region increase with increasing annealing temperature. This effect is related to the increasing densification of the material, so that the measured effective extinction coefficient is progressively raised up due to higher TiO_2 volume

fraction (i.e. reduced porosity) in the film. This can be easily seen from Eq. 5.3 and Eq. 5.4 expressing the effective refractive index and extinction coefficient of a two phase system derived from a Volume Averaging Theory [23].

$$n_{eff}^2 = \frac{1}{2}[A + \sqrt{A^2 + B^2}] \qquad \text{Eq. 5.3}$$

$$k_{eff}^2 = \frac{1}{2}[-A + \sqrt{A^2 + B^2}] \qquad \text{Eq. 5.4}$$

where $A = \phi(n_d^2 - k_d^2) + (1-\phi)(n_c^2 - k_c^2)$, $B = 2\phi n_d k_d + 2(1-\phi) n_c k_c$, n is the refractive index, k *is* the extinction coefficient. Subscripts "*c*" and "*d*" refer to the continuous phase (i.e. the matrix) and the dispersed phase (i.e. the inclusions) respectively, while "*eff*" designates the optical constants of the overall resulting material with a volume fraction ϕ of the dispersed phase.

These relationships were found to be in good agreement with numerical simulations of porous structures to a better extent than other frequently used models [23]. From Eqs. 5.3 and 5.4 it is apparent that not only the refractive index is modified upon variation of the relative volume fraction of the constituent phases, but also the extinction coefficient is obviously affected.

Another possible reason of this behavior can be related to the different band gap due to different particle size (quantum size effect), which was shown to increase with annealing temperature (see section 4.3.1). In this case, pristine particles have a band gap almost equal to bulk TiO_2 (see section 4.3.1). Particles annealed at higher temperatures are bigger, thus band gap should remain unchanged. The observe *k* behavior is thus most likely to be entirely explained with the structural evolution of the deposition.

The method described in this thesis gives the possibility to obtain highly porous nanocrystalline titania coatings at temperatures below 400°C, while keeping the particles in a very small size range necessary for large surface area. This allows for films with good optical quality, transparency and porosity which is particularly interesting for a great variety of applications including gas sensing, catalysis and incorporation of other types of nanoparticles or organic molecules.

5.2.2 High refractive index thin films from Tetramethylammonium hydroxide derived titanates (TMA-Ti)

5.2.2.1 Titanate film synthesis and modification and Distributed Bragg Reflector fabrication

The powders obtained as described in section 4.3.3 was first dispersed in water with a *TMA* concentration of 0.03M obtaining a clear colloidal solution with a titanate concentration of 200 g/L. To improve film quality under spin casting this solution was twofold diluted with methanol and spun at 3000 pm for 20 seconds on quartz and silicon substrates for ellipsometry and FT-IR measurement respectively.

These films were first stabilized at 100°C for 30 minutes and then treated at 200 °C, 300 °C, 400 °C and 500 °C or exposed to UV radiation for 0.625, 1.25, 2.5, 5, 12.5 and 15 minutes. These depositions will be referred to as **200**, **300**, **400**, **500** for thermally treated samples and **35''UV**, **75''UV**, **2.5'UV**, **5'UV**, **12.5'UV** and **15'UV** for UV treated samples. Finally also combined thermal and UV treatments were investigated. For example, **15'UV + 200** refers to a treatment where the deposition is first UV treated for 15 minutes and then heated at 200°C temperature for one hour. If the time of thermal treatment is varied, it will indicated in minutes before in the sample name.

UV irradiation was performed with a mercury-xenon lamp (Hamamatsu LC6) with a an intensity estimated to be 460mW/cm^2 at 365 nm. UV light relevant in this application is that emitted at 250 nm, where the employed lamp has an emission band. If a 0.15 ratio is assumed between the band at 250 nm and that at 365 nm (as inferred from spectral radiance provided by the lamp's supplier), an intensity emission at 250 nm of about 70mW/cm^2 can be estimated.

The obtained depositions were investigated with XRD, spectroscopic ellipsometry and FT-IR spectroscopy.

The photocatalytic properties of titanate depositions annealed at different temperatures on silicon substrates were investigated with the stearic acid method [41]. Stearic acid was dissolved in methanol and spun on the titanate films. The films were exposed at UV radiation and FT-IR measurements were carried out every 1minute of irradiation.

Furthermore, the solubility of the titanate films in aqueous 0.001M, 0.01M and 0.1M Tetramethylammonium hydroxide solutions and pure water of TiO_2 films was tested for a dipping time of 60 seconds.

In order to investigate the ion-exchange properties of such titanates, films previously stabilized at 100°C for 30 minutes were dipped in a 0,75 M of copper chloride or silver nitrate solution in methanol for 24 hours. These depositions were rinsed with water and analyzed with XRD before and after baking at 200 °C for one hour. Depositions prior to and after heating will be referred to as **Cu** and **Cu 200** for copper exchanged samples, **Ag** and **Ag 200** for silver exchanged films respectively.

Cu 200 and **Ag 200** were also analyzed through spectroscopic ellipsometry.

Composite films were realized by mixing the titanate colloidal solution with polyvinilpirrolidone previously dissolved in methanol. Composite films with 20%wt, 50%wt and 80%wt of titanates were realized and spun on quartz substrates.

Since the above-described treatments of the titanates lead to high refractive index films, we employed these processing conditions for Distributed Bragg Reflectors (DBR) fabrication.

DBRs are structures consisting of an alternating deposition sequence of two materials with different optical constants. The most common design is based on layers with thickness equal to one quarter of the wavelength for which the mirror is designed to have the maximum reflectivity. The maximum reflectivity and width of the reflection stopband (i.e. the wavelength range where reflectivity is high) increase with the refractive index difference of the employed materials.

Bragg gratings designed for highest reflectivity at 620 nm were realized on quartz substrates by spin coating titanate and silica films with a quarter wavelength thickness calculated through the following relationship :

$$t = \frac{\lambda}{4n}$$

where *t* if the film thickness, λ is the maximum reflectivity wavelength in vacuum and n is the refractive index value of the film.

Silica sol was obtained from standard sol-gel processing of Tetraethoxysilane following the method described in [28]. Spin coating conditions for obtainments of the target film thicknesses were optimized by ellipsometry measurements of the thickness prior to Bragg grating fabrication.

Two strategies were adopted for grating fabrication. The first, **grating 500**, consists in thermal treatment of each layer at 500 °C for 15 minutes, while the second, **grating UV**, involves a treatment at 200 °C for 5 minutes which followed a 5 minute UV irradiation (**5'UV+5'200**) in the case of the titanate layer.

5.2.2.2 Results and discussion

In the table 5.2, refractive indexes, interlayer distance estimated from XRD data and solubility behavior under all processing conditions employed in this work are reported.

Sample	Refractive index	Thickness contraction (%)	D (nm)	H_2O	0,001 M TMA	0,01 M TMA	0,1 M TMA
100	1.78	0	1.14	yes	-	-	-
32''	1.94	21	1.14	yes	-	-	-
75''	1.98	27	1.13	yes	-	-	-
2.5'	1.99	37	1.12	no	yes	-	-
5'	2.01	38	0.93	no	yes	-	-
7.5'	2,04	42	0.93	no	no	yes	-
10'	2,04	41	0.92	no	no	yes	-
12.5'	2,04	41	0.92	no	no	yes	-
15'	2,05	42	0.93	no	no	yes	-
200	1,91	24	1.14	yes	-	-	-
15'UV+200	2.28	57	0.92	no	no	no	no
300	2.17	46	1.00	no	no	no	no
15'UV+300	2.29	60	0.68	no	no	no	no
400	2.31	57	-	no	no	no	no
15'UV+400	2.34	60	-	no	no	no	no
500	2.32	59	-	no	no	no	no
5'UV+5'200	2.26	-	-	no	no	no	no
UV+500	2.34	59	-	no	no	no	no
Cu 200	2.22	56	0.71	-	-	-	-
Ag 200	2.17	44	-	-	-	-	-

Table 5.2 Refractive index at 630 nm, film's thickness contraction, interlayer distance calculated from Bragg relationship using diffraction peak position from XRD analysis ($\lambda=2dsin\theta$), and solubility in aqueous solutions with increasing *TMA* concentration for all employed titanate film modifications (yes=soluble, no=not soluble, -=not evaluate).

For thermally treated samples, the same structural evolution of TiO_2 powders is observed with increasing temperature. Figure 5.7A shows the XRD pattern of titanates films annealed at different temperatures.

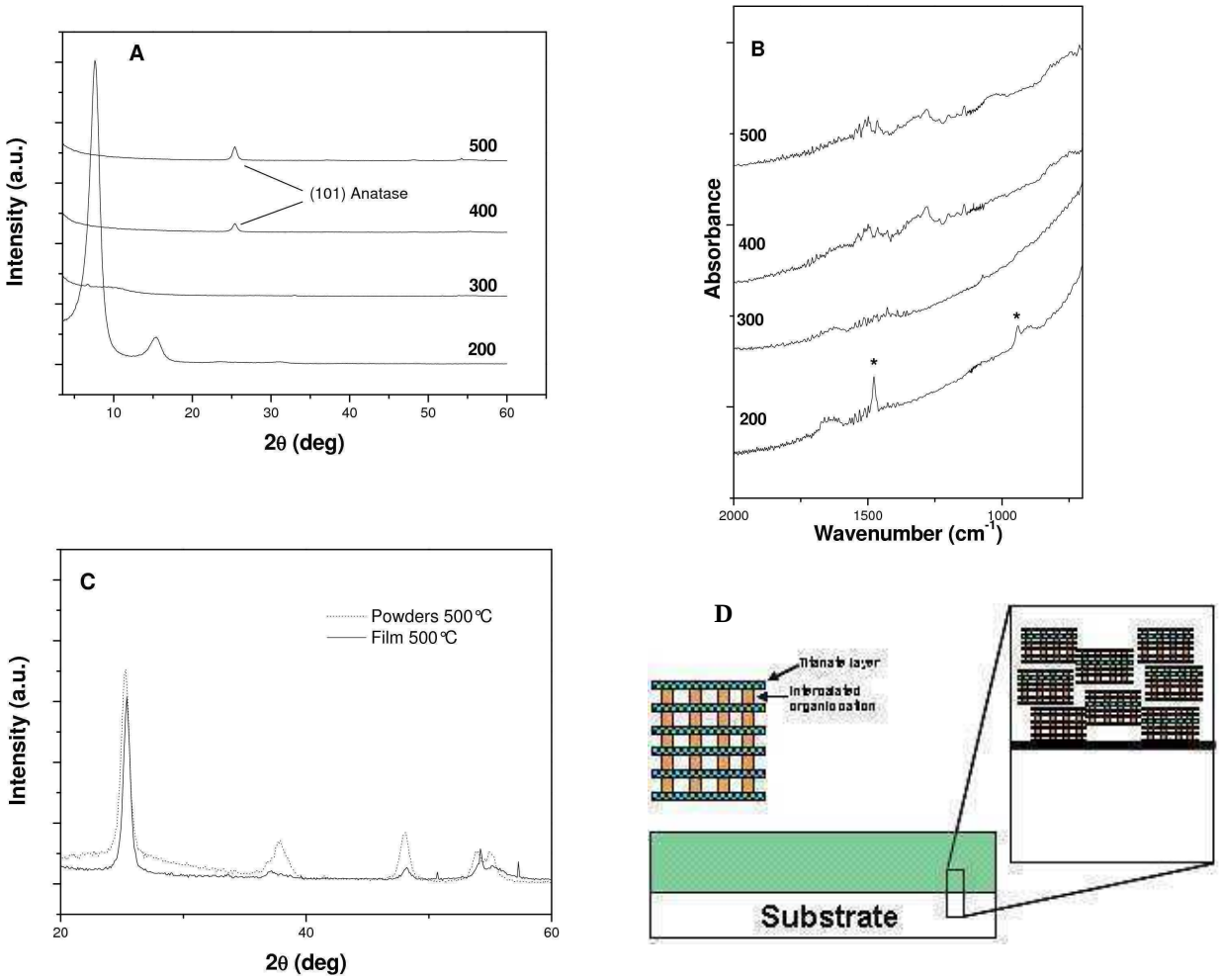

Figure 5.7 XRD pattern (A) and FT-IR spectra (B) for titanate depositions annealed at different temperatures. (C) XRD data for titanate film on silicon substrate and the same material in powder form heat treated at 500°C. (D) Schematic showing the suggested deposition structure

Peaks at 7.7 deg and 15.4 deg related to interlayer distances are observed in **200** while peaks at wider diffraction angles are not detectable, suggesting for an orientation of titanate sheets parallel to the substrate. From peak's linewidth, a mean dimension of 3.9 nm can be assigned to the domains at normal direction to layer's plane using Scherrer equation. The number of stacked layers is thus approximately equal to 3 or 4, less than values obtained for the same material in the powder condition (section 4.3.3). The peak width can also be related to the degree of structural order. Thus, for the same number of stacking layers, XRD peak relative to interlayer diffraction gets wider if, for example, interlayer distances

are spread over a range of values [33]. Thus, titanate layers in the deposition are stacked with a minor number or in a less ordered fashion.

If we assume that the starting titanates solution consists of titanate nanosheets with an high degree of exfoliation, we can argue that such nanosheets restack during the drying stage of the coating process. Thus, the fast evaporation experienced during spin coating do not allow for titanate stack with long range order. On the other hand, the restacking rate during the process used to obtained the powders is likely to be slower leading to a slightly higher number of stacked layers.

Even if we have no characterization of the state of titanate layers in the colloidal solution, the dependence of the stacked state on material processing point out a scenario where titanate layers exist in a highly exfoliated state [29].

When this solution is spun over the substrate, the liquid flow established during spinning can give an orientation to these layers, which restack again upon solvent evaporation to give the low-angle diffraction peaks observed in XRD spectra of thin films.

This orientation seems to influence the formation of anatase structure in **400** and **500** samples, resulting in a preferred orientation. In fact**,** the diffraction peak at 25.3° was much more intense with respect to other peaks if compared to the same material at the same treatment temperature analyzed in the randomly oriented powder state (Figure 5.7C).

Elimination of organic matter such as TMA^+ at elevated temperatures is evident from FT-IR shown in figure 5.7B. The decomposition of the organic cations also led to destabilization of the layered structure, which disappear at 300 °C.

Elimination of organic matter along with crystallization and densification leads to high refractive index values as high as 2.31 in the visible range (see table 5.2).

A qualitative appreciation of film densification can be gained looking to the film thickness contraction (final thickness/**100** sample thickness %) also reported in table5.2. This is seen to increase after thermal treatment at 200 °C caused by evaporation of residual solvent retained after the initial stabilization at 100 °C. Annealing at higher temperatures leads to increasing thickness contraction.

These data also suggest that an ordered structure such as that represented by titanate sheets favors better densification and crystallization of the material. This leads to higher refractive indexes and lower crystallization temperature if compared to titania films prepared from other conventional sol-gel routes or to the previously described TiO_2 NCs films, whose inherent porosity limits the refractive index value at around 2.2 after thermal treatment at 500°C.

Layered titanates have been investigated for their photocatalytic activity resulting in decomposition of organic matter. This capability has also been exploited to decompose intercalated organic material allowing for material densification, enhanced hardness and refractive index [30,31].

We studied these properties for the titanates here reported looking at their photocatalytic behavior by the stearic acid method as described in the experimental.

The disappearance from FT-IR spectra of the C-H bonds in the 2750-3000 cm^{-1} range of stearic acid deposited on **200**, **300**, **400**, **500** films was monitored every 60 seconds of UV irradiation time at room temperature. The results are shown in figure 5.8, where the areas under the C-H bands normalized to the their initial values are shown. It is apparent that **200**, **400** and **500** samples shows comparable photocatalytic behavior, while **300** sample shows a strong decrease of stearic acid degradation.

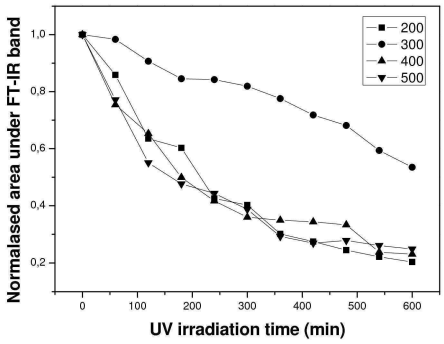

Figure 5.8 Evolution of normalized area under C-H vibration of stearic acid deposited on titanate films heat treated at different temperature versus UV irradiation time in a photocatalytic test

Layered titanates (sample **200**) shows photocatalytic activity similar to anatase samples, even if a suitable comparison should take into consideration also inherent surface area of the material. Loss of crystallinity and arising of structural defects are, most likely, to be responsible of the diminished catalytic behavior of the **300** sample.

The possibility of decomposing organic matter under UV irradiation has been exploited for titanate film modification [31], since elimination of the intercalated tetramethyl ammonium caion is possible.

The effect of combined thermal and UV treatment has been thoroughly studied on the material described in this thesis.

Refractive index and XRD evolution has been first followed with increasing UV irradiation time (see table 5.2 and figure 5.9A). Broadening of the main diffraction peak is observed

after 75'' irradiation time along with a continuous shift toward higher diffraction angles which corresponds to diminishing interlayer distances (reported in Table 5.2). This behavior is kept till 5 minutes of irradiation time and a constant value of interlayer distance is then reached. The shift of XRD peaks is correlated with the disappearance of *TMA* from the FT-IR spectra shown in figure 5.9B.

From a structural point of view, UV irradiation results in loss of coherency or order of the layer stacking sequence due to decomposition of the organic cation which is necessary for the stabilization of the layered structure. This can be inferred by XRD peak broadening, as simulated for similar systems by Sasaki et al. [33]. The decomposition of intercalated compounds obviously results also in a decreased interlayer distance to an almost constant value of 0.92-0.94 nm, similar to that reported for analogue UV irradiated layered titanates in ref. [30,31].

It is likely that small cations fragments like NH_4^+ and $H^+(H_3O^+)$ ions are left after the decomposition process as as they keep charge neutrality [31].

The UV treated film is not readily soluble in water (see Table 5.2), while it can be exfoliated and colloidaly dispersed in aqueous solution containing TMA. This is a behavior ha been found also for a protonic titanate [31] which have a denser and more stable structure than TMA intercalated compounds.

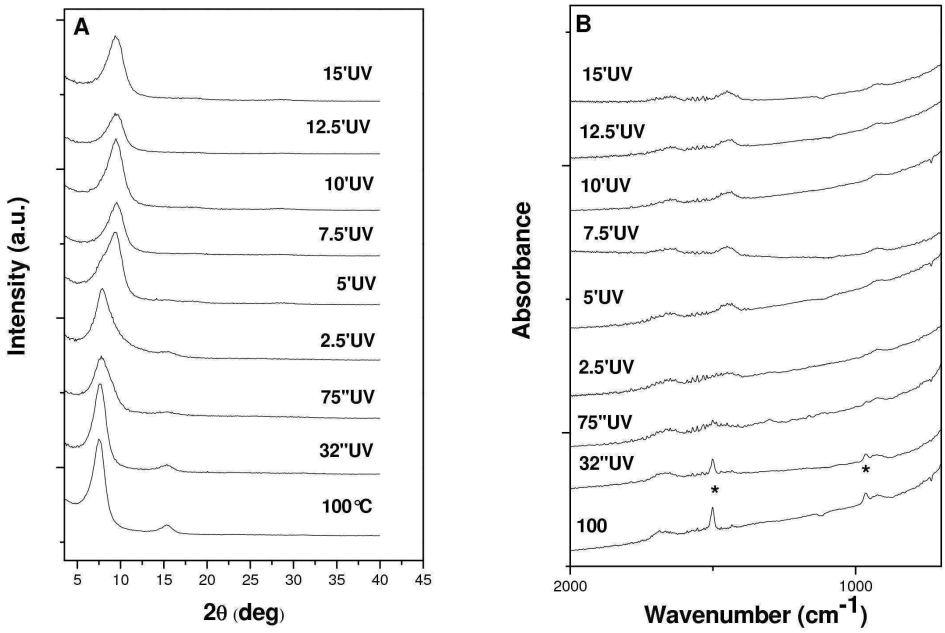

Figure 5.9 XRD (A) and FT-IR (B) spectra for titanate films on silicon substrate UV-treated for different irradiation time. IR peaks labeled with * are assigned to TMA vibration.

Refractive index values show a quite steep increase up to 7.5 minute irradiation time at which a constant value is reached (see table 5.2). Refractive index is slightly enhanced

with respect to pristine layered titanate films heat treated at 200 °C because of the higher degree of densification as evidenced from contraction of interlayer distance.

The structure assumed after UV treatment is not the stable one, since we realized that if subsequent thermal treatment is applied, a further interlayer contraction is obtained, reaching an interlayer spacing of almost 0.7 nm which approaches that of dried FeOOH lepidocrocite structure (0.66 nm) without any interlayer guests [32]. This suggests an almost complete contraction of the layers likely due to removal of the H_3O^+ or other small molecules present as interlayer hosts produced by the previous UV treatment.

Very interestingly, these films could not be dissolved in highly concentrated TMA aqueous solutions analogously to those synthesized at higher temperatures, further confirming the obtainment of a different and more compact structure.

It has to be noticed that after thermal annealing, only broad peaks are seen indicating almost complete disappearance of order in the stacking sequence. Thus, at this point the most probable situation consists of incoherently closely packed titanate layers with a preferential orientation parallel to the substrate.

XRD pattern of samples irradiated 15 minutes before heat treatment are shown in figure 5.10, in comparison with the patterns of thermally treated and UV treated samples. In the same figure a scheme of the possible layer titanate film evolution is presented.

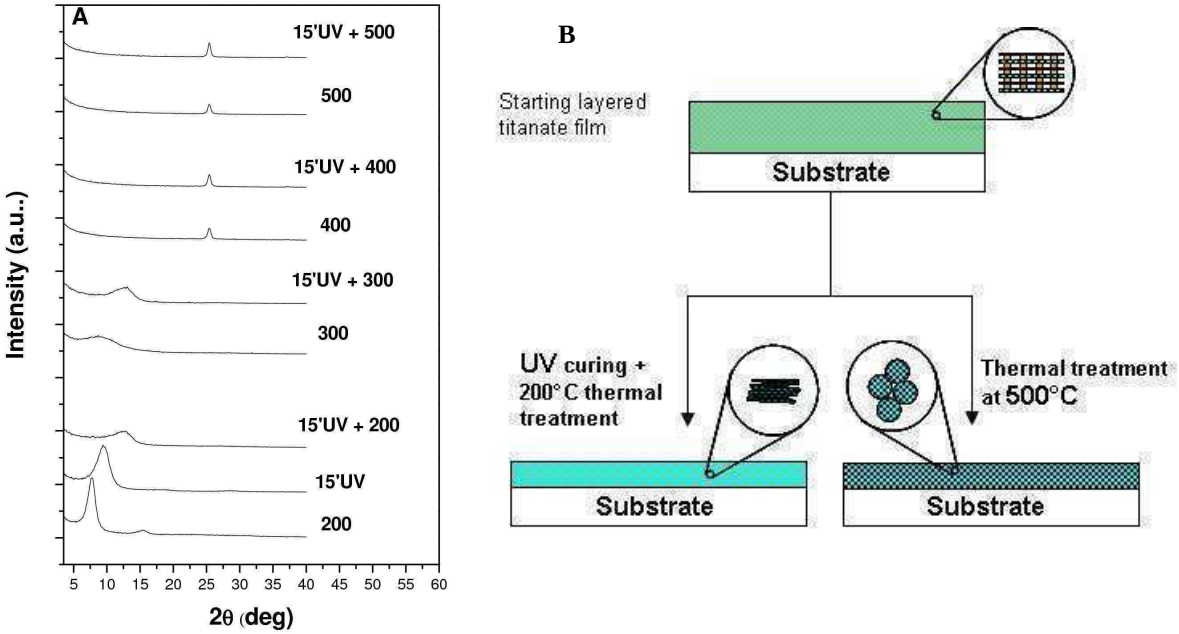

Figure 5.10 XRD patterns of titanate films after combined thermal and UV treatment.(A); Schematic representation of suggested structural modification obtained after UV and thermal treatment. (B)

Refractive index values largely increase with such thermal treatment after UV irradiation, reaching values as high as 2.28 at 200°C, very similar to values obtained with heat-treatments at much higher temperatures.

If the samples are UV irradiated before thermal treatment, much higher refractive index values can be obtained with respect to only thermally treated samples. This effect is evident in the case of samples treated at 200 °C and 300 °C, where previous elimination through UV light of TMA cations allows for enhanced contraction of the layers leading to higher densification and refractive index. This is evident also from thickness contraction which is much higher in the case of samples treated with UV irradiation (see table 5.2).

At 400 °C and 500 °C the structure is determined by the crystallization of a new phase, i.e. anatase. Thus, in this case UV treatment seems to have much less effect on refractive index.

Since we were interested in producing high refractive index depositions, we further investigated these procedures in order to find the minimum UV exposure and heat treatment time to achieve high refractive index values.

Thus, one hour of heating time at 200 °C was applied to **2.5'UV**, **5'UV**, **10'UV** and **15'UV** samples. XRD data and refractive index values are shown in figure 5.11. It is evident that almost 5 minutes of UV irradiation are needed to get almost the ultimate refractive index value, while slightly longer time is necessary to achieve the final structure which still retains pristine interlayer distances. This is most likely due to non uniform irradiation over the whole thickness of the film. Higher irradiation time is needed to get uniform structure.

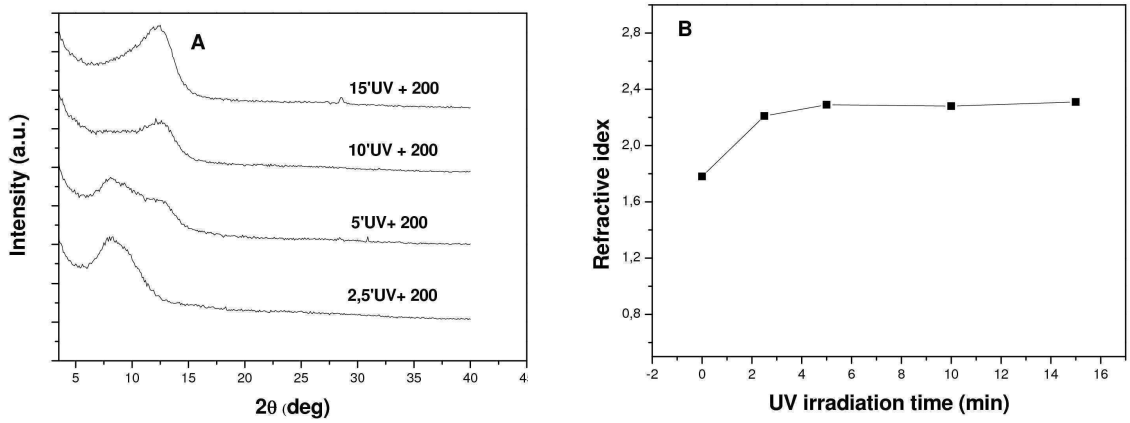

Figure 5.11 XRD patterns (A) and refractive index at 630 nm (B) of titanate films treated under different UV radiation times and subsequently annealed at 200°C for one hour.

Analogously, for **15'UV** depositions, it has been verified that a post-thermal treatment of five minutes at 200°C is sufficient to obtain complete shrinkage of interlayer distances and the highest refractive index, as shown in the figure 5.12.

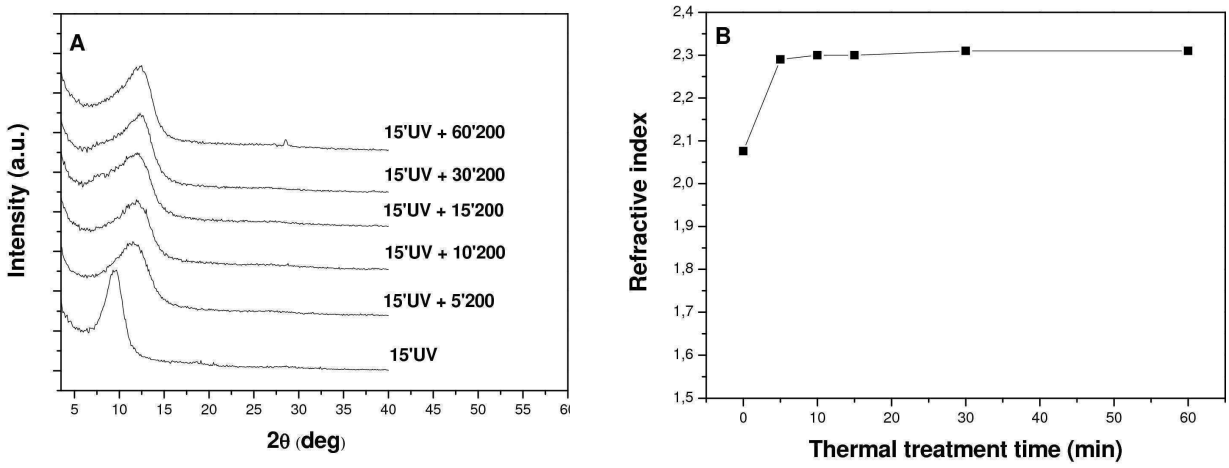

Figure 5.12 XRD patterns (A) and refractive index at 630 nm (B) of titanate films treated under UV radiation for 15 minutes time and subsequently annealed at 200°C for different times.

In conclusion, a treatment consisting of five minutes UV irradiation time followed by five minutes at 200°C (**5'UV+5'200** sample) was verified to be sufficient to obtain a material with a refractive index as high as 2.26 (see table 5.2), almost equal to the **15'UV+200** sample, even if complete titanate layer contraction is not achieved.

Ion exchange with copper and silver ions has also been used to induce modifications of titanate thin films. XRD data for ion exchanged films are shown in figure 5.13, with corresponding FT-IR spectra.. These data refers to as-exchanged (**Cu** and **Ag**) and further thermally treated samples (**Cu200** and **Ag200**).

In the case of copper exchanged films, the diffraction peak of **Cu** deposition is consistently shifted with respect to **200** sample (also reported as reference in the figure). This suggests the exchange between bulky TMA ions and Cu ions resulting in interlayer distance contraction, even if compositional analyses should be performed to confirm this hypothesis. In ref [34], ammonium cations were successfully exchanged with Ni ions, while other cations (Cs^+, K^+) were found not to maintain the layered structure. Furthermore the Ni exchanged material was stable untill very high temperatures.

In our case, thermal annealing results in further contraction and consistent loss of order as deduced from line broadening, revealing the instability of this structure.

Silver doesn't allow for layered structure stability even before heat treatment. Such films do not show any diffraction peak at low angles. These films looked colored, due to silver reduction and metallic particles formation responsible for the surface plasmon absorption in the visible.

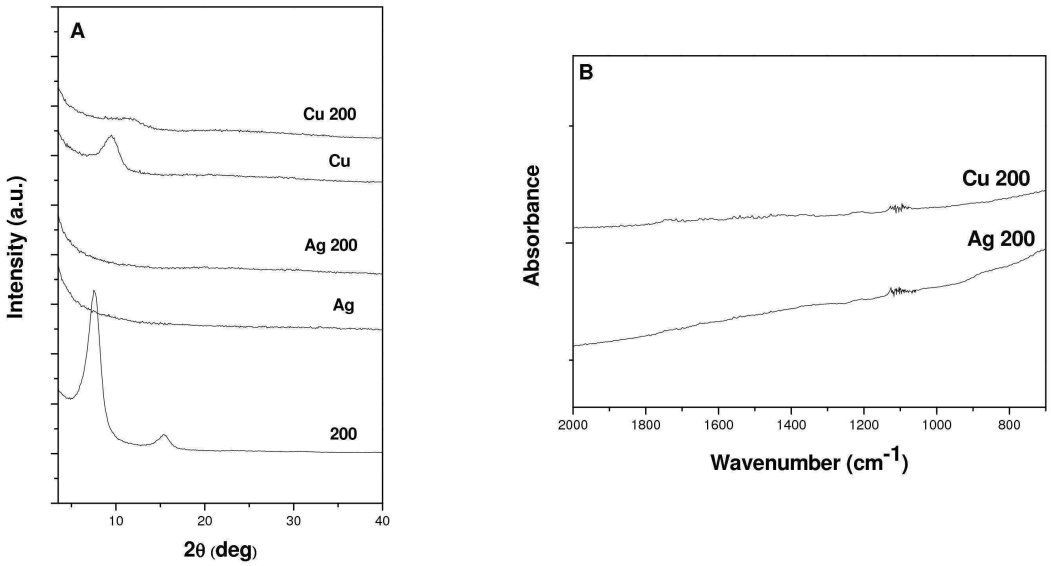

Figure 5.13 XRD pattern (A) and FT-IR spectra (B) of ion exchanged samples. XRD data for a sample only annealed at 200°C is reported for comparison

Refractive index is largely enhanced in both cases, even if transparency in the visible is lost in silver containing depositions.

Cu 200 deposition was transparent and the refractive index in the visible range was 2.22. This suggests for another low temperature alternative for high refractive index obtainment.

Refractive index and extinction coefficient curves are reported in figure 5.14 for selected samples described in this section.

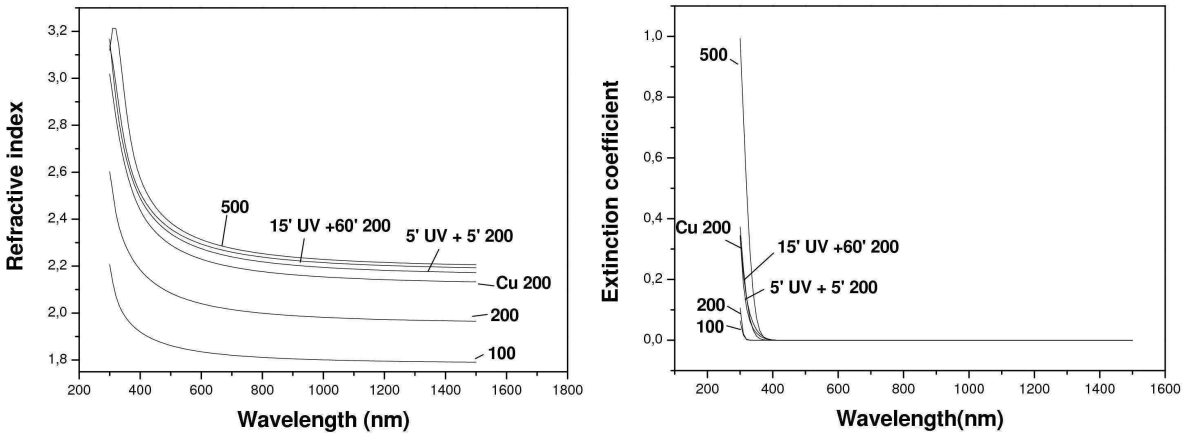

Figure 5.14 Refractive index (A) and extinction coefficient curves (B) of samples processed under selected treatments.

It can be seen that procedures employing UV light allow to achieve refractive index values approaching those of **500** samples, and treatment of **5'UV+5'200** samples give almost the same optical properties than **15'UV+60'200** samples**.** Also **Cu 200** sample shows refractive index enhancement and very good transparency, suggesting.

Extinction coefficients increase in the UV range with thermal annealing, UV and ion-exchange densifying treatments. In this case, the effect can be both related to the film densification and the variation of crystal structure. In fact, depositions still possessing a lamellar structure have higher band gap energy (see section 4.3.3) than those with the anatase structure as for materials annealed at 500 °C. Thus the absorption behavior cannot be completely attributed to structural or morphological evolution, but also to variation of material's electronic structure.

Finally, SEM morphological characterization of **200**, **15'UV + 200**, **Cu 200**, **Ag 200** samples are reported in the micrographs of figure 5.15 .Silver particles are clearly seen in the **Ag 200** sample, while quite homogeneous depositions are obtained in the other samples.

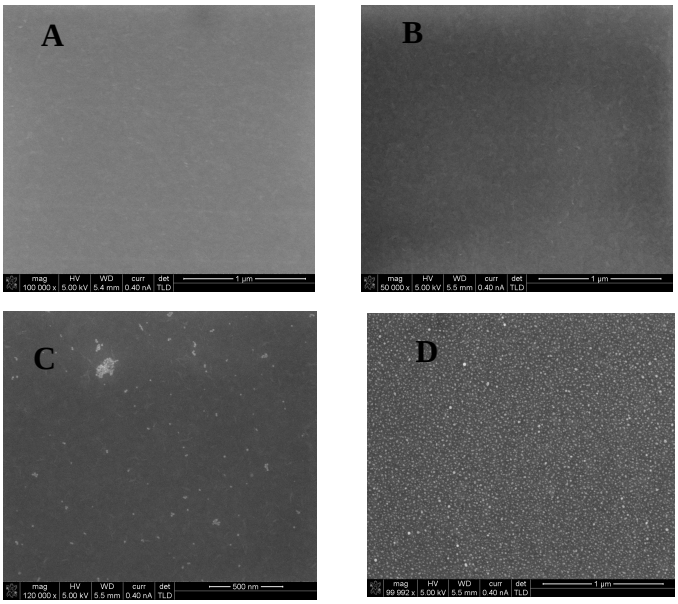

Figure 5.15 FEG-SEM micrographs for **200** (A), **15UV + 200** (B), **Cu 200** (C) and **Ag 200** (D) samples

Particles seen in **Cu 200** sample are likely due to residual copper chloride salt after water rinsing of the sample after the dipping stage

5.2.2.3 Layered Titanates applications

In this section, some applications of *TMA-Ti* layered titanate will be described.
In particular, titanate nanocomposite films depositions using polivinypirrolidone (PVP) as matrix and Distributed Bragg Reflectors (DBR) are described.
Nanocomposite films were prepared by simply mixing a colloidal solution of titanate with PVP previously dissolved in methanol.
Different weight percentages of titanate in PVP have been realized by changing the relative amount of these solutions. Transparent materials have been obtained with 20%wt, 50%wt and 80%, with a refractive index of 1.57, 1.79, 1.89 respectively. This allows for a convenient and straightforward method for obtaining tunable refractive index materials. XRD of such composites (figure 5.16) shows similar features as those reported for **200** film, with peak intensity accordingly decreasing with increasing amount of PVP.

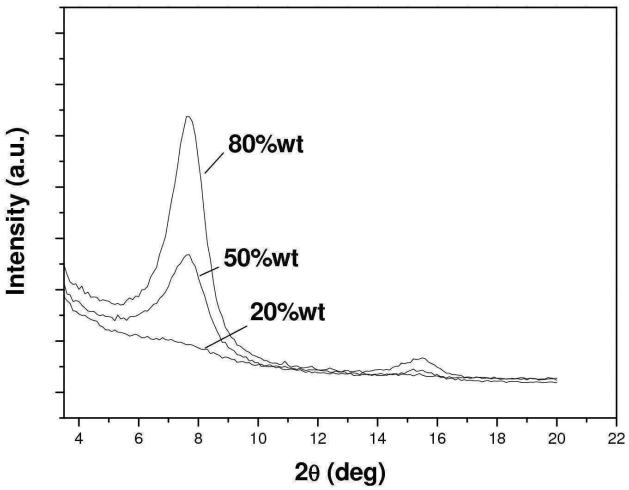

Figure 5.16 XRD patterns of PVP-Titanate composite film with different inorganic content

The employment of such materials in multilayer fabrication, such as Bragg gratings, is particularly convenient because high refractive indexes can be achieved at very low temperature. The main problem encountered in these structures deals with thermal stresses arising during temperature cycling between annealing and ambient temperatures. This in turn causes severe cracking and limitation in number of layers that can be deposited without defects formation, unless annealing schedule is found [35].
It has been shown that an annealing temperature of 500 °C is sufficient for satisfactory titanates treatment, leading to crystallization of the anatase.phase. DBRs without cracks

have been obtained by heat treating both silica and titanate layer at 500 °C . This will be referred to as **grating 500**.

Analogues DBRs were conveniently fabricated applying five minutes of UV irradiation followed by five minutes of annealing at 200 °C as described in the experimental for the **grating UV** procedure.

Both these procedures allowed for multilayer deposition up to ten silica/titanate doublets without appearance of cracking.

Refractive index of silica layer was measured to be 1.44 for both type of annealing processes, while refractive index of titanate layers have already been discussed and are reported in table 5.2. From these refractive index values the thicknesses of the SiO_2 and TiO_2 layers are calculated as explained in the experimental section for a designed maximum reflectivity value at 620 nm wavelength. The obtained thickness values are about 108 nm for the SiO_2 layer, 67 nm for titanate layer in **grating 500** and 69 nm in **grating UV**.

In figure 5.17 transmission spectra of gratings composed of six and ten silica/titanate doublets are shown for both treatments. Transmittance is lowered in a specific wavelength range (the stopband region) since reflectivity is enhanced near the wavelength for which the mirror is designed.

Since thermal treatments at 500 °C lead to higher refractive index values, transmittance inside the stopband (i.e. high reflectivity wavelength region) is lower with respect to Bragg gratings with the same number of layers obtained with the UV treatment. In fact, higher differences in refractive indexes between the materials employed for grating fabrication lead to more efficient mirrors with higher reflectivity and wider stopband.

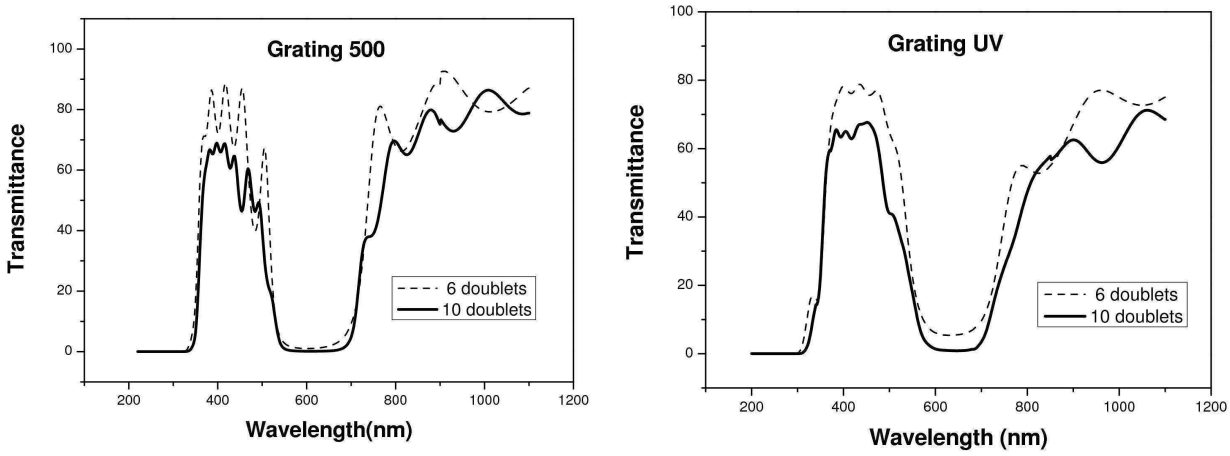

Figure 5.17 Transmission spectra for **grating 500** and **grating UV**

Reflectance spectra measured on the ellipsometry instrument for different incident angles are shown in figure 5.18 for **grating 500** and **grating UV** for 6 high/low index layer doublets.

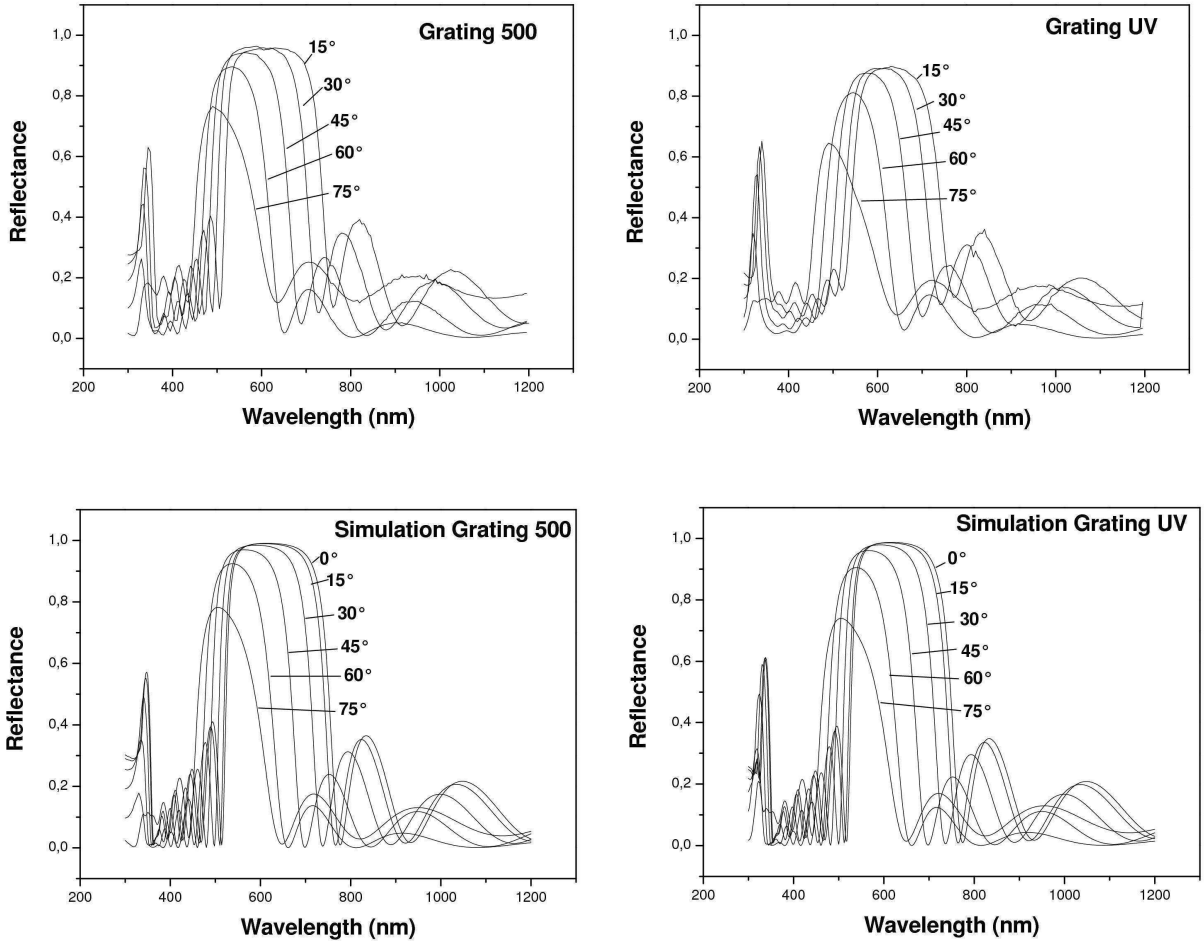

Figure 5.18 Measured reflectance spectra for **Grating 500** and **Grating UV** at different angles and ellipsometer software simulations of the same structure (0° reflection spectra is also reported in this case)

Due to physical limitation of the instrument, it was not possible to measure the reflectance at normal incidence. Reflection at 15° can nonetheless be taken as a good estimation of normal reflectivity, since this does not vary significantly in a small angle range around perpendicular direction. Simulations carried out with the software of the ellipsometry instrument (V-Wase32, J.A. Woolam Co., Inc.) using the measured optical constant values of titanate and silica film (for the same treatment conditions of grating fabrication) are also shown in figure 5.18.

Reflectivity values of 0.95 and 0.9 at 620 nm were measured for **grating 500** and **grating UV** consisting of 6 high/low index doublets respectively. The simulated value for 15° reflection at 620 nm are 0.99 and 0,98 for **grating 500** and **grating UV** respectively.
Measured values are lower than simulated ones. This is likely due partly to surface quality of the deposition, that must be improved in order to increase specular reflection, and partly to differences between target and obtained film thicknesses. The latter problem is enhanced in **grating UV** fabrication since several steps are included in the process (deposition, UV irradiation and thermal treatment), each of them can introduce experimental errors. In this case, experimental setup has to be improved to gain better reproducibility.
The possibility of creating inorganic gratings at low temperature is particularly useful not only for defects minimization but also for optically active devices that involve materials that cannot sustain high temperature treatment. Utilization of these gratings for optical micro-cavity fabrication incorporating quantum dots is described in Chapter 6.

In conclusion, the change in solubility behavior induced by UV irradiation (see table 5.2) motivated some attempts in the UV patterning of *TMA-Ti* depositions.
These experiments were performed by irradiating some depositions through a mask with a 20 μm pitch and further thermal annealing at 200°C. Even if an optical contrast could be detected under optical microscope observation after this treatment, subsequent dipping in water or *TMA* aqueous solutions in order to remove the non-irradiated part did not result in a well developed morphological pattern.
Since the patterning of titanate can result in high refractive index material surface structure or in crystalline titania by subsequent thermal treatment, with enormous interest for photonic applications, we believe that further research by improving setup conditions and changing the type of intercalated organic cations should be carried on.
Analogue Electron Beam Lithography (EBL) patterning was applied without results.

5.3 Multifunctional material for optical waveguides and conformal coatings for LED encapsulation

Materials satisfying different requirements at the same time are of interest in many technological fields.

In this section, the use of a multifunctional material is described and exploited for planar waveguides and conformal coating fabrication. Such coatings have been applied to LED devices not only to impart proper packaging and protection but also novel functionalities. In particular, high refractive index, incorporation of optically active materials and proper attitude towards processing conditions have been considered in the synthesis of a novel material.

The approach to introduce in the same material all the above-mentioned features is described in the following.

First, we made use of the *AH-Ti* titanates described in section 4.3.1 as the high refractive index component. This material could be processed in alcohol media and resulted to be compatible with quantum dots, which were used as the optically active component. The resulting *multifilled*-composite (defined in this way since it incorporates different nano-sized inclusions) was used for film deposition and luminescent optical waveguides.

The use of this material to create coatings for LED devices is then described in section 5.3.2. This application has been further developed with the employment of a hybrid sol-gel matrix giving better results.

5.3.1 Multifunctional material from 6-amino-1-hexanhol derived titanates (AH-Ti)

5.3.1.1 Synthesis

In the following, the synthesis of nanocomposite depositions using alcohol soluble titanates (*AH-Ti*) embedded in polymer and hybrid sol-gel material is described

Two materials were chosen as host for titanate nanosheets. The first is polyvinylpirroldone (**PVP**, 10000 average molecular weight), a polymer which was found to be highly compatible with titanates colloids. The polymer was dissolved in ethanol obtaining a solution with a concentration of 100 mg/ml which was used for composite fabrication. The second matrix is a material derived from the functionalization of polyethylene glycol (**PEG** 1000 molecular weight) with an equimolar amount of 3-isocyanatopropyl-

trimethoxysilane, here referred to as **PEG-SiO_2** . This is obtained through reaction between the hydroxyl group of **PEG** with isocyanate group of the silane molecule, as described in [36]. **PEG** is first melt at 60°C under vacuum and then mixed with 3-isocyanatopropyltrimethoxysilane. The reaction is carried out at 80 °C for four hours. This material is then diluted with ethanol obtaining a solution with a concentration of 100 mg/ml.

In a typical composite fabrication, 2.5 ml of *AH-Ti* as-synthesized solution were processed as described in section 4.3.2 to obtain about 0.4 ml of TiO_2 solution in methanol.

100 µl, 200 µl, and 400 µl of **PVP** or **PEG-SiO_2** solution were added to the titanates nanosheets solution corresponding to theoretical concentrations of 79%wt, 65%wt and 48%wt of titanates respectively. These sols will be respectively labeled as **PVP1**, **PVP2** or **PVP3** when **PVP** is used as matrix, and **PEG1**, **PEG2** and **PEG3** if **PEG-SiO_2** is used. Finally all the solutions were diluted to 1 ml with ethanol and spun at 3000 rpm for 20 seconds. These films were annealed at 100 °C, 200 °C and 300 °C for one hour in air.

Titanate films were also obtained by spinning the *AH-Ti* colloidal solution with the same processing parameters and will referred as **Ti**. Spectroscopic ellipsometry and FT-IR analyses were carried out on films deposited on quartz and silicon substrate, respectively.

Quantum dots emitting at 610 nm were used for doping **Ti** and **PEG2** depositions. These particles were of the Core@Shell type with the **CSSS** shell structure synthesized as described in section 3.4.2.

Loading of QD's was performed by mixing 100 µl of the matrix solution (**Ti** or **PEG2**) with 300 µl of a colloidal solution of 6-amino-1-hexanol functionalized CdSe@ZnS in ethanol, obtained as described in section 6.3.1. The absorbance at first exciton peak of the 10-fold diluted QDs solution used for doping was 0.5. An exact estimation of the QDs concentration is not possible since the extinction coefficient for these particle is not known. However, if the extinction coefficient of CdSe cores with the same first absorption peak position is assumed, a concentration of $1.7x10^{-5}$ mol/L can be estimated.

PVP based materials were not doped with QDs since m-line measurements results were not satisfactory, as will be described in the next section.

Four layers were realized by spinning the resulting solutions at 3000 rpm on quartz substrates and annealing each layer at 250 °C for five minutes in air.

QD-doped and undoped **Ti** and **PEG2** depositions were tested with m-line technique to analyse waveguiding properties.

Nanoimprinting lithography was applied to the **PEG2** material doped with QDs using a PDMS mould with 4 μm pitch and 110 nm features depth, which was applied to a film spun at 1000 rpm for 5 seconds immediately after deposition. The whole assembly was treated in an oven at 100°C for 30 minutes. After that, the mould was removed and the structure was further treated at 150°C for 30 minutes.

5.3.1.2 Results and discussion

The reason for employing **PVP** or **PEG-SiO_2** as matrices is due to their good compatibility with the obtained *AH-Ti* material and to the plasticity of the final composite material necessary for the processing of defect-free structures.

The use of **PVP** to improve processing of TiO_2 based material has already been reported [37]. **PEG-SiO_2** has been adopted with the aim of taking advantage of the possible interactions between silica alkoxides and titanate resulting in functionalization with PEG molecules, contributing to suppress interactions between titanates nanosheets.

FT-IR spectra of a **PEG-SiO_2** film (normalized to the CH band) showing the silane coupling between hydroxyl group of PEG and the isocyanate group of the organosilane forming the urethane group is shown in figure 5.19A. The resulting target molecule is depicted in figure 5.19B.

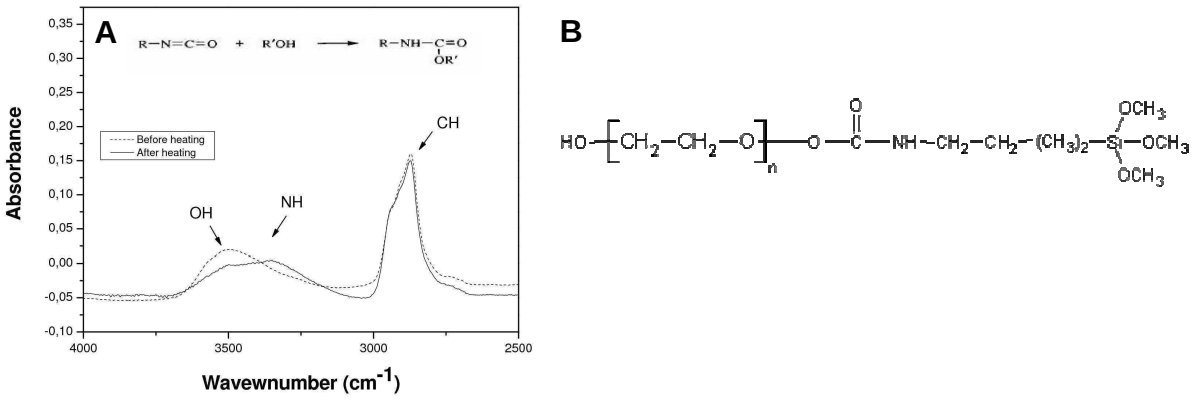

Figure 5.19 FT-IR of a **PEG-SiO_2** film on silicon substrate before and after heating the PEG and organo-silane mixture (A). Scheme of the target final silane functionalized polyethylene glycole (B)

The OH band intensity diminishes while a band assignable to NH vibration belonging to the urethane group appears after the reaction.

Figure 5.20 shows the FT-IR spectra of pure **Ti** and **PEG-SiO_2** and **PVP** composite films annealed up to 300 °C.

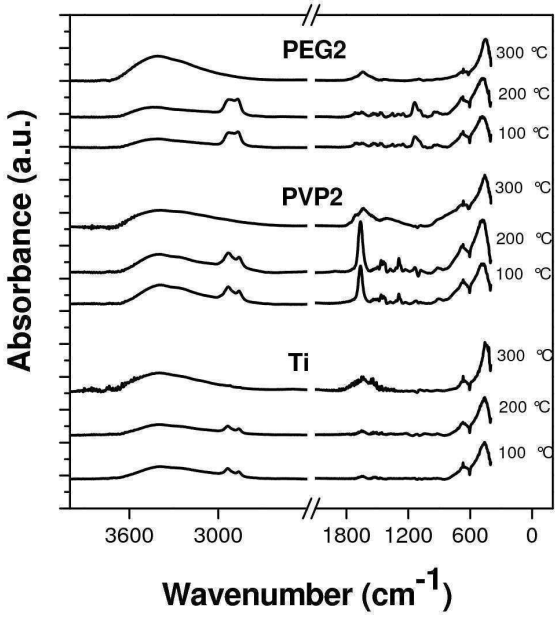

Figure 5.20 FT-IR spectra of **PEG2**, **PVP2** and Ti samples at different treating temperatures

The FT-IR spectra of all films shows a broad absorption in the low wavenumber region which can be related to Ti-O bond vibrations. The presence of ethylene glycol molecules (C-O-C vibration in the 105-1150 cm^{-1} region [51]) are not seen in **Ti** films, probably due to the low content and thickness of the analyzed film. Instead it was detected in the titanate powder (see section 4.2.2).

In **PEG2** sample bands in the 1050-1150 cm^{-1} region can be assigned to PEG molecule of the matrix [51]. Bands belonging to titanium glycolate complex are not clearly identified in our spectra. This can be due to the small absorbance of these bands in this films, even if complexation of some titanium site by ethylene glycol molecules cannot be excluded since this complex is known to be stable toward hydrolysis. The presence of ethylene glycol chelating titanium would be desirable to have stable materials with limited interactions between titanate sheets in order to reduce stiffness and improve stress-relief properties of the composite material during solvent evaporation involved in films or bulks fabrication.

Analyzing the evolution of the FT-IR spectra of the heat-treated films (figure 5.20), it can be concluded that the films are stable up to 200 °C. In fact, at 300 °C the peaks in the 2850-3000 cm^{-1} region (C-H vibrations), at 1050-1150 cm^{-1} (C-O-C bond of PEG [51]), at

around 1660 cm^{-1} (C=0 bond of PVP [52]) disappear due to thermal decomposition. Contributions of hydroxyl vibrations at 3000-3600 cm^{-1} are always present.

The stability of titanate component was tested by TGA/DTA analysis as reported in Chapter 4, and it was found to be stable for temperatures below 300 °C.

Bands assignable to Si-O-Ti bond (at 940 cm^{-1} [49]) could not be detected in the FT-IR spectra of **PEG** nanocomposite films. This can be due either to difficulty in observing these bands due to low absorption or too little (or not at all) reaction of the titanates with the siloxane network. The latter may result from the stability of the titanium sites or from unfavorable conditions employed in our procedure to promote silane coupling.

Ti deposition on silicon treated at 200°C was analyzed by XRD. The diffraction data are reported in figure 5.21 and shows the presence of a broad and weak peak in the low angle region supporting the presence of a layered structure also in the deposition.

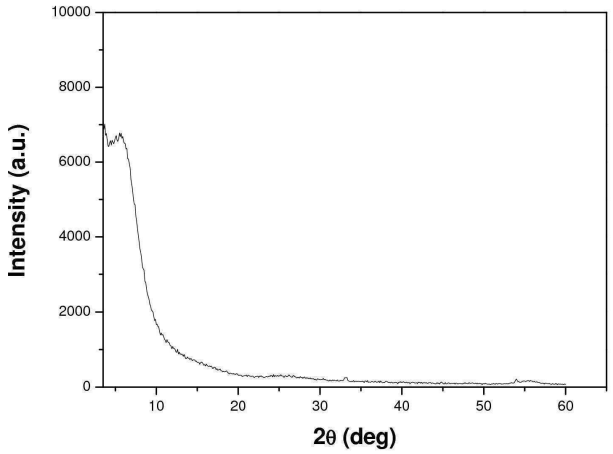

Figure 5.21 XRD diffraction pattern of *AH-Ti* titanates deposited on a silicon substrate and annealed at 200°C

The layered nature of this material can affect the structure of the deposition since titanate nanosheets can assume a preferential orientation parallel to the substrate when deposited by spin coating or dip coating, as already observed in previous works [34]. This is supported by the diffraction pattern shown in figure 5.21, since no peaks at wider diffraction angle are detected.

In table 5.3 the refractive indexes evaluated by spectroscopic ellipsometry for pure **Ti** and composite films are reported for different compositions and annealing temperatures.

T (°C)	Ti	PEG1	PEG2	PEG3	PVP1	PVP2	PVP3	Ti + QD	PEG2 + QD
100	1,81	1,76	1,69	1,61	1,74	1,7	1,64	-	-
200	1,83	1,81	1,74	1,65	1,76	1,74	1,64	1.81	1.72
300	1,83	1,81	1,74	1,65	1,80	1,75	1,68	-	-

Table 5.3 Refractive index at 630 nm for **Ti** and nanocomposite samples at different temperatures

The refractive index increases with titanate content in the nanocomposite films achieving the maximum value of 1.83 for pure **Ti** film. This value is much lower than crystalline TiO_2 (n = 2.493-2.554 for anatase and n = 2.616-2.903 for rutile [26]) due to the presence of organic moieties such as 6-ammino-1-hexanol and ethylene glycol. In fact, the amount of organic matter has been measured to be roughly 32%wt from thermogravimetric analysis of the powders.

Films without cracks with thicknesses up to few microns were obtained with **PEG2** composition by spin casting and annealing at 200 °C, showing the effectiveness of this synthetic approach.

Ti, **PEG2** and **PVP2** films annealed at 200 °C with thicknesses (estimated from spectroscopic ellipsometry measurements) of 170, 240 and 260 nm respectively were characterized also with M-line technique in order to test the optical waveguiding behaviour. The small size of the employed nanostructured titanates is particularly useful for this application, since optical losses related to scattering should be minimized. These measurements are shown in figure 5.22 for TE polarization mode, where an optical mode is clearly seen for 543.5 nm, 632.6 nm and 1319 nm. **PVP2** shows the broader features in the M-line measurements, suggesting stronger optical losses or higher surface roughness probably caused by an initial degradation of the matrix. It is likely that 200 °C is a too high temperature for this material. Measurements under TM polarization mode are analogue at 543.5 nm and 632.6 nm, while no optical mode could be detected at 1319 nm.

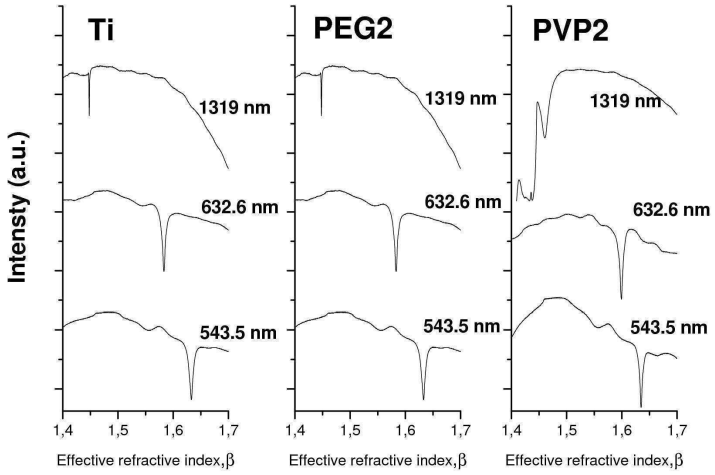

Figure 5.22 M-line measurements in TE polarisation mode of **Ti**, **PEG2** and **PVP2** samples at different wavelengths

QD-doped waveguides were realised introducing CdSe@ZnS QDs in pure **Ti** and **PEG2** material. Since 6-amino-1-hexanol has been used as ligand for both titanates solutions and QDs, the solution comprising both components resulted to be very stable and could be used to obtain optically transparent materials without aggregates formations.

In figure 5.23, m-line results for TE polarization are reported for QD doped **Ti** and **PEG2** with a thickness of 188 nm and 240 nm respectively (estimated from spectroscopic ellipsometry measurements). They show the presence of a waveguiding mode, even if they are less evident than undoped samples.

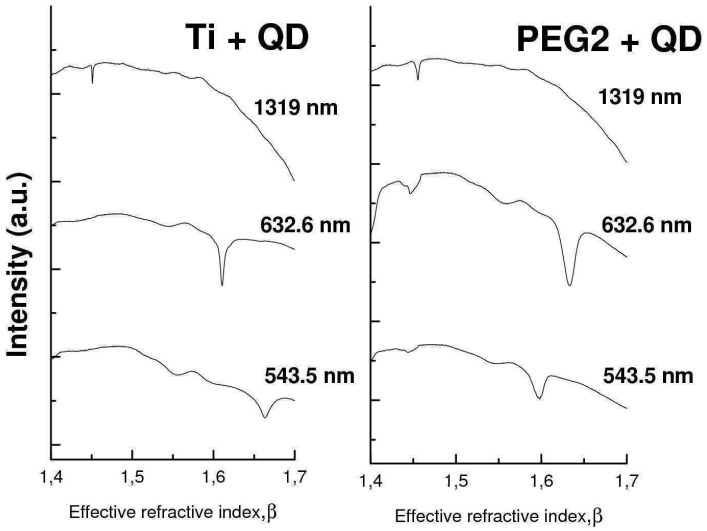

Figure 5.23 M-line measurements in TE polarisation mode of QD loaded **Ti** and **PEG2** samples at different wavelengths

Refractive index and extinction coefficient curves measured with spectroscopic ellipsometry are reported in figure 5.24. QDs introduction leaves the refractive index almost unchanged with a refractive index value of 1.81 and 1.72 (at 630 nm) for QD loaded **Ti** and **PEG2** matrix respectively, while extinction coefficient is consistently raised below quantum dots absorption edge wavelength around 600 nm and steeply increases at about 330 nm due to titanate onset absorption. Exciton peak of quantum dots is not seen in the extinction coefficient curves due to low nanoparticles concentration.

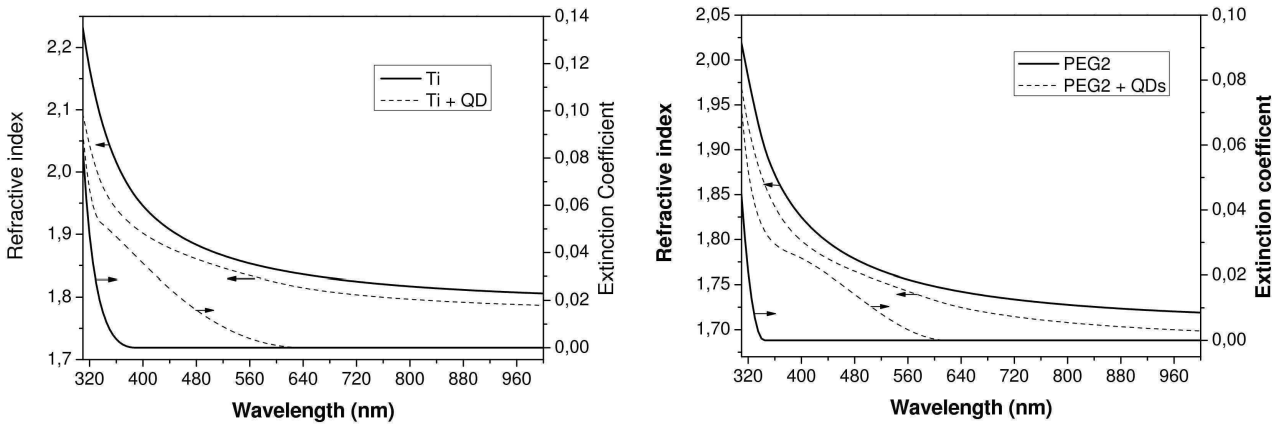

Figure 5.24 Refractive index and extinction coefficient curves for QD doped and undoped **Ti** and **PEG2** samples

	Ti	**Ti + QD**	**PEG2**	**PEG2 + QD**	**PVP2**
Film thickness (nm)	170	188	240	275	260
n at 543.5 nm, TE	1.845	1.855	1.738	1.748	1.759
n at 543.5 nm, TM	1.773	1.809	1.695	1.709	1.729
n at 632.6 nm, TE	1.825	1.832	1.731	1.735	1.746
n at 632.6 nm, TM	1.752	1.792	1.684	1.697	1.719
n at 1319 nm, TE	1.783	1.773	1.694	1.677	1.709

Table 5.4 Refractive index estimated by M-line measurements in TE and TM polarization mode. Film thicknesses reported in the table are estimated by spectroscopic ellipsometry measurements and used in the calculation of refractive index by modal propagation measurements.

In table 5.4 the refractive indexes estimated from m-line measurements assuming the thicknesses found from the spectroscopic ellipsometry measurements are reported for different wavelengths and polarizations. It can be seen that they are in good agreement with the values measured by spectroscopic ellipsometry for TE polarization. In TM polarization, refractive indexes are significantly lower. This can be related to an anisotropic structure of the depositions caused by the orientation of titanate sheets parallel

to the substrate, as previously suggested. This can result in birefringence of the deposition explaining the observed different optical constants observed under different polarization mode.

The UV-Vis absorption and photoluminescence spectra of QDs in solution are shown in figure 5.25. The PL peak position is 610 nm with a FWHM of 27 nm. The PL quantum yield of these NPs measured with respect with an organic standard was found to be approximately 23%.

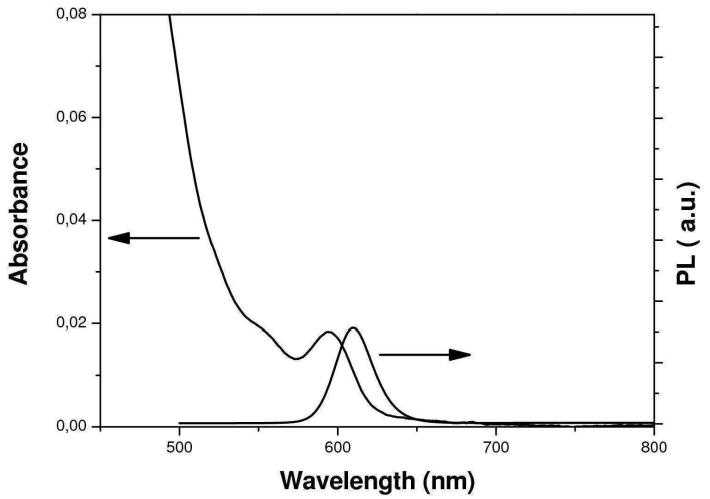

Figure 5.25 Absorption and PL measurements of the QDs dispersed in solution used for film doping

The possibility to obtain high refractive index at temperature as low as 200°C is beneficial for retaining the emission properties of QDs, which are otherwise degraded at higher temperatures [38]. PL emission from QD-loaded depositions is shown in figure 5.26. The PL peak position (608 nm and 604 nm for **Ti** and **PEG2** film, respectively) and the FWHM (29 nm and 30 nm for **Ti** and **PEG2** film, respectively) are only slightly different form those of QDs in solution, indicating that the developed synthesis is not affecting significantly the optical properties of the QDs.

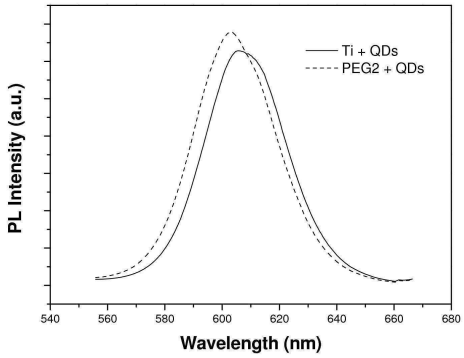

Figure 5.26 PL measurements of **Ti** and **PEG2** films loaded with QDs

The possibility to process this material as thick films is related to the very good stress-relief behavior and plasticity of the developed nanocomposites that are capable of sustain stresses arising during film casting. This represents an improvement with respect to other TiO_2 based materials for high refractive index applications

For these reasons, **PEG2** material doped with QDs has been tested in nanoimprinting lithography..

This technique consists in reproducing a surface pattern by embossing a deposition with a nanopatterned mould. Sufficient plasticity of the material to be embossed is required to achieve the desired surface pattern.

AFM images in figure 5.27 demonstrate that the plasticity of the developed nanocomposite is suitable for pattern formation, even if the process can be optimized by minimization of shrinkage (due to solvent evaporation) and by application of an external pressure to favor better filling of the mould. In fact, the pattern is about 60nm high while mould's one is 110 nm.

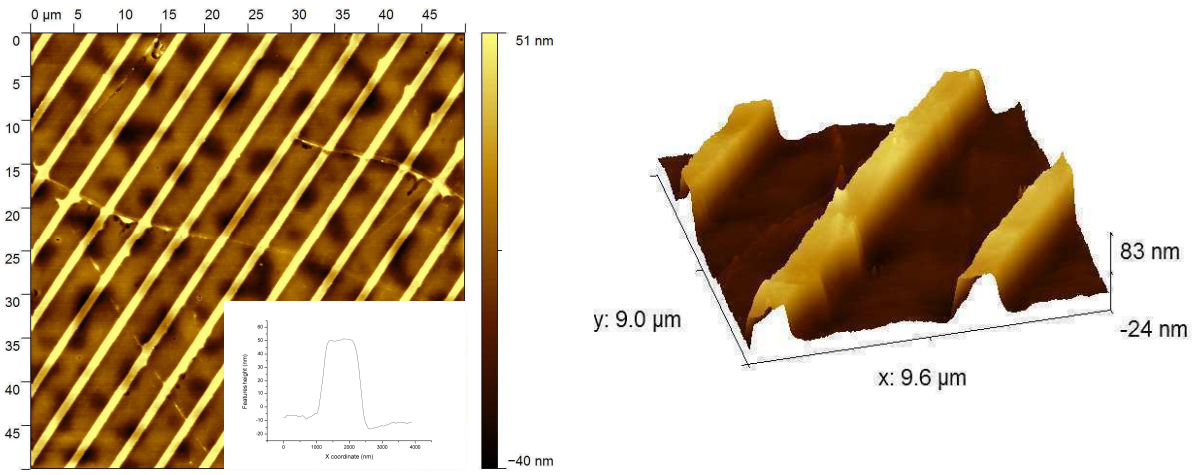

Figure 5.27 2D and pattern profile (left) and 3D detail (right) of AFM image of **PEG2** doped with QDs film patterned by nanoimprinting lithography

5.3.2 LED encapsulation

In this section, the above described materials are applied in a practical application consisting in encapsulation of LED devices.

The aim of this work was both to improve light extraction from LED chip and to convert part of LED chip light output to white light production working on the encapsulating material.

Light extraction from the emitting LED chip is limited from internal reflection due to the high refractive index of the semiconductor material constituting the LED chip. Thus, a consistent fraction of generated light remains trapped in the LED.

To diminish this effect, a polymeric coating (refractive index around 1.5) is normally applied since the fraction of reflected light is diminished due to lower refractive index difference between LED material and the medium above the device.

From results summarized in figure 5.30, it is concluded that the higher is the refractive index of the coating the higher is the light extraction. This effect is observed only if the shape of the coating is hemispherical, otherwise the effort in raising the refractive index is vanished if the coating has flatter shapes. Thus, also a correct coating shape is of great importance for maximizing light extraction.

A scheme of the target structure is shown in figure 5.28 along and the parameters influencing light extraction for the red and blue emitting LED used in this work are summarized in figure 5.29.

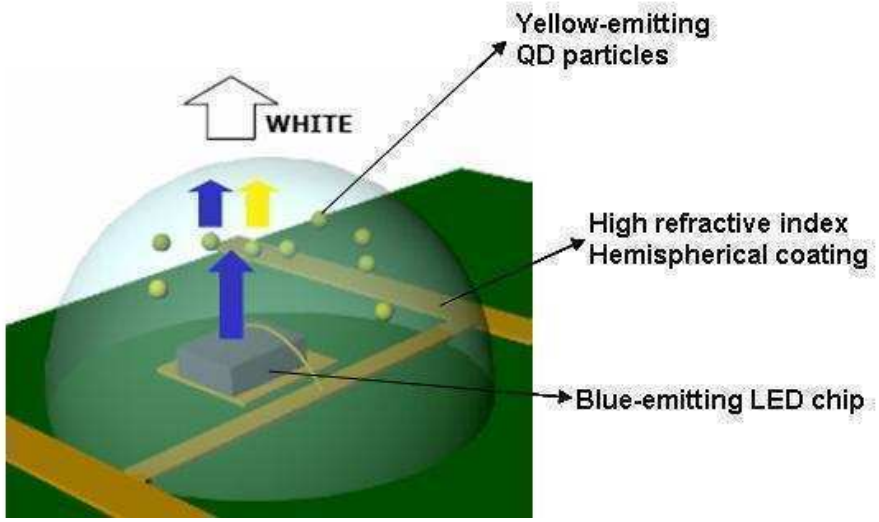

Figure 5.28 Schematic representation of the designed coating on LED

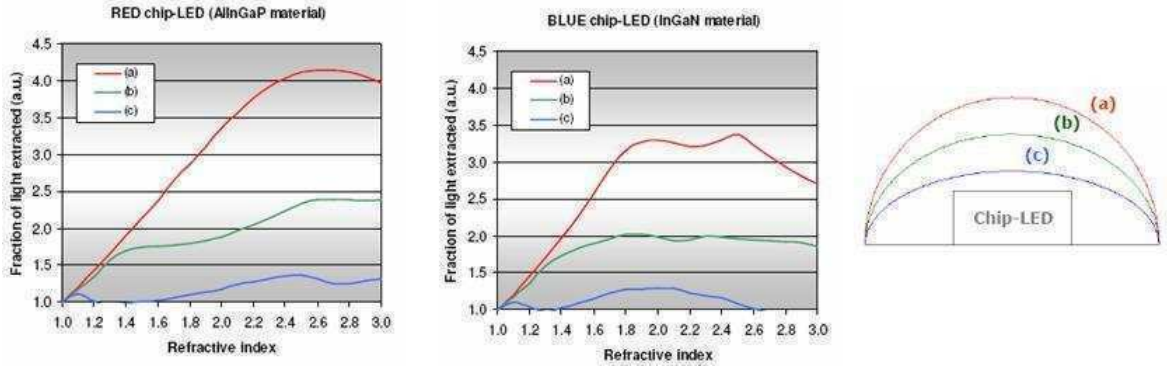

Figure 5.29 Light extraction dependence on coating refractive index and shape calculated from ray-tracing simulation. Shape geometry "a" correspond to an hemisphere, while geometries "b" and "c" present increasing flatness

It can be seen that in order to maximize light extraction a good hemispherical shape (geometry "a" in figure 5.29) is needed. In fact, flatter shapes (geometries "b" and "c" in figure 5.29) dramatically reduces the light extraction

The problem of white light production has been dealt with the introduction in the coating of compounds able to down-convert part of the light emitted by the LED. In our case, QDs have been used due to their stability, continuous absorption above ban-gap energy and tunable emission color with particle dimension. Down-conversion has been applied to blue-emitting LED at about 450 nm. At this wavelength QDs efficiently absorbs radiation. Emission color of quantum dots should be in the 570-580 nm range (yellow light) in order to produce white light in combination with 450 nm radiation of LED.

Finally, the employed material has to be transparent and possibly absorbs UV light for protection purposes.

Two techniques have been used to deposit the material on the LED. The first is based on a simple dispensing technique in which a controlled syringe deposits a droplet of material on LED top. By adjusting the syringe movement, it is possible to obtain an hemispherical coating. This technique need to process materials with quite high viscosity in order to obtain the correct droplet formation and to avoid swelling of the droplet once deposited. The so-obtained coating is then cured.

The other technique is based on aerosol-deposition, using an aerosol printing technology (Aerosol Jet®) from Optomec Inc. The process consists in creating an aerosol of the desired solution within a carrier gas flow. Subsequently the aerosol is carried to the print head and focused inside the nozzle using a sheath gas (e.g. nitrogen). Aerosol Jet® offers the possibility to pattern the material in the 10-1000 μm dimensional range.

A schematic representation of the process is shown in Figure 5.30.

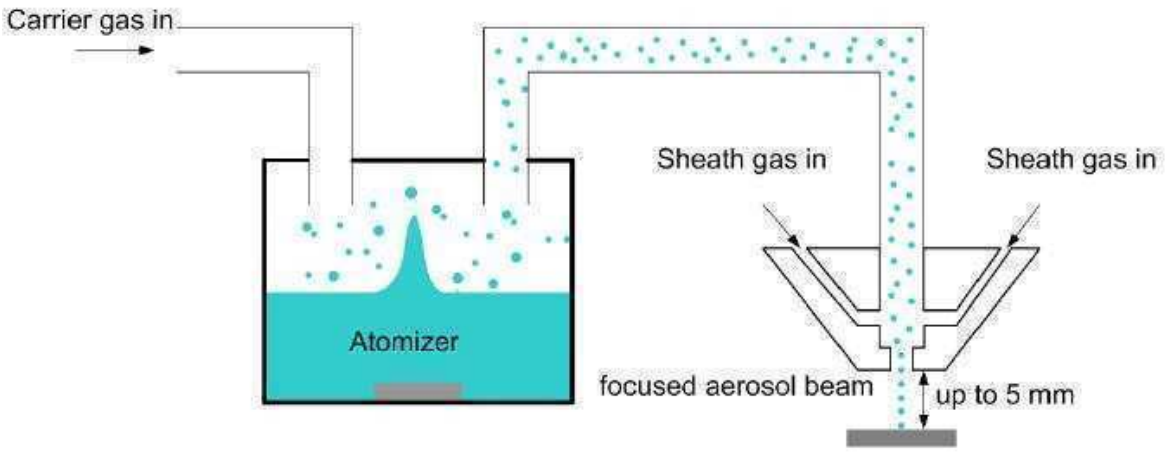

Figure 5.30 Schematic representation of the employed aerosol printing technology

The Aerosol Jet® requires solutions that have to be fluid enough to create an aerosol.
While the aerosol-based technique requires the material to be in a solvent medium, a solvent-free material would be desirable for the dispensing technique. In fact, solvent evaporation leads to dramatic change of the coating shape and to drying stresses which leads to extensive cracking if the material becomes too stiff before evaporation is completed, limiting plasticity and stress-relief behavior.

One of the approach followed to create high refractive index materials has been based on the introduction of titania nanoparticles in the material. First attempts in this direction were accomplished using TiO_2 anatase particles described in section 4.3.1 and 5.2.1.
Different epoxy based matrix similar to those described in section 5.2.1 were used as host matrices for these particles.
In the dispensing technique, viscous solutions are required, so we were obliged to remove the solvent component under vacuum until the desired viscosity was obtained.
Removal of solvent is also beneficial to minimize coating change effect and cracking during solvent evaporation.
Since the cracking tendency increased with the amount of inorganic filler, we have taken into consideration this parameter by adjusting the concentration to give a refractive index of about 1.7.
In order to minimize risks of cracking, a thermal curing profile was adopted, comprising two hours at ambient temperature, 1 hour at 60 °C, 1 hour at 80 °C and 30 min at 100 °C.

We realized that this material was not the best choice since it led to extensive cracking after evaporation of the solvent even in the early stages of the thermal curing treatment. Titania particles probably interact strongly when they become closer due to solvent evaporation. These interactions lead to a rigid skeleton well before evaporation is completed. Stresses arising from further evaporation cannot be relaxed, causing extensive cracking.

Furthermore, the acidic environment necessary to keep colloidal stability of TiO_2 NCs most likely accelerates the kinetics of hydrolysis and condensation leading to enhance gelling tendency of the solution.

These are the causes for the unsuccessfully deposition with the aerosol based technique. Even if a clear colloidal solution was used, the fast evaporation process, which inherently accomplishes the small droplets forming the aerosol, resulted in fast gelling. Only opaque depositions were obtained in this case since the material depositing on the substrate consisted in already gelled droplets.

Finally, acidic environment damages QDs particles (sulfide or selenide readily dissolve in acidic media) preventing their utilization.

Thus, remaining on a nanocomposite concept of the material, we tried to move toward different synthesis of titania and to work on the matrix material to enhance cracking resistance. Finally, environments with weak basicity were sought to limit gelling tendency and to be compatible with semiconductor QDs.

These considerations brought to develop the material described in the previous section.

PEG2 composition was thus tried in this application. The solvent component of this solution was removed under vacuum until a viscous solution was obtained which could be dispensed to form droplets on the LED device.

The behavior of this material was much better then the previous one tested in this application. Once treated, the coating appeared transparent but cracks were still present in the material, even if cracking was much less extensive than previous attempts. Furthermore, too much solvent was still present in the material causing extensive shape change and very flat geometries.

PEG2 material was also deposited with aerosol printing technology (Aerosol Jet®).

In this case, the solution was diluted with ethanol in order to achieve the conditions for aerosol formation and the substrate was heated to 80 °C during deposition. The printing velocity was 5 mm/s and the nozzle diameter 200 µm. The obtained structure were

annealed at 100°C for 30 minutes in air. Results were quite good and are shown in figure 5.31.

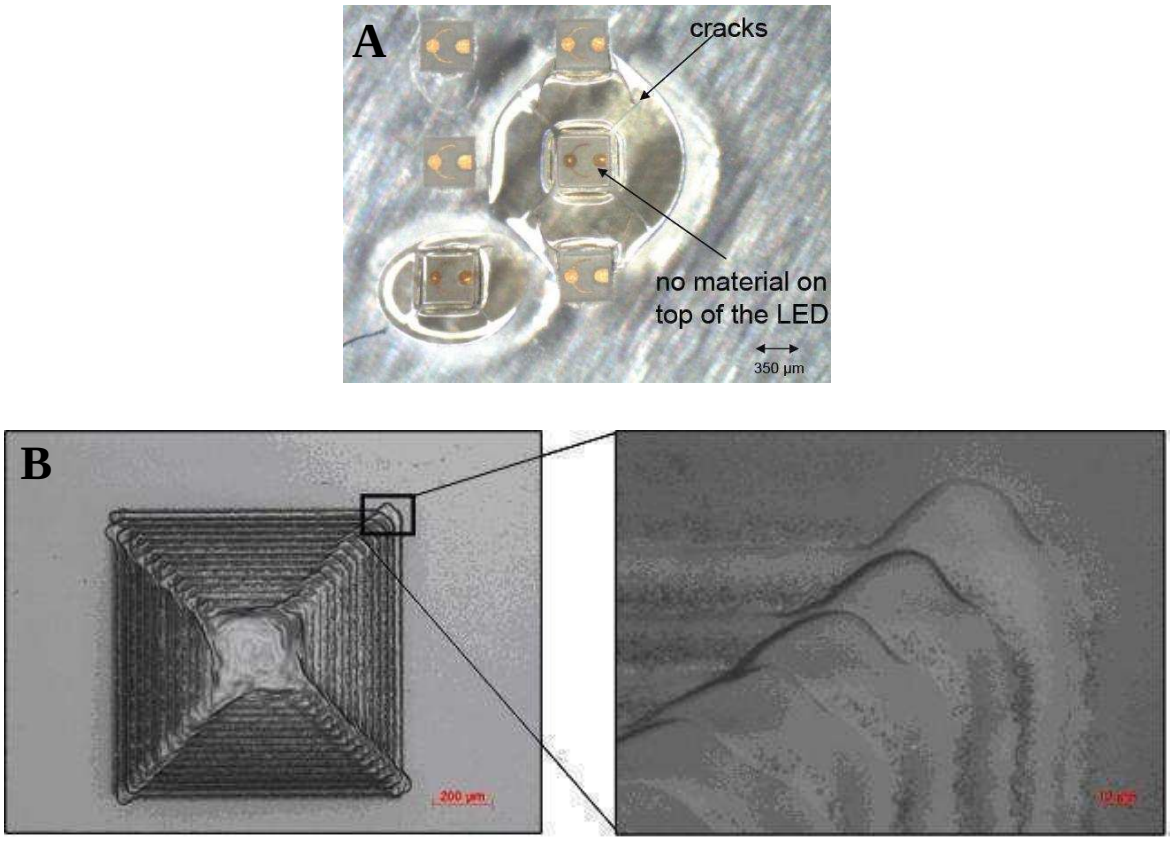

Figure 5.31 Depositions of PEG2 material on LED chips and with a pyramid-like structure on glass substrate (A) obtained with aerosol deposition technology (B)

Using this technique, a transparent material could be deposited also allowing to build more complex shapes (see Figure 5.31B). Even if some cracks are present at the edge of the structure, the results obtained with this technique are satisfactory demonstrating the possibility to use **PEG2** nanocomposites not only for the realization of thin films but also for the realization of high aspect ratio 3D microstructures with 3D mesoscale maskless direct writing technique.

Cracking is minimized and is seen only at the LED edges. Another problem encountered was the excessive swelling of the material during the deposition, resulting in material displacement from LED top. This problem will be discussed later on.
Interestingly, aerosol technique allows for enhanced material processing with respect to dispensing method. This can be explained by two main reasons. The first is related to the

fact that smaller depositions can be made. It is known the bigger bulky samples are more difficult to process since mechanical stresses are higher. The second can be related to a technique peculiarity. In the aerosol condition the solution is divided in small droplets and solvent is likely to begin evaporation at this stage. So, when the material is deposited on the substrate, part of the solvent has already been removed when no geometrical constraint are present, contrary to the situation in which evaporation is accomplished in a bulky state where shrinkage is impeded by the substrate or by a thick geometry.

Even if these results were quite encouraging, we decided to look for materials with lower refractive indexes but with enhance processing behavior with respect to cracking, in order to make use also of the available dispensing technology.

The material we've chosen to continue this work is an epoxy based sol-gel hybrid material. This is obtained through conventional sol-gel processing of Titanium-tetraisopropoxide (30% molar), diphenyl-dimethoxysilane (60%mol) (see figure 5.32B) and an epoxy based polymer (10%mol) obtained through solution polymerisation of bis(4-glycidylphenyl)methane with 3-glycidoxypropyl-dimethoxymethylsilane. This solution will be referred to as **DphTi**.

In this case the material has not the structure of a composite but it is meant to be an inorganic network with homogeneity at a molecular level. Phenyl groups introduced with the organosilane are used because they contribute to increase the refractive index.

The epoxy polymer is here used as a plasticizer. If only alkoxides are used, cracking easily occurs. The addition of this polymer has been found to enhance stress relief properties almost eliminating cracks formation during drying stages. If the quantity of this component is further raised up, refractive index diminishes and the material is more difficult to harden with thermal treatment.

This solution could be concentrated by removing the solvent under vacuum to achieve desired viscosity and resulted to be compatible with 6-amino-1-hexanol functionalized quantum dots particles.

The refractive index of **DphTi** material at 630 nm is 1.62, well below titania nanocomposite but with improved processing behavior.

Refractive index and extinction coefficient curves for **DphTi** and **DphTi** loaded with yellow emitting quantum dots (**C1-CSS** sample described in section 3.4.2) are shown in figure 5.32A.

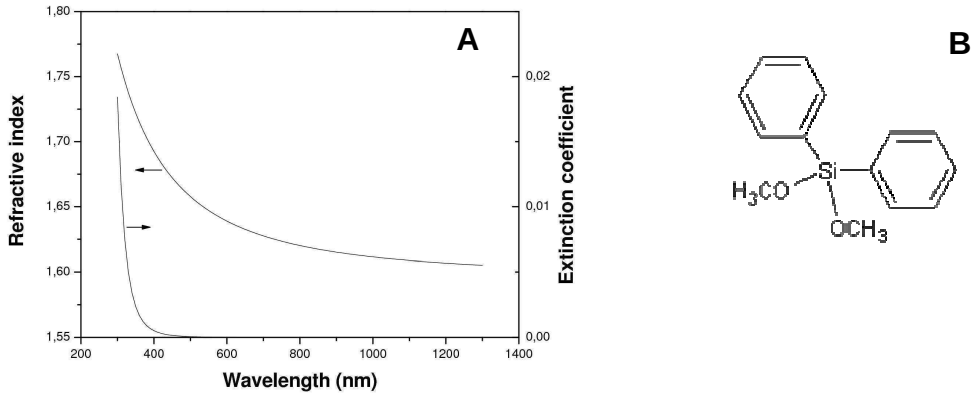

Figure 5.32 Refractive index and extinction coefficient curve for DphTi deposition on silicon substrate (A). Structure of the employed diphenyldimethoxysilane precursor (B)

This material has been used in both deposition techniques. The curing profile is as follows:

- *Step 1* 1 hours at 60°C
- *Step 2* 3 hour at 80 °C
- *Step 3* 1 hour at 110°C
- *Step 4* 30 minutes at 150°C

The evolution of coating with curing profile is shown in figure 5.33. Soon after the deposition, an almost hemispherical shape is obtained.

With the ongoing of the evaporation, the coating flattens even if to a much less extent than titania composite. The most striking effect of evaporation is the formation of bubbles inside the cured material, which is obviously an adverse effect .

Bubbles are probably originated from residual solvent that remains trapped since it is not removed before material starts to stiffen. We couldn't manage to avoid this problem by changing the curing profile in terms of temperatures and times. Interestingly, bubbles are originated from LED chip surface. In fact, analogues depositions on glass slides or on LED support board where no LED chips were present did not show any bubble formation. It is likely that LED provide surface nucleation sites (such as asperities or roughness) for bubble formation.

Figure 5.33 **DphTi** depositions through the syringe dispensing method soon after depositions and at different stages of the curing profile

With the ongoing of the evaporation, the coating flattens even if to a much minor extent than titania composite. The most striking effect of evaporation is the formation of bubbles inside the cured material, which is obviously an adverse effect .

Bubbles are probably originated from residual solvent that remains trapped since it is not removed before material starts to stiffen. We couldn't manage to avoid this problem by changing the curing profile in terms of temperatures and times. Interestingly, bubbles are originated from LED chip surface. In fact, analogues depositions on glass slides or on LED support board where no LED chips were present did not show any bubble formation. It is likely that LED provide surface nucleation sites (such as asperities or roughness) for bubble formation.

Analogue problems were encountered in the processing of sol-gel hybrids [39]. In that case the problem was solved by increasing the networking kinetics (using more effective catalyst) in order to stiffen the material more rapidly. Probably this is correlated with the deformation of the material when a bubble is formed. If the material is more stiff, a bubble cannot be originated in the material.

This problem was much less evident when using the aerosol printing technology, as shown in figure 5.34.

In the left picture of this figure, bubbles are clearly seen originating from LED chip edges, but the problem is much less pronounced than in samples obtained with the other technique. Analogously to titania composites, swelling of the material from LED chip is observed, creating a cup-like deposition.

The shape could be improved with a second deposition in order to "fill" the previous cup-like shape. In this way a good coverage of the chip was obtained.

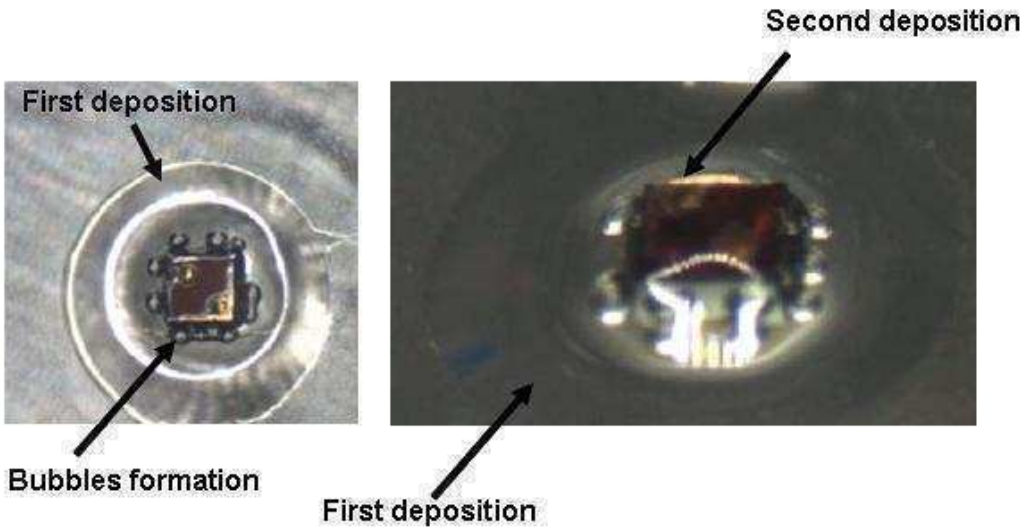

Figure 5.34 Aerosol depositions of **DphTi** material. Single coating and double coating are shown at the left and right pictures respectively

Flux extraction measurements were performed on LED covered with **DphTi** using the dispensing technique. Main results are summarized in Figure 5.35. Simulations of flux extraction enhancement are presented using different geometries for coating with refractive index of 1.62, equal to **DphTi** material.

Measured values of flux enhancement (calculated as the ratio between the flux before and after LED encapsulation) lie between simulated values for low and high ellipsoid, in agreement with the achievement of a non hemispherical shape.

With the aim of improving flux extraction, we deposited a second coating consisting of a commercial resin with lower refractive index (about 1.5) but which could be shaped into desired hemispherical shape. Simulations showed that this strategy greatly enhanced the flux extraction of the first coating, even if it is very flat.

An increase in flux extraction is indeed observed in the measured values after the deposition of a second coating of the above-describe commercial resin.

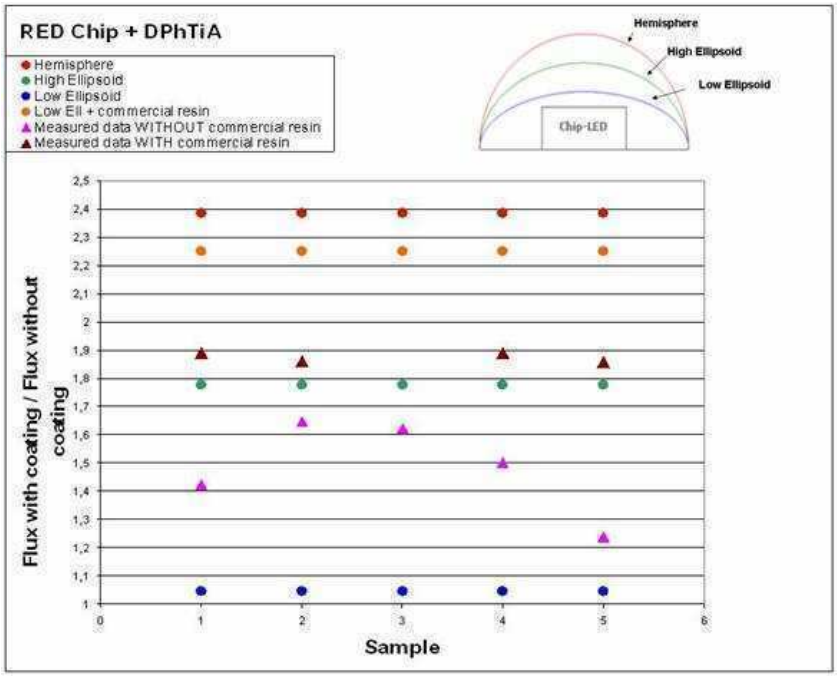

Figure 5.35 Simulated and experimental flux extraction (determined as the ratio between the flux before and after LED encapsulation) for different coating geometries

Analogue measurements were performed on blue emitting LEDs. In this case, LED coated with **DphTi** always showed a diminished extracted flux with respect to uncoated samples. This is most probably because these materials tend to become yellow particularly after heat-treatment. This means that **DphTi** absorbs in the blue region as it is apparent , diminishing LED's light output. Thus, such hybrid material cannot be used for enhancement of light extraction for blue LEDs.

As far as down conversion for white light production is concerned, the introduction of QDs is effective indeed, as demonstrated in figure 5.36.

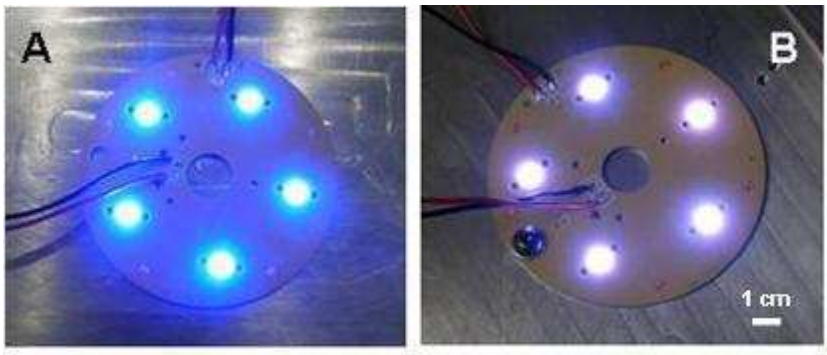

Figure 5.36 Light emission from a blu emitting LED covered with DphTi with lower (A) and higher (B) concentration of yellow emitting quantum dots.

In both the pictures reported in figure 5.36, blue emitting chip are covered with **DphTi** material containing yellow emitting quantum dots. In the coatings of figure 5.36A, the concentration of emitting particles is less then those for samples shown in Figure 5.36B.

Concordantly, the increasing quantity of particles leads to major light conversion with a resulting light output which is more white light resembling.

Further measurements on samples of Figure 5.36B are shown in Figure 5.37. In the spectral emission of the device, both LED and QD emission are apparent. The determination of the color coordinates indicate that the obtained light output is quite far from white coordinates as defined from automotive standards.

Achievement of the right color requires further optimization based on quantum dots concentration tuning and coating geometry. In fact, it is apparent that not only a major amounts of quantum dots is needed to improve color conversion, but also the thickness of the coating is important since thicker deposition favors blue light absorption from the quantum dots and , as a consequence, higher conversions.

Nevertheless, the obtained results demonstrate the great potentiality of the developed multifunctional nanocomposites which have high refractive index, down conversion properties and processability with industrial techniques.

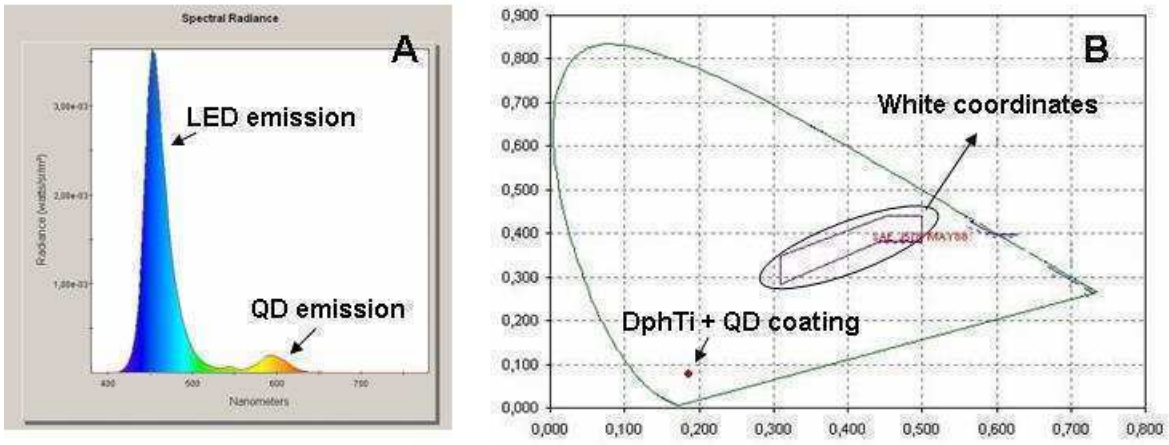

Figure 5.37 Emission output of sample shown in figure 5.36B (A) and determination of colour coordinates (B)

5.4 Gold NCs loaded titanium dioxide nano-composites

5.4.1 Composites from anatase-TiO_2 and gold colloids for optical gas sensing applications

The obtainment of transparent, crystalline, porous nanostructured thin films of titanium dioxide is particularly interesting in gas sensing applications since interactions with gas analytes is enhanced and charge carrier densities as well as dielectric properties of titanium dioxide can be altered in presence of particular species in the atmosphere.

Gold nanoparticles have a strong absorption in the visible range due to Surface Plasmon Resonance (SPR). The characteristics of this absorption feature are extremely dependent on the dielectric properties of the material surrounding gold nanoparticles.

This property has led to the utilization of gold nanoparticles in optical gas sensing with the aim of emphasizing dielectric or electronic changes of the surrounding matrix through optical detection of the induced variation in gold plasmon resonance.

Titania-gold composites has already been used for sensing purposes [40]. Samples were prepared by mixing gold colloids with a sol-gel titania precursors obtained from a titanium alkoxide chelated with acetylacetone. Good optical response was observed under CO exposure only if samples were annealed at 500 °C. At this temperature crystallization of titania matrix occurs. Samples annealed at 400 °C, still presenting amorphous titania, presented poor optical response toward CO exposure.

These samples were also tested for H_2 detection. In this case both amorphous and crystalline titania samples showed good optical response.

The idea behind the use of crystalline titania colloids as the matrix where to embed gold particles is related to the possibility of having crystalline titania without annealing at a temperatures as high as 500°C. In this way higher porosity and controlled morphology.

In fact, such a system can be viewed as an ensemble of particles whose morphology evolution in terms of crystalline domain's ripening and porosity has been described in section 5.2.1 with increasing annealing temperature.

This represents an advantage with respect to the conventional sol-gel method since we can play with annealing temperature without worrying about titania crystallization.

5.4.1.1 Titania/Gold composite film synthesis

Anatase TiO_2 colloids in methanol were prepared as described in section 4.3.1.
Gold colloids were prepared according to the Turkevich method [50] by reducing $HAuCl_4$ salt with trisodium citrate in water. After 2 hours the solution was concentrated in a rotary evaporator and Au nanoparticles (NPs) were precipitated with acetone, centrifuged at 4000rpm for 5 minutes and re-dispersed in ethanol leading to a 30mM concentration solution.
The starting solutions were prepared by mixing the methanol suspension of TiO_2 NCs with PVP-capped Au NPs in ethanol (**TiG** samples series) leading to a final TiO_2 concentration of 33 g/l and a Au:Ti molar ratio of about 0.05.
Au-free samples were prepared for comparison purposes by simply substituting the Au ethanol suspensions with pure ethanol, obtaining **Ti** samples.
All the samples were deposited by spin coating at 2000 rpm for 30 seconds on either quartz or silicon substrates and heated in a muffle furnace at 300 °C, 400 °C or 500 °C for 1 hour. Annealing temperature is indicated with numbers 3, 4, 5 respectively at the end of the sample name.
Film thicknesses are all in the 35-55 nm range, as measured with spectroscopic ellipsometry.

5.4.1.2 Results and discussion

TiO_2 NPs adopted in this work have been characterized in section 4.3.1 and were found to be anatase with a mean dimension of 4-5 nm, while gold colloids were synthesized with a mean dimension of 15 nm, proved from TEM characterization (data not shown).
XRD measurements performed on thin films (figure 5.38) confirm the crystalline anatase phase of TiO_2 [42] and show also Au peaks [42] for **Ti** and **TiG** series.
Diffraction peaks from titania are not clearly detected in **Ti3** and **TiG3** samples and become more intense with increasing temperature treatment, even if starting TiO_2 material is crystalline, due to reason analogue to those discussed in section 5.2..
Thermal treatment also affects XRD peak width due to crystallite size evolution. TiO_2 NCs grow in size at higher temperatures, due to coarsening of particles, as already discussed.
From these data, it is also shown that gold peaks do not undergo any relevant change in shape and intensity, indicating good Au NPs stability in this TiO_2 matrix.

Scanning electron microscopy was used to characterize the surface morphology of the samples and Au NCs distribution inside the TiO_2 matrix. Micrographs of **TiG3** and **TiG5** are reported in figure 5.39.

Au nanocrystals of spherical shape are homogeneously and statistically dispersed in a micron scale, and only very few small aggregates can be seen.

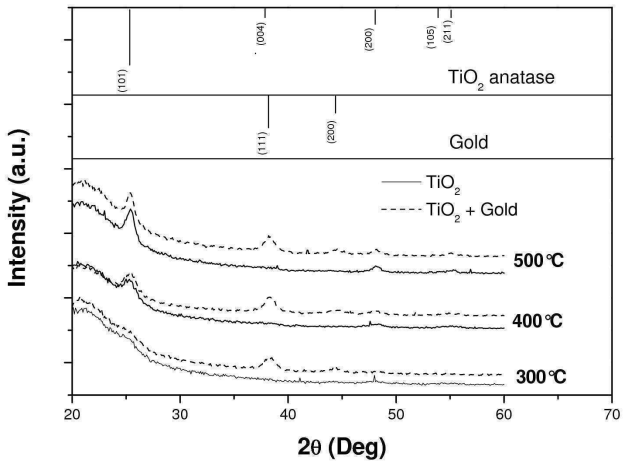

Figure 5.38 XRD data of **Ti** and **TiG** films at different annealing temperatures

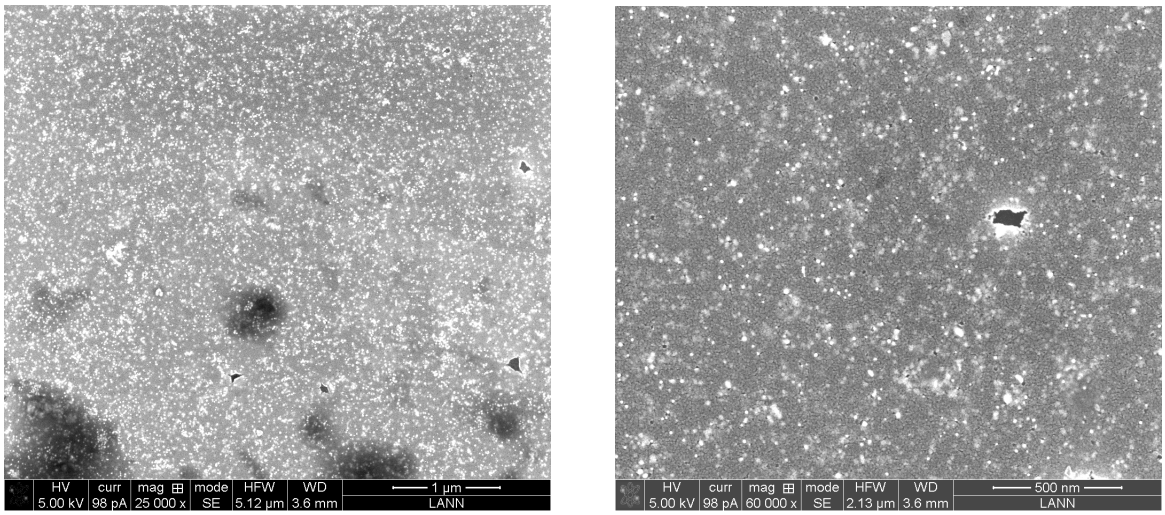

Figure 5.39 SEM micrographs for **TiG3** and **TiG5** films

Optical data are now described and used to retrieve a deeper insight in film structure.

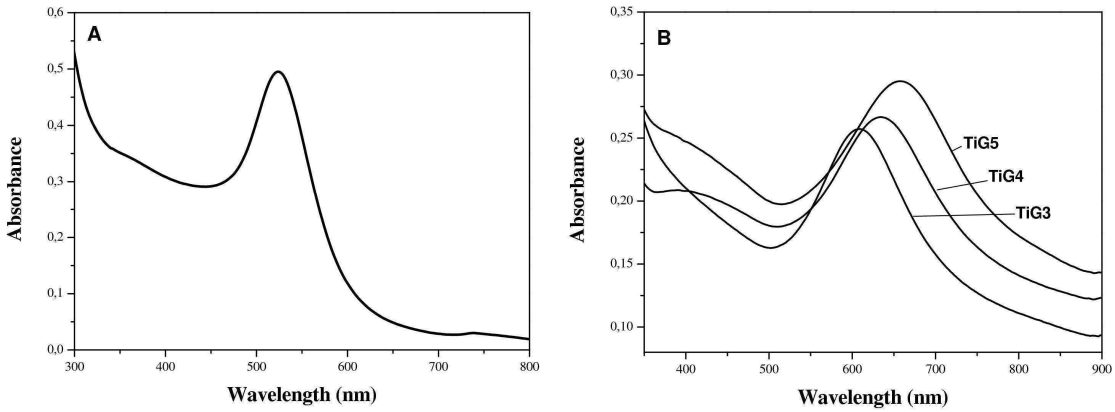

Figure 5.40 Uv-Vis spectra of gold colloids in ethanol (A) and TiG samples treated at different temperatures (B)

In figure 5.40A, UV-Vis spectra of gold colloids in ethanol is reported and a clear SPR peak at about 525 nm is present.

Figure 5.40B reports the absorption spectra of **TiG** films. SPR peak of gold particles is clearly visible, and a progressive red-shift with increasing annealing temperature can be observed.

It is well known that SPR frequency is strongly related to the dielectric properties of the material surrounding gold NCs: from SEM images and XRD spectra almost no morphology changes or aggregation phenomena of Au particles can be observed, thus any change in SPR peak position is directly related to refractive index of the surrounding matrix. In each samples series, SPR wavelength is progressively red-shifted with increasing temperature, and this result is associated with the increase of the refractive index of the material surrounding gold particles. This fact is confirmed by ellipsometry data and discussed in the following.

In fact, at a first approximation the SPR peak have been related to dielectric constants of the matrix from the following relationships [40].

$$\lambda_{SPR}^2 = \lambda_p^2(\varepsilon_\infty + 2\varepsilon_m) \qquad \lambda_p = \sqrt{\frac{4\pi^2 c^2 m\varepsilon_0}{Ne^2}} \qquad \text{Eq. 5.2}$$

where λ_p is the bulk plasma wavelength of gold, ε_∞ is the high frequency value of the dielectric function and ε_m is the dielectric constant of the matrix. These values are respectively 131 nm and 12.2 for gold.

N, m and ε_0 are the electron concentration, the effective mass of the electron in gold and vacuum permittivity respectively.

For a non-absorbing matrix ε_m is related to its refractive index n through $n = \sqrt{\varepsilon_m}$.

From this relationship one can easily see that SPR wavelength red-shifts with increasing refractive index of the matrix.

Refractive index curves of un-doped and gold-doped composite films have been estimated from ellipsometry measurements and refractive index values are reported in table 5.5 for selected wavelengths of interest.

Sample	Refractive index @ 1100 nm	Average Porosity (%)	Exp SPR peak position (nm)	Refractive index @ SPR wavelength	Matrix Refractive index from SPR position
Ti 3	1.968	45	-	1.97	2.16
Ti 4	2.038	38	-	2.04	2.37
Ti 5	2.153	28	-	2.15	2.55
TiG 3	2.117	-	608	2.18	-
TiG 4	2.154	-	634	2.21	-
TiG 5	2.277	-	658	2.35	-

Table 5.5 Refractive index values, SPR wavelengths and estimated porosity for all produced samples

Refractive index values at 1100 nm were chosen as reference because sufficiently away from SPR region and not to be strongly affected by optical absorption of Au NPs.

Refractive index is observed to increase for **Ti** samples with increasing annealing temperature. These data can be used to get some information about average film densification and porosity, which has been calculated as described in section 5.2.1 using refractive index at 1100 nm and a value of 2.44 for TiO_2 anatase at this wavelength [43].

Differences in refractive index can be interpreted as differences in amount of porosity by means of effective medium optical models, where the most densified material has the highest refractive index.

These calculations has been made only for undoped samples since the model used take into account only two non-absorbing phases (TiO_2 and air), while gold containing samples strongly absorbs in the visible. **TiG** films have higher indexes at 1100 nm with respect to

Ti, but this may be related to modification of optical constant by the presence of a third phase rather than minor average porosities.

The refractive index difference between 400 °C and 300 °C annealed samples is around 0.04, while the difference in refractive index between 500 °C and 400 °C is around 0.12; a greater increment of n occur between 400 °C and 500 °C, as can be clearly seen from figure 6, indicating that densification process of TiO_2 colloids is activated at higher temperatures, affecting global porosity of the matrix.

Interestingly, optical data can be used also for a deeper appreciation of local structure of the composite film.

SPR frequencies are, in fact, related to local dielectric properties of the matrix around the Au particles, and the theoretical refractive index calculated from the SPR peak results to be greater than experimental refractive indexes of both doped and undoped TiO_2 matrix (see Table 5.5). This is in countertendency with previous results concerning TiO_2 sol-gel thin films doped with Au nanoparticles [44], where the experimental refractive index resulted to be slightly higher than the theoretical value, probably because of higher amount of amorphous matrix or porosity facing Au crystals, compared to the average value of the sample.

In this work, the optical characterization results suggest that the material structure just around gold surface is more densified, if compared to the to the average structure of the films, and thus preferential organization or coverage of titania on gold particle can be inferred by these data.

These observations are summarized in figure 5.41, where the SPR peak position of Au-doped samples associated with refractive index of undoped matrix measure at the corresponding SPR wavelength is reported, together with the theoretical refractive index calculated from SPR peaks by means of Eq. 5.2.

Moreover, increasing annealing temperature leads to further coverage of Au nanoparticles, because the difference between theoretical and experimental refractive index becomes higher. Thus, it is likely that in **TiG3** sample, TiO_2 nanoparticles are in poor contact with gold, while in **TiG4** and **TiG5** the coverage of Au becomes higher, while the global matrix densification is still far to be complete.

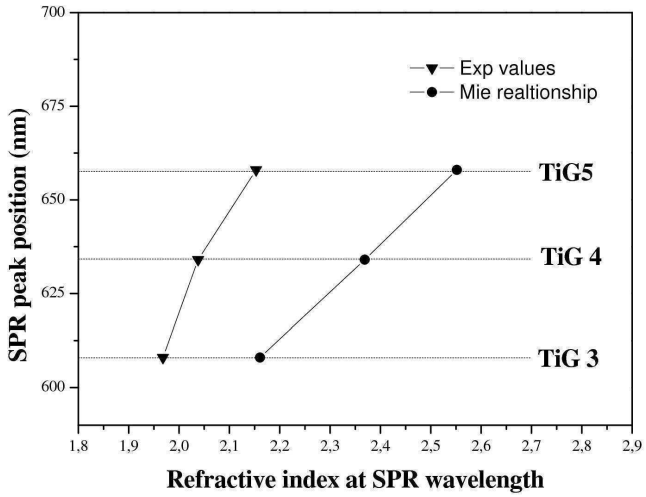

Figure 5.41 SPR wavelength correlated to experimental refractive index values of undoped matrix at SPR wavelength and to matrix refractive index values obtained using Eq. 5.2

In summary, the extent by which gold "feels" titania is not strictly dependent on the overall degree of densification of the matrix.

All the samples show an experimental refractive index much lower than the theoretical value predicted by Mie theory, so preferential organization of TiO_2 on gold leading to extensive anatase/gold interface is here addressed as the key idea for optical data interpretation.

Gas sensitivity behavior toward CO was tested by measuring change in absorption spectra of **TiG** films under exposure to an atmosphere of 1%v/v of CO in air.

In order to activate the gas sensing response, the depositions are tested between 250°C and 350°C 300°C operative temperature (OT).

TiG3 sample was tested only at 250 °C to avoid structural changes in the film, but they show instable baseline, maybe because of the residual organic compounds still present inside the film, or to the matrix not fully stabilized after the 300°C annealing, so only the results of 400°C and 500°C treated samples will be presented.

Figure 5.42 shows the optical absorbance change ($A_{air} - A_{gas}$) of the samples, that is the difference between the absorbance measured in air, and the absorbance measured during target gas flowing, performed at 350°C for CO.

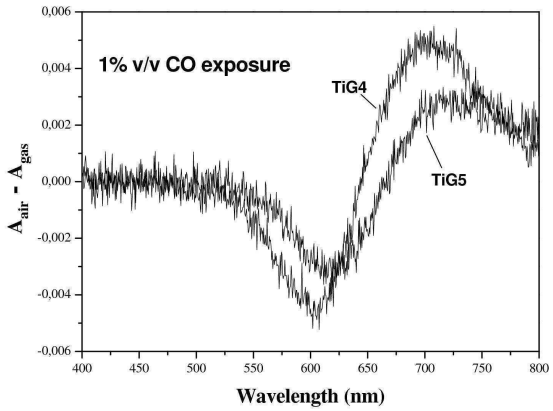

Figure 5.42 Absorption spectra difference between absorption spectrum in air and under CO gas exposure for **TIG4** and **TIG5** depositions at an operating temperature of 350°C

TiG4 and **TiG5** give response to both gases, with a wavelength dependence of optical sensitivity. The Au plasmon peak undergoes a blue-shift during gas exposure. This effect can be related to the interaction of reducing gases with the n-type semiconductor TiO_2 matrix, that can promote a catalytic oxidation of the gas, causing an increase in the amount of conducting electrons *N*. This results in a shift of the plasmon band at higher frequencies as deduced from Eq.5.2 [40]; this behavior can be due also to the adsorption of target gases in the matrix sites, leading to a local change in the refractive index, causing the observed shift of the Au SPR frequencies.

The absorption change curves reported in figure 5.42 presents one absolute maximum and one minimum. The temporal response of both samples operating at a wavelength near the absolute minimum of the absorbance change curves are presented in figure 5.43.

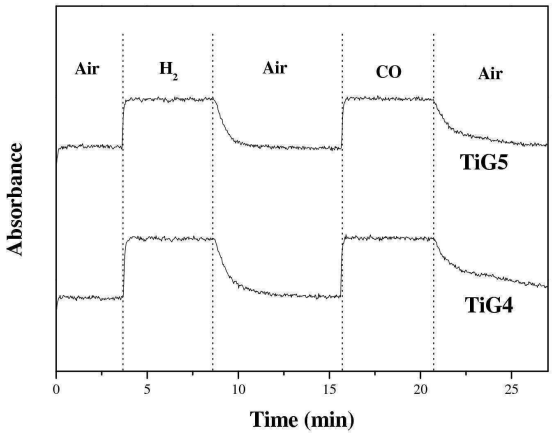

Figure 5.43 Dynamic optical absorption evolution under H2 and CO exposure for **TIG4** and **TIG5** depositions at an operating temperature of 350°C

The dynamic performance of the sensors is quite good, with an almost square output signal: very fast response time, satisfactory recovery time, and good recovery of the baseline level.

Contrary to films derived from conventional sol-gel processing, sensitivity toward CO detection is good also for 400 °C annealing temperature and recovery of the baseline after switching between CO to air is better.

This confirms that crystalline anatase is needed for CO detection. Since catalysis of CO oxidation has been argued to be enhanced by a well developed anatase-Au interface [45], the synthetic scheme we utilized to produce TiO_2-Au composites is particularly advantageous not only for employment of crystalline materials, but also for the preferential facing of TiO_2 on gold particles that seems to be suggested from our optical characterization.

In figure 5.45 the sensitivity toward H_2 is also shown and the results are similar to CO sensitivity in terms of optical changes. In this case, the literature on H_2 reaction is limited with respect to CO, even if a similar oxidation reaction was suggested to explain conductometric as well as optical sensing [40].

A comprehensive description of sensing behavior will be reported elsewhere.

5.4.2 Enhancement of gold nanorods stability in TMA-Ti titanates.

In this section gold nanorods are introduced in a titanate matrix. The effect of film treatments described in section 5.2.2 on the thermal stability of gold nanorods will be described.

Gold nanorods are interesting materials in optical applications since they present two surface plasmon resonances associated with transverse and longitudinal rod direction. Furthermore, the SPR position of the longitudinal plasmon is strongly dependent on its aspect ratio. Higher aspect ratio leads to higher wavelengths for longitudinal plasmon resonance.

This material is not stable under intense radiation, leading to loss of their original shape due to their tendency toward spheroidization. This effect is believed to be caused by the fast heating to high temperature induced by laser absorption. This temperature rise enhances the energy of the lattice promoting the achievement of the lowest surface energy which is assumed by the spherical shape.

The activation energy necessary to induce this shape change was demonstrated to be increased if the nanorods were covered by a silica shell [46], a stiffer environment, making rods more stable toward heat effects.

Water soluble titanates were densified at low temperatures if UV treatment was first applied.

We made use of this behavior to investigate the thermal stability of gold nanorods in such titanate matrix with or without UV treatment before subsequent thermal treatment.

5.4.2.1 Film synthesis

35 mg of titanate powder was dissolved in 0,175 ml of water with 6 µl of a 25% wt solution of TMAH in methanol. After complete dissolution, 0.175 ml of methanol were further added to dilute the solution, resulting in a final 100 gr/L titanate concentration.

Gold nanorods with an aspect ratio of 2.4 as estimated from optical spectra [48] (see figure 5.44) in water were used in these experiments.

A known amount of gold nanorods in water was mixed with 50 µl of titanate solution.

The resulting sol was spun on quartz or silicon substrates at 2000 rpm for 20 sec

All samples were first treated at 100°C for 20 minutes to let evaporation of more volatile solvents.

Processing conditions are summarized in table 5.6.

The samples were treated for 30 minutes from 200 °C to 700 °C with 100 °C increasing step either with or without a densifying treatment stage applied before thermal annealing. Such densifying treatment consisted in 15 minutes of UV irradiation followed by 5 minutes of annealing at 200 °C. This treatment is the same as that described in section 5.2.2 where it was referred to **15'UV + 5'200**.

UV-Vis absorption spectra were taken for each sample in order to investigate the thermal stability of the rods. In table 5.6, sample name are also reported.

Sample treatment	**Sample name**
20' 100 °C (reference)	**100**
15'UV + 5' 200 °C "densifying treatment stage"	**PT** *(Pre-treatment)*
15'UV + 5' 200 + 30' 200 °C	**PT 200**
15'UV + 5' 200 + 30' 300 °C	**PT 300**
15'UV + 5' 200 + 30' 400 °C	**PT 400**
15'UV + 5' 200 + 30' 500 °C	**PT 500**
15'UV + 5' 200 + 30' 600 °C	**PT 600**
15'UV + 5' 200 + 30' 700 °C	**PT 700**
30' 200 °C	**200**
30' 300°C	**300**
30' 400°C	**400**
30' 500°C	**500**
30' 600°C	**600**
30' 700°C	**700**

Table 5.6 Processing conditions employed in this work for Au-nanorods loaded titanate films

5.4.2.2 Results and discussion

Optical spectra of gold nanorods in solution are shown in figure 5.44. Two SPR absorption are seen at 519 nm and 636 nm corresponding to transverse (SPR_T) and longitudinal (SPR_L) plasmon oscillation respectively. From these data an aspect ratio of about 2.4 can be estimated [48]. In the same figure optical spectra of **100** and **PT** samples are shown.

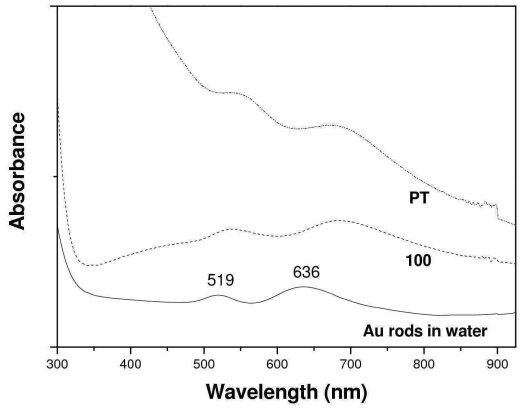

Figure 5.44 Absorption spectra of gold nanorods in water in **100** and **PT** depositions

SPR_T and SPR_L wavelength positions are slightly red-shifted in **100** and **PT** samples treatment, due to higher refractive index of surrounding medium. In particular, the SPR_L band results to be more shifted if compared with SPR_T. This is in agreement with theoretical model results, which predict an higher sensitivity of SPR_L toward changes in dielectric properties of the surrounding medium [47].

SEM analyses should be performed to confirm that under processing condition of sample **100** and **PT**, the nanorods are unchanged in their shape. This characterization is not yet available. Evolution of the optical spectra with increasing annealing temperature is shown for samples with and without UV treatment in figure 5.45.

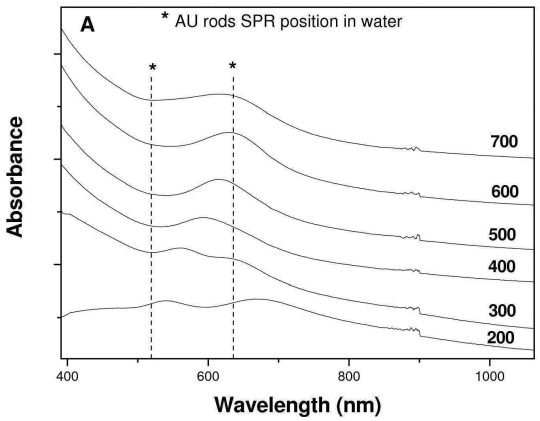

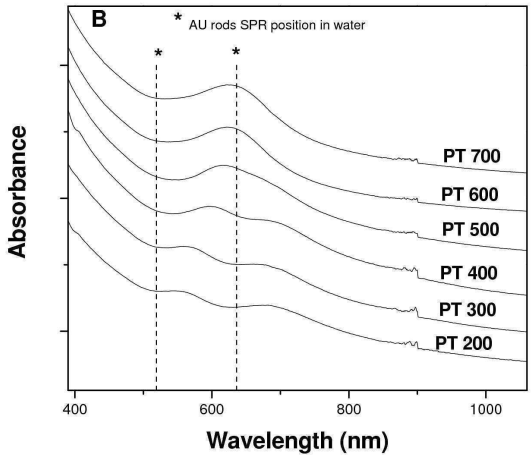

Figure 5.45 Uv-Vis spectra evolution of only thermally treated samples (A) and with a UV densifying treatment before thermal annealing

In samples only thermally treated a blue-shift of the SPR_L is observed indicating the beginning of rod's long axis shortening. At 400 °C only one plasmon resonance is observed at 594 nm corresponding to spherical gold nanoparticles absorption. The red-shift of this resonance with respect to gold particles in water is due to the high refractive index of the matrix, which has been demonstrated to be anatase when treated at 400°C.

At higher annealing temperatures only one plasmon peak is observed which further shifts to higher wavelengths.

Samples that were subjected to a PT stage (see figure 5.45B) before thermal annealing showed a different behavior.

First, it is apparent that the SPR_T wavelength position is progressively red-shifted with increasing temperature, which is correlated with increasing refractive index of surrounding medium.

Second, the presence of the SPR_L position is clearly observed till 400°C, which results to be almost unchanged with increasing temperature.

At the moment we cannot separate the effect related to the red-shift of gold rods's SPR in a matrix with increasing refractive index and that due to blue shift caused by diminishing aspect ratio.

Even if morphological analyses need to be performed, we can state that an increased thermal stability is achieved if the titanate matrix is made stiffer around gold rods before thermal annealing. This is more clearly seen in figure 5.46 , where samples with or without UV treatment at the same subsequent thermal annealing treatment are compared.

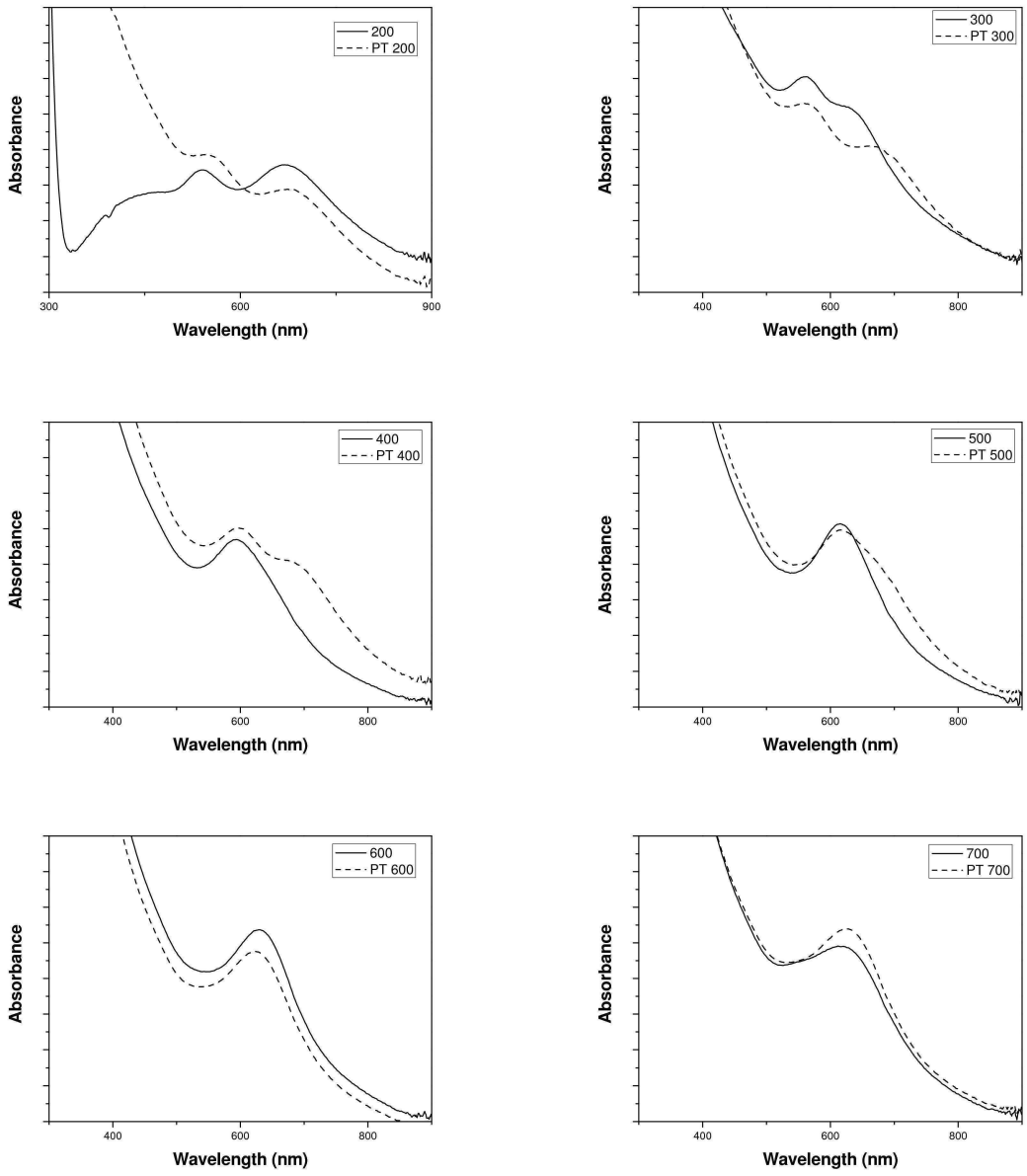

Figure 5.46 Comparison between samples annealed at different temperatures with or without UV treatment

References

[1] Nussbaumer R., Caseri W.R., Smith P., Tervoort T., Macromol .Mat. Eng.., 2003, **288**, 44

[2] Innocenzi, P., Lebeau, B., J. Mater. Chem,. 2005, **15**, 3821

[3] Yuwono A. H., Xue J., Wang J., Elim H. I., Ji W., Li Y., White T. J., J. Mater. Chem., 2003, **13**, 1475

[4] Yuwono A. H., Liu B., Xue J., Wang J., Elim H. I., Ji W., White T. J., J. Mater. Chem., 2004, **14**, 2978

[5] Sanchez C., Escuti, M. J., van Heesch, C., Bastiaansen C. W. M., Broer, D. J.; Loos J., Nussbaumer R., Adv. Funct. Mater., 2005, **15**, 1623

[6] Wang H. T., Xu P., Meng S., Zhong W., Du W. C.; Do, Q. G., Polym. Degrad. Stab. 2006, **91**, 1455

[7] Khaled S. M., Sui R., Charpentier,P. A., Rizkalla A. S., Langmuir, 2007, **23**, 3988

[8] Scholz S., Kaskel S., J. Colloid Interface Sci**.,** 2008, **323**, 84

[9] Kickelbick G., J. Sol-Gel Sci. Technol,. 2008, **46**, 281

[10] Lee L.H., Chen C.W., Chem. Mat., 2001, **13**, 1137

[11] Nussbaumer R.J., Caseri W., Tervoort T., Smith P., J. Nanop. Res., 2002**,4** 319

[12] Convertino A., Leo G., Tamborra M., Sciancalepore C., Striccoli M., Curri M.L ,Agostiano A., 2007, Sens. Act. B, **126,** 138

[13] Oliveira P.W., Krug H., Frantzen A., Mennig M. and Schmidt H., 1997 Proc.SPIE, **3136**, 452

[14] Nakayama N., Hayashi T., J. Appl. Polym. Sci., . 2007, **105**, 3662

[15] Zhou S. X., Garnweitner G., Niederberger M., Antonietti M., Langmuir, 2007, **23**, 9178

[16] Chau J. L. H., Lin Y. M., Li A. K., Su W. F., Chang K. S., Hsu S. L. C., Li T. L. Mater. Lett., 2007, **61**, 2908

[17] Yuwono, A. H., Xue, J. M., Wang, J., Elim, H. I., Ji, W. *J.*, Electroceram., 2006, **16**, 431

[18] Yuwono A. H., Zhang Y., Wang, J., Zhang X. H.; FanH. M.; Ji W. ,Chem. Mater., 2006, **18**, 5876

[19] Matsuda A., Kotani Y.; Kogure T., Tatsumisago M., Minami T., J. Am. Ceram. Soc, 2000, **83**, 229

[20] Niederberger M., Garnweitner G., Chem. Eur. J., 2006, **12**, 7282

[21] Koziej D., Fischer F., Kranzlin N., Caseri W.R., Niederberger M., Applied. Mat. and Interfaces 2009, **1**, 1097

[22] Caseri W., Macromol. Rapid Commun, *2000*, **21**, *705*

[23] Garahan A, Pilon L., Yin J., Saxena I., J. Appl. Phys, 2007, **101**, 014320

[24] Kyprianidou-Leodidou T., Caseri W.R.,Suter U.W., 1994, J. Phys Chem., **98**, 8992

[25] Della Giustina G., Brusatin G., Guglielmi M., Romanato F., Mat. Sci. Eng C. 2007, **27**, 1382.

[26] Handbook of Chemistery and Physics, Lide D.R., 72nd edition.

[27] Bruggeman D.A.G.., Ann. Phys., 1935, **24**, 636

[28] Fardad M. A., Yeatman E. M., Dawnay E. J. C., Green M. and Horowitz F., J.Non-Cryst. Solids, 1995, **183**, 260

[29] Sasaki T., Watanabe M., Hashizume H., Yamada H., Nakazaw H., J Am. Chem Soc., 1996, **118**, 1329

[30] Sasaki T., Ebina Y., Fukuda K., Tanaka T., Harada M., Watanabe M., Chem.. Mat. 2002, **14**, 3524

[31] Ohya T., Nakayama A., Ban T., Ohya Y., Takahashi Y., Bull. Chem. Soc. Jpn, 2003, **76**, 429

[32] Gao T., Fjellvag H., and Norby P., Chem. Mater, 2009, **21**, 3503

[33] Sasaky T., Ebina Y., Tanaka T., Harada M., Watanabe M., Chem. Mat. 2001, 13, 4661

[34] Abe R., Shinohara K., Tanaka, A., Hara M., Junko N. Kondo, Domen K., Chem. Mater., 1998, **10**, 329

[35] Rabaste S., Bellessa J., Brioude A., Bovier C., Plenet J.C., Brenier R., Marty O., Mugnier J., Dumas J., Thin Solid Films, 2002, **416** , 242

[36] Surivet F., Lam T.M., Pascault J.P., Pham Q.T., Macromol., 1992, **25**, 4309

[37] Yoshida M., Prasad P.N., Chem. Mat., 1996, **8**, 235

[38] Jaseniak J., Pacifico J., Signorini R., Chiasera A., Ferrari M., Martucci A., Mulvaney P., Adv. Fun. Mat., 2007, **17,** 1654

[39] Epifani M., Leo G., Lomascolo M., Vasanelli L., Journal of Sol-Gel Sci. and Technol., 2003, **26**, 441

[40] Buso D., Post M., Cantalini C., Mulvaney P., Martucci A., Adv. Funct. Mater., 2008, **18**, 3843

[41] Enustun B.V., Turkevich J., J. Am. Chem.Soc. 1963, **85,** 3317

[42] JCPDS #040714 for Gold ; JCPDS #841285 for TiO_2 anatase

[43] Jellison G. E., Boatner L. A., and Budai J. D., Jeong B.S., Norton D. P.
J. Appl. Phys, 2003, 93, 9537

[44] Buso D., Pacifico J., Martucci A., Mulvaney P., Adv. Funct. Mater., 2007, **17**, 347

[45] Haruta M., Daté M., Appl. Catal. A: Gen,l 2001, **222**, 427

[46] Chang S.S., Shih C.W., Chen C.D., Lai W.C.,Wang C.R.C., Langmuir, 1999**, 15**, 701

[47] Perez-Juste J., Pastoriza-Santos I.,. Liz-Marzan L.M., Mulvaney P., Coordination Chemistry Reviews, 2005, **249**, 1870

[48] "Semiconductor and metal nanocrystals" edited by Victor I. Klimov, 2004 (Marcell Dekker, Inc)

[49] Yang L.L., Lay Y.S., Chen J.S., Tsai P.H., Chen C.L., Chang C.J., J Mat. Res., 2005, **20**, 3141

[50] Enustun B.V., Turkevich J., J. Am. Chem.Soc., 1963, **85,** 3317

[51] Mansur H.S., Oréfice R.L., Mansur A.A.P., Polymer, 2004, **45**, 7193

[52] Moharram M.A., Khafagi M.G. J Appl. Polymer Sci., 2007, **105**, 1888

Chapter 6

Waveguides and Vertical Optical Microcavities incorporating CdSe@ZnS NPs

6.1 Introduction

Quantum dots have been exploited for nanocomposite fabrication both in polymer and sol-gel derived inorganic matrices[1-8].

Embedding of nanoparticles in solid matrices allows for chemical and mechanical stability while preventing particles aggregation.

The main difficulties arising from the fabrication of such materials can be individuated in:

- achieving good compatibility between particles and host matrix material in order to keep nanoparticles homogeneously dispersed and retain optical quality.
- retaining optical properties of QD (PL-QY and monodispersion) inside the matrix.

Thus matrix material is not just a host, but it needs to have particular requirements to achieve the desired functional properties. Also the ligands introduced on particle surface have an important role. Proper ligand's choice or surface modification strategy is generally the only tool for QD compatibilisation with host material.

A great variety of strategies for QD surface fuctionalization has been developed includes: a) direct exchange of pristine ligands which usually expose hydrophobic chains such as trioctylphosphine oxide (TOPO); b) direct functionalization of particle's surface with polymers ("grafting to" approaches) from which macromolecular architecture can be grown; c) polymer growth initiated from the particle surface functionalized with suitable polymerization inititators ("grafting from" approaches); d) particle "encapsulation" in macromolecular structures such as dendrimers or micelles. These structures can be built using amphiphilic molecules which bind through hydrophobic interactions with pristine QD ligands. (see figure 6.1).

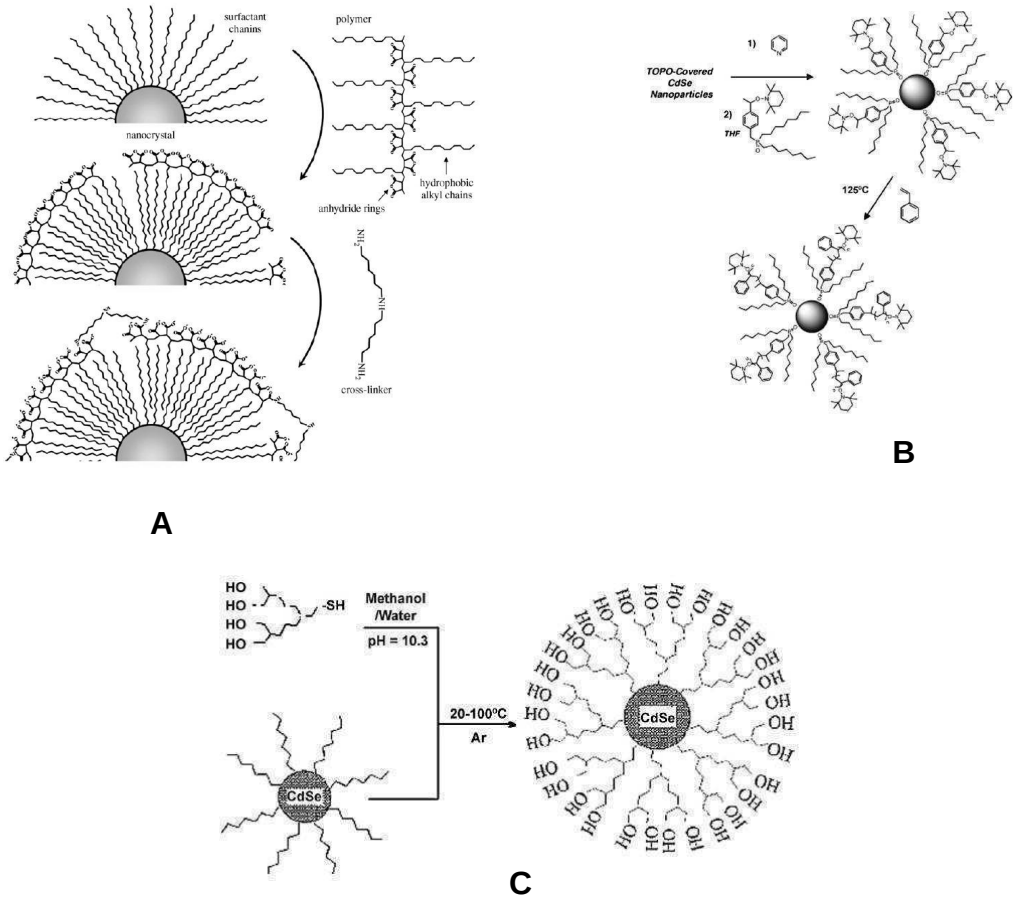

Figure 6.1 Functionalization of a particle covered with TOPO to which poly (maleic anhydride *alt*-1-tetradecene) is bound by means of hydrophobic interactions with alkyl chain of TOPO. The opening of the anhydride ring gives carboxylic acid able to stabilize the particle in water. An amino functionalized cross linker agent is added to stabilize the organic shell. [8] (A); Capping exchange of particle pristine ligands with nitroxide-functionalized molecules. This group can be used as initiator of styrene polymerization [9] (B); Capping exchange with thiol based hydroxyl terminated organic dendrons resulting in a water soluble particle with improved oxidation resistance [7] (C)

These strategies rely on exposing at the outer surface of ligands shell specific functionalities which can develop favorable interaction with host material, preventing or limiting the driving force toward aggregation. In some cases the exposed functionalities have been exploited in "grafting from" approaches, where moieties able to initiate polymerization reaction have been used along with the precursor monomers of the matrix in order to start the polymer chain directly from the particle surface[9]. The negative aspect of this approach is the incompatibility of particles with common polymerization methods, such as anionic or radical polymerization, which results to be too harsh for retainment of

optical properties. In figure 6.1 examples of interesting developments in QD's surface chemistry are given.

Furthermore, applications where matrix material need to have electronic accessibility toward nanoparticles, such as solar cells or light emitting devices [31], careful choice of surface ligands able to facilitate charge transfer between polymeric matrix and nanoparticles is necessary for the improvement of device performance.

Oxide material from sol gel processing have been used as matrices for QD composites used mainly in optical and photonic application, such as optical gain materials showing amplified stimulated emission (ASE).

The use of inorganic matrices provide enhanced stability and processability, along with high refractive index necessary if waveguiding configurations are used.

Silica, titania and zirconia have been used as host for semiconductor nanocrystals. Titanium oxide has been probably the most used for optical gain composites or fluorescent materials.

As synthesized nanocrystals are generally soluble in non-polar media and they are not compatible with sol-gel synthesis usually carried out in alcoholic solvents.

The general approach consists first to perform a capping exchange between the original ligands (generally TOPO or long chain alkyl carboxylic, phosphininc or phosphonic acids) with an amino-alcohols such as 5-amino-1-pentanol (AP) or 6-amino-1-hexanol (AH) [2,3] or *Tris*-hydroxylpropylphosphine [4,27] or both [6].

These molecules have functionalities such as phosphorous or amino groups that bind to the particle surface leaving hydroxyl groups to be exposed to the outer environment. Amino groups binds to the metal sites of particle surface, while phosphine based ligands binds to chalcogen sites [11]. Simultaneous usage of both type of molecule is probably the best solution for optimization of capping exchange.

This procedure not only allows for transfer from non-polar solvents to alcoholic solvents with good colloidal stability, but provides efficient compatibilization with sol-gel environment.

In fact, the presence of outer hydroxyl groups can be used for anchoring the particle to sol-gel precursors through OH condensation with hydrolyzed metal alkoxides., as schematically shown in figure 6.3

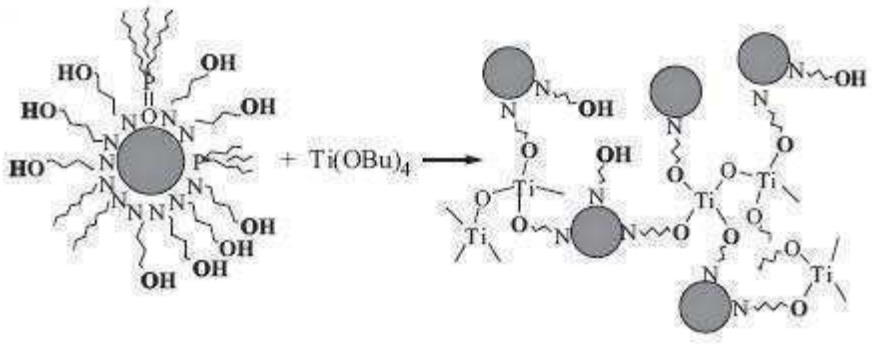

Figure 6.2 Ligand exchange with AP molecules and further hydroxyl condensation with hydrolyzed titanium alkoxide leading to particle immobilization in the sol-gel matrix (Source : Petruska et al.[5])

Accurate choice of sol gel precursors with organic functionalities (organo-alkoxides) able to bound directly to particle surface can be used to improve particles' homogeneity in the matrix. This has been done using 3-aminopropyltrimethoxysilane (APS) and (triethoxysilyl)propyl isocyanate (TSPI) as silica precursors [2]. In this case, after amino-pentanol functionalization and phase transfer in ethanol, organosilicon compounds were added. It was observed that APS was effective for preparing highly loaded composites but precipitation of QD occurred if it was employed as the only matrix precursor. This was attributed to the strongest affinity of amino functionality of the APS compared to AP which is thus displaced from particle surface causing QD aggregation. If TSPI is also used, better stability is obtained since isocyanate group is thought to have lower binding activity. The nanocomposite film obtained with this method showed high stability, absence of cracks formation as opposed to titania matrix films. Furthermore, high volume fractions of quantum dots were incorporated which allowed for high refractive index compared to the otherwise too low index values of undoped silica for waveguiding. These conditions are necessary for ASE.

In applications where stability of luminescence properties is required, such as ASE, electronic properties of the matrix material should be such to prevent excited QD charge carrier to leak into the matrix [10]. These arguments were used to explain the poor stability of luminescence and ASE of CdSe@ZnS particles in titania matrix with respect to zirconia both derived in an analogue method from sol-gel processing. In fact, since band gap of zirconia is wider than the titania one, carrier confinement in the particle is supposed to be enhanced in titania, leading to loss of emission stability and, likely, enhanced photo-oxidation (figure 6.3).

Beyond matrix consideration, the employed particles need to be the most stable is possible assuring absence of structural defects and the best confinement as possible in order to limit surface traps competitive with radiative recombination. Furthermore, surface stoichiometry has been found to play an important role in CdSe quantum dot photostability [11]. In particular, it was shown that a cadmium rich surface consistently enhanced the photostability if compared to a selenium rich surface. This suggest that a metal rich particle surface is much more desirable for stable devices.

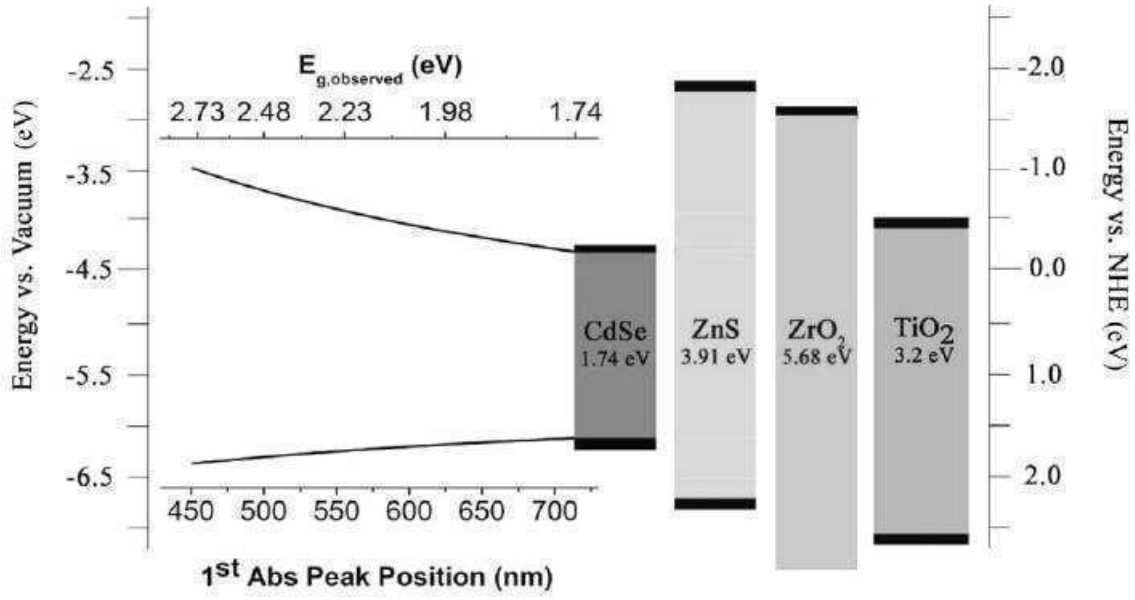

Figure 6.3 Comparison of CdSe band gap with varying size with TiO_2, ZrO_2 and ZnS. Zirconia provides the best insulation being the material with the wider band gap (Source : Jaseniak et al. coworkers [10])

Once a stable emission medium is obtained with these composites, their processability can be exploited in a number of application including, as an example, their introduction in structures possessing cavity or feedback mechanisms for the production of lasers.

In particular, coupling of QD emission with photonic structures to create distributed feedback gratings or co-planar microcavities have been exploited, allowing for lasing or study of cavity modification of the spontaneous emission[12-18].

In the following, amplified stimulated emission using QD is briefly discussed. In the experimental section nanocomposite film synthesis is described along with optical, ellipsometric and ASE characterization. Finally, the first results regarding the fabrication and optical characterization of a vertical co-planar microcavity are described.

6.2 Amplified stimulated emission with CdSe@ZnS quantum dots

Semiconductor lasers are extensively used in a number of fields. Quantum-confined lasers are expected to be more advantageous over semiconductor bulk devices due to lower lasing thresholds and minor performance sensitivity toward temperature due to discretization of electronic levels and consequent lower thermal depopulation of band edge states, while maintaining high gain values.

For these reasons, employment of semiconductor quantum dots for lasing purposes is considered very promising. The size dependence of luminescence spectrum also allows for easy tuning of emission color over almost all the visible range. Furthermore, established method for solvent processing and introduction in different matrices makes it possible to extend the use QD-based material in different photonic structures or devices.

The understanding of fundamental processes underlying optical gain in quantum dots has been addressed by Klimov and co-workers [22] and Woggon and co-workers [23].

If the band edge emission of a quantum dot is modeled with a two-level system with two-fold degeneracy, population inversion should begin for $N_{e\text{-}h}$ =1 while complete population inversion should be reached at $N_{e\text{-}h}$ =2, where $N_{e\text{-}h}$ is the average number of e-h pair in a dot. Thus, optical gain in semiconductor quantum dot should arise primarily from two e-h pair emission.

In order to obtain materials capable of optical amplification, also processes which acts to deplete the population of inverted states need to be considered, since they are competitive with gain achievement. In the case of quantum dots, such mechanisms are charge carrier trapping by surface states and Auger processes. For moderately well passivated particles, surface trapping effect can be neglected with respect to Auger process. As discussed in Chapter 3, in quantum confined system the rate by which Auger process depopulates excited levels is very fast and scales with R^3, where R is the particle radius. In particular, for the biexciton state the time (τ_2) for the Auger relaxation has been found to scale as $\tau_2 = \beta R^3$ with β equal to about 5 ps/nm^{-3} [25].

In order to observe optical amplification, the gain buildup time τ_s, i.e. the time necessary for light amplification to be established in the material, needs to be shorter than competitive gain states relaxation.

The gain buildup time depends on the volume fraction of quantum dots in the material and the gain cross section through [22] :

$$\tau_s = \frac{4\pi R^3}{3}\frac{n_r}{\xi\sigma_g c} \qquad \text{Eq. 6.1}$$

where σ_g is the gain cross section (defined as material gain g divided by the volume concentration of particles n_0), ξ is the particle volume fraction, n_r the refractive index of the gain material and c is the speed of light in vacuum.

For optical amplification τ_s has to be minor than τ_2. This condition leads to a minimum volume fraction of particle in the material to observe amplified emission, defined from Eq. 6.2.

$$\xi > \frac{4\pi}{3}\frac{n_r}{\sigma_g c\beta} \qquad \text{Eq. 6.2}$$

Inserting typical values for the quantities in this relationship (n_r=2, σ_g= 10^{-17} cm^2, β= 5 ps/nm^{-3}), a volume fraction of 0.005 is obtained. For these reasons, early attempts to obtain amplified emission with QDs precipitated from molten glass were unsuccessful since the achieved concentration was very low.

Klimov et al. [22,24] demonstrated ASE in closely packed films of quantum dots where the volume fraction was about 0.2. At increasing excitation pump fluence *f* (photon/cm^2) emission spectra are recorded (figure 6.4).

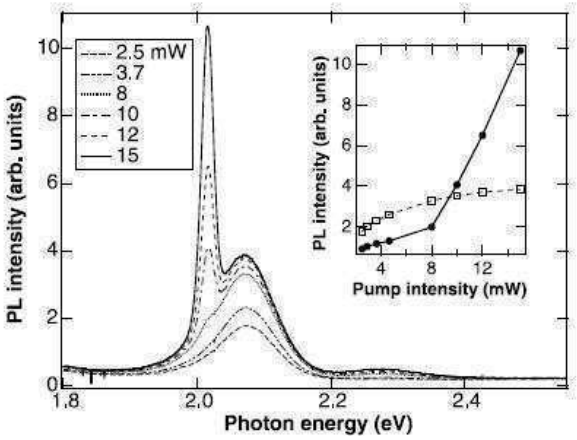

Figure 6.4 ASE emission spectra taken at increasing pump fluence. Inset: Emission intensity over pump intensity at the ASE peak (solid squares) and at spontaneous emission peak (opened squares) (Source : Klimov et coworkers [24])

Above a specific excitation power, the threshold power, a narrow peak, corresponding to the amplified emission, appears on the red side of the spontaneous fluorescence emission peak. This shift is a clear evidence that the gain state from which the amplified emission occurs is a biexciton state, due to coulomb interaction between the e-h pairs as explained in section 3.2.1.

Furthermore, using fs pulse excitation, the average number of *e-h* pair per particle can be estimated as $N_{e\text{-}h}= f\sigma_0$, where σ_0 is the absorption cross section at the excitation wavelength. The $N_{e\text{-}h}$ value at the threshold energy was determined to be 1.4, in agreement with the bi-excitonic nature of the gain process in quantum dots.

An advantage of quantum dot over other systems for optical gain is the high absorption cross section with respect, for example, to organic dyes. This leads to lower thresholds, since a lower excitation power is necessary to achieve the threshold value of $N_{e\text{-}h}$ for population inversion. Quantum dots also possess high absorption cross section in two-photon absorption processes, which has been used in ASE experiment showing the feasibility of up-converting wavelength lasing systems [27].

A method to study the amplified emission of a material is the variable strip length method (VSL)[28], where an optically active film is excited perpendicularly to the film plane over a stripe-type region whose length is varied. The emission is then probed laterally from the edge of the film.

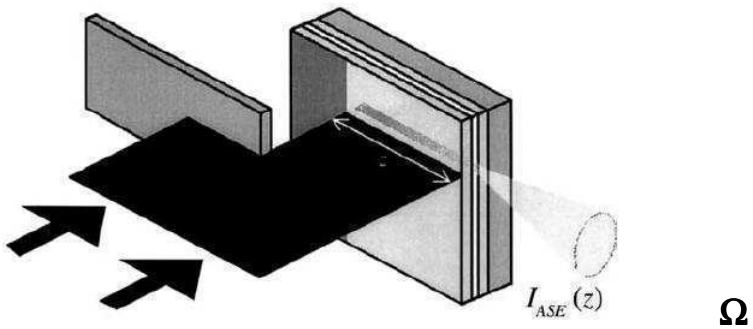

Figure 6.5 Schematic representation of ASE measurement with Variable Strip Length method (Source: Dal Negro et co-workers [28])

The active film needs to have a sufficiently high refractive index to be a waveguide. In these conditions the emitted light is coupled into the allowed mode of the waveguide, defined by an angle of propagation inside the waveguide.

As the emitted light propagates, it will experience light amplification along the ray path if the material is in the condition of population inversion, which in turn depends on the excitation fluence. This amplified emission is not a *lasing* emission, since it does not have complete coherence as in devices with feedback mechanisms. Thus it is called Amplified Stimulated Emission (ASE).

The intensity dependence on stripe length can be at first modeled within the 1D-amplifier model [29]. In figure 6.6 a two level system comprising an exited level with energy E_2 with a population N_2 and a ground level with energy E_1 and a population N_1 is represented.

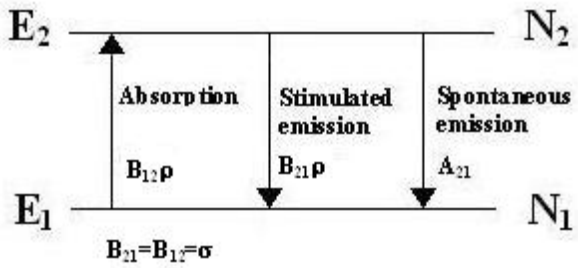

Figure 6.6 Two level system showing spontaneous emission, stimulated emission and absorption. $B_{21}\rho$, $B_{12}\rho$ and A_{21} are the transition rates and ρ the electromagnetic energy density

This system can undergo spontaneous emission, absorption and stimulated emission with the two latter processes depending on the field intensity, while the probability of each to occur is proportional to the population. From this model the following equation for intensity dependence on length can be derived [29]:

$$\frac{dI}{dz} = (N_2 - N_1)\sigma I(z) + N_2 \frac{\Omega}{4\pi} A_{sp} h\nu \qquad \text{Eq. 6.3}$$

Where σ is the cross section of absorption and stimulated emission, A_{sp} the spontaneous emission transition rate and Ω the solid angle viewed by the detector as shown in Figure 6.5.

If $N_2 > N_1$, the population inversion condition is achieved and quantity $(N_2 - N_1)\sigma$, which is the material gain coefficient g, is a positive quantity and the material acts as an optical amplifier. If Eq. 6.3 is integrated over length the following is obtained:

$$I(Z) = \frac{J_{sp}}{g}(e^{gZ} - 1) \qquad \text{Eq. 6.4}$$

J_{sp} is $N_2 A_{sp} \frac{\Omega}{4\pi} h\upsilon$.

This relationship accounts for the typical super-linear intensity profile versus stripe length, as shown in the inset of figure 6.4.

In quantum dot composites, Auger effect diminishes the gain lifetime. This effect must be considered for fitting experimental data and can be taken into account by the following equation proposed by Chan et al. in ref. [26] and used also in ref [27].

$$I(Z) \propto e^{gl_a(1-e^{-z/l_a})} \qquad \text{Eq. 6.5}$$

where l_a is the effective gain length and takes into account for the fact that the inverted species (biexciton states) diminishe over a length scale l_a due to Auger process.

Eq. 6.5 is used for fitting VSE data for QD loaded material. An example of ASE for QD loaded films is given in figure 6.7 along with the fitting curve obtained using Eq. 6. 5 .

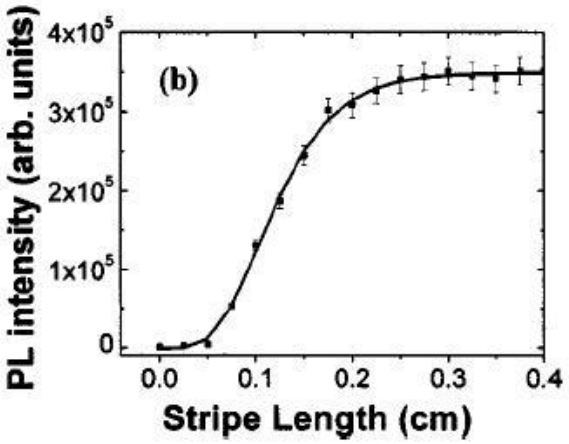

Figure 6.7 Typical ASE profile fitted with Eq. 6.5 for a quantum dot loaded silica nanocomposite (Source: Chan et co-workers [26)]

Typical modal gain values estimated from VSE methods for quantum dot nanocomposites are around 100 cm^{-1}.

6.3 Experimental

6.3.1 *QDs functionalization and preparation of QDs loaded thin films*

In this section the procedure for embedding quantum dots in sol-gel derived zirconia film for optically active waveguide is described.

The first step is a proper functionalization of QDs in order to make them stable in sol-gel environment.

1-amino-1hexanol (AH) was employed in the capping exchange procedure where lipophilic ligands attached to particle surface (TMPPA and ODA in our case) is displaced by AH imparting solubility in alcoholic media and stability in the sol-gel matrix, as described previously.

The procedure, analogue to that reported in refs.[10,27] and can be summarized as follows:

- The purified CdSe@Shell dispersed in 4 ml of chloroform deriving (derived from a typical batch described in Chapter 3) are precipitated by adding 10 mg of AH dissolved in chloroform. The solution becomes turbid soon after AH addition due to instability of particles with an outer coverage of hydroxyl groups in chloroform. The solution is let to stir in an heterogeneous state for 3 hours. Then the particles are precipitated at 4000 rpm for 3 minutes. For this procedure to work particle surface should be metal rich since amine functionality binds to metal sites.
- The particles are then dispersed in 1 ml of a 0.1M AH ethanolic solution and 1 ml of chloroform is added. In this solvent mixture the particles are stable and are left under stirring for at least 24 hours or prior to usage in sol-gel films.
- The particles are again precipitated from this solution by adding excess hexane and dispersed in iso-propanol. The concentration is such that the absorbance of the 100-fold diluted solution is 0.25 at the band edge. This solution is further used for doping sol-gel solutions. In the case of C2-CSS particles, solutions with optical absorbance at the band edge of 0.125 and 0.05 if 100-fold diluted were also prepared for doping sol-gel matrices. We made use of the solution optical absorbance to refer to different particles concentrations since the molar extinction coefficient necessary to calculate the molar concentration is not known for the core@shell NPs obtained in this work.

This procedure has been followed for all type of particles employed for film fabrication.
A slight variation has been introduced from particles obtained using $(TMS)_2S$ for ZnS shell growth. In this case 5 mg of Zinc Acetate is introduced in the second stage of the described procedure to enrich the particle surface with zinc atoms, otherwise dispersion in alcohol was not possible due to less efficient *AH* exchange on a sulfur rich surface.

QD-doped zirconia film were prepared as follows:

- Zirconia sol was prepared by dissolving 0.23 ml in 6 ml of isopropanol and then adding 1 ml of $Zirconium(Isopropoxide)_4$.
- 100 µl of Zirconia sol is mixed with 200 µl of QD sol and spun on quartz substrates at 3000 rpm for 20 seconds. Four or five layers are deposited to have film with a sufficient thickness in order to get waveguiding properties at the emission wavelength of quantum dots. Each layer was treated at 250°C for 5 minutes. This thermal treatment has been chosen as a compromise between the need of material densification necessary for high refractive index and the degradation of QD [10]. In order to obtain films with different QD concentrations, the same procedure was adopted in terms of mixed volumes but using colloidal QD solutions with different concentrations prepared as previously described. This was done only with C2-CSS type particles and deposition with increasing concentration will be referred to as **QD 5**, **QD 12,5** and **QD 25** respectively.

6.3.2 *Optical and ASE characterisation of QDs-Zirconia depositions*

The introduction of QDs in zirconia has been mainly characterized with ellipsometry technique and UV-Vis spectroscopy.

The effect of quantum dots on the optical properties of the films can be analyzed from refractive index and extinction coefficient determination with increasing particle concentration. These data are shown in figure 6.8 for films prepared using a batch of particle with the C2-CSS structure whose concentration has been varied as explained in the experimental.

The introduction of quantum dots results in an increase of the refractive index for **QD 25** and **QD 12.5** concentrations, while for the lower **QD 5** concentration the refractive index is almost unchanged with respect to undoped ZrO_2 film. This can be explained by the introduction of high-refractive index (around 2.3) semiconductor particles. The extinction coefficient values resemble the typical absorption spectra of quantum dots, even if at the lower concentration the excitonic peak cannot be distinguished from fitting of ellipsometry data

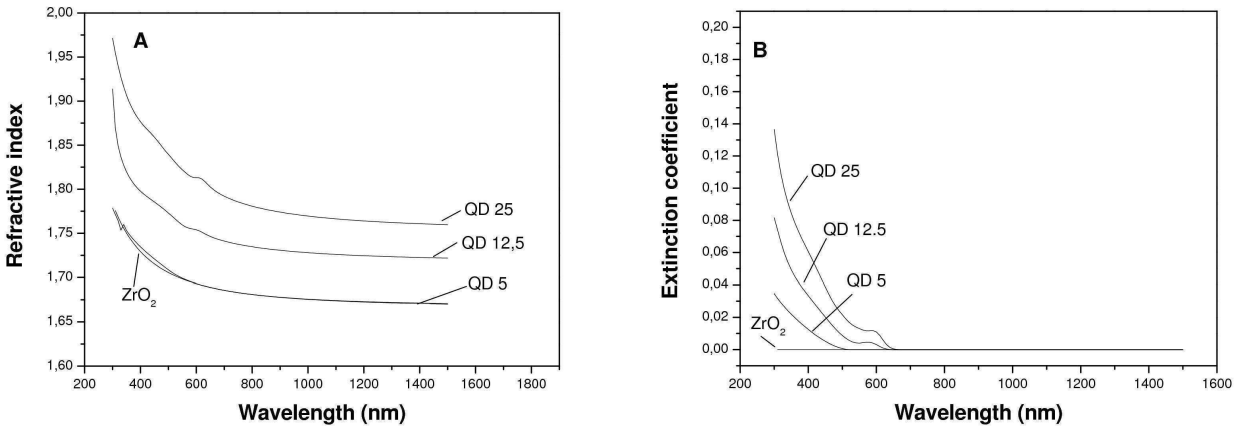

Figure 6.8 Refractive index (left) and extinction coefficient (right) curves for undoped ZrO_2 matrix and QD nanocomposite with different concentrations

Films with **QD 25** concentration were prepared with C2-CSS, C1-CSSS and C2-CSSS type particles. Ellipsometry data are presented below in figure 6.9.

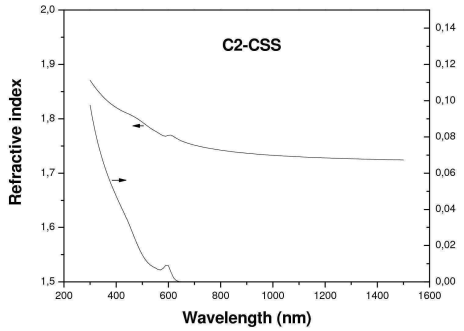

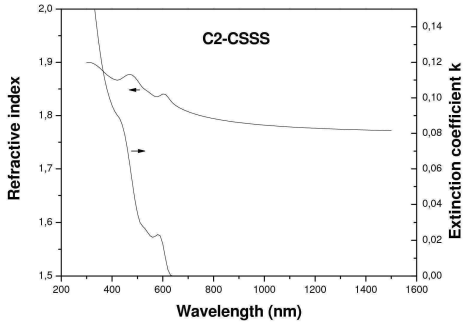

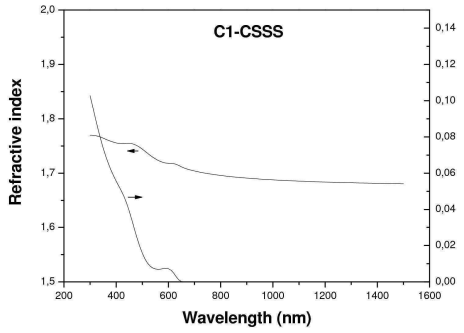

	From ellipsometric data			From R and T data	
	n (630 nm)	**k_{ell}** at λ_{abs}	**t** (nm)	**λ_{abs}**	**$k_{R,T}$** at λ_{abs}
C2-CSS	1.76	0.0089	352	598	0.0068
C1-CSSS	1.71	0.0072	602	596	0.0037
C2-CSSS	1.82	0.0224	664	610	0.0049
Undoped ZrO_2	1.69	-	-	-	-

Figure 6.9 Refractive index and extinction coefficient curves for zirconia films with different types of quantum dots at a concentration QD 25. In the table the refractive index n ar 630 nm, the extinction coefficient k_{ell} (at λ_{abs}) and film thickness t are estimated from ellipsometry data fitting, while the position of the first absorption peak λ_{abs} and extinction coefficient $k_{R,T}$ are estimated from *R* and *T* measurement of the nanocomposite film

The absorption of QDs in the deposited films can be extracted from transmittance and reflection measurements of composite films. These data were collected using an integrating sphere and allows for determination of total reflectance and transmittance. The absorption can be evaluated as *1-R-T* where *R* and *T* are the reflectance and transmittance of the composite film on quartz substrate. In this way we can eliminate the interference fringes from absorption spectra of the film isolating pure absorption component. The absorption measured in this way is presented in figure 6.10.

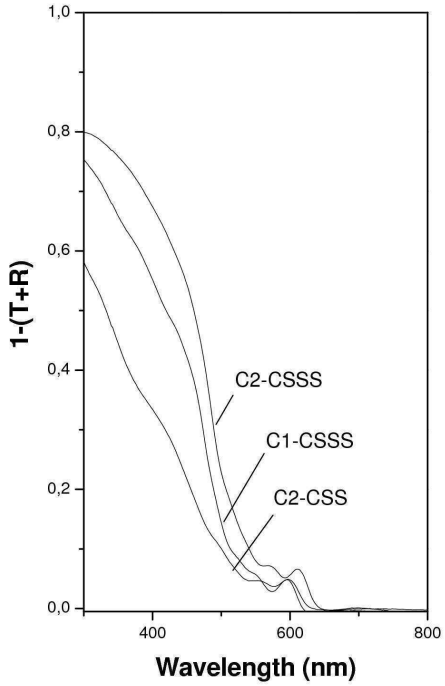

Figure 6.10 Absorption of QD-loaded films at a concentration QD 25 estimated from total reflectance and transmission measurements using an integrating sphere for different particles type

From these data we can retrieve the first absorption peak position and width. They are found to be almost the same as in solution, indicating no dissolution or broadening under film treatment.

Extinction coefficient values at the first absorption peak can also be evaluated from these data, $k_{R,T}$ through the following relationships:

$$k_{R,T} = \frac{\lambda_{abs}\alpha}{4\pi} = \frac{\lambda}{4\pi}\frac{(-\ln(R+T))}{t} \qquad \text{Eq. 6.6}$$

being α the absorption coefficient which can be evaluated from the Lambert-Beer formula $\alpha = \frac{-\ln(T)}{t}$.

where T is substituted with $T+R$ to isolate the pure absorption component. Then the extinction coefficient k is linked to α through $\alpha = \frac{4\pi k}{\lambda}$. Using the film thicknesses estimated from ellipsometry data, $k_{R,T}$ are calculated and presented in the table of figure 6.8. These values are smaller than those estimated from ellipsometry data fitting.

The obtained samples often present typical surface roughness caused by striations phenomena occurring during spin casting. Thus, scattering caused by surface

inhomogeneities of the film can be taken as a possible explanation of the difference of *k* values estimated by different methods. In fact, *k* values from ellipsometry are obtained from fitting the ellipsometry parameters along with transmission data measured with a standard configuration, that is without the integrating sphere. In this case transmission losses due to scattering are accounted as higher *k* values in the data fitting procedures.

The use of an integrating sphere apparatus allows to detect also the scattered light and the pure absorption component is retrieved. For these reasons, *k* values retrieved with this method are more reliable.

A tentative estimation of the volume fraction of quantum dots in the film can be made from the knowledge of extinction coefficient values of the nanocomposite material and particle absorption cross section at the band edge. Since the latter quantity has not been determined for the QD used, an estimated value need to be taken from the literature. One possibility is to use the cross section value for CdSe core absorbing at the same wavelength of our core@shell C2-CSS particles, obtaining a value of 1.209×10^{-15} cm^2. In ref [27] the cross section at 400 nm for a core@shell particle similar to our C2-CSS sample has been reported. This value is larger than that relative to the first absorption peak because absorption is larger at smaller wavelengths. We can account for this by simply normalizing the absorption from an absorption spectrum of our particles, obtaining a value of 0.4×10^{-15} cm^2.

If these two values are used, the volume fraction of C2-CSS particles in the zirconia film can be estimated in the range 0.09-0.26, where $k_{R,T}$ has been used for these calculations.

Arguing similar values for the other samples, we can state that the quantum dots volume fraction is very likely larger than the 0.005 estimated threshold value necessary to have ASE.

These films underwent ASE experiments in order to test the possibility to use such materials as gain media for lasers. The experimental setup used is described in Chapter 2.

All the described depositions showed the appearance of ASE peak above a definite value of pumping intensity, both under 1-photon excitation at 400 nm wavelength and 2-photo excitation wavelength, as shown in figure 6.11.

ASE threshold power and VSE measurements are presented in figure 6.11 for both 1-photon and 2-photon excitation.

ASE threshold at 1-photon excitation is around 0.1 mJ/cm^2 fluence, which is typical for this systems. The same is true for 2-photon excitation but with much higher threshold values .

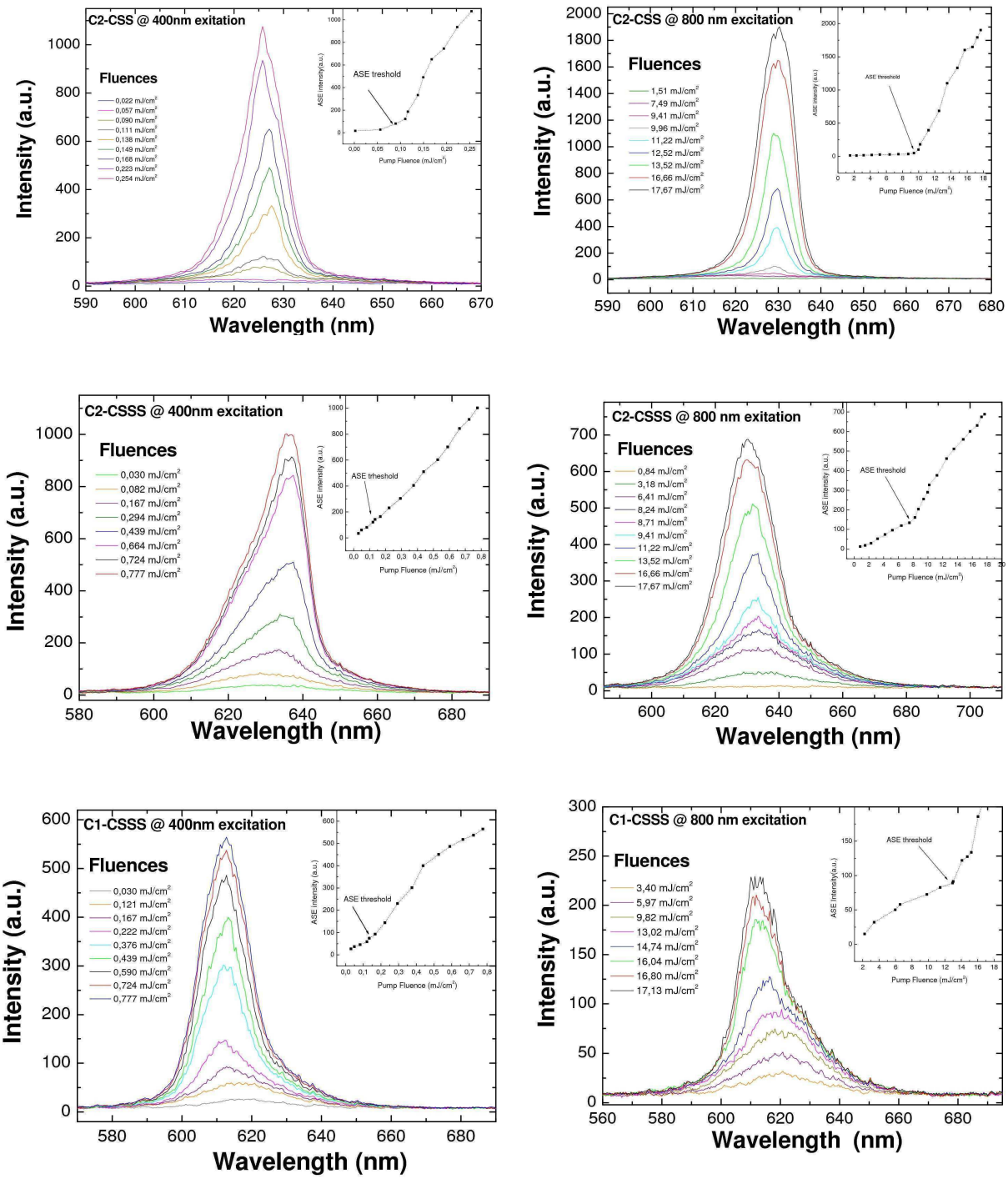

Figure 6.11 ASE emission profile and threshold for different particles at 400 nm and 800 nm excitation wavelength

A red-shift of the ASE peak is present in these C2.CSS and C2-CSSS samples due to the negative interaction energy of the bi-exciton state. For the C1-CSSS, a blue-shift of the peak is observed, suggesting for a positive interaction energy. This fact is unusual in ASE experiments and it lacks of explanation at the moment.

The stability of the ASE peak over excitation time is shown in figure 6.12 only for C2-CSS sample, being the behavior of the other samples analogue.

Stability was not satisfactory particularly under 2-photon excitation. The intensity of the ASE peak shows about a 30% decrease within one hour under 1-photon excitation and a fast disappearance in about 5 minutes under 2-photon excitation.

The poor stability is likely due to the thin ZnS layer on these particles (see section 3.4.2.3), which do not offer resistance against photo-oxidation, which can be responsible of degradation of the emission properties.

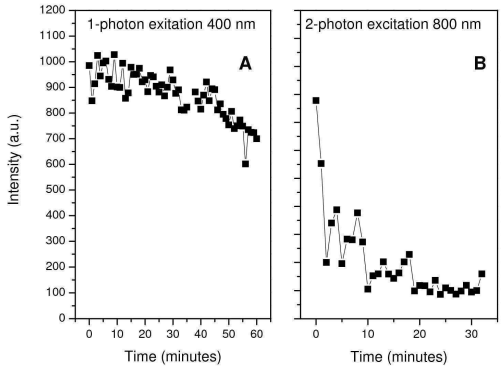

Figure 6.12 ASE intensity evolution with time under 1-photon and 2-photon excitation

VSL measurements are presented in figure 6.13 for C2-CSS particles in zirconia films. Data fitting was performed with the integrated form of Eq. 6.7. This model has been proposed by Jaseniak et al.[27] and it is analogue to that expressed from Eq. 6.5.

$$\frac{dI_{bx}}{dz} = g(z)e^{-\frac{(z-z0)}{l_a}} I_{bx}(z) \quad \text{where } g(z) = 0, I_{bx} = 0 \quad \text{if } z < z_0 \text{ and } g(z) = g \text{ if } z > z_0$$

$$\frac{dI_{sx}}{dz} = J_{sp} \qquad \text{Eq. 6.7}$$

$$I = I_{sx} + I_{bx}$$

In this case the total intensity I is separated in biexciton (I_{bx}) and single exciton (I_{sx}) emission intensities contributions. The former gives rise to optical amplification while the latter accounts for the spontaneous emission. The spontaneous emission from the biexciton state is neglected.

Z_0 is an offset fitting parameter accounting for pump beam inhomogeneity at the sample edge and J_{sp} is a factor related to the spontaneous emission generation. As previously

described, l_a is the effective gain length related to the biexciton lifetime (limited by Auger process) and can be defined as the biexciton lifetime multiplied by the speed of light in the medium.

This fitting procedure allows determining the gain coefficient g. Values in the order of few hundred cm^{-1} were obtained in agreement with those usually found in the literature [24,27]. Analogue results have been obtained for samples prepare with other shell structure.

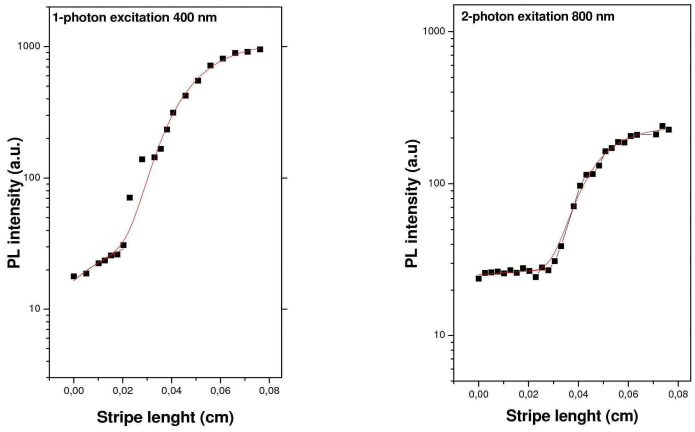

Figure 6.13 VSE measurements and fitting using Eq. 6.5 for C2-CSS particles containing zirconia films

Main data retrieved from ASE measurements are summarized in Table 6.

	1-photon 400 nm excitation		2-photon 800 nm excitation	
	ASE Threshold (mJ/cm^2)	**Stability** (% decreasein 60 min)	**ASE Threshold (mJ/cm^2)**	**Stability**
C2-CSS	0.073	24.8	9.405	*
C2-CSSS	0.172	12.2	9.013	*
C1-CSSS	0.158	40.7	14.064	*

(*stability are not reported since ASE peak decrease in a period minor to 5 minutes)

Table 6.1 ASE threshold, gain factor g and stability (defined as % decrease of ASE peak after one hour of excitation) are reported for different type of particles in zirconia under 400 nm and 800 nm excitation wavelength

ASE threshold are much lower for 1-photon excitation than 2-photon excitation. This is related to the lower 2-photon absorption cross section causing much higher fluences to achieve population inversion. Furthermore, the employment of a CSSS structure seems to result in higher ASE threshold values. This suggests that under the synthetic procedures adopted, the growth of more complex shell structures can result in higher probability of structural defects leading to lower PL efficiency and need of higher pump intensity to obtain optical amplification.

Even if the stability needs to be improved, our samples demonstrate the possibility to obtain up-conversion, i.e. emission of higher energy radiation than that used for excitation.

With the aim of increasing ASE stability, particles with improved ZnS shell (synthesized using $(TMS)_2S$ as sulfur precursor as described in section 3.4.2) were embedded in ZrO_2 films with concentration corresponding to **QD 25**.

In this case ASE emission was observed under 2-photon excitation which soon disappeared after few seconds. If the deposition was again exited in the same point, ASE occurred again showing the same behavior. We cannot find an explanation to this behavior that does not seem to be related to degradation of the particles, otherwise further excitation should not be accompanied from ASE emission.

It is likely that trap states are involved which might arise from structural defects in the shell structure. Even if a thicker ZnS shell has been developed, it has probably been grown with poor epitaxial matching on the pristine core structure. It is apparent that synthesis need further optimization.

6.3.3 *Optical microcavities incorporating QDs*

6.3.3.1 Basic principles of coplanar microcavities

Radiative transitions occur in two distinct ways: stimulated emission and spontaneous emission. The first depends on the electromagnetic field in the active medium and can be manipulated in order to have lasing emission by coupling it to feedback mechanisms.

Spontaneous emission has long been believed to be a process which could not be controlled. In the few last decades, it has been shown that if an active medium is put in microscopic optical cavities or photonic crystals, the spontaneous emission rates and profile are altered.

Among all available optical structures, Fabry-Perot resonator is the most simple. It consists of two co-planar mirrors separated by a distance which is of the order of the wavelength of light in the case of microcavity structures.

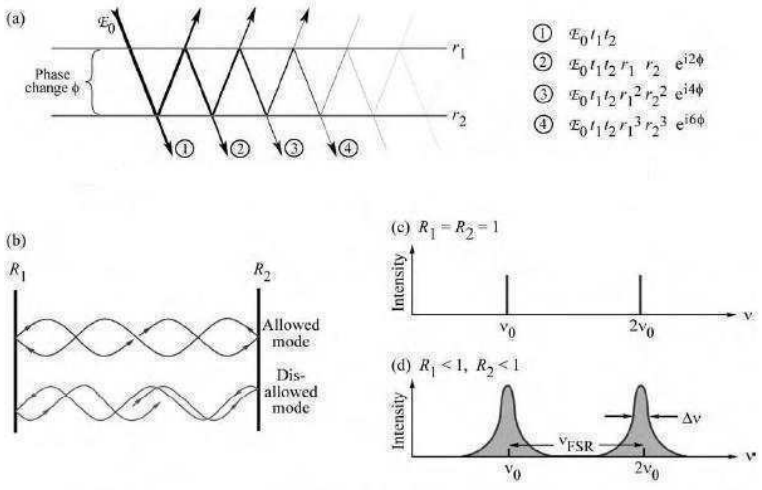

Figure 6.14 Schematic representation of electromagnetic waves in a cavity defined by two mirrors with reflectivity R_1 and R_2 (Source : Schubert [30])

The transmitted waves emerging from a cavity is the sum over all the waves generated from internal reflection at the cavity interfaces, as shown in figure 6.14a. The phase difference ϕ (here defined for a single pass between the two reflectors) between these waves determines the transmittance of the cavity which finds its maximum when

$2\phi = 0,2\pi,4\pi...$,where constructive interference is achieved, while for different ϕ transmittance decreases with a Lorentzian type profile (at least near the maximum value). The maximum transmittance and the phase change $\phi_{1/2}$ at which transmittance decreases to half its peak value can be estimated from the following equations [30]:

$$T = \frac{T_1 T_2}{(1-\sqrt{R_1 R_2})^2} \qquad \text{Eq. 6.7}$$

$$\phi_{1/2} = \frac{[1-\sqrt{R1R2}]}{[4(\sqrt{R_1 R_2})^2]^{1/2}} \qquad \text{Eq.6.8}$$

Where R_1 and R_2 are the reflectivity of the mirrors delimitating the cavity.

For symmetric cavities where $R_1 = R_2$ the maximum value of transmission is 1 independently of the reflectivity value of the mirrors, while for asymmetric cavities ($R_1 \neq R_2$), the transmittance peak value is lower than 1.

From another point of view, the possibility to have a transmitted wave through the cavity corresponds to the existence of an allowed mode, as shown in figure 6.14b. In our case, this condition is fulfilled when a standing wave can be sustained inside the cavity.

From a practical point of view, it is more convenient to use frequency or wavelength instead of the phase. These are all equivalent quantities through the following relationships:

$$\phi = \frac{2\pi n L_{cav}}{\lambda} = \frac{2\pi n L_{cav} \nu}{c} \qquad \text{Eq. 6.9}$$

where n is the refractive index of the cavity, ν and λ are the frequency and the wavelength of the light in vacuum.

Thus the condition for fundamental frequency or wavelength of the allowed optical modes is :

$$N = \frac{2nL_{cav}}{\lambda} = \frac{2nL_{cav}\nu}{c} \qquad \text{Eq. 6.10}$$

with N being an integer number and L_{cav} the cavity thickness.

From figure 6.12c it is possible to see that in the case of unity reflection of both mirror the width of the transmittance peak is zero and it tends to broaden with decreasing reflectivity of the mirrors.

The cavity finesse, *F*, is a parameter which takes into account the peak width and is defined as the separation in frequency between two allowed modes and the peak width in frequency Δν. Another frequently used parameter is the quality factor, *Q*, defined as ν/Δν, where ν is the fundamental frequency of the allowed mode. Using the previous relationships, Q can be calculated as follows:

$$Q = \frac{\nu}{\Delta\nu} \approx \frac{\lambda}{\Delta\lambda} \qquad Q = \frac{2nL_{cav}}{\lambda}\frac{\pi}{(1-\sqrt{R_1R_2})} \qquad \text{Eq. 6.11a,b}$$

High quality cavity imply high *Q* values.

When an emitter is inserted in a cavity, enhancement of the spontaneous emission is observed if the emission wavelength is the same as the wavelength of the allowed mode of the cavity. Emission in a spectral region which does not overlap the transmittance peak of the cavity is instead suppressed.

This effect can be understood on the basis of the following quantum-mechanical expression for the rate of the radiative transition W_{spont}:

$$W_{spomt} = \int_0^\infty W_{Spont}^{(l)} \rho(\nu_l) d\nu_l \qquad \text{Eq. 6.12}$$

where $W_{Spont}^{(l)}$ is the spontaneous emission rate into the optical mode *l* and $\rho(\nu_l)$ is the optical mode density [30]. While the first term in the integral depends only on the wavefunction of the initial and final states of the transition, the density of optical modes can be modified.

In a coplanar microcavitiy, the density of optical modes is greatly enhanced for allowed mode frequencies and suppressed elsewhere with respect to the constant free space optical mode density, as shown in figure 6.15.

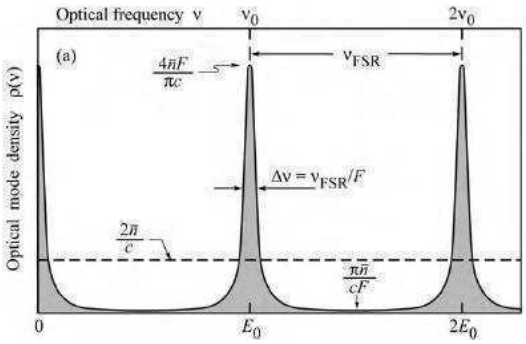

Figure 6.15 Optical mode density in a coplanar cavity (Source Shubert [30])

Thus, emission rate and intensity from an emitter inside a cavity is greatly enhanced with respect to free-space emission. This enhancement (also referred to as the Purcell effect), *G*, increases with the finesses F or quality factor *Q* of the cavity and can be estimated below for emission at the fundamental wavelength of the cavity :

$$G = \frac{2}{\pi}\frac{\pi(R_1R_2)^{1/4}}{(1-\sqrt{R_1R_2})} \qquad \text{Eq. 6.13}$$

As for the integrated enhancement one should take into account the overlap between the emission in free-space and cavity resonance. If the latter is narrower than the former, suppression of emission at wavelengths located out of the cavity mode occurs. Thus emission spectral narrowing is observed in this case.

Another interesting feature is the cavity resonance and cavity emission position dependence on the direction from which the structure is observed. This dependence is originated from the fact that light emerging from the structure at an observation angle ψ different from normal direction is originated from light rays traveling in the cavity at an angle θ with respect to normal (see figure 6.16). This introduces a different optical path and phase differences ϕ with respect to the normal direction. The dependence of resonance wavelength λ(θ) on θ is given from by Eq. 6.14.

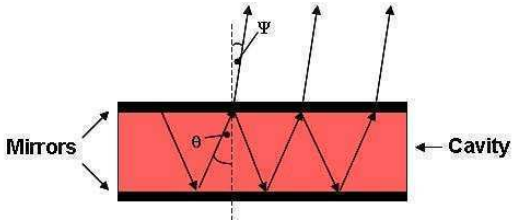

$$\lambda(\theta) = \lambda(0)\cos(\theta) \qquad \text{Eq. 6.14}$$

Figure 6.16 Detection angle (Ψ) dependence of mode position

where $\lambda(0)$ is the resonance wavelength at normal direction as defined from Eq. 6.10.
Thus, by tuning the observation angle also the emission wavelength range that are enhanced is varied, this causing a shift of the cavity emission peak.

6.3.3.2 Fabrication of optical micro-cavity incorporating QDs

In order to fabricate the micro cavity, we decided to use silica-titania Bragg grating structures as mirrors since they allows to obtain high reflectance using simple spin coating techniques.
The cavity layer is made using zirconia's doped quantum dots prepared as described previously.
A difficulty which is encountered in fabricating such devices is related to the compatibility of the material treatment used. In our case, a serious limitation is given by the high temperature involved in the creation of the high refractive deposition of the Bragg grating mirror, since temperature higher than 250°C are forbidden to quantum dots. This problem can be solved by using low temperature techniques such as rf-sputtering which allows to deposit high refractive index without further thermal treatment. This technique is time consuming and it is not available in our laboratories. Another possibility is to grow a Bragg mirror by conventional sol-gel techniques treating the material at elevated temperatures. Then the defect layer with quantum dots is deposited but a second Bragg grating cannot be deposited in the same manner. So a sputtered metal mirror (for example silver) can be deposited as the cladding mirror obtaining an asymmetric cavity. This procedure retain emission properties of QD, but the reflectivity of silver is limited to 0.9, limiting Q values and the possibility to play with mirror reflectivity if lasing applications are considered.

In Chapter 5, we showed the possibility to produce Bragg gratings at low temperature as 200°C using lamellar titanates after exposure to UV radiation, suggesting the utilization of this procedures for fabrication of the microcavity .
The target structure we designed includes a first Bragg grating on quartz substrate where both silica and titanate layers are treated at 500°C (labeled as **grating 500** in Chapter 5), the deposition of the ZrO_2-QD layer with concentration **QD 12,5** (C2-CSS particles were used) and a final Bragg grating by exploiting the UV treatment on titanate films (labeled as **grating UV**). The procedure for grating fabrication is given in Chapter 5.
A schematic representation of the structure is given in figure 6.17.

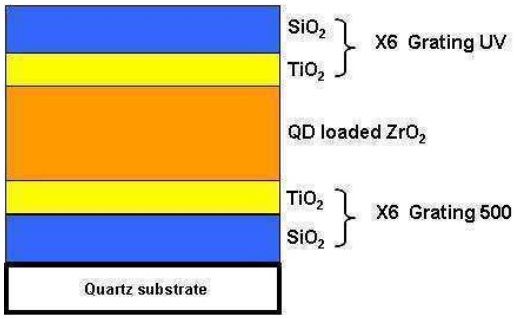

Figure 6.17 Schematic representation of the target microcavity structure

The Bragg gratings consists of six silica-titania doublets. Reflectivity can be enhanced by simply increasing the doublets number. In this first attempts, we decided to stop to 6 doublets value since in both type of mirrors quite high reflectivity was reached and problems arising from possible stress build-ups are minimized, even if deposition of more layers can be exploited. Reflectivity at 620 nm was evaluated to be 0.95 and 0.9 for **grating 500** and **grating UV** respectively.

A concentration QD 12,5 in the defect layer was employed in these first attempts to avoid risk of too high absorption of the cavity which can limit the cavity effect.

After the growth of **grating 500** on a quartz substrate, the defect layer was deposited.

The refractive index of the zirconia doped film with concentration **QD 12.5** was first measured and the cavity thickness was calculated using Eq. 610 in order to have a cavity resonance at 620 nm overlapping the spontaneous fluorescence emission of the nanoparticles embedded in the film.

The defect later with the exact thickness was the most difficult step since only slight variation of few nanometers can significantly shift the cavity position. For the measured refractive index of 1.76, a layer thickness of about 176 nm is calculated. We decided to grow the cavity depositing 3 consecutive layers. Spin coating conditions for obtaining the required layer thickness were calibrated measuring the thickness by spectroscopic ellipsometry on silicon substrates. The active material was then deposited on the Bragg reflector and an annealing step at 250°C for 5 minutes was applied at each deposited layer.

A reference sample consisting of a deposition o QD doped zirconia on a quartz substrate prepared in the same conditions as for the cavity in order to obtain has been prepared. An absorption spectrum derived from total reflectance and transmittance measurements of the reference sample is reported in figure 6.18.

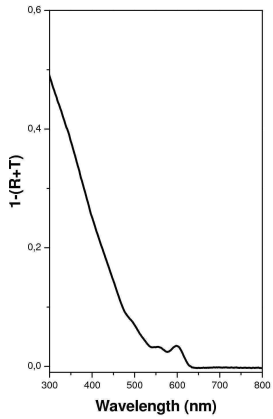

Figure 6.18 Absorption spectrum of the reference sample from total reflectance (R) and transmittance (T) measurements

The final **grating UV** was deposited. The resulting structure have the optical properties shown in figure 6.17.

In figure 6.19A, transmission and reflectance spectra are taken using an integrating sphere. The experimental set-up is such that absorption is taken perpendicularly to the surface, while reflectance is taken at an incident direction which slightly differs from normal one of few degrees. This allows to have an estimate of the cavity position at normal direction both in transmittance and reflectance. In the same figure, the emission spectra of a deposition of the same cavity material on quartz substrate measured with a standard spectrofluorimeter is also included. Very good overlap between spontaneous emission of the quantum dots and cavity position is seen.

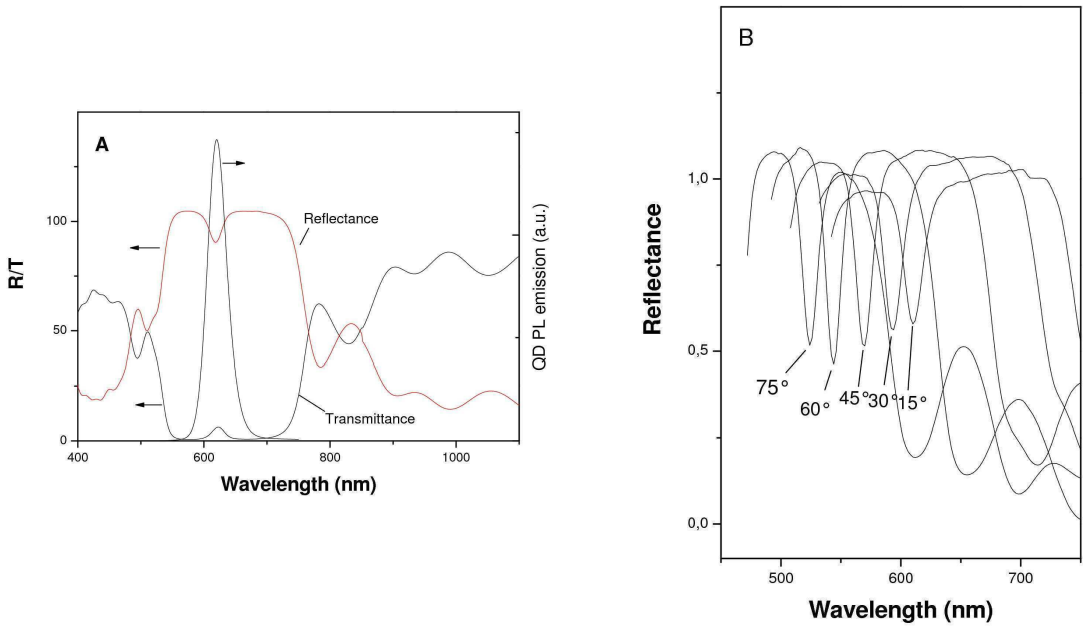

Figure 6.19 Transmission and reflectance (normal incidence) and spectrum taken with an integrating sphere set-up with PL emission of a QD loaded zirconia reference film (A); Specular reflectance spectra taken on ellipsometry at different reflection angles in the 15°-75° degree range (B)

The software of the ellipsometer allows to simulate the optical properties of the structure shown in figure 6.17 using previously measured optical parameters of the material of each layer. Silica and titania film thicknesses were set equal to the values necessary to maximize the reflectivity at 620 nm. Then reflectance spectra are simulated by varying the thickness of the cavity layer. The obtained results are reported in table 6.2.

In figure 6.19B, specular reflectance spectra at different incident angles measured with the ellipsometer are presented. In this case, measurements could be taken only for reflection angles higher than 15° due to physical limitation of the instrument. The expected dependence of the cavity position on the reflection angle is observed.

The cavity positions obtained with this measurement can be compared with simulation carried out for the same reflection angles. In this case the best accordance is found for a cavity layer with a thickness of 174 nm (see table 6.2), in good agreement with the target value of 176 nm.

Angle (°)	**Simulated cavity position with 174 nm thickness (nm)**	**Simulated cavity position with 178 nm thickness (nm)**	**Observed cavity position (nm)**	**Observed FWHM cavity peak width (nm)**
0	618	622	618 (*)	20(*)
10	615	619	-	-
15	611	616	611	19.2
20	607	611	604	19.6
30	596	599	592	18.1
45	571	574	567	18.2
60	546	548	542	16.3
75	526	528	522	15.6

(*) obtained from transmission data taken on ellipsometer in the same sample conditions as for reflection data

Table 6.2 Simulated cavity position using ellipsometer software for different cavity thickness, observed cavity position from reflectance data and observed cavity emission position and peak width

At normal direction the cavity position has been estimated from transmission spectra taken with the ellipsometer with the same sample orientation and position with respect to light beam used for reflectance, and found to be at 618 nm. The estimated *Q* value from this transmission spectrum is 31 and an analogue value of 35 is retrieved from reflectance spectrum at 15°.

The emission of the cavity has been characterized using the apparatus schematized in figure 6.19.

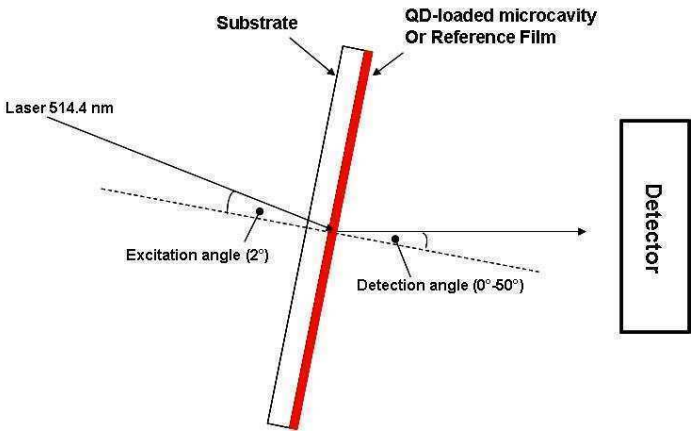

Figure 6.20 Schematic of set-up used for characterisation of optical microcavity incorporating QD emitters

The excitation laser was at 514.4 nm wavelength and with 1.6mW power. Measurements were performed at 2° incident angle with respect to normal direction to the substrate. In these conditions, the transmitted intensity was 0.8 mW and 1.5 mW for cavity and reference samples respectively.

The emission from the cavity was collected at different detection angles in the 0°-50° range, while emission from the reference sample was detected at 0° and 50°.

Cavity emission results are summarized in figure 6.20.

The normalized emission spectra are reported in figure 6.21A at 0° detection angle for the cavity and for the reference sample. The shape of the cavity emission taken in two different regions of the sample is also reported and it appears to be different.

The effect of the cavity is apparent leading to narrowing of the emission peak with respect to reference emission. The coupling of the photonic structure with the QD's emission is also proved by the expected angular dependence of the emission peak which is seen to move toward shorter wavelengths (see figure 6.21B and table 6.3), while reference emission peak position and width are practically unchanged at different detection angles. The *Q* value retrieved from cavity emission at 0° is 53, which is larger than the value obtained from transmission or reflectance measurements.

This can be related to the inhomogeneity of the defect layer thickness. Smaller area of the sample are probed during cavity emission measurements than reflectance or transmission ones due to the small dimension of the laser spot used to excite the cavity. Thus the

negative effect of thickness inhomogeneity of the defect layer on the cavity peak width will be diminished if smaller area are probed, leading to cavity narrowing.

Furthermore, cavity emission was not equal if measured at different points supporting inhomgeneity of the defect layer. Also the angular dependence of peak position in the low angle region did not follow a regular trend for some angles (which are not shown in the figure). It is likely that the procedure for device fabrication need to be optimized to improve the quality of the depositions and their thickness homogeneity.

Imperfections in the structure can also be responsible for the presence of uncoupled emission clearly seen at 50° detection angle.

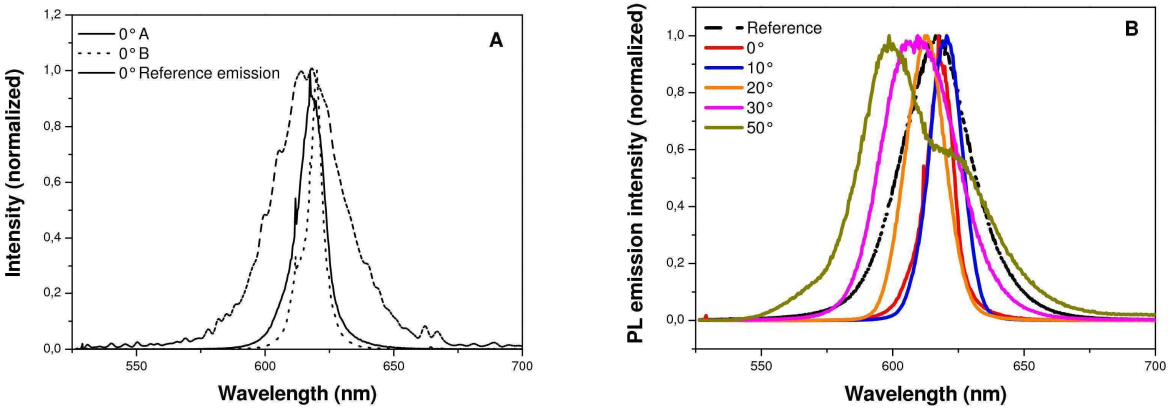

Figure 6.21 Normalized emission spectra of reference emission (taken at 50° detection angle) and cavity emission at 0° detection angle taken at two different points of the sample (A); Cavity emission at different observation angles (B)

The width of the emission cavity is also seen to increase at higher detection angles (see Table 6.3) leading to lower *Q* values. This was also observed by Jaseniack et al. [32] and Rabaste et al. [15] and it was explained by the higher QD absorption at shorter wavelength. This has an adverse effect on *Q* factor.

Angle (°)	Cavity emission position (nm)	Cavity emission FWHM peak width (nm)	Reference e,mission peak position (nm)	Reference FWHM emission peak width (nm)
0	618	11.14	618	32
10	620	14.54	-	-
20	612	17	-	-
30	608	30.12	-	-
50°	598	44.66	617	30

Table 6.3 Observed cavity emission position and peak width and reference emission position and peak width

The peak position at normal direction is at 618 nm, in agreement with observed cavity position and with simulations for a 1.74 nm thick cavity as shown from results in table 6.2. The agreement of simulated and experimental cavity peak position is not good which can again be attributable to defect layer thickness inhomogeneity.

In order to have information on the emission enhancement, the as-detected emission intensity of the reference and cavity emission at normal direction are reported in figure 6.22.

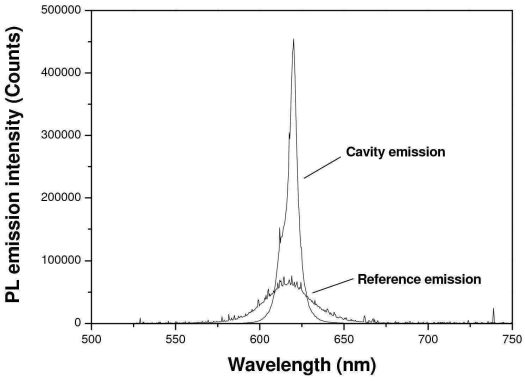

Figure 6.22 Spectral enhancement of cavity emission with respect to reference emission at 0° detection angle

The emission is strongest in the case of quantum dots in the cavity, with a spectral enhancement factor of about 7, indicating the modification of the emission properties of QD.

In order to see if lasing emission was possible with this device, emission measurements were performed under increasing excitation power using the experimental setup described in Chapter 2 employed for ASE experiments. The excitation wavelength was 400 nm and the geometry configuration of the experiment was analogue to that depicted in figure 6.18. Data are shown in figure 6.23.

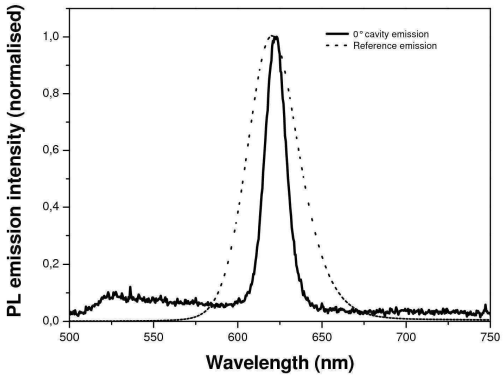

Figure 6.23 Cavity and reference emission under femptosecond laser excitation at 400 nm. No lasing was seen at increasing excitation power

Spectral narrowing was again observed with respect to reference spectrum, even if no lasing emission was detected, probably because of low concentration of quantum dots or insufficient feedback due to low mirror reflectivity. These parameters can be adjusted along with overall improvement of device quality, motivating further attempts in laser emission obtainment.

Despite the absence of lasing, the data presented so far suggest that the described cavity fabrication procedure is compatible with quantum dots, whose emission properties are maintained and could be studied under microcavity effect.

In particular, the UV treating of the titanate has proved to be a useful method to couple high refractive index materials with QDs emitters.

This possibility can be exploited for further studies of quantum dots emission in an optical cavity, for lasing conditions tailoring and fabrication of other type of 1D optically active photonic structures similar to those presented in ref.s [19-21].

References

[1] Tomczaka N, Janczewski D., Hana M., Vancsoa G.J., Progress in Polymer Science, 2009, **34**, 393

[2] Chan Y., Snee P.T., Caruge J.M., Yen B.K., Nair G.P., Nocera D.G., Bawendi M.G., J. Am. Chem. Soc., 2006, **128**, 3146

[3] Selvan S.T., Bullen C., Ashokkumar M., Mulvaney P., Adv. Mater., 2001, **13**, 985

[4] Sundar V.C., Heisler H.J., Bawendi M.G., Adv. Mater., 2002, **14**, 739

[5] Petruska M., Malko M.V., Voyles P.M., KlymovV.I,, Adv Mat, 2003,**15**, 610

[6] Snee P.T., Chan Y., Nocera D.G., Bawendi M.G., Adv Mat, 2005, **17**, 1131

[7] Wang Y.A., Li J.J., Chen H., Peng X., J. Am. Chem. Soc. 2002, **124**, 2293

[8] Pellegrino .T, Manna L, Kudera S., Liedl T, Koktysh D, Rogach A.L., al. Nano Lett., 2004, **4**, 703

[9] Sill K., Emrick T., Chem. Mater., 2004, **16**, 240

[10] JasieniakJ., Pacifico J., Signorini R., Chiasera A., Ferrari M., Martucci A., Mulvaney P., Adv. Funct. Mater., 2007, **17**, 1654

[11] Jacek Jasieniak, Paul Mulvaney, J. Am. Chem. Soc, 2007, **129**, 2841

[12] Almeida R. M., Goncalves M. C. , Portal S., J. Non. Cryst. Solids, 2004, **345&346**, 562

[13] Yoon J., Leea W., Caruge J.M., Bawendi M, Thomas E.L., Kooi S., Prasad P. N., Appl. Phys. Lett., 2006, **88**, 091102

[14]Chiasera A, Belli R., Bhaktha S. N. B., Chiappino A. , Ferrari M., Jestin Y. , E. Moser, Righini G. C. , Tosello C., Appl. Phys. Lett., 2006, **89**, 171910

[15] Rabaste S., Bellessa J., Bonnand C., Plenet J., Spanhel L., Eur. Phys. J. B, 2004, **42**, 47

[16] Poitras C.B., Lipson M., Du H., Hahn M.A., Krauss T..D., Appl. Phys. Lett., 2003, **82**, 4032

[17] Schubert E.F., Hunt N. E. J., Malik R.J., Micovic M., Mliller D.L., J. of Lightwave technology, 1996, 14, 1721

[18] Yoon J., Lee W., Thomas E.L., Nano Lett. 2006, **6**, 2211

[19] Scotognella F., Monguzzi A., Cucini, M. , Meinardi F., Comoretto D., Tubino R. **I**nternational Journal of Photoenergy, 2008, Article ID 389034

[20] Dowling J.P., Scalora M., Bloemer M.J., Bowden C..M., J. Appl. Phys., 1994 , **75**, 1896

[21] Komikado T., Yoshida S., Umegaki S., Appl. Phys. Lett., 2006, **89**, 061123

[22] "Semiconductor and metal nanocrystals" edited by Victor I. Klimov, 2004 (Marcell Dekker, Inc)

[23] Woggon, U., *Optical properties of semiconductor quantum dots*. Vol. 136. 1996: Springer

[24] Klimov V. I., Mikhailovsky A. A., Xu S., Malko A., Hollingsworth J. A., Leatherdale C. A., Eisler H.-J., Bawendi M. G., Science ,2000, **290**, 314

[25] Klimov V. I., Mikhailovsky A. A., McBranch D. W., Leatherdale C. A., Bawendi M. G., Science, 2000, **287**, 1011

[26] Chan Y., Steckel J.S., Snee P.T., Caruge J.M., Hodgkiss J.M., Nocera D.G., Bawendi M.G., Appl. Phys. Lett., 2005, **86**, 073102

[27] Jasieniak J. J., Fortunati I., Gardin S., Signorini R., Bozio R., Martucci A., Mulvaney P., Adv. Mater., 2008, **20**, 69

[28] Dal Negro L., Bettotti P. , Cazzanelli M., Pacifici D., Pavesi L., Optics Communications 2004, **229**, 337

[29]Svelto O., Hanna D., Priciples of lasing, Springer,4th edition

[30] Schubert E. F., "*Light-Emitting Diodes*", 2nd ed., Cambridge University Press, Cambridge 2006

[31] Liu J.S., Tanaka T., Sivula K., Alivisatos A.P., Fréchet J..M.J. J. Am. Chem. Soc., 2004, **126**, 6550

[32] Jasieniak J., Sada C., Chiasera A., Ferrari M., Martucci A., Mulvaney P., Adv. Fun. Mat., 2008, **18**, 3772

Chapter 7

ZnS NCs loaded hybrid matrix composites

7.1 Introduction

Nanocomposites made from a sol-gel hybrid materials as matrix and nanoparticles as fillers are particularly interesting for the tuning of optical properties. In fact, this can be achieved by acting on the type of both the employed organosilane and the embedded nanoparticles.

In particular, we focused our attention in obtaining high refractive index materials and the synthesis of nanocomposites from sol-gel derived hybrid matrix as host for zinc sulfide nonoparticles has been worked out.

Among semiconductors materials, zinc sulfide exhibits interesting properties for optical application due to its transparency in the visible range, large refractive index value (n = 2,36 at 620 nm) [1], UV filter behavior and, if doped with particular ions, luminescence properties. For these reasons, it has been exploited and introduced in various types of matrices to obtain functional materials [2-8].

The host material used herein consists in a hybrid organic-inorganic epoxy-based material containing phenyl groups, which have been proved to modify both thermal and optical properties [9]. Hybrid materials possess some advantages over organic polymers, such as improved thermal and physical properties. The sol-gel route for the synthesis of these materials allows a simple way to homogeneously introduce organic moieties by using specific organosilanes, thus changing and tuning physical and functional features [10-13].

ZnS nanocrystals (NCs) have been introduced in these materials and nanocomposite thin films have been obtained. In particular, refractive index changes upon introduction of phenyl groups and zinc sulfide nanocrystals are here addressed.

Both these components have been proved to raise refractive index and to be transparent in the visible range.

7.2 ZnS nanocomposite depositions

7.21 ZnS NCs and nanocomposite synthesis

Two hybrid sols, named sol **GZ** and sol **DGZ**, with different compositions have been prepared using Glycidoxypropyltrimethoxysilane (*GPTMS*), zirconium tetraisopropoxide (Zr*(OPr^i)*) and dyphenyldymethoxysilane (*DPDMS*) as precursors.
GZ and **DGZ** solutions were synthesized using *GPTMS*/Zr*(OPr^i)* = 75:25 and *DPDMS*/*GPTMS*/ Zr*(OPr^i)*= 50:25:25 precursors' molar ratios, respectively.
Sol GZ was prepared hydrolyzing GPTMS with a stoichiometric amount of water at ambient temperature for 5 hours, after that a solution of methoxyethanol, Zr*(OPr^i* and *NaOH* (NaOH:Alkoxides = 0.001) was added drop wise.
Sol DGZ was synthesized by mixing *DPDMS* and Zr*(OPr^i* and adding drop wise a solution containing water (*H_2O*/(Zr*(OPr^i)* r+*DPDMS*) = 0.33), NaOH, (NaOH:Alkoxide = 0.001) and methoxyethanol. After stirring for 15 minutes, *GPTMS*, hydrolyzed as previously described, was added. These solutions were refluxed for 2.5 hours at 80°C. Alkoxide concentration was kept constant and equal to 2.5

ZnS NCs have been synthesized adapting the procedure described by Kho et al. [14]. First, 20 ml of a 1M water solution of Tris(hydroxymethyl)aminomethane was prepared. Then cystein, mercaptoethanol and a 1M solution of zinc sulfate (*$ZnSO_4$*) in water was poured in the reaction flask. The concentration of Zn precursor in this solution was 0.1 M. Cysteine and mercaptoethanol were added to give a molar ratio of 0.25 and 2.5 with respect to the zinc precursor. This solution was stirred for 10 minutes. Finally, sodium sulfide (*Na_2S*) (Zn/S = 1) dissolved in water was added under stirring. The solution was incubated for 1 hour at 50°C. ZnS NCs were flocculated by adding ethanol and collected by centrifuging at 4000 rpm. The precipitate was dispersed in 8 ml water. At this stage, tetrahydrofuran (*THF*) and 400 μl of mercaptohexanol were added and an opaque solution was obtained. This dispersion became transparent after stirring for 12 hours. Finally, ZnS NCs were precipitated with acetone and redispersed in about 4 ml of 2:1 v/v mixture of *THF* and water to give a clear and concentrated ZnS NCs solution which was used for nanocomposite synthesis.

Nanocomposite depositions were obtained with two different concentrations, referred to as *loading level 1* and *loading level 2*. These have been prepared by mixing 250 μl (*loading level 1*)and 100 μl (*loading level 2*) of either **DGZ** or **GZ** solutions with 0.5 ml

of ZnS NCs colloids. To improve NCs compatibility with the matrix 10 μl of mercaptopropyltrimethoxysilane were also added.
The obtained solutions were aged 12 hours, after which they were three-fold diluted with methoxyethanol.
These solutions were spun on a silicon substrate at 5000 rpm for 20 sec to obtain thin films that were heat treated at 150°C for 30 minutes. Thick films (up to 10 μm) were also obtained by casting the solution on a quartz substrate at 80°C.
Films were analogously obtained from **GZ** and **DGZ** solutions without ZnS NCs.

7.2.2 Results and discussion

Among the large number of synthetic procedures proposed in the literature [15-21], the synthetic route for ZnS NCs described in ref. [14] has been taken into account due to its easiness, high yield and good colloidal stability. Cysteine was there employed as the capping ligand for such NCs. This molecule forms a Zn-S complex, thus it binds to the Zn sites of NC surface. The resulting NCs expose the carboxylic functionality of cysteine to the outer environment leading to very hydrophilic surface which makes NCs very stable only in water media, while colloidal stability is lost in organic solvents.
Cysteine capped ZnS are thus not compatible with the developed hybrid sol whose environment is hydrophobic, since organic solvents and phenyl groups are used in such materials. This would eventually leads to the precipitation of the NCs from the solution, preventing the realization of homogeneous nanocomposites.
In order to make the ZnS NCs compatible with the hybrid materials, we developed an analogous procedure for making the as-synthesized water soluble NCs compatible with the sol-gel matrices. Mercaptohexanol and mercaptopropyltrimethoxysilane are proper ligands for good compatibility with the hybrid environment and the described procedure has been designed to enrich the ZnS NCs surface with these molecules.
Mercaptoethanol was used in the ZnS synthesis as the main capping agent instead of cysteine since this resulted to facilitate the subsequent exchange with mercaptohexanol.
In fact, cysteine probably bounds too strongly to ZnS NCs surface, making it more difficult to be displaced by a new capping agent, while this procedure is more efficient if mercaptoethanol is used as the pristine ligand.

In order to easily extract the particles by flocculation with ethanol, the usage of a small amount of cysteine was found to be necessary. Probably this makes NCs surface sufficiently hydrophilic to allow separation by addition of an organic solvent from the original solution and unreacted reagents.

It is likely that the residual presence of cysteine or mercaptoethanol bound on ZnS NCs surface after mercaptohexanol exchange makes it necessary to add water in the final solvent mixture in order to obtain a stable colloidal solution.

The described functionalization procedure for ZnS NCs was found to be compatible with the sol-gel matrices synthesized in this work.

UV-Vis absorption spectra of ZnS NCs after each stage of the synthesis or functionalization procedure are reported in figure 7.1.

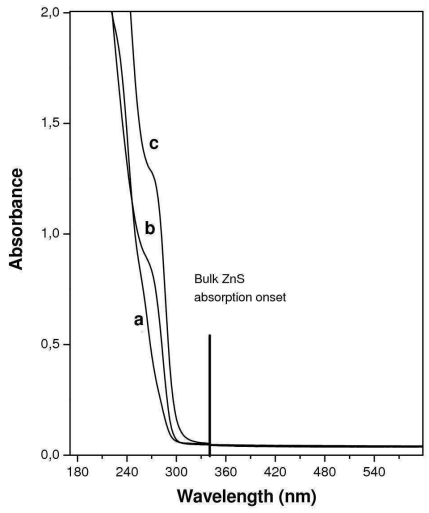

Figure 7.1 Absorption spectra of as synthesized ZnS nanocrystals solution (a), after ethanol precipitation and redispersion in water (b) and final doping solution (c). All spectra were taken with a dilution of 1:400. The vertical line represents the position of the absorption band of bulk ZnS.

The absorption band due to ZnS nanoparticles is blue shifted compared to bulk ZnS (absorption onset at 340 nm, [15]). After the first ethanol precipitation and dispersion in water, the absorption feature of ZnS NCs appears as a shoulder at around 270 nm (figure 1 curve b), similarly to spectra reported in other works [21]. Concentration of particles in solution is increased after each stage of the described processing, reaching a final concentration in the *THF*/water mixture of about 35 g/L (figure 7.1 curve c), as estimated from the weight of dried powder.

XRD pattern (figure 2) of the dried precipitate obtained from final doping solution can be assigned to sphalerite ZnS (JCPDS 05-0566). The same diffraction pattern has been obtained also for the ZnS NCs loaded DGZ sol-gel film (see figure 7.2).

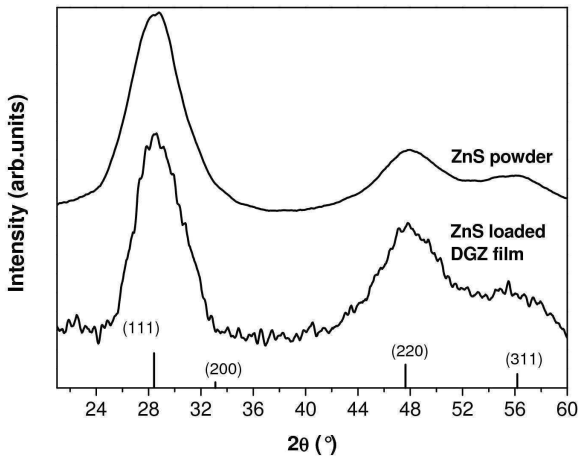

Figure 7.2 XRD patterns of dried ZnS powders and of GZ film doped with the same ZnS nanoparticles. The main diffraction planes with their relative intensity (ZnS sphalerite JCPDS 05-0566) are also indicated at the bottom of the picture.

HR-TEM images showed the presence of nanoparticles having an almost spherical shape with a mean diameter D = 4.8 nm and standard deviation σ = 1.0 nm (see figure 7.3a).

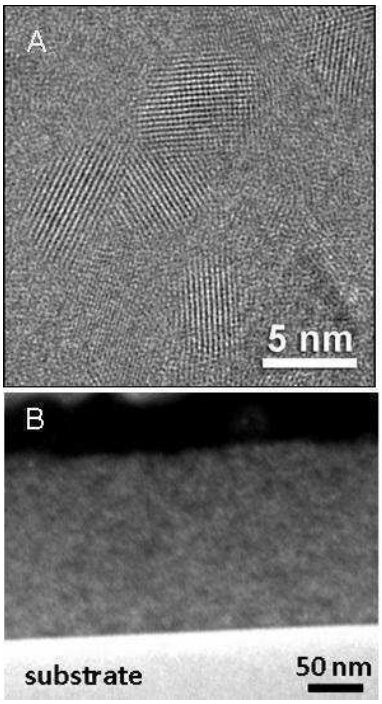

Figure 7.3 (A) High-resolution image of ZnS NCs showing <111> lattice planes fringes of sphalerite ZnS; (B) Cross-sectional Dark-Field S-TEM image of the DGZ hybrid film containing ZnS NCs corresponding to *doping level 2* (see text)

From EDX compositional analysis it was evaluated an atomic ratio Zn/S of about 0.9 ± 0.1. Figure 7.3b shows the cross-sectional dark-field S-TEM image of the ZnS NCs loaded **DGZ** film in which the contrast is related to the atomic number of the elements present in the different region of the sample. The film appears quite homogeneous and no large aggregates (in the order of tens of nanometers) able to scatter light significantly are seen. This degree of homogeneity is important for keeping transparency.

The film thickness is (160 ± 10) nm as retrieved from STEM image. From EDX compositional analysis it was evaluated an atomic ratio Zn/S of about 0.9 ± 0.1 also in the case of the **DGZ** nanocomposite film.

The hybrid material used as the matrix has been synthesized from *GPTMS*, an organoalkoxide presenting an epoxy ring functionality that can be polymerized to give a polyethylene oxide network. *DPDMS* is also added in order to homogeneously introduce phenyl groups by co-condensation of the alkoxides groups of *DPDMS* with those of the other. Zr*(OPr^i)* is finally introduced in the reaction system both to catalyze the epoxy ring polymerization [24] and to promote the development of a stiff SiO_2-ZrO_2 mixed oxide network. The refractive index of ZrO_2 is quite high (in the 2.13-2.20 range for monoclinic ZrO_2 depending on the crystallographic axis [1]) and it also contributes to raise the overall refractive index.

Figure 7.4 shows the FT-IR spectra of undoped hybrid films. Peaks at 3075, 3046, 1229, 1191, 743, 700 and 520 cm^{-1} in **DGZ** spectrum can be assigned to phenyl vibrations [22,23]. No epoxy ring vibrations (2995-3060 cm^{-1} band) can be observed in **GZ** spectrum which can be related to the *GPTMS* epoxy group polymerization [24], while a partial overlapping with phenyl vibrations is present in **DGZ** films. The band around 1060 cm^{-1} and the doublet at 2900 cm^{-1} are assigned to silica and C-H vibrations respectively [22,23]. Very similar FT-IR spectra (data not shown) were obtained for hybrid films incorporating ZnS NPs.

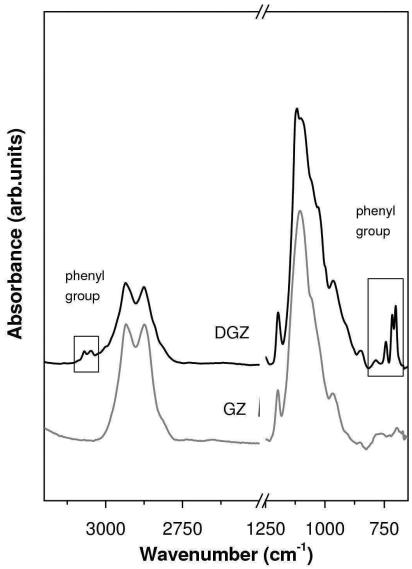

Figure 7.4 FT-IR spectra of undoped GZ and DGZ sol-gel hybrid matrices

UV-Vis measurements (figure 7.5) made on thick depositions on quartz substrate showed a clear change in the absorption edge after introduction of ZnS NCs.

Also in the case of the composite films, a blue shifting of the absorption edge, compared to bulk ZnS, is evident. This is less pronounced in the case of **DGZ** matrix due to absorption contribution of phenyl groups at higher wavelengths, which is evident by comparing **GZ** and DGZ matrices spectra.

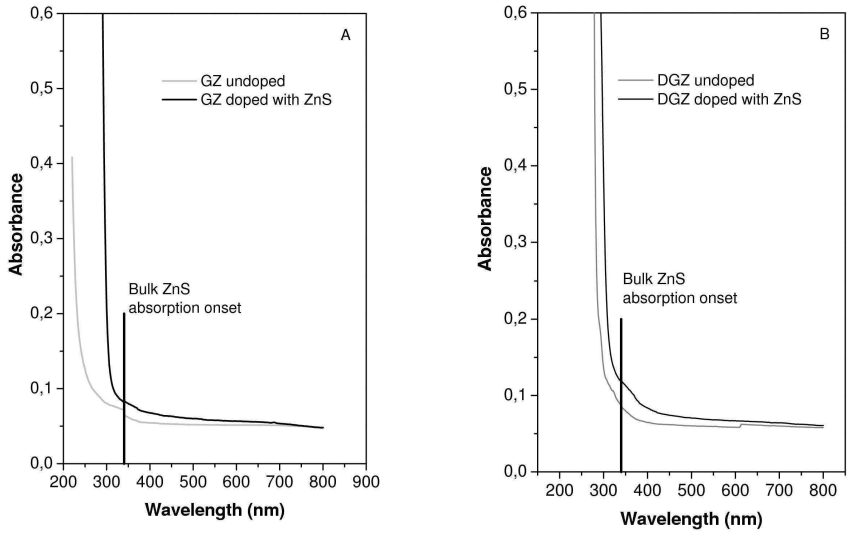

Figure 7.5 UV-Vis absorption spectra of GZ (A) and DGZ (B) films deposited on quartz substrate. The vertical line represents the position of the absorption band of bulk ZnS

In figure 7.6 it is reported the photoluminescence spectrum of the ZnS NCs loaded DGZ film (with the corresponding optical absorption spectrum): the PL band centered on 420 nm can be correlated to defect-type luminescence likely arising from defective surface states [22].

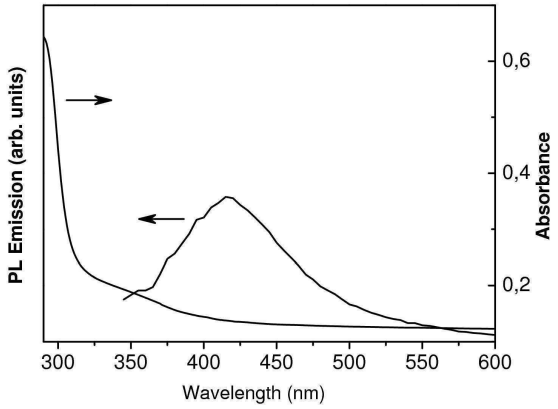

Figure 7.6 UV-Vis absorption and photoluminescence spectrum (excitation wavelength 337 nm) for ZnS NCs doped DGZ hybrid film.

In order to have a rough estimate of the filling factor *f* (i.e., the volume fraction) of ZnS particles in the nanocomposite depositions, we used the ZnS NCs solution concentration and densities of ZnS (4 Kg/m^3 [1]) while the densities used for hybrid materials were measured by Archimedean method on bulky samples and found to be 1.26 Kg/m^3 and 1.32 Kg/m^3 for bulk **DGZ** and **GZ**, respectively. The values of *f* for ZnS NCs were estimated to be about 0.04 and 0.1 for *loading level 1* and *loading level 2* respectively.

As expected, ellipsometry measurements showed an increase in refractive index upon increasing concentration of ZnS NCs (Table 7.1). Analogously, the effect of refractive index enhancement upon introduction of phenyl groups can be appreciated by comparing **GZ** and **DGZ** hybrids at the same ZnS loading level.

	Refractive index (@ 630 nm)	**Film thickness (nm)**
GZ	1.50	576
GZ + ZnS Loading level 1	1.52	257
GZ + ZnS Loading level 2	1.56	162
DGZ	1.53	115
DGZ + ZnS Loading level 1	1.56	231
DGZ + ZnS Loading level 2	1.59	149

Table 7.1 Refractive index and film thickness of nanocomposite thin films

To evaluate the ZnS NCs concentration in the films, we used Maxwell-Garnett theory which is an effective medium model which can be applied to materials embedding spherical inclusions.

This model was used to calculate the refractive index change of the nanocomposite over the measured wavelength range as a function of the ZnS NCs filling factor, *f* (i.e., the volume fraction): we used for the matrix the measured ellipsometric data and ZnS literature data [27] for the NCs (assuming the average size measured by TEM).

Finally, we used the Maxwell-Garnett theory to model the refractive index change upon variation of the ZnS NCs content in order to compare the theoretical results with the experimental ones. This was done only for ZnS NCs doped **DGZ** matrix as representative example.

Calculations were carried out over the wavelength range of the experimental measurements as a function of the ZnS NCs filling factor *.f.* We used for the matrix the measured ellipsometry data and ZnS literature data [27] for the NCs and the TEM measured average size was assumed. In figure 7.7A, the calculated change of the refractive index curves is shown. A linear trend of the refractive index evaluated at 630 nm is found in the 0-0.3 filling factor range (see figure 7.7B). This is in agreement with the reported linear dependence of refractive index on volume fraction of the inorganic NCs [23].

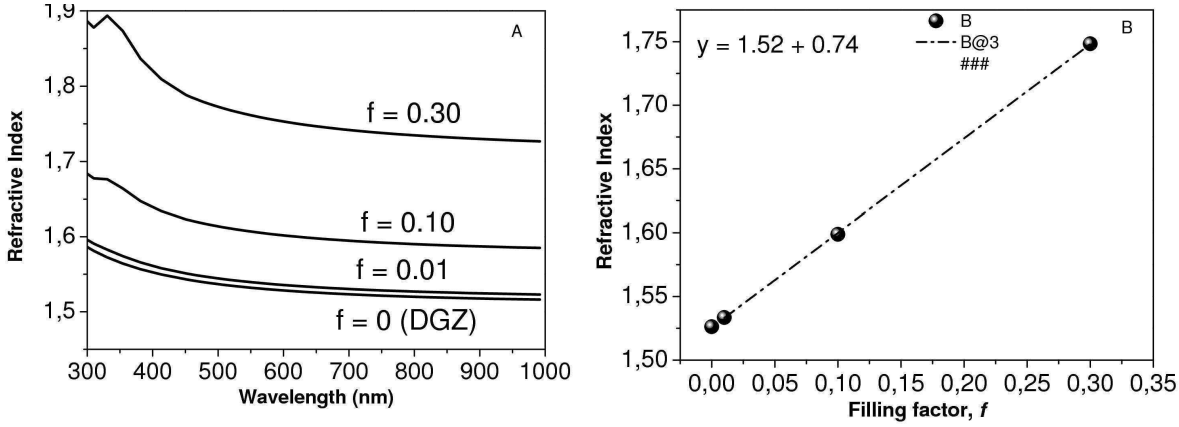

Figure 7.7 Maxwell-Garnett simulations of the refractive index of ZnS NCs loaded **DGZ** as a function of the ZnS filling factor *f* (A) and linear evolution of the refractive index computed at 630 nm (B)

A best fit procedure has been used to evaluate the ZnS volume fraction from the measured refractive index (see figure 7.8). A filling factor value *f* of 0.024 and 0.077 for ZnS loaded **GZ** hybrid has been found for *loading level 1* and *loading level 2*, respectively. Analogously, a filling factor of 0.033 and 0.081 was calculated for **DGZ** nanocomposites, in good agreement with the nominal values.

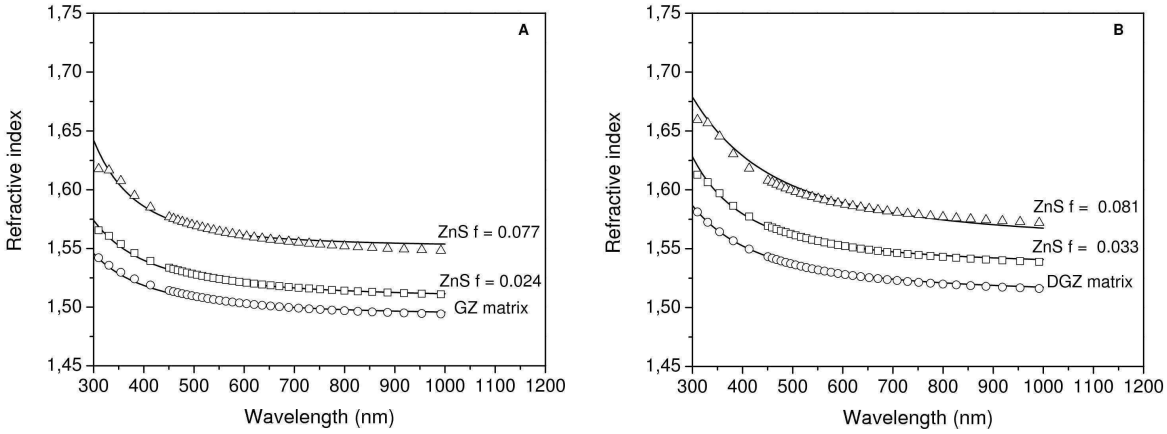

Figure 7.8 Experimental refractive index curves (solid line) and corresponding Maxwell-Garnett fit (open symbols) for **GZ** nanocomposites (A) and **DGZ** nanocomposites (B). The corresponding filling factor *f* is indicated.

References

[1] Lide D. R., Handbook of Chemistry and Physics, CRC Press, 72nd edition.

[2] Lu C., Gao J., Fu Y., Du Y.,. Shi Y, Su Z., Adv. Fun. Mat. 2008, **18,** 3070

[3] Chung S., Zhu J., Shen Y., Hu C., Chen L., Langmuir 2007, **23,** 850

[4] C. Lu, Z. Cui, Y. Wang, Z. Li, C. Guan, B. Yang, J. Shen, J. Mat. Chem. 2003, **13,** 2189

[5] Yang Y., Huang J., Liu S., Shen J., J. Mat. Chem. 1997, **7**,131

[6] H. Althues, R. Palkovits, A. Rumplecker, P. Simon, W. Sigle, M. Bredol, U. Kynast,L. Kaskel, Chem. Mat. 2006, **18**, 1068

[7] J. Zhuang, X. Zhang, W. Gang, D. Li, W. Yang, T. Li, J. Mat. Chem. 2003, **13**, 1853

[8] T. Kezuka, M. Konishi, T. Isobe, M. Senna, J. Lum. 2000, **87-89**, 418

[9] S. O' Brien, M. Copuroglu, G. M. Cren, Appl. Surf. Sci. 2007, **253**, 7969

[10] P. Judeinstein, C. Sanchez, J. Mat. Chem. 1996, **6**, 511

[11] C. Sanchez, J. Beatriz, P. Belleville, M. Popall, J. Mat. Chem. 2005, **15**, 3559

[12] U. Shubert, N. Husing, A. Lorenz, Chem. Mat. 1995, **7**, 2010

[13] D. Buso, G. Della Giustina, G. Brusatin, M. Guglielmi, A. Martucci, A. Chiasera, M. Ferrari, F. Romanato, J. Nanosc. Nanotech. 2009, **9**,.1858

[14] R. Kho, C. Torres-Martinez, R. Mehra, J. Col. Inter. Sci. 2000, **227**, 561

[15]J. Nanda, S. Sapra, D. Sarma, Chem. Mat. 2000, **12**,1018

[16] G.Ghosh, M. Naskar, A. Patra, M. Chatterjee, Opt. Mat. 2006, **28**, 1047

[17] T. Kuzuya, Y. Tai, S. Yamamuro, K. Sumiyama, Sci Tech. Adv. Mat. 2005, **6**, 84

[18] L. Li, N. Pradhan, Y. Wang, X. Peng, Nano Letters 2004, **4**, 2261

[19] Y. Zhao, Y. Zhang, H. Zhu, G. Hadjipanajis, J. Xiao, J. Am. Chem. Soc. 2004, **126,** 6874

[20] P. Calandra, M. Goffredi, V. Liveri, Col. Surf. A 1999, **160**, 9

[21] A. Celikkaya, M. Akinc, J. Am. Ceram. Soc. 1990, **73**, 2360

[22] L. Prado, E. Radovanovic, H. Pastore, Y. Yoshida, I. Torrioni, J. Polym. Sci. A 2000, **38**, 1580

[23] D. Ou, A. Seddon, J. Non Cryst. Solids 1997, **210**, 187

[24] G. Philipp, H. Schmidt, J. Non Cryst. Solids 1986, **82**, 31

[25] H. Tang, X. Guoyue, W. Luquian, P. Lijia, W. Ling, Acta Mat. 2004, **52**, 1489

[26] L. Zimmerman, M. Weibel, W. Caseri, U. Suter, J Mat. Res. 1993, **8**, 1742

[27] E.D. Palik, Handbook of Optical Constants of Solids; Academinc Press, 1985

Chapter 8

Conclusions

In this work, the synthesis and processing of nanostructured materials for optical applications has been described.

With the aim of introducing specific functionalities and variations in the dielectric properties of the materials, NPs of the desired materials, obtained by means of colloidal synthetic routes, have been introduced in host matrices to obtain multifunctional nanocomposite materials.

The activity can be divided in:

a) synthesis and characterization of nanocrystals based on cadmium selenide, titanium dioxide, zinc sulfide and layered titanates and
b) their applications in active waveguides with photoluminescence or optical gain properties, conformal coating and coplanar microcavities with cadmium selenide NPs emitters.

The procedures for the synthesis of CdSe particles with tunable size have been presented in Chapter 3. In order to increase the stability of these particles, surface coverage with larger band gap semiconductor has been addressed. This was accomplished adopting the SILAR procedure which allows tailoring the composition of the shell by growing monolayers one at a time. A shell with graded composition was adopted by growing a CdS layer on pristine CdSe surface and ending with a ZnS layer. A cadmium zinc sulfide alloy was also attempted. A synthetic procedure was developed by successive steps which finally resulted in the desired shell structure, even if further optimization is required to achieve greater particles stability.

These particles were introduced in ZrO_2 sol-gel waveguides and tested in ASE (Amplified Spontaneous Emission) experiments.

The obtained samples showed optical gain properties under both 1-photon and 2-photon excitation. The stability under excitation need to be further improved, particularly under 2-

photon excitation. This requires further work, which has to be manly directed toward thicker ZnS layer coverage with better structural quality. Precursor's reactivity, role of the complexing agents and synthetic parameters are all key parameters that must be tailored to improve shell quality.

A sol-gel synthesis for TiO_2 nanoparticles has been developed and described in Chapter 4.

Synthetic parameters have been optimized in order to have transparent colloidal solutions of crystalline titania particles. Nanocrystals in the anatase crystal structure in the 3-5 nm diameter range have been obtained.

The obtained particles could be extracted from the solution and introduced in an epoxy-based sol-gel matrix.

This allows for transparent depositions with tunable refractive index in the 1.51-1.89 range.

In order to extend the processing and engineering of titanium oxide materials, layered titanates compounds were taken into consideration. This class of lamellar compounds are constituted of nanosheets where $[Ti_mO_{m+1}]^{2-}$ usually units arrange themselves in a two-dimensional crystalline layer intercalated by cations necessary for charge balance. We have developed a synthetic route in which titanate nano-sheets are produced by reaction of a titanium alkoxide and an organic base. Titanate nanosheets have been obtained which are at least partially exfoliated resulting in transparent colloidal solution.

TEM characterization showed the lamellar nature of the obtained materials where also the lateral extension of the sheet was in the nanometric (about 5 nm) range.

Depending on the type of organic base used, Tetramethylammonium hydroxide (*TMA*) and 6-Amino-1-hexanol (*AH*), titanates with different structural characteristics and processing behavior have been obtained. In particular, those derived from *TMA* are stable in aqueous solutions, while those derived from *AH* could be used also in alcoholic media. The former will be referred to as *TMA-Ti*, the latter as *AH-Ti*.

These materials could be modified by UV curing or ion-exchange processes, allowing for modifications or treatments by methods other than thermal annealing.

The behavior of *TMA-Ti* titanates under UV irradiation and thermal treatment has been investigated through X-Ray Diffraction and ellipsometry. Enhancement of refractive index was correlated with the contraction of titanate layers leading to densification of the material. This permitted to obtain high refractive index depositions at temperature as low

as 200°C. This was applied in DBR (Distributed Bragg Reflectors) obtained by alternatively depositing titanate and silica as the high and low refractive index layers. Low temperature processing not only allowed to obtain more favorable conditions for grating fabrication in terms of defects formation, but also to make high index material processing compatible with Quantum Dots. This was exploited for the fabrication of a coplanar microcavity incorporating quantum dots. This structure has been described in Chapter 6. The modification of the spontaneous emission of the QD emitters under cavity effect has been characterized. This confirmed the possibility of coupling the developed high refractive index material processing with quantum dots. No lasing emission was observed with this device, possibly due to low concentration of QDs in the defect layer or low reflectivity of the mirrors. These parameters can be enhanced along with the overall quality of the fabrication procedure thus greatly motivating for future work or improvement of this device.

In Chapter 5 it was shown that UV irradiation resulted also in the change of solubility behavior. Thus, interesting future perspectives are also related to exploitation of UV-induce solubility change for UV patterning of titanates depositions.

One goal of the present work was to synthesize a material presenting a luminescent functionality, high refractive index and good processability allowing for defect free bulk samples.

This task has been approached synthesizing a nanocomposite material by mixing different functional NPs with suitable matrices.

AH-Ti titanates have been used to enhance the refractive index, QDs were used as the active component and the processing behavior of this material has been tailored with proper choice of the matrix material (a polyethylene glycol functionalized silane) with the aim of enhancing the plasticity allowing for stress relaxation during drying processes involved in sample fabrication. The latter is a serious problem for thick coatings or bulk samples often leading to severe cracking or damage.

AH-Ti titanates are compatible with QDs, allowing for optically transparent materials.

By varying the amount of titanates and matrix, the refractive index could be varied from 1.5 to the 1.8. The last value was obtained with a pure titanate matrix at an annealing temperature of 200°C which does not damage QDs particles.

Such nanocomposites were used as waveguides and thick films with a refractive index of 1.7 were patterned with nanoimprinting techniques.

This strategy was also used for encapsulation of LED devices, where thick coatings with high refractive index embedding luminescent material are desirable to enhance light extraction from LED and to produce white light through down-conversion.

The above described QD-loaded titanate material was used for this application and it has proved to be quite promising if used with aerosol based deposition techniques, even if cracking problems could not be solved completely. Thus, this activity was continued with a sol-gel hybrid material doped with quantum dots since it showed more favorable processing conditions.

The properties of titanium dioxide can be exploited for optical gas sensing applications if gold nanoparticles are introduced in a crystalline TiO_2 matrix.

The anatase-TiO_2 particles have been successfully used as matrix material for this application allowing for porosity tailoring, morphological and gold-titania interface to be studied from optical measurements.

Optical sensing were proved by variation in thin film absorbance at wavelengths near the plasmon resonance of gold NPs caused by presence of gas analytes

Gold nanorods were introduced in *TMA-Ti* titanates. Gold nanorods are known to spheroidize upon thermal treatment, losing their peculiar optical properties. We found that the developed UV densifying treatment applied prior to heat treatment results in the retainment of rod optical features to higher temperature. Improved stability of such nanostructures is very interesting since it allows extending their exploitation in optical applications.

Finally, composites with enhanced refractive index were realized by introducing ZnS NCs in hybrid sol-gel materials based on Diphenyl Dimethoxysilane and Zirconium isopropoxide.

A synthesis of ZnS NPs, which could be functionalized in order to be introduced sol gel matrix, has been developed.